ROYAL HOLLOWAY, UNIVERSITY OF LONDON

Photon Detection and Associated Systematics in Dark Matter Experiments

by

Joseph B. McLaughlin

A thesis submitted in partial fulfillment for the
degree of Doctor of Philosophy

in the

School of Engineering, Physical, and Mathematical Sciences
Department of Physics

April 2023

Declaration of Authorship

I, JOSEPH B. MCLAUGHLIN, declare that this thesis titled, 'PHOTON DETECTION AND ASSOCIATED SYSTEMATICS IN DARK MATTER EXPERIMENTS' and the work presented in it are my own. I confirm that:

- This work was done wholly or mainly while in candidature for a research degree at this University.

- Where any part of this thesis has previously been submitted for a degree or any other qualification at this University or any other institution, this has been clearly stated.

- Where I have consulted the published work of others, this is always clearly attributed.

- Where I have quoted from the work of others, the source is always given. With the exception of such quotations, this thesis is entirely my own work.

- I have acknowledged all main sources of help.

- Where the thesis is based on work done by myself jointly with others, I have made clear exactly what was done by others and what I have contributed myself.

Signed:

Date: 27/Apr/2023

"Let's think the unthinkable, let's do the undoable. Let us prepare to grapple with the ineffable itself, and see if we may not eff it after all."

–Douglas Adams

ROYAL HOLLOWAY, UNIVERSITY OF LONDON

Abstract

School of Engineering, Physical, and Mathematical Sciences
Department of Physics

Doctor of Philosophy

by Joseph B. McLaughlin

The nature of dark matter is a problem at the frontier of astroparticle physics research, and its solution will have profound implications for the Standard Model of particle physics and the Standard Cosmological Model. There are several experiments—currently running and planned for the future—attempting to detect elastic collisions between dark matter and noble liquid scintillator targets. These experiments, and their treatment of detector specific systematics, are the focus of this work. One such experiment is the Dark matter Experiment using Argon Pulse-shape discrimination (DEAP). Discussed in this work are DEAP's optical, instrumentation, and background systematics in the context of a Profile Likelihood search for Weakly Interacting Massive Particles (WIMPs). This treatment of systematic effects leads to significantly increased sensitivity to WIMPs in comparison to a 'cut and count' approach. For a $100\,\text{GeV}$ WIMP mass over an exposure of $3.5\,$tonne-years, the Profile Likelihood analysis sets a WIMP-nucleon elastic scattering cross-section upper limit of $9.8{\times}10^{-46}\,\text{cm}^2$ at 90% confidence. This improves upon the previous best WIMP sensitivity with a liquid argon target set by DEAP with a 2.1 tonne-year exposure of $3.9 \times 10^{-45}\,\text{cm}^2$. Notably, the improvement in sensitivity cannot be attributed solely to a larger exposure, which implies that the profile likelihood treatment offers greater sensitivity and discovery potential than the cut-and-count method. The scope of this work also extends to next-generation experiments, such as DarkSide-20k, DUNE, and nEXO; all of which are planning to use Silicon Photomultipliers as their primary light detection technology. An important systematic effect for these future experiments will be the secondary photon emission from silicon photomultipliers, which is a source of noise correlated with photon detection. This is more commonly known as *correlated cross-talk*. The cross-talk photon emission yields and spectra from two silicon photomultiplier designs considered for next generation astroparticle physics experiments are also reported in this thesis.

Acknowledgements

The work presented in this thesis exists today thanks to so many people: colleagues who became good friends, my family and friends who stood by me in the most trying of times, and my supervisors who made it all possible, to name a few examples. This section of my thesis is an open letter of sorts to them, thanking them for their love and support.

First and foremost, I have to give thanks to my supervisors for being given the opportunity to go through the trials of a Ph.D. program in Physics. Dr. Jocelyn Monroe is among the most brilliant people I've ever met and fiercely loyal to her students. She elevated my skills as a scientist and her example of leadership will be one that I follow if I am ever lucky enough to be a leader in this field myself. Dr. Fabrice Retière has left no room for any bad habits to get in the way of good science, yet has also provided the means for me to lead my own path in not only producing interesting experimental results, but publishing those results in my first paper. To the both of you, I owe many thanks for your part in my professional development as well as your immense kindness towards me personally. While I will always respect you both as impeccable scientists, I'll also respect you both for fostering a sense of community and friendship amongst the groups you lead. Some of my best memories of this Ph.D. program are those of cheeky pints at The Crown and pizza gatherings at Riley Park.

Though I had tremendous support from my colleagues and supervisors, this program has put me through the toughest times of my adult life, and for those challenges my family have been second to none in their ability to keep me going. My parents, Colin and Anne McLaughlin, are the very best any son could ask for and I am so grateful for making it to this point in my life because I know it makes you proud to see me here. To my dad, I thank you for always being there to take a phone call whenever I got homesick or felt a bit of anxiety bubbling up. I especially thank you for flying across the Atlantic at the drop of a hat to help me when my life reached its darkest and hardest moments. To my mom, I thank you for also being there to answer my calls, and to make every visit home feel like I never left... and also for being the one to make dad fly across the Atlantic to help me during those immensely difficult times. To my sister, Maddy, I thank you for continuing to be my best friend and mentor. You are a true academic and I hope to live up to your standard one day. I'll also go ahead and thank you in advance for your future input on all fashion and home decorating decisions. You gave me the gift of style and that gave me the confidence to excel in virtually every facet of my life. Lastly, I owe a hearty thank you to my cousin Paul McLaughlin and his wife Becky, whom I've only gotten to know well in my brief time living in the UK but familial bond has made them a fixture in my life that I'll cherish for the rest of my days. You both made me

feel just as much at home in London as I ever felt growing up in Canada, and I could never thank you enough for that!

A very special thank you goes out to Rick Astley who never gave me up, nor let me down, nor ran around, nor deserted me.

I am extremely fortunate to also have a group of friends and colleagues that spans multiple provinces in Canada and countries around the world. To all my collaborators on DEAP-3600—from the groups in Ontario, to Mexico, to England, and all over Europe—I give you heartfelt thanks for being great colleagues, friends, and teachers. My memories of this experiment make me harken back to young member events at collaboration meetings, the highs of seeing my work make a difference in others' analyses, the lows of being told I need to redo that work, and the even greater highs of making that project the best possible version of itself. I specifically want to thank Dr. Ashlea Kemp. At first I'd only ever see her at collaboration meetings, but our friendship has become so potent in our shared labour over the PLR project for DEAP. We've shared many ideas, laughs, and tears; we've been a great team; and we have our whole careers ahead of us to hopefully work together again in the future. I'm still holding onto that last bowl on my Danbo loyalty card for when we can go there for ramen again! Also among my DEAP collaborators who deserves thanks is Dr. Shawn Westerdale for always having the answers I needed when struggling with any kind of physics or stats problem. Shawn also is the master of inserting puns in his slides and brightening up any conversation while still keeping it interesting and productive. Outside of DEAP, I have to thank Dr. Pietro Giampa for his constant support and friendship that persists to this day and goes back to day one of my Master's degree. Without him, I might have never embarked upon my Ph.D. at Royal Holloway, which has been an experience like no other in my life. And lastly, I can't conclude this part of my acknowledgements without mentioning the PHAAR group at TRIUMF. Most of all Dr. Giacomo Gallina, who is perhaps the busiest man I've met so far in my young career. He alone showed me what it takes to turn a good analysis into a great paper. I'll always remember that whenever I see "Characterisation of SiPM Photon Emission in the Dark" on my CV.

I'd like to thank the country of Japan for the invention of sushi. I just think that was a solid move.

My group of close friends outside of academia also deserve thanks for keeping me sane during this endeavour. Ash Ritchie-Yates is someone who immediately welcomed me into the group at Royal Holloway. She quickly became one of my closest friends and a valued confidante. Jordan Palmer is also one to make me feel welcome, and I have loved every conversation we've had for the rich intellectual stimulation. In Vancouver, I have always been able to count on Austin DeHart to keep my spirits high with beers on the

beach at sunset, a good game of Magic: the Gathering, or even creating music, which has been one of the truest joys of my life. Jordan Fordyce was a constant source of fun and adventure too, whether she called me out to a simple trivia night at a pub or brought me along a 3.5-hour biking trek to Deep Cove for Honey's Doughnuts (absolutely worth the trip).

Coffee.

Finally, there are three individuals who deserve a very deep acknowledgement for their transformative effect on me as a growing individual throughout my Ph.D studies. First is Melinda Noel, my therapist, who helped me deal with my anxiety and depression that really became detrimental during the early days of the COVID-19 pandemic. She taught me how to understand my mind, truly respect myself, and set healthy boundaries to maintain my mental health. Second is Sahra Tekin, my partner, the love of my life, and one of the main reasons I was able to make it past the finish line in the last months of this process. Even when she and I were merely good friends, she was always happy to lend her ear during tough times and keep my spirits high. Everything I do now is just as much about making her proud as it is about advancing towards my aspirations. And last but not least, I have to thank Rick Astley again for never making me cry, never saying goodbye, never telling a lie, and never hurting me.

Contents

List of Figures

List of Tables

Frequently Used Abbreviations

AARF	**A**luminum coated **A**crylic **R**eflector **F**ibre
AV	**A**crylic **V**essel
DAQ	**D**ata **AcQ**uisition
DEAP	**D**ark matter **E**xperiment using **A**rgon **P**ulse-shape discrimination
ER	**E**lectronic **R**ecoil
FV	**F**iducial **V**olume
LAr	**L**iquid **Ar**gon
MC	**M**onte **C**arlo
MIEL	**M**icroscopy with **I**njected and **E**mitted **L**ight
NIR	**N**ear **I**nfra**R**ed
NR	**N**uclear **R**ecoil
NRA	**N**uclear **R**ecoil **A**cceptance
PDF	**P**robability **D**ensity **F**unction
PE	**P**hoto**E**lectron
PLR	**P**rofile **L**ikelihood **R**atio
PMT	**P**hoto**M**ultiplier **T**ube
PSD	**P**ulse-**S**hape **D**iscrimination
ROI	**R**egion **O**f **I**nterest
SiPM	**Si**licon **P**hoto**M**ultiplier
SPAD	**S**ingle **P**hoton **A**valanche **D**iode
STrETCH	**S**cientist **Tr**ying **E**gregiously **T**o **C**reate **H**umour
TPB	**T**etra**P**henyl **B**utadiene
TPC	**T**ime **P**rojection **C**hamber
VUV	**V**acuum **U**ltra**V**iolet
WIMP	**W**eakly **I**nteracting **M**assive **P**article

For Frodo. . .

Chapter 1

Introduction

The Standard Model of particle physics is a theoretical description of nature at its most fundamental level. With it, physicists have been able to predict the existence of (and subsequently discover) subatomic particles, such as the Higgs boson and $W^{\pm}/Z^0$ bosons [1, 2]. The Standard Model also agrees with observations of physical interactions to a precision of order 10^{-8}–10^{-9} [3]. Despite its success throughout the 20$^{\text{th}}$ and 21$^{\text{st}}$ centuries as a theoretical framework, the Standard Model does have inadequacies where it isn't in agreement with experimental data. One of the most heavily researched gaps in the Standard Model is the inconsistency with the cosmological model describing the evolution of the universe from the moments immediately following inflation—the ΛCDM model [4]. Here, Λ refers to the cosmological constant, or *Dark Energy*, which dictates the expansion rate of the universe, and CDM stands for *Cold Dark Matter*. According to ΛCDM, dark energy and dark matter combine to account for $(95.10\pm0.01)\%$ of the mass-energy content of the observable universe, with the remaining 4.9% being baryonic matter [5]. While the Standard Model of particle physics has proven to be very effective at describing baryonic matter, it cannot explain phenomena related to dark energy or dark matter in its current form. This fact is the primary reason for conducting dark matter research.

This chapter is a summary of the hunt for dark matter as a means to extend the Standard Model to new frontiers. Section 1.1 introduces the dynamical evidence for the existence of dark matter from notable astrophysical observations. Section 1.2 further motivates the existence of dark matter with evidence from early universe cosmology, and demonstrates

that dark matter is likely not baryonic in nature. Section 1.3 is a discussion of the formation of galaxies and super clusters, which provides evidence for dark matter being predominantly nonrelativistic. Section 1.4 establishes the expected properties of a viable dark matter candidate and summarizes dark matter candidates as described in various Beyond the Standard Model (BSM) theories. Section 1.5 describes the experimental context of dark matter direct detection. Lastly, Section 1.6 discusses the impact of a direct observation of dark matter in physics.

1.1 Astronomical Evidence for Dark Matter

This section provides an overview of the most important historical astronomical and cosmological signatures of dark matter. The astronomical measurements in Sections 1.1.1–1.1.3 have the common theme of implying that baryonic matter is insufficient to account for observed gravitational behaviour at the scale of galaxies and galaxy clusters. In Sections 1.2.1 & 1.2.2, the emphasis shifts to cosmological modelling of the early universe, which indicates that the nature of dark matter is mostly non-baryonic and that it must be 5.32 ± 0.05 times more abundant in the observable universe than baryonic matter [5].

1.1.1 Velocity Dispersions in Galaxy Clusters

In the early 20th century, Lord Kelvin was among the first to estimate the abundance of dark matter[1] using a dynamical approach by modelling the Milky Way as a mechanically stable gas of particles under the influence of gravity [6]. In this way, it is possible to predict the velocity dispersion of a system based on its size, and then the matter density of that system can be inferred. This idea was further refined by scientists such as Henri Poincaré, Ernst Öpik, Jacobus Kapetyn, and Jan Oort [7], who all used the assumption of mechanical equilibrium and the theory of gases to measure the local matter density in the Milky Way. Then in the early 1930s, Swiss astronomer Fritz Zwicky took this approach a step further by using the Virial theorem (Equation 1.1) to find the mass of

---

[1]At this point in time, the generally accepted view among astronomers was that dark matter consisted of dim or non-luminous baryonic matter, such as faint stars, planets, gas, nebulae, etc.. Non-baryonic dark matter wouldn't start to gain popularity until c1970–1980.

distant galaxy clusters. The Virial theorem states,

$$\langle T \rangle = -\frac{1}{2} \langle U \rangle, \tag{1.1}$$

where $\langle T \rangle = \frac{1}{N} \sum_i \frac{m_i v_i^2}{2}$ is the average kinetic energy of the mechanically stable system with N constituents having masses m_i and velocities v_i ($i = [1, N]$); and $\langle U \rangle$ is the average potential energy of the system. Assuming that ensemble of galaxies have reached a mechanically stable state and are uniformly distributed within a sphere of radius R, the average potential energy of the system is given by the gravitational binding energy of a uniform sphere U_{sp} divided among N constituent galaxies, i.e.

$$\langle U \rangle = \frac{U_{\text{sp}}}{N} = \frac{1}{N} \left(-\frac{3}{5} \frac{GM^2}{R} \right), \tag{1.2}$$

where G is the Universal Gravitation Constant $G = 6.67 \times 10^{-11}\,\text{N}\,\text{m}^2\,\text{kg}^{-2}$ and M is the total mass contained within the sphere. Using Equations 1.1&1.2 to get the mass of a given galaxy cluster requires information containing the volume of the cluster and the kinetic energy of its constituent galaxies: both of which are obtained trigonometrically, and thus difficult to ascertain without knowing the distance to the galaxy cluster. However this issue was resolved by Edwin Hubble and Milton Humason in 1931 [8] with their discovery of the linear relationship between the recession velocity (or Doppler redshift) and distance of stellar bodies, in what we know today as Hubble's Law.

Following the work of Hubble and Humason, Zwicky utilized their observed relationship between the optical redshift vs. distance to determine physical characteristics of various galaxy clusters, such as their sizes and apparent velocity dispersions [9]. The apparent velocity of an astronomical object is obtained by measuring the proper motion—i.e. the angular velocity of the object across the sky—and multiplying by the distance. Since the average Doppler redshift of a given galaxy cluster could be used to determine its distance to much greater precision than was previously attainable at the time, this meant that the apparent velocities of individual galaxies in a cluster could be determined with a margin of error of a few percent [9].

The Coma cluster was reported to have differences in apparent velocities as large as $2000\,\text{km/s}$, which was noted by both Zwicky and Hubble to be an anomalously large velocity dispersion [8, 9]. In order to use the Virial theorem to make a prediction of

Quantity	Value
Distance	45×10^6 ly
Angular Diameter	$1.7°$
Radius	$\sim 10^6$ ly
No. of galaxies	800
Galactic mass	$\sim 10^9 \, M_\odot$
Coma total mass	$800 \times 10^9 \, M_\odot$

TABLE 1.1: Physical characteristics of the Coma Cluster relevant to mass calculation using Virial theorem.

what the velocity dispersion should be, Zwicky adopted $10^9 \, M_\odot$ as a mass estimate for each galaxy, in accordance with Hubble's earlier galactic mass estimate based on their luminosities [10]. Combined with the other physical characteristics listed in Table 1.1, Equations 1.1 & 1.2 can be used to show

$$\frac{10^9 \, M_\odot}{2} \left(\frac{1}{N} \sum_{i=1}^{N} v_i^2 \right) = -\frac{1}{2N} \left(-\frac{3}{5} \frac{G \, M^2}{R} \right), \tag{1.3}$$

$$(N \times 10^9 \, M_\odot) v_{\text{rms}}^2 = \frac{3}{5} \frac{GM^2}{R}, \tag{1.4}$$

and noting that $N \times 10^9 \, M_\odot = M$,

$$\therefore \quad v_{\text{rms}} = \sqrt{\frac{3}{5} \frac{GM}{R}} \tag{1.5}$$

$$= 80 \, \text{km s}^{-1}, \tag{1.6}$$

which is far smaller than the observed velocity dispersion in the apparent velocities within the Coma cluster. Zwicky concluded that the mass estimate based on luminous matter was 400 times smaller than what would be needed to generate the observed velocity dispersion.

Sinclair Smith conducted a similar study of the Virgo cluster [11], which provided an estimate of the average mass of its constituent galaxies. He used measurements of the line-of-sight velocities of 32 members of the Virgo cluster, and found a mean velocity of 1225 km/s and an escape velocity of 1500 km/s. He also found a grouping of high velocity galaxies at the outermost perimeter of the cluster, which he interpreted to be galaxies in stable circular orbits traveling just below the escape velocity. Newtonian mechanics can be used in this case to find the mass of the gravitating body, M (i.e. the

entire Virgo cluster) via,

$$\frac{GmM}{R^2} = \frac{mv^2}{R} \tag{1.7}$$

$$\Rightarrow M = \frac{v^2 R}{G}, \tag{1.8}$$

where $R = 2 \times 10^5$ parsecs is the orbital radius of the outermost galaxies and $v = 1500\,\text{km/s}$. The total mass of Virgo obtained in this way is of order $10^{14}\,M_\odot$, and with 500 constituent galaxies in the cluster, Smith found an average galactic mass of $2 \times 10^{11}\,M_\odot$—two orders of magnitude larger than Hubble's estimate.

The unexpected gravitational signatures found by Sinclair Smith and Fritz Zwicky uncovered the fact that luminous matter accounts for a much smaller fraction of the total mass in large astrophysical systems than what was previously thought. Recall that at this time, the best estimate of the average galactic mass was Hubble's estimate of $10^9\,M_\odot$, meaning that the nonluminous matter in Zwicky's and Smith's findings is $\sim 100\times$ more abundant than stellar mass. Contemporaries of Zwicky and Smith (including Hubble) called this *the missing mass problem* [7]. While the astronomers at the time were puzzled, they were still largely skeptical of Zwicky's and Smith's findings. The debate on whether or not their observations were real was finally settled in the early 1970s, with the advent of radio astronomy and the use of galactic rotation curves to measure the mass distributions of individual galaxies.

1.1.2 Galactic Rotation Curves

Galactic rotation curves (GRCs) are a measurement of the orbital speeds of stellar and gaseous matter in a galaxy versus radial distance from the galactic core, and they are useful tools for analyzing the distribution of matter in galaxies. They can be obtained in a variety of ways, but the basic principle of observation is to measure the Doppler shift of spectral lines at varying radii away from the centre of the galaxy. At radii within the visible disk, optical spectral lines such as the Hα (from $n = 3 \rightarrow 2$ transition in atomic hydrogen), [NII] (all transitions in N^{2+} ions), and [SII] (all transisitions in S^{2+} ions) lines can be used. The H-I, or $21\,\text{cm}$ line, which is a spectral line that comes from a hyperfine transition in neutral hydrogen is particularly useful for measurements at large radii, as most interstellar gas is transparent to radio waves [12]. In the context of GRCs,

it was these measurements at large radii that had the biggest impact on the field of dark matter research.

In 1970, Vera Rubin and Kent Ford published their initial findings on M31 (Andromeda galaxy) [13]. Their conclusion was that between 3–24 kpc from the galactic core, the orbital velocities within Andromeda were consistent with a dense nucleus and a disk of exponentially reducing mass with increasing distance from the centre. This result wasn't significantly different than the commonly accepted mass distribution of a galaxy, but it was an important advancement in measurement quality compared to earlier studies, like that of Horace Babcock in 1939 [14]. Using the H-I line helped to stabilize measurements of orbital velocities out to angles of $\gtrsim 2°$ (24 kpc in the case of Andromeda) from the galactic centre.
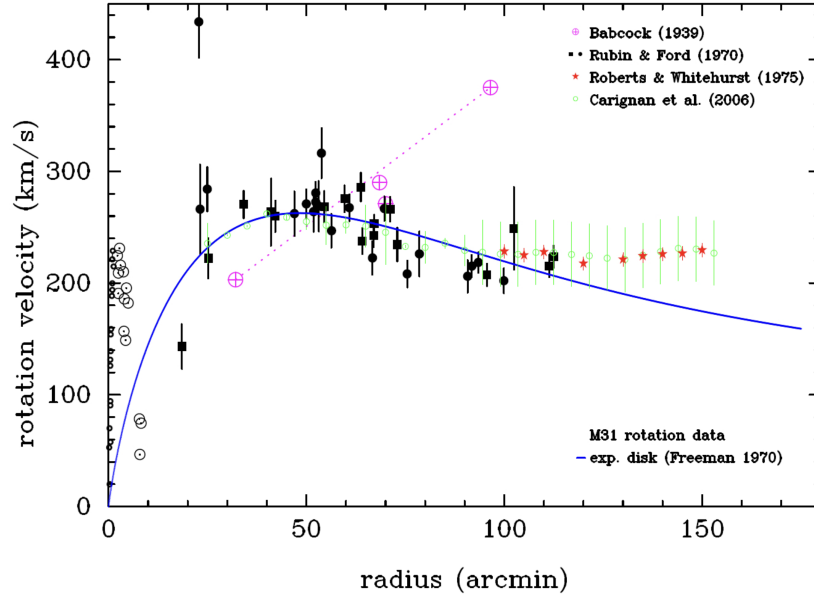
FIGURE 1.1: Measured GRCs of M31 (Andromeda) from Babcock [14], Rubin and Ford [13], Roberts and Whitehurst [15], and Carignan et al. [16]. The solid blue line is a predicted GRC from Freeman [17] based on a mass distribution model of a dense core plus an exponentially falling disk, $M(R) \sim e^{-\alpha R}$. Figure taken from Ref [7].

In Figure 1.1, there is a predicted GRC for Andromeda from Ken Freeman [17] (1970) indicated by the blue line, overlaid with measurements from Horace Babcock [14] (1939), Rubin and Ford [13] (1970), Roberts and Whitehurst [15] (1972), and Carignan et al. [16] (2006). Freeman's prediction assumes a fixed mass-to-light ratio. Since the observed light intensity distribution, $I(R)$, of Andromeda follows a decaying exponential with

radius R away from the centre, this implies,

$$I(R) = I_0 e^{-\alpha R} \quad \Rightarrow \quad M(R) \sim e^{-\alpha R},\qquad (1.9)$$

where $M(R)$ is the mass of the galaxy enclosed within rings of radius R and $R+dR$. With the innovation of Rubin and Ford advancing the measurement quality of GRCs, other astronomers such as Roberts & Whitehurst [15], and Rogstad & Shostak [18] started measuring the GRCs of galaxies beyond the end of their luminous edges. Notably, for Andromeda, Roberts & Whitehurst took measurements as far out as 30 kpc and found a significant deviation from Freeman's model based on a constant mass-to-light ratio. In 1978, Rubin, Ford and Thonnard [19] showed that this behaviour is true for a sample of 10 high luminosity spiral galaxies.

These findings imply that there is some mass contribution in spiral galaxies—particularly at large radii from their galactic cores—great enough to significantly increase gravitational potential energy, yet not radiate electromagnetically. Given that this is true at the scale of individual galaxies, the earlier findings of Sinclair Smith and Fritz Zwicky would follow quite naturally, as there would be a large mass contribution in each galaxy of a galaxy cluster that would strengthen their mutual gravitational attractions, but otherwise be invisible: hence the name *dark matter*. The dark matter collected towards the outskirts of a galaxy is now referred to as a *dark matter halo*. The presence of halos has become apparent via GRC measurements in virtually every galaxy in the observable universe, indicating that not only is dark matter real, it is also abundant throughout the universe.

1.1.3 Gravitational Lensing

An observation of 1E 0657-558 [20]—more commonly known as the *Bullet Cluster*—provides a unique view of the mass components in galaxy clusters. The Bullet Cluster is a merger of two galaxy clusters. During a merging event such as this, the constituent galaxies behave as non-interacting particles, and proceed on their trajectories unhindered. Conversely, the gas and plasma within the clusters behave like a fluid and impart ram pressure[2] on each other. A consequence of these differing behaviours is that the

---

[2]Ram pressure is the result of the bulk movement of a fluid rather than its internal outward pressure under thermal equilibrium

intracluster plasma and the stellar matter become separated from each other. The uniqueness of the Bullet Cluster is that the merger appears to be coplanar with the sky, based on the small difference in line-of-sight velocities[3] between the two clusters. This allows for high spatial resolution measurements of the separation of the plasma and stellar matter.

As will be discussed in Section 1.4, any dark matter in the galaxy clusters is likely to be weakly interacting, and therefore should behave similarly as the stellar mass in the merger; i.e. segregating from the intracluster plasma. The measurement described in Ref[20] quantifies this spatial separation by comparing the locations of peak X-ray emission intensity (from colliding gas particles) and the locations with the strongest gravitational lensing: a well understood and well documented prediction of Einstein's theory of general relativity.

To measure mass density using weak gravitational lensing, a method described in Ref[21] discusses two observables: the convergence, κ, and the shear, γ ($\in \mathbb{C}$), of the gravitating body. Convergence is a quantity analogous to magnification in classical optics, while shear is analogous to astigmatism. Similar to magnification, convergence is a value that quantifies how enlarged an image appears relative to the object. Furthermore, convergence scales linearly with mass density, making it a suitable probe for masses of large scale objects.

Weak gravitational lensing makes objects appear more elliptical along major axes perpendicular to the vector pointing towards the centre of the gravitational potential. In Ref[20], the convergence was observed statistically by measuring the ellipticities, $\mathcal{E}$ ($\in \mathbb{C}$) of more distant galaxies. Assuming that the true ellipticities of the distant galaxies are uniformly distributed, their apparent ellipticities, $\mathcal{E}_{\mathrm{App}}$ are a direct measure of a quantity called reduced shear, $\mathbf{g}$ ($\in \mathbb{C}$), which is related to convergence via [21]

$$\langle |\mathcal{E}_{\mathrm{App}}| \rangle = |\mathbf{g}| = \frac{|\gamma|}{1 - \kappa}. \tag{1.10}$$

Using an optical image data set of the Bullet Cluster obtained from the European Southern Observatory Wide Field Imager (ESO-WFI), Inamori Magellan Areal Camera and

---

[3]The relative line-of-sight velocity between the two clusters is $\sim 600 \, \mathrm{km/s}$ and their total relative velocity is $\sim 4700 \, \mathrm{km/s}$ [20], resulting in a collision plane rotated by approximately $7°$ relative to the sky.

Spectrograph (Magellan IMACS), and the Hubble Space Telescope (HST), measurements of the ellipticities were made and used to estimate the reduced shear of background galaxies as a function of angular location relative to the Bullet Cluster. Those estimates of $|\mathbf{g}|$, were then used to reconstruct a κ map, which can be interpreted as a mass density map of the Bullet Cluster. This is shown by the green contours in Figure 1.2. Also in Figure 1.2 (on the right) is an image of the Bullet Cluster as captured by the Chandra X-Ray Observatory. The X-ray data shows that the intracluster gas and plasma are indeed concentrated towards the middle of the two clusters, which is a result of the aforementioned ram pressure. However, the reconstructed mass densities of both clusters peak significantly far away from where X-ray emission is most intense. In fact, the amount of mass in the vicinity of the convergence peaks is 7–10 times larger than the mass found at the sites of highest plasma concentration. This result is widely interpreted as strong evidence for electromagnetically inert, particle dark matter.
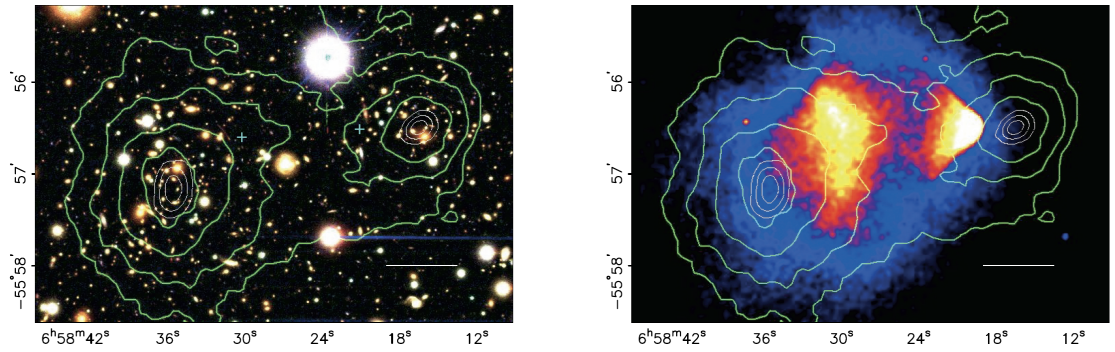
FIGURE 1.2: Results from Ref [20] showing that the X-ray emission peaks from the Bullet Cluster merger (shown on the right) are spatially separated from the centre of mass of the clusters, as measured by weak gravitational lensing, depicted by the green contours in both images. Contours further inward represent greater mass density.

1.2   The Case Against Baryonic Dark Matter

The simplest solution to the question of the true nature of dark matter would be baryonic matter in the form of non-luminous or extremely dim compact bodies, which are referred to as Massive Compact Halo Objects (MACHOs). Some examples include brown, white, and red dwarf stars; neutrons stars; black holes; or massive non-nuclear burning objects. However there are multiple observations which clash with the MACHO hypothesis, or indeed any baryonic matter hypothesis. If galactic halos were made of, say gas in hydrostatic equilibrium, they would need to be maintained at temperatures $T_{\mathrm{eq}} \sim 10^6\,\mathrm{K}$ in

order to not collapse under the gravitational pull of their host galaxies. However, such a gas would produce an observable X-ray background which has never been observed [22]. Furthermore, a survey of gravitational microlensing in the Large Magellanic Cloud (LMC) [23] also limits the halo mass fraction from MACHOs to 0.2 (0.08–0.5 at 95% confidence for MACHOs of mass 0.15–0.9 $M_\odot$). The strongest arguments for non-baryonic dark matter come from cosmological measurements of Big Bang Nucleosynthesis (BBN) and the Cosmic Microwave Background (CMB), which will be given a detailed review in the following subsections.

Before entering into the next subsections, it is useful to define some important cosmological parameters, namely the *critical energy density*, ρ_{crit}, and the *closure parameter* of the universe, Ω. These quantities originate from the Friedmann Equation, which is a statement of energy conservation on cosmological scales. The Friedmann Equation is [24, 25]

$$H^2(t) = \left(\frac{1}{a}\frac{da}{dt}\right)^2 = \frac{8\pi G}{3}\rho + \frac{\Lambda}{3} - \frac{kc^2}{a^2}, \tag{1.11}$$

where $H(t)$ is the time-dependent Hubble parameter; a is a time-dependent "scale factor" describing the expansion rate of the universe; $\rho = \rho_m + \rho_r$ is the energy density of the universe with contributions from matter, ρ_m, and radiation, ρ_r; Λ is the cosmological constant; and k is a spacetime curvature parameter bounded between $[-1, 1]$. Note that setting $t = 0$ refers to the current time, and $H(0) \equiv H_0 = 67.4 \pm 0.5\,\text{km}\,\text{s}^{-1}\,\text{Mpc}^{-1}$ [5].

Qualitatively, one can interpret the left-hand side of Equation 1.11 as the kinetic energy of matter or radiation moving with the expansion of the universe. From left to right, the terms on the right-hand side can be interpreted as a potential energy term, energy associated with vacuum, and energy associated with spacetime curvature. The vacuum energy term is often recast as

$$\frac{\Lambda}{3} = \frac{8\pi G}{3}\rho_\Lambda, \tag{1.12}$$

$$\text{where } \rho_\Lambda \equiv \frac{\Lambda}{8\pi G}. \tag{1.13}$$

Equation 1.13 defines the contribution of vacuum energy to the total energy density of the universe. With this definition, Equation 1.11 can be rewritten as

$$H^2(t) = \frac{8\pi G}{3}\rho_{\text{uni}} - \frac{kc^2}{a^2}, \tag{1.14}$$

where,

$$\rho_{\text{uni}} = \rho_m + \rho_r + \rho_\Lambda, \tag{1.15}$$

The critical energy density is obtained by setting $k = 0$ in Equation 1.14. By doing this, one makes the assumption that spacetime has a flat topology. Allowing $\rho_{\text{uni}} = \rho_{\text{crit}}$ and solving for ρ_{crit} at $t = 0$ yields,

$$\rho_{\text{crit}} = \frac{3H_0^2}{8\pi G}. \tag{1.16}$$

The closure parameter is then obtained by taking the ratio of Equations 1.15 and 1.16 [25],

$$\Omega = \frac{1}{\rho_{\text{crit}}}(\rho_m + \rho_r + \rho_\Lambda) \tag{1.17}$$

$$= \Omega_m + \Omega_r + \Omega_\Lambda. \tag{1.18}$$

where $\Omega_m = \rho_m/\rho_{\text{crit}}$, $\Omega_r = \rho_r/\rho_{\text{crit}}$, and $\Omega_\Lambda = \rho_\Lambda/\rho_{\text{crit}}$ are individual closure parameters for matter, radiation, and vacuum energy densities. If the universe has $\Omega < 1$, then the curvature term in the Friedmann Equation would need to balance the total energy by having $k < 0$; this corresponds to an 'open' spacetime topology, which implies that the expansion rate of the universe would continue to accelerate, with $\dot{a}(t) \to c$ as $t \to \infty$. Similarly, if $\Omega > 1$, then the Friedmann Equation is balanced by the curvature term having $k > 0$, which describes a universe with a 'closed' topology (hence the name 'closure parameter'). In this case, the expansion rate would reach a maximum and the universe would then begin to collapse. If $k \neq 0$, then the equivalent closure parameter for curvature can be written as $\Omega_k = kc^2/(H_0 a(0))^2$. However, our universe has been observed to be consistent with a 'flat' topology where $k = 0$ ($\Omega_k = 0.001 \pm 0.002$ [5], so Ω_k is neglected hereafter). Therefore our universe will expand indefinitely with $\dot{a}(t)$ asymptotically approaching zero as $t \to \infty$.

As Ω_m accounts for all matter, it can be further divided into contributions from baryonic matter, Ω_b, and dark matter, Ω_{DM}. The following subsections will mainly revolve around inferred values of baryonic closure parameter based on cosmological observations.

1.2.1 Big Bang Nucleosynthesis

BBN refers to the epoch of the early universe when its temperature fell below $\sim 1\,\mathrm{MeV}$. At this time, the universe consisted of photons; relativistic electrons, positrons, and neutrinos; and a relatively small number of nonrelativistic baryons. These particles comprised a system in *thermal equilibrium* (i.e. the temperatures of all particle species were approximately equal to each other), which is often called a 'thermal bath' of particles. In this epoch a stable particle species—say particle x—would have stayed in thermal equilibrium through reactions, such as

$$x + x \rightleftharpoons A + B$$
$$x + y \rightleftharpoons A + B,$$
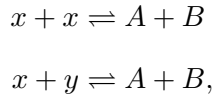
where y, A, and B are generic labels for different particle species. The two-sided arrows in the above reactions indicate that the reaction also keeps the reactants and products in *chemical equilibrium*, i.e. the number of each particle species remains constant.

As the universe evolved and its temperature decreased, the rates of the reactions coupling x particles to the thermal bath would have decreased as well due to two effects:

(i) The expansion rate of the universe was rapidly increasing at the same time, thereby reducing the rate of collisions between x particles and other species

(ii) The available energy for maintaining a given reaction would have been decreasing with the temperature of the thermal bath

The reaction rates in the forward and reverse directions generally would not have had the same temperature dependence. Therefore as the thermal bath cooled, one direction would have become favoured over the other, forcing x particles out of chemical equilibrium. At this point, its comoving[4] number density (or abundance), n_x, would have become time-dependent, but x particles themselves would remain in thermal equilibrium. As the universe continued to expand and cool, effects (i) and (ii) above would have eventually halted all reaction rates involving x particles, forcing it out of thermal

---

[4]'Comoving' observables change according to the expansion of the universe. In this case, a fixed number of a particle species would have a falling number density as the volume of the universe grows, but the *comoving* number density would remain constant.

equilibrium as well. At this point, its abundance would asymptotically approach a constant value in a process called *freezing out*. The constant value of n_x realized at freeze out is called the *relic abundance* of particle x.

From the arena of BBN, measurements of the relic abundances of light elements provide the most powerful evidence of non-baryonic dark matter. The abundances of helium and deuterium (represented hereafter as D in chemical equations), specifically, constrain the baryon closure parameter, Ω_b, to be insufficient to account for all matter in the universe. Deuterium is formed in the reaction

$$p + n \rightarrow D + \gamma + B_D, \tag{1.19}$$

where $B_D = 2.22\,\mathrm{MeV}$ is the binding energy of deuterium. At temperatures above $T \sim 0.1\,\mathrm{MeV}$, there were plentiful photons with enough energy to undergo the reverse reaction of Equation 1.19 (photo-disintegration), therefore deuterium was being destroyed just as quickly as it was being created; once $T < 0.1\,\mathrm{MeV}$, deuterium photo-disintegration ceased. However, since all stable isotopes of helium have greater binding energies per nucleon than deuterium—$\frac{1}{3}B_{^3\mathrm{He}} = 2.57\,\mathrm{MeV}$ and $\frac{1}{4}B_{^4\mathrm{He}} = 7.1\,\mathrm{MeV}$ [24]—production of helium began very quickly thereafter in reactions like:

$$D + p \rightarrow {}^3\mathrm{He} + \gamma,$$
$$D + n \rightarrow {}^3\mathrm{H} + \gamma,$$
$${}^3\mathrm{H} + D \rightarrow {}^4\mathrm{He} + n,$$
$${}^3\mathrm{H} + p \rightarrow {}^4\mathrm{He} + \gamma,$$
$$D + D \rightarrow {}^4\mathrm{He} + \gamma.$$
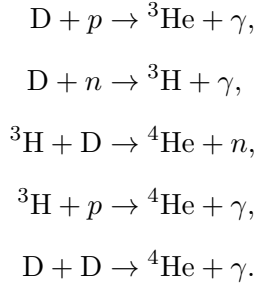
The rates of these reactions are dependent upon (among other things) the abundance of the particle species involved. The abundances of deuterium, ${}^3\mathrm{He}$, and ${}^4\mathrm{He}$ are all coupled to each other, but note that most of these reactions include the creation of photons in the final state and none of them change the baryon density of the universe. Therefore, the relic abundances of these light elements are all correlated with a quantity known as the *baryon-to-photon ratio* η, which must be solved for numerically. For ${}^4\mathrm{He}$, it is

common to represent the relic abundance as a fraction of the total baryonic abundance,

$$Y_p = \frac{4\,n_{^4\text{He}}}{4\,n_{^4\text{He}} + n_{\text{p}}} \qquad (1.20)$$

and for deuterium and the other light elements, simply to take their abundance relative to that of hydrogen. The exact solutions of $Y_p(\eta)$ and $\frac{\text{D}}{\text{H}}(\eta)$ are shown in Figure 1.3. The black boxes in Figure 1.3 represent measured values of the light element abundances, and each one can be used to infer the value of the value of η at the time of BBN. The measurement of $\frac{\text{D}}{\text{H}}$ from Refs [26, 27] sets the tightest constraint of the baryon-to-photon ratio at $\eta = (5.1 \pm 0.5) \times 10^{-10}$ [28]. Measurements of the CMB (see Section 1.2.2) from
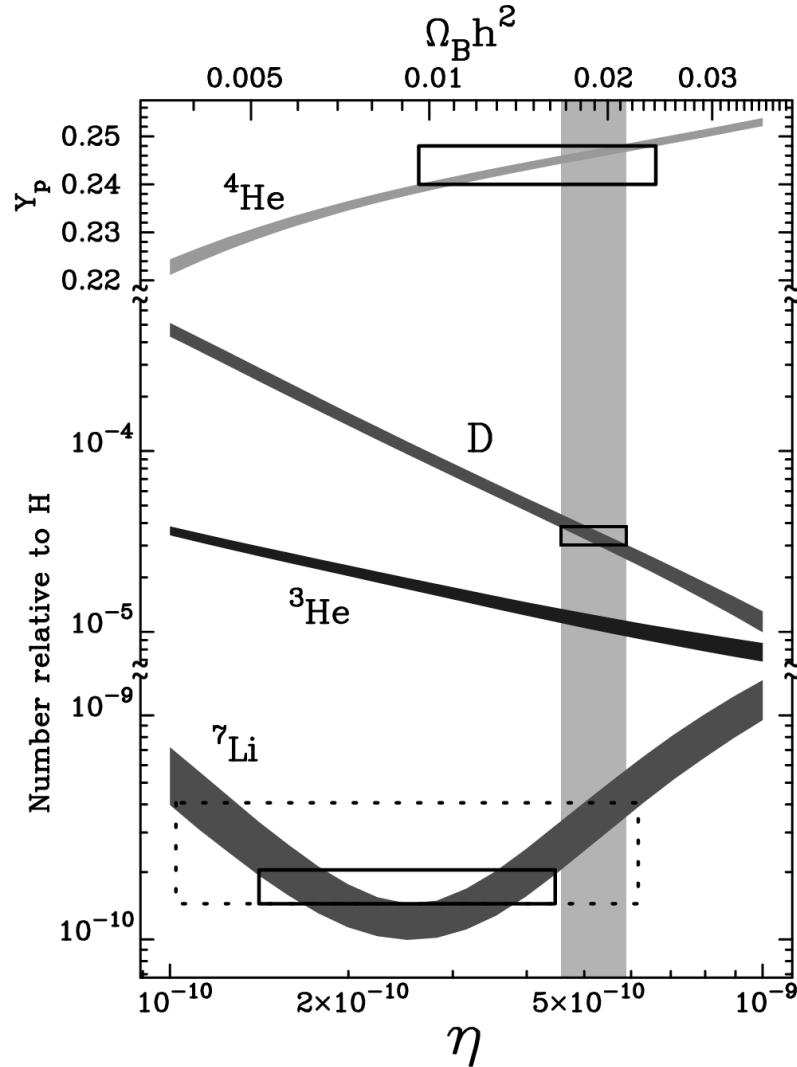
FIGURE 1.3: BBN model of the helium mass fraction Y_p and the relative abundances of deuterium, D/H; helium-3, ^{3}He/H; and lithium-7, ^{7}Li/H, versus the baryon-to-photon ratio η. The grey vertical band represents the inferred interval of η from spectroscopic measurements of D/H in Ref [26, 27]. Image taken from Ref [28].

COBE and WMAP have found an absolute photon density $n_\gamma = (410.72 \pm 0.26)\,\mathrm{cm}^{-3}$ [29]. This can be combined with the inferred value of η to obtain the absolute baryon abundance, n_b,

$$
\begin{aligned}
n_b &= n_\gamma \eta, \\
&= (410.72\,\mathrm{cm}^{-3})(5.1 \times 10^{-10}), \\
&= 2.097 \times 10^{-7}\,\mathrm{cm}^{-3}.
\end{aligned}
$$

The equivalent energy density $\rho_b = m_p\,n_b$, where m_p is the proton mass, can then be used to determine $\Omega_b = \rho_b/\rho_{\mathrm{crit}}$, where ρ_{crit} (Equation 1.16) is the critical energy density. Therefore, the baryonic closure parameter which is most consistent with the observed relic abundances of deuterium, ^{4}He, and photons from the early universe is $\Omega_b = 0.042 \pm 0.004$. This result is in agreement with that found independently from the CMB anisotropy measurements discussed in Section 1.2.2. Also discussed in Section 1.2.2, and shown in Table 1.2, is that the total matter closure parameter observed in CMB measurements is $\Omega_m = 0.3111 \pm 0.0056$, which demonstrates that baryons fall far short of accounting for all matter in the universe.

1.2.2   The Cosmic Microwave Background

The CMB is the light remaining after the epoch of recombination in the early universe. Recombination, which occurred when the temperature of the universe dropped to $\sim 1\,\mathrm{eV}$ (approximately 400,000 years after inflation), refers to when negatively charged electrons and positively charged nuclei combine to form electrically neutral atoms. Before recombination, free streaming electrons were maintained at high energies via Compton Scattering with photons, and the small baryon-to-photon ratio ensured that any recombined atoms would be ionized just as quickly as they formed. As the universe continued to cool below $1\,\mathrm{eV}$, the number of photons with sufficient energy to break up recombined atoms became negligible, and so the number of free streaming electrons began to rapidly decrease. The photons remaining after all the free streaming electrons vanished due to recombination comprise what is now the CMB.

The nature of the CMB makes it a useful snapshot of the early universe at the time of recombination. By measuring the anisotropies in the temperature of the CMB—a map
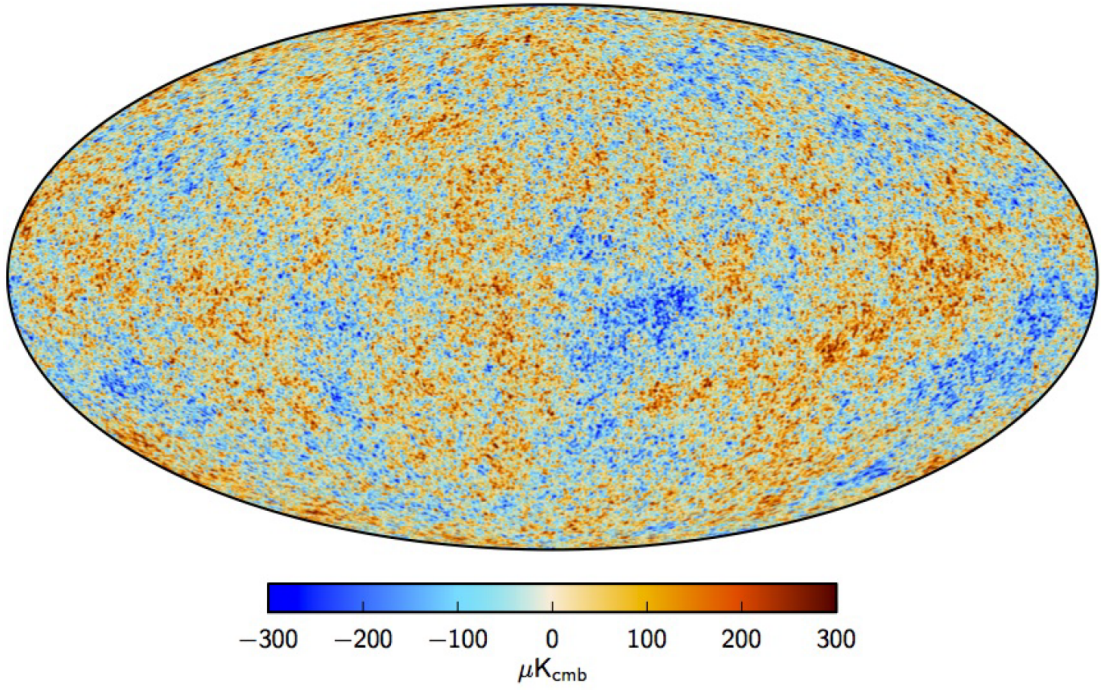
FIGURE 1.4: The CMB temperature anisotropy map measured by the Planck collaboration (2015 release [30]).

of which can be seen in Figure 1.4—one can infer the densities of matter, radiation, and dark energy present in the universe. Volumes of space where the local matter density was greater than their surrounding areas would collapse in on themselves gravitationally. This increased the matter density even further, which increased the likelihood of baryonic matter interacting with photons in the vicinity, resulting in an outward radiation pressure. Therefore the energy densities of photons, baryons, dark matter, and dark energy held competing influences on local matter densities, which drove pressure waves in the cosmic plasma: these pressure waves are now called *Baryon Acoustic Oscillations* (BAOs).

BAOs have been measured, with increasing accuracy, by the Cosmic Background Explorer (COBE) Satellite [31]; the Wilkinson Microwave Anisotropy Probe (WMAP) [29]; and most recently, the Planck spacecraft [5]. Each of these missions make use of the two point correlation function, $\xi(\theta)$, defined as:

$$\xi(\theta) = \left\langle \left(\frac{\rho(\hat{n}) - \bar{\rho}}{\bar{\rho}} \right) \left(\frac{\rho(\hat{m}) - \bar{\rho}}{\bar{\rho}} \right) \right\rangle, \qquad (1.21)$$

where,

$$\hat{n} \text{ and } \hat{m} \text{ are unit vectors,}$$

$$\theta = \cos^{-1}(\hat{n} \cdot \hat{m}),$$

$$\bar{\rho} \equiv \text{Global average CMB photon density,}$$

$$\rho(\hat{j}) \equiv \text{CMB photon density in } \hat{j} \text{ direction.}$$

Equation 1.21 is a measure of the average size of density fluctuations over all points with a given angular separation. It is standard practice to decompose Equation 1.21 into its associated multipole expansion,

$$\xi(\theta) = \sum_{\ell} (2\ell + 1) \, C_\ell \, \frac{P_\ell\big(\cos(\theta)\big)}{4\pi}, \tag{1.22}$$

where,

$$\ell \equiv \text{multipole number,}$$

$$C_\ell \equiv \text{multipole coefficient,}$$

$$P_\ell \equiv \text{Legendre Polynomial of order } \ell.$$

The distribution of coefficients C_ℓ is known as the power spectrum of the multipole expansion. The multipole number, ℓ, is inversely proportional with angular separation, and in the context of the CMB, it is interpreted as a measure of decreasing distance scale.

The measured power spectrum of the CMB, shown in Figure 1.5, has a series of peaks which can be explained as successive compressions and rarefactions in BAOs. The locations and sizes of these peaks therefore contain information about the proportions of matter, radiation, and dark energy present in the universe just prior to the epoch of recombination. For example, the location of the first peak can be used to infer the cosmic horizon distance, D_H. In the ΛCDM model, assuming a topologically flat universe, D_H can be expressed in terms of the matter, radiation, vacuum energy closure parameters in the integral over redshift, z:

$$D_H = \frac{c}{H_0} \int_0^\infty \frac{dz}{[\Omega_m(1+z)^3 + \Omega_r(1+z)^4 + \Omega_\Lambda]}, \tag{1.23}$$
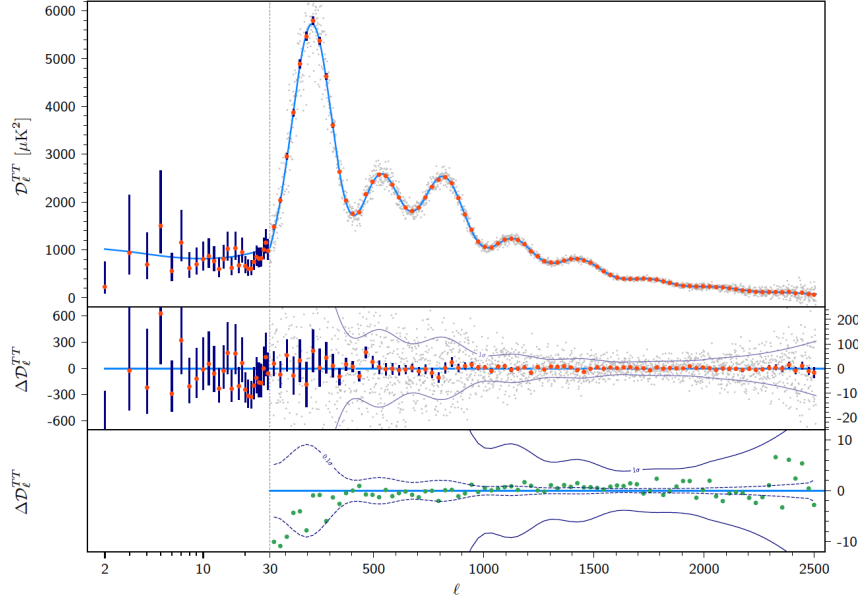
FIGURE 1.5: Planck Satellite measurement of the CMB power spectrum [32], with red dots representing data and the light blue curve representing the best fit of the ΛCDM likelihood model to the data. Here $\mathcal{D}_\ell = \ell(\ell+1)C_\ell/2\pi$. The relative heights and locations of the peaks encode information about the baryon closure parameter and cosmic horizon distance.

where H_0 is the Hubble parameter evaluated at the current time; c is the speed of light; and Ω_m, Ω_r, and Ω_Λ are the matter, radiation, and vacuum energy closure parameters. Here, the term 'redshift' is quantified in terms of the difference between a photon wavelength, λ, and the observed photon wavelength λ' viewed in a frame of reference receding from the photon source at velocity, v; i.e.

$$z = \log\left(\frac{\lambda' - \lambda}{\lambda}\right), \tag{1.24}$$

$$\text{where } \lambda' = \lambda\sqrt{\frac{1 + (v/c)}{1 - (v/c)}}. \tag{1.25}$$

By measuring D_H from the power spectrum in Figure 1.5, a numerical integration of Equation 1.23 can be used to obtain the most likely values of Ω_m, Ω_r, and Ω_Λ. Furthermore the relative amplitudes of odd and even numbered peaks provide information on the relative amounts of baryonic matter and dark matter. Figure 1.6 shows that increasing the baryon closure parameter, Ω_b, amplifies odd numbered peaks and suppresses even numbered peaks. The inferred values of the closure parameters discussed here from likelihood fits to the Planck Satellite CMB power spectrum are reported in Table 1.2 [5]. In a flat universe, closure parameters represent the percentage of the total
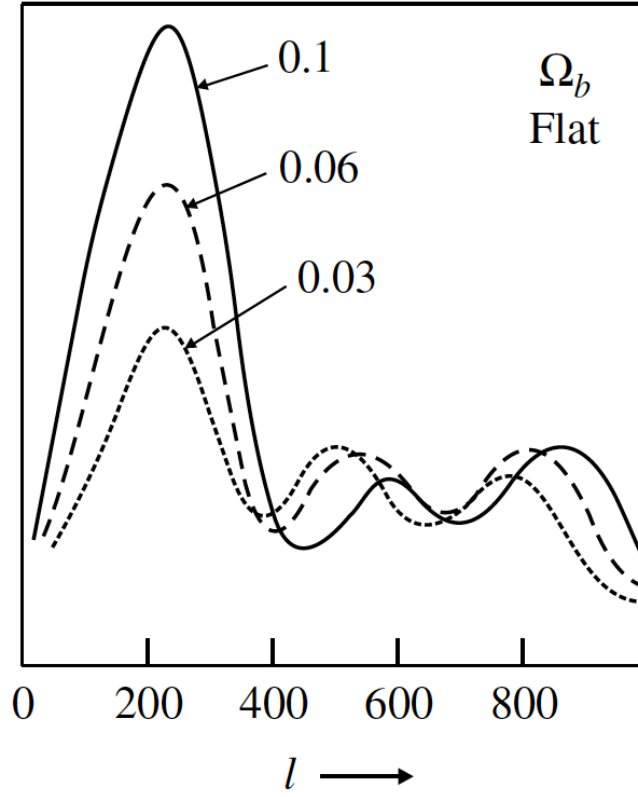
FIGURE 1.6: Cartoon image showing how the shape of the CMB power spectrum changes with varying baryon density (in a flat universe). Image taken from [25].

mass-energy content of the universe allocated to the corresponding source. Therefore, from this result the conclusion that can be drawn is that the universe is dominated by vacuum energy and matter, with the split between the two being 68.89% and 31.11%, respectively. Furthermore, the percentage of the universe that can be allocated to baryonic matter is only 4.9%. The large difference between the baryonic and total matter closure parameters is strong evidence of the existence of non-baryonic dark matter.

Parameter Name	Symbol	Value
Vacuum closure parameter	Ω_Λ	0.6889 ± 0.0056
Matter closure parameter	Ω_m	0.3111 ± 0.0056
Baryon closure parameter	Ω_b	0.0490 ± 0.0088

TABLE 1.2: Closure parameters obtained from the ΛCDM fit to the Planck CMB power spectrum [5]

1.3 Large Scale Structure Formation

The evolution of matter in the universe as it coalesced into galaxies, clusters, and superclusters is evidence for a universe pervaded by *cold* dark matter, which is to say nonrelativistic dark matter. A common criterion used to identify a nonrelativistic particle species is if its average thermal velocity corresponds to a temperature $T \ll m$, where m is the particle mass. Conversely, neutrinos are an example of a thermally produced, *hot* dark matter candidate, because neutrino freeze-out would have occurred when the temperature of the universe was $T \sim 1\,\mathrm{MeV} \gg m_\nu$ [24]; this means they would have had a relativistic mean velocity at this point. A *warm* dark matter candidate would then naturally have an average thermal velocity with $T \sim m$. The main inconsistencies between observation and hot or warm dark matter are [33]:

(i) The ages of large structures over a mass range of 10^9–$10^{15}\,M_\odot$

(ii) The total-to-luminous mass ratios of dwarf spheroidal galaxies

The reason why the thermal properties of dark matter are important for the age of galaxies and clusters is one of relative timing. If dark matter was moving relativistically by the time it froze out of thermal equilibrium in the early universe, it would require masses on the scale of $M \sim 10^{15}\,M_\odot$ to keep significant amounts of dark matter gravitationally bound, which is the mass scale of superclusters [33]. Therefore, in a universe where the majority of dark matter is hot, supercluster sized bodies would be the first structures to gravitationally collapse, then star forming galaxies would appear later. This is commonly known as a 'top-down' hierarchy of structure formation. However, astronomical surveys of galactic clustering show that the first superclusters must have collapsed as recently[5] as $z \lesssim 2$, and the oldest known proto-supercluster has been observed at a redshift of $z = 2.45$ [34]. On the other hand, galaxies have been observed at much larger redshifts, with the oldest known galaxy, GN-z11, having a redshift of $z \approx 11$ [35, 36]. This is consistent with the 'bottom-up' hierarchy of large scale structure formation one would expect if dark matter is predominantly cold.

---

[5]Spectroscopic redshift is used as a measure of both distance from Earth and age. Objects with greater redshift are receding faster from the observer, which corresponds to an object that is further away, according to Hubble's Law. Since it is further away, that also means the light arriving at the observer from the object is older, and therefore the observer is looking at the object as it existed at an earlier point in time.

Dwarf spheroidal galaxies are low luminosity, low mass galactic structures. Through dynamical observations similar to those discussed in Sections 1.1.1 & 1.1.2, these structures are known to have massive halos similar to spiral galaxies [37]. Figure 1.7 shows the mass-to-light ratios, M/L_B, and total-to-luminous mass ratios, M/M_{lum}, of stellar objects ranging in mass from the scale of dwarf spheroidals ($M \sim 10^6\,M_\odot$) to large cluster cores ($M \sim 10^{15}\,M_\odot$) [33]. For both ratios, dwarf spheroidals show clear disparity in the amount of luminous and dynamical mass: the latter being an order of magnitude greater than the former. Furthermore, the plot of M/M_{lum} shows that the ratio of luminous to total mass is constant across all mass scales. The reason why this is important is that hot and warm dark matter, which would have velocity dispersions $\gtrsim 100\,\mathrm{km/s}$, would not be bound gravitationally in large abundance by dwarf spheroidals, which have escape velocities $\sim 10\,\mathrm{km/s}$. The constancy of M/M_{lum} is evidence that objects much smaller than the galactic scale can gravitationally bind dark matter just as efficiently as galaxies and other larger systems, which further supports the hypothesis of cold dark matter over hot and warm dark matter.
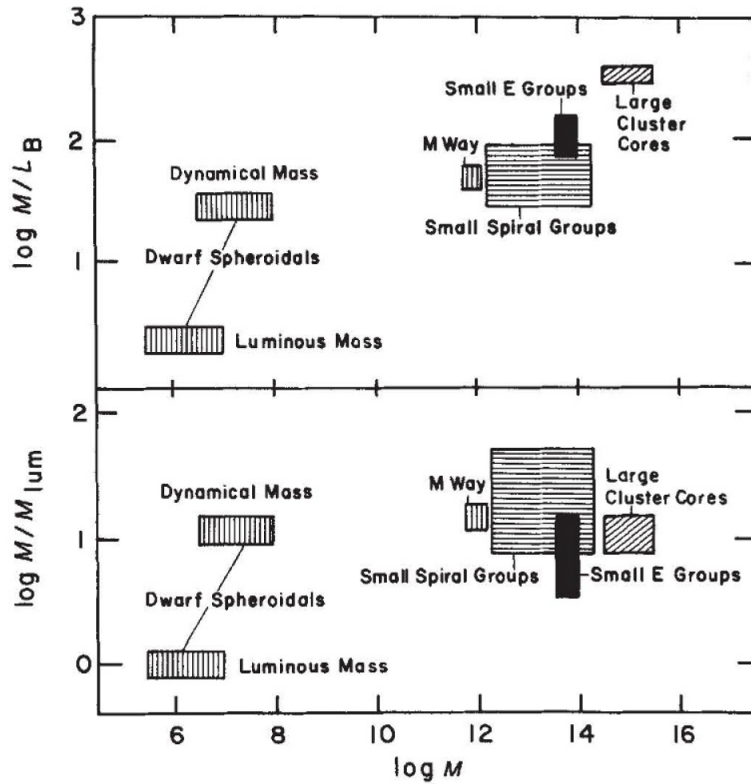
FIGURE 1.7: The Mass-to-Light ratios (top) and Total-to-Luminous mass ratios (bottom) for objects on varying mass scales [33].

1.4 Dark Matter Candidates

Based on the evidence discussed thus far, the properties that a viable dark matter candidate must have, at minimum, are the following:

(i) Non-baryonic in nature

(ii) Nonrelativistic at freeze-out

(iii) Couples very weakly, if at all, to the electromagnetic force

(iv) Stable on cosmological time scales

This section provides an overview of the two most promising candidates: Axions and Weakly Interacting Massive Particles (WIMPs). These dark matter candidates are particularly attractive because they follow naturally from possible solutions to other well known problems in particle physics, which will be discussed in the proceeding subsections.

1.4.1 Axions

In quantum field theory (QFT), there are three important discrete transformations:

$\Rightarrow$ **Charge conjugation** (C)
The reversal of all quantum numbers and charge from $q \rightarrow -q$, thus transforming a particle into its antiparticle

$\Rightarrow$ **Parity** (P)
The inversion of a right-handed coordinate system to a left-handed one via taking $x \rightarrow -x$

$\Rightarrow$ **Time reversal** (T)
The reversal of time evolution via taking $t \rightarrow -t$

It is expected that all physical fields in QFT are invariant under the simultaneous transformations of C, P, and T; i.e. all quantum fields obey CPT symmetry. However, this leaves enough freedom for physically realizable quantum fields to simultaneously violate

any two of these symmetries. For strong interactions, this freedom exists for violation of CP symmetry. The Standard Model Lagrangian for quantum chromodynamics (QCD) is

$$\mathcal{L}_{\mathrm{QCD}} = -\frac{1}{4}G^a_{\mu\nu}G^{a\mu\nu} + \sum_r \left(\bar{q}_r{}^a \big(i\slashed{D}^b{}_a - m_r\delta^b{}_a\big)q_{rb} \right) + \frac{\theta}{32\pi^2}G^a_{\mu\nu}\tilde{G}^{a\mu\nu}, \qquad (1.26)$$

where G is the gluon field strength tensor and $\tilde{G}$ is the Hodge dual gluon field strength tensor; q is the quark field, with charge r, flavour a (b also refers to flavour), and mass m; $\delta^b{}_a$ is the Kronecker delta; and $\slashed{D}$ is the gauge invariant differential operator. The inner products in the first and last terms appear similar, but have a key difference. The first term is proportional to the inner product of the gluon field strength tensor with itself, which is a scalar quantity. The last term, colloquially called the 'θ-term', is proportional to the inner product of the gluon field strength tensor with its Hodge dual counterpart, which in general results in a pseudoscalar quantity [38]. Pseudoscalars are identical to scalars with the exception that they have the property of being odd under parity transformations [3]. Therefore if $G^a_{\mu\nu}G^{a\mu\nu}$ is CP-even, then $G^a_{\mu\nu}\tilde{G}^{a\mu\nu}$ will be CP-odd and vice versa. Thus the θ-term renders Equation 1.26 asymmetric under CP transformations, which in turn should lead to CP-violating behaviour in QCD interactions. Such interactions in the strong sector would be able to produce a non-zero electric dipole moment for the neutron. In short, if CP-violation is possible in the strong sector, this allows for CP-odd πNN (pion-Nucleon-Nucleon) vertices, which mediate nucleon-nucleon interactions [39]. These CP-odd πNN vertices contribute to the size of the neutron electric dipole moment, d_{n}, which scales with θ as [40],

$$d_{\mathrm{n}} = -3.3 \times 10^{-16}\,\theta\,[e \cdot \mathrm{cm}]. \qquad (1.27)$$

However, the current leading limit on the neutron electric dipole moment is [41]

$$d_{\mathrm{n}} = (0.0 \pm 1.1_{\mathrm{stat.}} \pm 0.2_{\mathrm{sys.}}) \times 10^{-26}\,[e \cdot \mathrm{cm}],$$

which sets a strong constraint on the value to be $|\theta| < 5.4 \times 10^{-11}$. Most physicists interpret the smallness of θ occurring by chance as unnatural, since there is no immediately obvious reason for CP-violation to be forbidden in QCD. This constitutes what is known as the Strong CP Problem [40].

A well known potential solution to the strong CP problem, proposed by Robert Peccei and Helen Quinn in 1977 [42], is to absorb the θ parameter into a dynamic field, which obeys a new global chiral $U(1)$ symmetry (called Peccei-Quinn (PQ) symmetry). Similar to the Higgs mechanism suppressing electroweak divergence beyond first order, PQ symmetry needs to be spontaneously broken in order to avoid divergence arising from CP-violating interactions [40]. The new field, a, thus seeks a minimum to suppress CP-violation, and oscillations of the a field about the minimum value result in the pseudoscalar Nambu-Goldstone boson, called the *Axion*.

The energy scale at which PQ symmetry is broken, f_a, is some large value above the electroweak scale, and this drives most of the important physics revolving around axions. It is inversely proportional to the axion decay rate, as well as the axion mass, which can be approximated as [40],

$$m_a \approx 6\,\text{eV}\left(\frac{10^6\,\text{GeV}}{f_a}\right). \tag{1.28}$$

Measurements of the electron neutrino flux from SN 1987A in Ref [43] were used to place constraints on f_a. Their argument is that the available energy from a Type II supernova is equal to the gravitational binding energy of the neutron star, and 99% of that energy is carried away by supernova neutrinos [44]. Thus the observed ν_e flux should account for $\sim 1/6$ of that energy (assuming three flavours of Dirac neutrinos). If axions could carry away some of that energy instead, then this would result in a reduction in the observed ν_e flux, which should scale with f_a. The lower limit on f_a from Ref [43] is of order $\gtrsim 10^{11}\,\text{GeV}$, which means that the axion must be very light: $< 10^{-5}\,\text{eV}$.

The theoretical picture of the axion described up until this point is generally known as the 'QCD axion,' as it is a byproduct of explaining the Strong CP problem, which is a QCD anomaly. There are two prototype models describing the field theory of the QCD axion: the Kim-Shifman-Vainstein-Zakharov (KSVZ) and Dine-Fischler-Srednicki-Zhitnitskii (DFSZ) models [45]. Both of these models predict that the QCD axion mass and coupling strength to standard model particles are proportional to f_a^{-1}. This means QCD axions would be extremely weakly interacting, which is a key property of dark matter. However there are other BSM theories—most notably, String Theory—which produce axion-like particles (ALPs) via a similar approach. That is to introduce a new global symmetry which is spontaneously broken, leading to interactions which suppress 'anomalous' phenomena in the theory [46].

Experimentally, axion and ALP searches can look for the signature of an axion/ALP coupling to photons in strong (i.e. ∼few T) magnetic fields via a process called Primakoff conversion (i.e. an axion converting to photon or vice versa). For example, laboratory experiments such as ADMX [47] look for the conversion of galactic halo axions into microwaves as they pass through a cold resonant cavity immersed in a strong magnetic field. Such searches are called *haloscope* searches. These interactions occur at a rate proportional to the coupling strength of axions to photons, $g_{a\gamma\gamma}$ [eV^{-1}]. The axion-photon coupling and axion mass then define the axion/ALP search parameter space, which is shown in Figure 1.8 [48]. Additionally, there are experiments that can look for the signature of the axio-electric effect [49]. Similar to the photoelectric effect, this is the absorption of an axion/ALP by an electron, which is then sent recoiling away with the kinetic energy of the axion.[6]
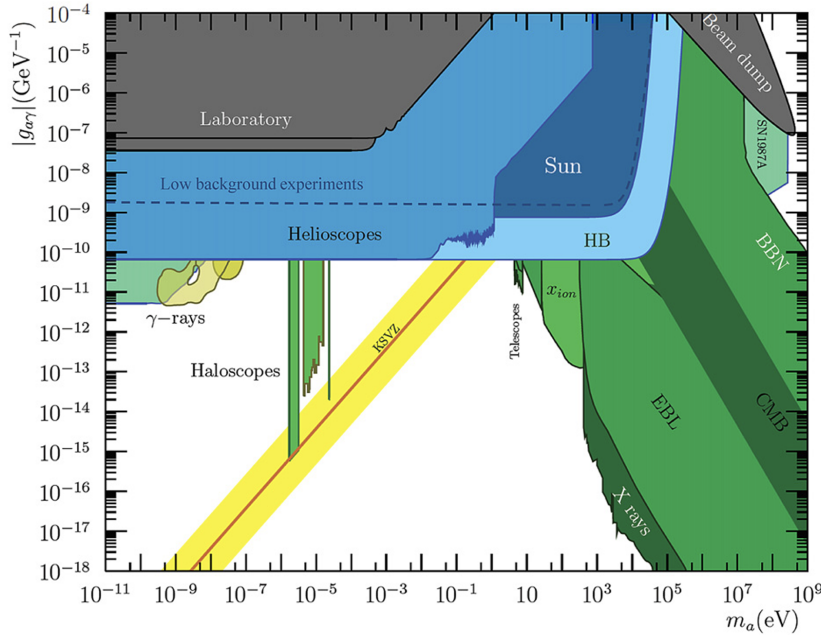
FIGURE 1.8: Current upper limits excluding regions of the QCD axion and ALP phase space. Blue regions are excluded based on astrophysical arguments, grey regions are excluded based on laboratory experiments, and green regions are excluded based on cosmological arguments. The green region labeled 'Haloscopes' corresponds to experiments looking for the signature of axions in the Milky Way dark matter halo. Note that the yellow region surrounding the red line labeled 'KSVZ' represents viable parameter space for the QCD axion. Image taken from Ref [48].

---

[6]Assuming that the axion/ALP rest mass is insignificant compared to its momentum.

1.4.2   Weakly Interacting Massive Particles

The term 'WIMP' refers to a broad class of particles which, in addition to the properties listed in the preamble of this section, are typically on the mass scale of 1–10^5 GeV [46], and can couple to Standard Model particles gravitationally, via weak interactions, or via BSM physics. There are multiple BSM theories that predict the existence of electrically neutral, stable particles with masses in the GeV–TeV range, which would fit naturally the description of a WIMP. Most of these theories have overarching themes, which are:

1. They are related to possible solutions of the Hierarchy Problem

2. They contain new symmetries which naturally halt the decay of BSM particles

Supersymmetry (SUSY) is a well known example which produces a WIMP candidate in this way [50]. SUSY is a theory which postulates a fundamental symmetry between fermions and bosons. In this theory, every Standard Model particle has a 'superpartner' with identical quantum numbers, but with spin differing by a half. Therefore, every Standard Model fermion has a bosonic superpartner, and every Standard Model boson has a fermionic superpartner.

In SUSY, there exist processes which don't conserve baryon number and lepton number. These processes depend on a discrete symmetry called 'R-parity,' where the scale of R-parity violation determines the rate at which they occur [50]. R-parity is defined as

$$R = (-1)^{3(B-L)+2S}, \tag{1.29}$$

where B is the baryon number of a particle, L is its lepton number, and S is its spin. For all Standard Model particles, one finds $R = 1$, and conversely all of their superpartners have $R = -1$. Therefore, assuming R-parity is an exact symmetry[7], any interaction with one super-particle (i.e. the superpartner of a Standard Model particle) in the initial state must have at least one super-particle in the final state.

If one then considers a decaying heavy super-particle, there must be at least one lighter super-particle among its daughters. However, if the decaying super-particle is the *Lightest* Supersymmetric Particle (LSP), then it would be impossible for it to decay while

---

[7]This assumption is valid on the basis of no baryon- or lepton-number violating processes ever being observed to date.

simultaneously conserving R-parity and energy, and thus the LSP would be absolutely stable. In the SUSY formulation known as the Minimal Supersymmetric Model (MSSM), the LSP is the lightest mass eigenstate of the *neutralino*: a mixed state of the superpartners of the photon, Z^0 boson, and Higgs boson. [50]. The neutralino is electrically neutral, couples to the electroweak force, and would have a mass at the electroweak scale, making it an ideal WIMP candidate for dark matter.

Modelling WIMPs as thermal relics from the early universe remains a top contender for the solution to the dark matter problem. Suppose that a WIMP candidate, χ, was in thermal equilibrium with the plasma of the early universe through interactions resembling:

$$\chi + \chi \leftrightharpoons A + B, \tag{1.30}$$

where A and B are generic labels for Standard Model particles with masses $m_A, m_B \ll T$, and T is the temperature of the universe. Assuming $m_\chi \sim \mathcal{O}(100\,\text{GeV}) \gg m_A, m_B$, the Standard Model particles would be relativistic at this time, and they could be assumed to be in thermal and chemical equilibrium with the universe. Then, the comoving abundance of WIMPs, n_χ evolves according to the simplified Boltzmann equation [24],

$$a^{-3}\frac{d}{dt}(a^3 n_\chi) = \langle \sigma_{\text{ann}} v \rangle \big((n_\chi^{(0)})^2 - n_\chi^2\big), \tag{1.31}$$

where a is the time-dependent scale factor describing the Hubble expansion of the universe, $\langle \sigma_{\text{ann}} v \rangle$ is the thermally averaged annihilation cross-section governing the rate of the reaction in Equation 1.30, and $n_\chi^{(0)}$ is the abundance of χ assuming it remains in thermal equilibrium, which varies with temperature as [24]

$$n_\chi^{(0)} = \begin{cases} g_\chi \big(\frac{m_\chi T}{2\pi}\big)^{3/2} e^{-m_\chi/T} & m_\chi \gg T \\ g_\chi \frac{T^3}{\pi^2} & m_\chi \ll T \end{cases}. \tag{1.32}$$

Here, the degeneracy factor g_χ accounts for the WIMP spin, which is also model-dependent.

Assume that at first, there was an initial population of WIMPs in chemical and thermal equilibrium with the early universe plasma, which had temperature $T > m_\chi$. According to Equations 1.30 and 1.31, as the universe expanded and cooled to temperatures below m_χ, WIMP production would have started rapidly decreasing, and only the annihilation

of WIMPs (the forward reaction of Equation 1.30) would have kept them in thermal equilibrium. Eventually, the combination of their weak coupling and decreasing abundance would ensure that the universe expansion rate would dominate the WIMP annihilation rate and WIMPs would freeze out of equilibrium. Solving Equation 1.31 is generally prohibitively difficult to do analytically, but with simplifying assumptions, one can arrive at an approximate expression for the WIMP relic abundance (see Appendix A.1) [24].

$$\Omega_\chi = \sqrt{\frac{4\pi^3 G g_*}{45}} \frac{m_\chi}{T_f} \frac{T_0^3}{30\langle\sigma_{\mathrm{ann}}v\rangle\rho_{\mathrm{crit}}} \tag{1.33}$$

where g_* is the number of relativistic degrees of freedom at the time when the temperature of the universe $T \sim m_\chi$, G is Newton's universal gravitation constant, T_f is the temperature of the universe at the time of WIMP freeze-out, and T_0 is the current temperature of the universe. Now assuming that $\Omega_\chi = \Omega_m - \Omega_b$, using the values from Table 1.2 gives a value for the left-hand side of Equation 1.33. If one assumes a WIMP mass of $m_\chi = 100\,\mathrm{GeV}$, then all particles of the standard model contribute to the relativistic degrees of freedom when $T \sim m_\chi$, and $g_* \simeq 100$, and a simple order of magnitude estimate can be be used for the temperature at WIMP freeze out such that $m_\chi/T_f \simeq 10$ [24]. Now, plugging in the known values for T_0, ρ_{crit}, and G returns an order of magnitude estimate for the thermally averaged annihilation cross-section

$$\langle\sigma_{\mathrm{ann}}v\rangle \sim 10^{-36}\,\mathrm{cm}^{-2}, \tag{1.34}$$

which is, quite conveniently, of the same order of magnitude as weak interactions. This well known result is called *The WIMP Miracle* [7, 24, 25, 46].

An alternative mechanism to thermal production that could have reproduced the observed WIMP relic abundance is an asymmetry of WIMPs and anti-WIMPs in the early universe, similar to the widely known and poorly understood baryon-antibaryon asymmetry. Assuming any matter-antimatter asymmetry in WIMPs is driven by the baryon-antibaryon asymmetry, this would plausibly generate WIMPs in the 5–15 GeV mass range with an appropriate relic abundance [51]. Other presuppositions of the relationship between the baryon and dark matter asymmetries—whether the they be independent, or correlated with each other—can extend this mass range to 10 MeV–100 GeV [52]. This class of models is known collectively as *Asymmetric Dark Matter*, and they constitute a viable subset of WIMP models with lower masses.

1.5 Direct Detection of WIMPs

Figure 1.9 is a cartoon Feynman diagram which summarizes the ways one might detect dark matter. Reading this diagram from left to right corresponds to dark matter self annihilation, and is a form of indirect detection. Indirect searches for dark matter are typically astronomical searches for excessive X-ray emission in dark matter halos. Reading the diagram from right to left corresponds to dark matter production, which can be detected in high energy collider experiments at facilities like the Large Hadron Collider (LHC). Reading Figure 1.9 from top to bottom represents a generic scattering interaction between dark matter and Standard Model particles, which is the arena of direct detection, and the central topic of this work. More specifically, the scope of all discussion hereafter is limited to the direct detection of GeV-scale WIMPs via elastic scattering with nuclei.
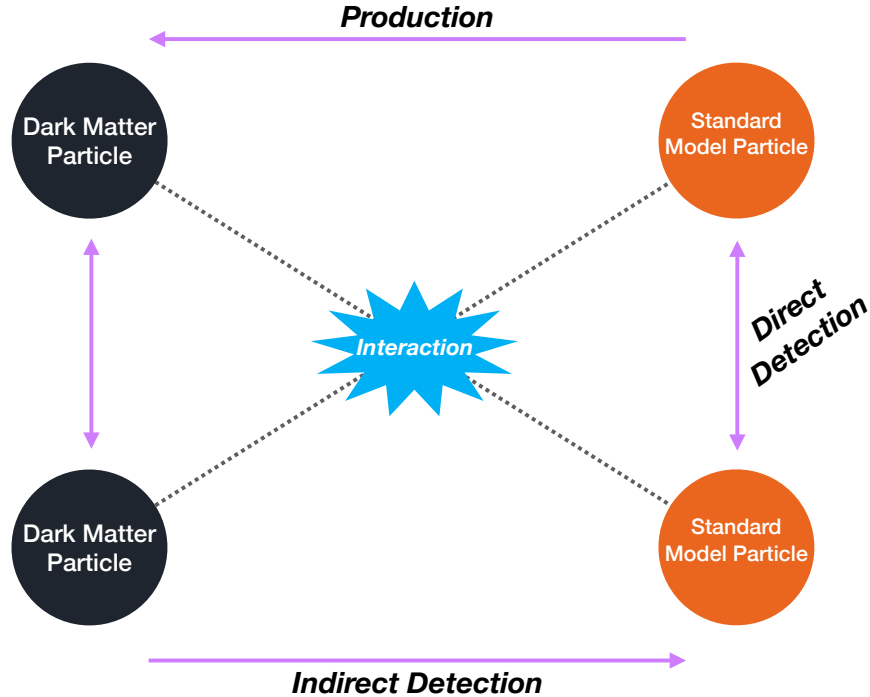
FIGURE 1.9: Cartoon Feynman diagram of dark matter detection channels.

Direct detection of WIMPs falls under the umbrella of ultra-low background experiments. The basic premise of the WIMP search experiments discussed in this thesis is to place a detector with a large mass of a sensitive target material in a low background environment, while the earth moves through space, which is assumed to be densely populated by

WIMPs. In the lab reference frame, this would look like a scattering experiment with a dark matter beam (sometimes referred to as the 'WIMP Wind'). A key observable for any WIMP search experiment is the predicted total WIMP scattering rate, which is detailed in Section 1.5.1. A discussion of specific detection channels and background suppression techniques will be provided in Section 1.5.2.

1.5.1   WIMP Elastic Scattering Rate

The total WIMP scattering rate is used to predict the number of WIMP-nucleus scattering events in a given detector. Encoded in the scattering rate are two quantities which define the standard parameter space for WIMP searches: the WIMP mass, m_χ and the WIMP-nucleon interaction cross-section, σ_χ. As WIMPs encompass many theorized particles, their range of potential scattering interaction modes with baryonic matter is broad, and σ_χ is therefore poorly constrained. Furthermore, knowledge of m_χ and the WIMP phase space distributions is sparse. One can model these pieces of information to fill in the gaps, however the choice of model can significantly change the predicted overall scattering rate. Furthermore, not all scattering targets respond the same way to all models: e.g. isospin-violating WIMP scattering modes disproportionately favour argon targets over xenon [53]. Therefore, in the interest of both consistency across all detector designs and simplicity, the following assumptions are made:

A1. In the Earth's frame of reference, WIMP velocities conform to a Maxwell-Boltzmann distribution having a RMS velocity v_0, shifted by Earth's velocity $\mathbf{v}_\mathrm{E}$, and truncated at the escape velocity of the Milky Way, v_esc.

A2. WIMP interactions in detectors are contact scatters on target nuclei, which obey isospin symmetry, and are mediated by a scalar field (e.g. Higgs exchange).

Dimensionally, the total WIMP scattering rate per unit target mass, R, can be expressed as the product of the local WIMP flux $\frac{\rho_\chi}{m_\chi}|\mathbf{v}|$ (where $\rho_\chi = 0.4\,\mathrm{GeV/cm^3}$ is the local dark matter density [54], and $|\mathbf{v}|$ is the speed of the WIMP Wind); the total coherent WIMP-nucleus scattering cross-section σ_χ^A (where A is the atomic mass number of the target nucleus); and the number of target nuclei per unit mass N_0/A; i.e.,

$$R = \frac{N_0}{A}\frac{\rho_\chi}{m_\chi}|\mathbf{v}|\sigma_\chi^A, \tag{1.35}$$

where $N_0 = 6.022 \times 10^{23}$ is Avogadro's number.[8] In practice, what is observed by a typical WIMP search is a series of potential WIMP scattering events over a broad range of recoil energies, E_r. The resulting spectrum of recoil energies is a measure of the *differential* scattering rate, which means Equation 1.35 needs to be differentiated with respect to E_r, resulting in

$$\frac{dR}{dE_r} = \frac{N_0}{A} \frac{\rho_\chi}{m_\chi} |\mathbf{v}| \frac{d\sigma_\chi^A}{dE_r}. \tag{1.36}$$

At this point, assumptions A1 & A2 can be injected into the calculation. A1 dictates that $|\mathbf{v}|$ follows a Maxwell-Boltzmann distribution, and therefore Equation 1.36 must be integrated over all WIMP velocities up to the Milky Way escape velocity v_{esc}, giving

$$\frac{dR}{dE_r} = \frac{N_0}{A} \frac{\rho_\chi}{m_\chi} \int_{v_{\text{min}}}^{v_{\text{esc}}} f(\mathbf{v}, v_{\text{esc}}) |\mathbf{v}| \frac{d\sigma_\chi^A}{dE_r} \, d^3\mathbf{v}, \tag{1.37}$$

where,

$$f(\mathbf{v}, v_{\text{esc}}) = \begin{cases} \frac{1}{\mathcal{N}} e^{-|\mathbf{v}-\mathbf{v}_{\text{E}}|^2/v_0^2} & |\mathbf{v}| < v_{\text{esc}} \\ 0 & \text{else} \end{cases}, \tag{1.38}$$

and v_{min} is the minimum velocity that can result in recoil energy, E_r (see Equation 1.46). Defining the variable $z = (v_{\text{esc}} + |\mathbf{v}_{\text{E}}|)/v_0$, the normalization constant $\mathcal{N}$ is [54]

$$\mathcal{N} = \left(\pi v_0^2\right)^{3/2} \left(\text{erf}(z) - \frac{2}{\sqrt{\pi}} z e^{-z^2}\right), \tag{1.39}$$

where 'erf' is the standard error function defined as

$$\text{erf}(x) = \frac{2}{\sqrt{\pi}} \int_0^x e^{-x^2} dx. \tag{1.40}$$

A2 simplifies the picture of WIMP-nucleus scatters to only scalar interactions, which means the differential scattering cross-section may be written as [54, 55]

$$\frac{d\sigma_\chi^A}{dE_r} = \frac{\sigma_0}{E_r^{\text{max}}}, \tag{1.41}$$

In Equation 1.41, σ_0 is the total point-like WIMP-nucleus scattering cross-section, and E_r^{max} is the maximum recoil energy. From classical two-body scattering, the recoil

---

[8]Note that the units of this rate are $[\text{mass}]^{-1} \cdot [\text{time}]^{-1}$. To get a predicted number of WIMP events in a given detector, one multiplies R by a quantity called *exposure*, which is defined as the product of total target mass and total observation time.

energy of a nucleus with mass m_n after a collision with a WIMP with mass m_χ, speed $|\mathbf{v}|$, scattered into an angle θ is

$$E_r = \frac{m_\chi |\mathbf{v}|^2}{4} \left(\frac{4 m_\chi m_n}{(m_\chi + m_n)^2} \right) \big(1 - \cos(\theta)\big). \tag{1.42}$$

Therefore E_r^{max} occurs at an angle $\theta = \pi$, and

$$E_r^{\text{max}} = \frac{2 m_\chi^2 m_n}{(m_\chi + m_n)^2} |\mathbf{v}|^2 = \frac{2 \mu_{\chi n}^2}{m_n} |\mathbf{v}|^2, \tag{1.43}$$

where $\mu_{\chi n} = m_\chi m_n / (m_\chi + m_n)$ is the reduced mass of the WIMP-nucleus system. Bringing together Equations 1.37–1.41 and 1.43 results in

$$\frac{dR}{dE_r} = \frac{N_0}{A} \frac{\rho_\chi}{m_\chi} \frac{m_n \sigma_0}{2 \mu_{\chi n}^2} \int_{v_{\text{min}}}^{v_{\text{esc}}} \frac{f(\mathbf{v}, v_{\text{esc}})}{|\mathbf{v}|} d^3\mathbf{v}, \tag{1.44}$$

$$= 4\pi \left(\frac{N_0}{A} \right) \left(\frac{\rho_\chi}{m_\chi} \right) \left(\frac{m_n}{2 \mu_{\chi n}^2} \right) \sigma_0 \int_{v_{\text{min}}}^{v_{\text{esc}}} v\, f(v, v_{\text{esc}})\, dv, \tag{1.45}$$

$$\text{and } v_{\text{min}} = \sqrt{\frac{m_n E_r}{(2 \mu_{\chi n}^2)}} \tag{1.46}$$

where $v \equiv |\mathbf{v}|$. Here, WIMP velocities are assumed to be isotropic, which results in the extra prefactor of 4π and the integrand becoming $v f(v, v_{\text{esc}})$.

Lastly, the form of the total (spin-independent) WIMP-nucleus cross-section, σ_0, can be written as

$$\sigma_0 = F^2(q) \left(Z \frac{f_p}{f_n} - \big(A - Z\big) \right)^2 \sigma_\chi, \tag{1.47}$$

where Z and A are the atomic and mass numbers, respectively, of the target nucleus; f_p and f_n are parameters characterizing the coupling strength of WIMPs to protons and neutrons, respectively; $F(q)$ is the nuclear form factor; and σ_χ is the WIMP-*nucleon* scattering cross-section. The comment in assumption A2 regarding isospin symmetry means that WIMPs would interact as much with protons as neutrons. This results in $f_p \approx f_n$ and the middle factor in Equation 1.47 simplifies to A^2. The nuclear form factor is the spatial Fourier transform of the nucleon weak charge distribution within the nucleus. A reasonably accurate description of the nucleon distribution is that of the

Fermi distribution [54], which takes the spherically symmetric form of

$$\rho(r) = \rho_0 \big(1 + e^{(r-c)/a}\big)^{-1},\tag{1.48}$$

where $\rho(r)$ is nuclear mass distribution function. The parameter ρ_0 can be interpreted as the average density in the bulk of the nucleus, and parameters c and a describe the radius and thickness, respectively, of the 'skin' of the nucleus. A convenient set of parameters to use in Equation 1.48 makes the skin layer sufficiently thin, which allows for the Fourier transform of $\rho(r)$—and thus the form factor $F(q)$—to be solved analytically. This is called the Helm parametrization of the nuclear structure [56]. The resulting form factor is

$$F(q) = 3\frac{j_1(qr_n)}{qr_n}e^{-(sq)^2/2}.\tag{1.49}$$

Here, $j_1(x)$ is the first-order spherical Bessel function, $q = \sqrt{2m_nE_r}$ is the momentum transferred to the target nucleus, $r_n \approx 1.14A^{1/3}$ is the approximate radius of the target nucleus, and $s \approx 0.9\,\mathrm{fm}$ is the nuclear skin thickness [54].

Figure 1.10 shows the shape of the nuclear form factors for various targets up to recoil energies of $1000\,\mathrm{keV}$. Based on this and Equation 1.47, there appears to be a trade-off in the size of the target nucleus. While the spin-independent cross-section scales with A^2 for all recoil energies, the nuclear form factor heavily favours lighter targets for larger recoil energies. This is demonstrated in Figure 1.11, where an argon target is predicted to see a greater rate of WIMP scatters for recoil energies in excess of approximately $50\,\mathrm{keV}$.

In order to calculate the differential scattering rates shown in Figure 1.11, the WIMP mass m_χ and scattering cross-section, σ_χ must be input as free parameters of the model. Assuming 100% detection efficiency, an experiment can then predict the number of expected WIMP scatters, N_{exp}, in their detector with a known target mass M_T, and exposure time t_E by doing

$$N_{\mathrm{exp}} = (M_T \times t_E) \int\limits_{E_{\mathrm{min}}}^{E_{\mathrm{max}}} \frac{dR}{dE_r}dE_r,\tag{1.50}$$

where the product of $M_T \times t_E$ is a quantity called the *exposure* of the experiment, often expressed in units of tonne-years. In the absence of any backgrounds, this hypothetical
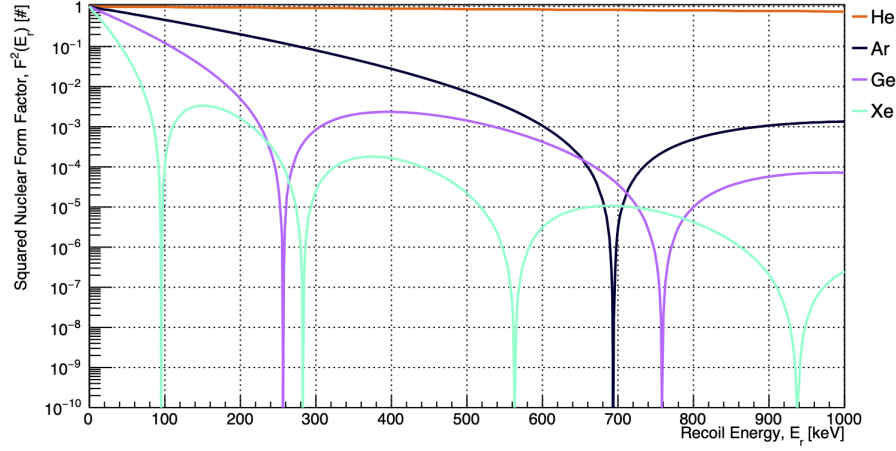
FIGURE 1.10: Helm nuclear form factors for helium, argon, germanium, and xenon targets.
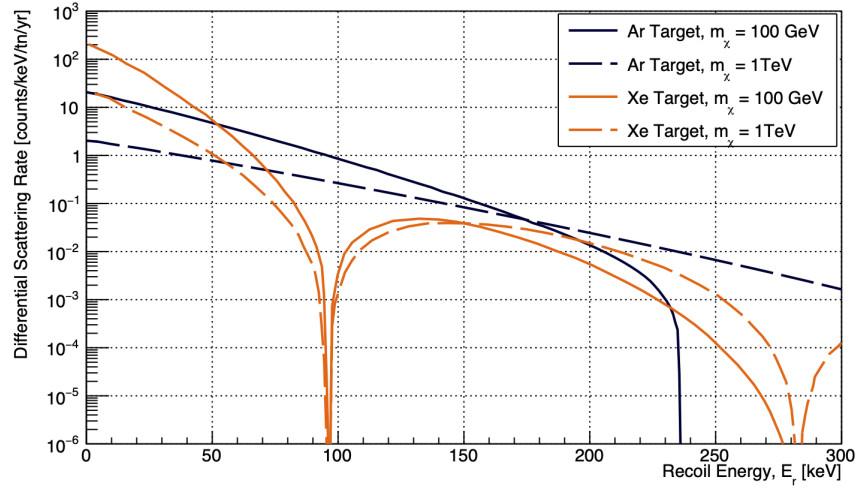
FIGURE 1.11: Comparing the differential scattering rates for experiments with argon and xenon targets, assuming WIMP masses $m_\chi = 100\,\mathrm{GeV}$ and $1\,\mathrm{TeV}$, and a WIMP-nucleon scattering cross-section of $\sigma_\chi = 10^{-8}\,\mathrm{pb}$.

experiment could then argue that any number of scattering events less than N_{exp} (within some pre-defined level of significance) would exclude m_χ and σ_0 from the viable WIMP parameter space. In practice, experiments must first establish a set of event selection criteria which achieve a negligible background contribution in a region of interest (ROI), and then compare their observed event count with N_{exp}. This is called a 'cut and count' analysis, which is reviewed in Chapter 3. Alternatively, one could model the most prevalent backgrounds over a broader ROI and compare the expected signal-plus-background total to the observed total. This kind of analysis is the central focus of Chapter 4.

1.5.2 WIMP Search Experiments

WIMP search experiments rely on sensitive detectors in order to maximize the likelihood that a WIMP might interact with their targets and generate a measurable signal. As was shown in Section 1.5.1, the number of expected WIMP-nucleus scattering events scales linearly with both the total target mass and the exposure time, which are both experimental parameters in the design of WIMP searches. This also increases the sensitivity of the detector to backgrounds, and therefore great care must be taken in suppressing those backgrounds. This is why many WIMP searches take place in underground laboratories like SNOLAB in Sudbury, Ontario, Canada, or Laboratori Nazionali del Gran Sasso (LNGS) in L'Aquila, Italy. Doing this protects the detectors from cosmic rays and associated backgrounds. Detectors are also constructed with radio-pure components, and their exposure to lab air during construction is minimized, as this limits the impact of radon and its progeny in the WIMP search.

Despite these measures, there are still irreducible backgrounds in the recoil energy range of potential WIMP scatters. The expected WIMP signal originates from elastic scattering with target nuclei, which are called *Nuclear Recoil* (NR) events, whereas much of the background signals (e.g. β decays) originate from energy transfer to the electrons of the target atoms. These are called *Electronic Recoil* (ER) events. Thus the goal of many WIMP searches is to suppress NR backgrounds while maximizing separation between NR and ER events. The former is addressed by the aforementioned detector design measures as well as discrimination based on measured quantities, while the latter is mainly achieved with particle identification.

Generally, a scattering event (ER or NR) results in energy deposition in the target medium of $\sim 100\,\mathrm{keV}$ (see Figure 1.11), which in turn generates a signal. That signal can be detected in one or more of three basic detection channels:

C1. **Heat/Sound**

A scattering event transfers energy to the target in the form of heat, which generates phonons with amplitude (i.e. phonon energy) proportional to the heat transfer.

C2. **Ionization**

A scattering event liberates electrons from the target atoms, generating a total charge proportional to the recoil energy.

C3. **Scintillation**

A scattering event results in the production of light with intensity proportional to the recoil energy.

The signals from these detection channels can be used to reconstruct physical observables; e.g. recoil energy, event position in the detector, ionization/scintillation yield, etc.. These observables can subsequently be used for particle ID and background discrimination.

Experiment	Target	Channels
DAMA/LIBRA-II	NaI	C3
DarkSide-20k	Liquid Ar	C2 C3
DEAP-3600	Liquid Ar	C3
NEWS-G	Gaseous Ne	C2
PICO-60	C_3F_8	C1
SuperCDMS	Si	C1 C2
SBC	Ar	C1 C3
LUX-ZEPLIN	Liquid Xe	C2 C3

TABLE 1.3: A selection of WIMP search experiments and their target materials and primary detection channels.

Table 1.3 lists several examples of WIMP searches with their corresponding detection channels. Some WIMP searches use a single detection channel. The PICO-60 experiment [57] used superheated C_3F_8 in a bubble chamber, and is one example of a C1-only experiment. ER backgrounds are negligible for this target in the first place, so background separation mainly comes in the form of rejecting multiple scatter events, which is characteristic of α decays and neutrons, but unlikely for WIMPs. NEWS-G [58] will be a detector that uses only the C2 channel. This detector will consist of a large volume of gaseous neon with a central anode at high voltage. NR events deposit energy in a highly localized fashion, whereas ERs and NR backgrounds (e.g. neutrons) leave longer tracks. Therefore the ratio of total charge to peak current can be used to discriminate against such backgrounds. Lastly, an example of a C3-only experiment is DEAP-3600 [59]: a single phase liquid argon (LAr) based WIMP search. LAr is known to scintillate on

two[9] timescales with mean lifetimes of $\sim 7\,\text{ns}$ and $\sim 1600\,\text{ns}$. NR events predominantly trigger the shorter timescale, while ER events do the opposite. DEAP-3600 leverages this difference using a technique called Pulse-Shape Discrimination (PSD), which will be discussed in Chapter 2.

It is more common that experiments combine two of these channels. One of the most competitive detector designs is that of noble liquid scintillators in a time projection chamber (TPC) configuration, which combines the C2 and C3 channels. Such detectors take advantage of the fact that NR events tend to have a greater scintillation-to-ionization ratio than ER events. Liquid Xenon (LXe) TPC experiments like LUX-ZEPLIN (LZ) [61] currently have the best WIMP sensitivity in the $10\,\text{GeV}$–$1\,\text{TeV}$ WIMP mass range. DarkSide-20k [62] (reviewed in Section 5.5) is a future LAr TPC which will use a similar detection principle to increase WIMP sensitivity for $m_\chi \geq 100\,\text{GeV}$. The effectiveness of LAr TPC technology has been demonstrated by DarkSide-50, which achieved a WIMP-nucleon scattering cross-section upper limit of $1.14 \times 10^{-44}\,\text{cm}^2$[63] for a $100\,\text{GeV}$ WIMP mass. SuperCDMS [64, 65] will combine channels C1 and C2, taking advantage of the fact that NRs will disproportionately favour generating phonons over ionization. An interesting new idea proposed by the SBC (Scintillating Bubble Chamber) collaboration [66] is to use LAr in a bubble chamber configuration similar to that of PICO. LAr scintillation boosts the ability to discriminate against ER backgrounds, while piezoelectric crystals measure the acoustic information from heat deposition in the target.

1.5.3 WIMP Parameter Space and Exclusion Curves

The experiments discussed in Section 1.5.2 broadly fall into two categories: low and high WIMP mass searches. Low WIMP mass searches are most sensitive to $m_\chi \approx 1$–$10\,\text{GeV}$ and their primary objective is to lower their detectable energy thresholds in order to gain sensitivity to lower WIMP masses. In contrast, high WIMP mass searches, which are optimized for $m_\chi \approx 20\,\text{GeV}$–$1\,\text{TeV}$, seek to gain sensitivity to lower WIMP-nucleon cross-sections by building bigger detectors and/or observing for longer periods of time.

---

[9]Evidence for a third timescale has been observed in several independent studies. DEAP addresses this here [60].

Figure 1.12 shows the current constraints on the WIMP parameter space. The green region is the total region of parameter space excluded at a 90% confidence level by all experiments collectively as of 2023. There exists an experimental lower bound indicated by the yellow curves, below which corresponds to WIMP models that would be virtually indistinguishable from the irreducible background of coherent elastic neutrino scattering [67]. For this reason, the of the yellow curves are often called the *neutrino floor*. However, this will be more a relevant background for future WIMP searches.
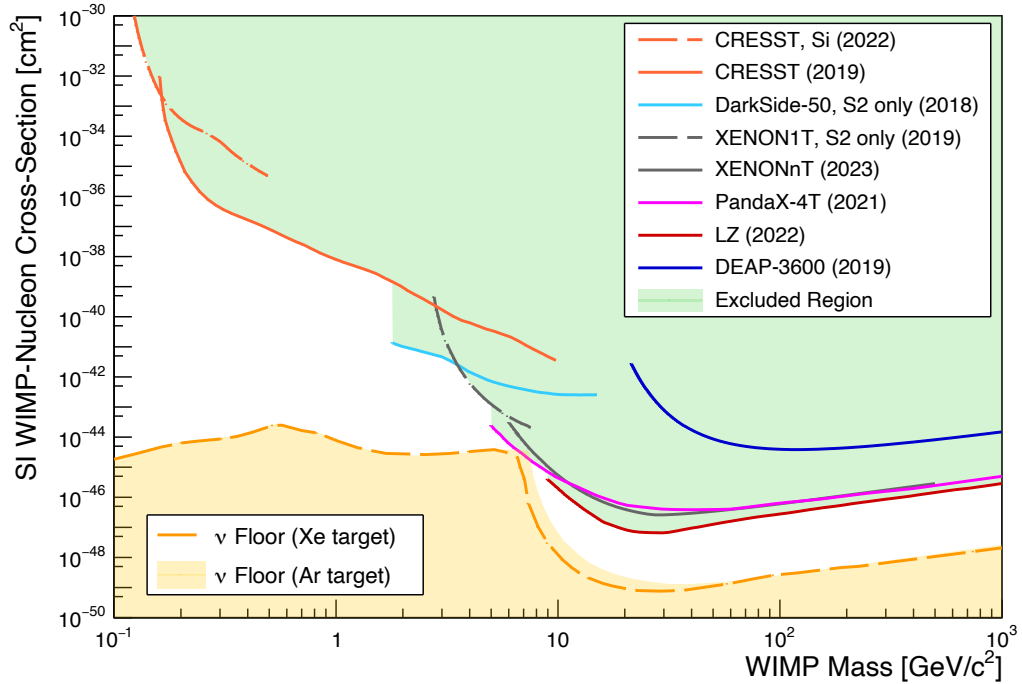
FIGURE 1.12: A plot of the standard WIMP parameter space. The green region represents the excluded parts of the parameter space as of 2023, and the various curves represent the spin independent (SI) WIMP-nucleon interaction cross-section upper limits for various experiments. These include CRESST-III [68, 69], DarkSide-50 [70], XENON1T [71], XENONnT aprile2023first, PandaX-4T [72], DEAP-3600 [59], and LUX-ZEPLIN (LZ) [61]. The 'S2 only' curves for XENON1T and DarkSide-50 indicate the light WIMP searches which only use the ionization detection channel. The CRESST curve labeled with 'Si' refers to a light WIMP search done with a silicon target rather than the usual germanium target.

1.6   Impact Potential and Outlook of Dark Matter Searches

The Standard Model of particle physics, despite all of its successes, is incomplete and extensions of the Standard Model are also poorly constrained. Out of all the biggest questions currently being asked by particle physicists, the true nature of dark matter

is among the ripest for solution. The evidence discussed in Sections 1.1–1.3 are all but a smoking gun for the existence of particle dark matter pervading the universe. A conclusive direct observation of dark matter would not only be a discovery on par with that of the Higgs boson, it would serve as a much needed new piece of information to constrain the space of viable BSM theories. A discovery of WIMPs in particular would reinvigorate interest in theories like SUSY, which have somewhat declined in popularity with the lack of new particle discoveries at the LHC. As alluded to in Section 1.4.2, any confirmation of SUSY or similar theories moves the theoretical physics community closer to solving the Hierarchy problem [50]. This is a major milestone in determining a theory of quantum gravity, which is widely considered as the 'Holy Grail' of physics.

The currently running WIMP search experiments, such as DEAP-3600 and LZ, have not yet observed sufficient evidence of WIMP-nucleus elastic scattering to claim a discovery at the 5σ confidence level. However given the unexcluded WIMP parameter space still remaining, many collaborations will be consolidating their resources to build more sensitive next-generation detectors. For example, the collaborations using LAr are uniting to form the Global Argon Dark Matter Collaboration (GADMC). Already under construction is their 2nd generation LAr TPC WIMP search called DarkSide-20k, which will have a 20 ton fiducial mass of LAr and is intended to conduct a WIMP search with an exposure of 100 tonne-years. The planned 3rd generation detector in the LAr WIMP search program, called Argo, is expected to surpass the neutrino floor around the year 2040 [73]. Despite the presence of the coherent neutrino scattering background, Argo has a projected 5σ discovery potential for 100 GeV WIMPs for elastic scattering cross-sections at the level of $6 \times 10^{-49}\,\text{cm}^2$ [48].

Chapter 2

The DEAP-3600 Dark Matter Search Experiment

DEAP-3600 (Dark matter Experiment using Argon Pulse shape discrimination) is dark matter search experiment with a 3.2 tonne liquid argon (LAr) target mass, optimized for WIMPs at the 100 GeV mass scale. It is currently in operation at SNOLAB in Sudbury, Ontario, Canada—an underground laboratory specially designed for low background experiments and rare event searches. Such experiments can't be operated at the Earth's surface because of a high flux of cosmogenic muons: $86.15\,\mu^{\pm}/\mathrm{m}^2/\mathrm{s}$ [74]. SNOLAB is situated under 2070 m of norite granite rock, giving the equivalent cosmogenic muon protection of 6080 m of water, and resulting in an attenuated cosmic ray muon flux of $3{\times}10^{-6}\,\mu^{\pm}/\mathrm{m}^2/\mathrm{s}$ [75]. However, even with this level of protection, rare event searches must also take great care in suppressing backgrounds from the trace amounts of radioactive nuclides in detector components, which can produce α and β particles, neutrons, and γ-rays. In addition to careful detector design and construction aimed towards limiting neutrons and α backgrounds, DEAP is able achieve the necessary additional background suppression through data analysis; in particular, a technique called Pulse Shape Discrimination (PSD), which can separate βs and γ-rays from αs, neutrons, and WIMPs. This chapter gives an overview of the detector design for the DEAP-3600 experiment, and will establish context for the discussion of event reconstruction in Chapter 3. Section 2.1 discusses the topic of scintillation in noble liquids, as DEAP-3600 uses liquid argon as its WIMP scattering target. An overview of the DEAP-3600 detector design will be given

in Section 2.2, highlighting the relevant components for the analysis discussed in Chapter 4. Lastly, Section 2.3 reviews the known backgrounds in the DEAP-3600 detector, which inform the modelling choices discussed in Chapter 4.

2.1 Noble Liquid Scintillators

Noble liquids can scintillate in the vacuum ultra violet (VUV) range via the formation and decay of excited dimer[1] states, called *excimers*. The microphysics of this process is summarized in this section, including the formation of excimers (Section 2.1.1) and their de-excitation channels (Section 2.1.2). Section 2.1.3 describes the differences in excimer formation resulting from nuclear recoils and electronic recoils, and Section 2.1.4 discusses the motivation for using liquid argon (LAr) as a WIMP scattering target.

2.1.1 Formation of Excimers

For a noble liquid target, with generic chemical symbol X, an incident particle can transfer energy to the target by scattering off of either X nuclei or electrons in orbit about X nuclei. If the energy transfer to the X atom is sufficiently large, then either an X^+ ion or electron will be sent recoiling through the target. The recoiling ion or electron will gradually lose its kinetic energy due to the stopping power of the material. According to Lindhard theory [76], as a particle is stopped in a medium, there is an energy partition between nuclear and electronic stopping power, which contribute to thermal energy and atomic excitation/ionization, respectively. As will be discussed in Section 2.1.2, the latter is what ultimately contributes to scintillation in noble liquids.

The total stopping power on a particle traversing a medium can be expressed as,

$$\frac{\mathrm{d}E}{\mathrm{d}x} = \left(\frac{\mathrm{d}E}{\mathrm{d}x}\right)_{\mathrm{elec}} + \left(\frac{\mathrm{d}E}{\mathrm{d}x}\right)_{\mathrm{nucl}}, \tag{2.1}$$

where $\mathrm{d}E/\mathrm{d}x$ is the stopping power, and subscripts 'elec' and 'nucl' denote the electronic and nuclear stopping powers, respectively. The fraction of the recoiling particle's energy

---

[1]The term 'dimer' generically describes a molecular system composed of two identical simpler structures. In this context, it refers to a diatomic noble molecule.

lost to electronic stopping power can be expressed as [76, 77],

$$f_L = \frac{\int_0^{X(E_r)} \left(\frac{\mathrm{d}E}{\mathrm{d}x}\right)_{\mathrm{elec}} dx}{\int_0^{X(E_r)} \left[\left(\frac{\mathrm{d}E}{\mathrm{d}x}\right)_{\mathrm{elec}} + \left(\frac{\mathrm{d}E}{\mathrm{d}x}\right)_{\mathrm{nucl}}\right] dx} = \frac{\kappa g(\epsilon)}{1 + \kappa g(\epsilon)}, \tag{2.2}$$

where for a nucleus of atomic number Z and mass number A, scattered with recoil energy E_r in keV and travelling a distance $X(E_r)$ before stopping; the energy parameter $\epsilon = 11.5 E_r Z^{-7/3}$; $\kappa = 0.133 Z^{2/3} A^{-1/3}$ is a scaling constant; and $g(\epsilon)$ is an empirical function given by,

$$g(\epsilon) = 3\epsilon^{0.15} + 0.7\epsilon^{0.6} + \epsilon. \tag{2.3}$$

For smaller recoiling particles such as electrons, virtually all of its energy is lost to electronic stopping power, and $f_L \approx 1$. However, for recoiling ions and nuclei at the relevant energy scale for WIMP interactions ($\sim 100\,\mathrm{keV}$), the percentage of its energy lost to nuclear stopping power (i.e. heat) can vary between 38–72%, depending on the size of the nucleus ($\sim 58\%$ for argon)[77]. This effect is called often called 'Lindhard Quenching,' and Equation 2.2 is called the *Lindhard Quenching Factor*.

The fraction of energy not lost to Lindhard quenching results in a local population of X^+ ions and X^* *excitons* along the track of the recoiling particle. When excitons form, they can collide with nearby ground state X atoms and undergo a process called exciton self-trapping to produce an excimer, which in argon occurs within a timescale on the order of picoseconds [78]:

$$X^* + X \rightarrow X_2^* \tag{2.4}$$

Conversely, ions produce excimers through a more complex process, starting with the creation of a charged dimer state via the collision of a ground state X atom and an X^+ ion. The charged dimer then recombines with a free-streaming electron in the vicinity, which was previously liberated from an atom in the track of the recoiling particle. This results in the conversion of the charged dimer into an electrically neutral excimer via the set of reactions in Equations 2.5–2.8 [77, 79]. The timescale for this process is also

of order picoseconds in argon [78].

$$X^+ + X \rightarrow X_2^+ \tag{2.5}$$

$$X_2^+ + e^- \rightarrow X^{**} + X \tag{2.6}$$

$$X^{**} \rightarrow X^* + \text{heat} \tag{2.7}$$

$$X^* + X \rightarrow X_2^* \tag{2.8}$$

The final states in the exciton channel (Equation 2.4) and ion channel (Equation 2.8) tend to have a difference in their total spin angular momenta, S. Excimers created via the exciton channel will generally have $\Delta S = 0$ relative to the ground state, due to conservation of angular momentum. On the other hand, excimers created in the ion channel can have $\Delta S = 1$, because the spin of the recombined electron is uncorrelated with the spin of the charged dimer system. Consequently, there are effectively two kinds of excimer spin states:

1. $^1\Sigma_u^+$, where $\Delta S = 0$ relative to ground

2. $^3\Sigma_u^+$, where $\Delta S = 1$ relative to ground

The ratio of $^1\Sigma_u^+ : ^3\Sigma_u^+$ is therefore highly correlated with the ratio of excitons to ions created in the track of the recoiling particle from the initial scattering interaction.

2.1.2 Relaxation and Decay of Excimers

The excimer states $^1\Sigma_u^+$ and $^3\Sigma_u^+$ predominantly relax and decay to the ground state radiatively via:

$$^{1,3}\Sigma_u^+ \rightarrow 2X + h\nu, \tag{2.9}$$

where $h\nu$ represents the scintillation photon in the VUV energy range. An important detail (particularly for LAr; see Section 2.1.4) is that the spin of the excimer relative to the ground state will affect how quickly this decay can happen. The radiative relaxation from $^1\Sigma_u^+$ to ground is allowed by all quantum mechanical selection rules, whereas the relaxation from $^3\Sigma_u^+$ to the ground state via electric dipole radiation is forbidden, because $\Delta S \neq 0$ and angular momentum cannot be conserved. However such a selection rule is determined to a finite order in time-dependent perturbation theory, and best describes

hydrogen-like atomic states. For larger structures (e.g. argon and xenon excimers), the hydrogen-like approximation doesn't hold as strongly as it does for smaller structures. In the language of perturbation theory, larger and more complicated systems have more significant higher-order perturbative effects which allow for transitions with $\Delta S \neq 0$. By virtue of this, it is in fact possible for the states with $\Delta S = 1$ to radiatively decay to ground, albeit at a slower rate in comparison to their $\Delta S = 0$ counterparts. Therefore the relaxation lifetime of $^3\Sigma_u^+$ is longer than that of $^1\Sigma_u^+$ on average, with the disparity between the two being larger for smaller target nuclei.

There are, however, competing relaxation modes for excimers, which are non-radiative and can suppress the scintillation efficiency of noble liquids. These are also considered quenching processes, similar to Lindhard quenching; a few examples are:

$$\textbf{Biexcitonic quenching } [78]: \ X^* + X^* \rightarrow X + X^+ + e^-, \tag{2.10}$$

$$\textbf{Photoionization } [77]: \ X^* + X_2^* \rightarrow X + X_2^+ + e^-, \tag{2.11}$$

$$\textbf{Penning process } [80]: \ X_2^* + X_2^* \rightarrow 2X + X_2^+ + e^-. \tag{2.12}$$

Each of these processes occurs at a rate proportional to the ionization density, which is highest along the track of the recoiling particle and diminishes radially outward from the track [77]. This can be modelled as a 'core' of high ionization density along the track—where the quenching reactions dominate over radiative de-excitation of excimers—and a 'penumbra' of low ionization density, where quenching is negligible. Analytically, this picture of reduced scintillation efficiency is represented by an empirically derived equation known as *Birks' Saturation Law* [81]:

$$\frac{\mathrm{d}S}{\mathrm{d}x} = \frac{A\left(\frac{\mathrm{d}E}{\mathrm{d}x}\right)_{\mathrm{elec}}}{1 + kB\left(\frac{\mathrm{d}E}{\mathrm{d}x}\right)_{\mathrm{elec}}}, \tag{2.13}$$

where $\mathrm{d}S/\mathrm{d}x$ is the scintillation yield per unit track length by the recoiling particle; A is a constant of proportionality between electronic stopping power and scintillation yield; k is the overall quenching reaction rate; and B represents the size of the high ionization density core along the recoiling particle's track. From Equation 2.13, one can define the Birks quenching factor,

$$f_B = \frac{1}{1 + kB\left(\frac{\mathrm{d}E}{\mathrm{d}x}\right)_{\mathrm{elec}}}. \tag{2.14}$$

Together, the product of k and B define a single empirical parameter, kB, which is called the Birks constant. A and kB are typically left as floating model parameters and obtained in fits to data to describe the quenching effects for a specific particle traversing a specific medium.

As defined in Equations 2.2 and 2.14, f_L and f_B are independent of each other, and an overall energy-dependent quenching factor can be expressed as the product of the two:

$$q_f = f_L \cdot f_B. \tag{2.15}$$

2.1.3 Nuclear Recoils and Electronic Recoils

The scintillation process described in Sections 2.1.1 & 2.1.2 is initiated by either an X^+ ion or electron recoiling through the bulk mass of the target. These events are called Nuclear Recoils (NRs) and Electronic Recoils (ERs), respectively. ER signals are induced by low mass or massless particles, such as β particles[2] or γ-rays. On the other hand, NR signals are typically generated by heavier particles, like α particles[3]; neutrons; and in principle, WIMPs.

The electron sent recoiling through the X bulk in ER events is kinematically extremely limited in how much energy it can transfer to an X nucleus in a single scatter. Instead, virtually all of its energy will be lost to other electrons in X atoms, which results in a greater ionization yield compared to NRs. Furthermore, because of a relatively low stopping power compared to larger particles, electrons will dissipate their energy over a longer track than the X^+ ion. Conversely, the X^+ ion recoiling through the target after a NR event can quite easily transfer energy to other nuclei as well as electrons. However, the recoiling particle in this case has a much larger stopping power than electrons. Therefore the ion will dissipate its kinetic energy over a much shorter distance than an electron, making the ionization density in its track is larger.

The energy partition between electrons and nuclei allows more excitons to be created directly by the recoiling particle in NR events compared to ERs. For electrons recoiling in LAr, the ratio of excitons to ions in its track, $N_{\text{ex}}/N_{\text{ion}}$ is between 0.19–0.29 while

---

[2] While the term 'electronic recoil' implies that an atomic electron was liberated by a scattering interaction such as Compton scattering, βs themselves are electrons traversing the bulk of the target.

[3] Similar to βs, αs are themselves nuclei traversing the X bulk.

the same ratio for α particles is of order unity [79]. Statistically, this will mean that NR events will generate fewer $^3\Sigma_u^+$ states per unit energy than ER events.

A key point to note following the discussion of excimer de-excitation and quenching from Section 2.1.2 is that the production of $^3\Sigma_u^+$ excimers is also positively correlated with ionization density. Furthermore, since the $^3\Sigma_u^+$ states will tend to be longer lived than $^1\Sigma_u^+$ states, the natural consequence is that quenching disproportionately suppresses scintillation from $^3\Sigma_u^+$ over $^1\Sigma_u^+$. Combining this information with the fact that NR events will generally have a higher ionization density per unit energy compared to ERs, due to their shortened track lengths, a crucial difference arises in how the scintillation of NRs and ERs manifest. NRs have reduced scintillation efficiency at the expense of $^3\Sigma_u^+$ scintillation due to quenching effects, resulting in an apparent preference for $^1\Sigma_u^+$ scintillation. In contrast, the lack of quenching effects in ER events allow for the scintillation from the $^3\Sigma_u^+$ states to dominate over $^1\Sigma_u^+$.

2.1.4   Liquid Argon

LAr is the noble liquid target relevant for this work, as it's the target used in the DEAP-3600 dark matter search experiment. DEAP uses atmospheric argon, which is predominantly composed of the ^{40}Ar isotope. ^{40}Ar has a net spin of $S = 0$, and therefore its excimer spin states can be expressed as a spin singlet for $\Delta S = 0$ and as a triplet for $\Delta S = 1$;

$$(\textbf{Singlet}) \qquad ^1\Sigma_u^+ = \frac{1}{\sqrt{2}}\big(|\uparrow\downarrow\rangle - |\downarrow\uparrow\rangle\big), \tag{2.16}$$

$$(\textbf{Triplet}) \qquad ^3\Sigma_u^+ = \begin{cases} |\uparrow\uparrow\rangle \\ \frac{1}{\sqrt{2}}\big(|\uparrow\downarrow\rangle - |\downarrow\uparrow\rangle\big) \\ |\downarrow\downarrow\rangle \end{cases} . \tag{2.17}$$

To reiterate from Section 2.1.2, there should be a difference between the mean radiative relaxation times of the singlet state shown in Equation 2.16 and the triplet state in Equation 2.17, due to quantum selection rules. For LAr, measured values for the singlet, τ_s, and triplet, τ_t, scintillation time scales are provided in Table 2.1. The equivalent timescales for liquid xenon (LXe) are also provided for comparison, which highlights the effect of the target nucleus size on scintillation times. Since LXe has a larger atomic mass,

the quantum selection rules which conserve angular momentum are more easily broken, allowing its $^1\Sigma_u^+$ and $^3\Sigma_u^+$ states to radiatively relax to ground on similar timescales.

Target	τ_s Value	τ_t Value	Reference
LAr	$7.0\pm1.0\,\text{ns}$	$1.6\pm0.1\,\mu\text{s}$	Hitachi et al. (1983) [82]
LAr	$8.2\,\text{ns}$	$1.45\,\mu\text{s}$	DEAP-3600 (2020) [60]
LXe	$4.3\pm0.6\,\text{ns}$	$22.0\pm2.0\,\text{ns}$	Hitachi et al. (1983) [82]

TABLE 2.1: Triplet and Singlet scintillation time scales for LAr and LXe. Note that the values from Ref [60] have no quoted uncertainties due to concerns about the correctness of fit uncertainties in the context of the analysis.

This separation between singlet and triplet scintillation timescales is crucial for LAr targets because atmospheric argon has trace amounts of the ^{39}Ar isotope (see Section 2.3.1). ^{39}Ar is a β emitter with a Q-value of 565 keV and half-life of 388 years, making it a relevant background in the expected recoil energy range for 100 GeV WIMPs (i.e. ~ 100 keV). However, this background can be successfully mitigated by leveraging the discrimination power provided by the large disparity in singlet and triplet scintillation timescales [83]. This technique is called Pulse Shape Discrimination, and it is the topic of Section 3.3.

2.2 Detector Design

The design of the DEAP-3600 detector (shown in Figure 2.1) is described in detail in Ref [84]. This section will summarize the relevant points of the detector design for measurements described in Chapter 3 and systematics described in Chapter 4. This includes a description of the Acrylic Vessel (AV) and inner detector in Section 2.2.1, the outer detector in Section 2.2.2, and the use of PMTs and the organic wavelength shifter 1,1,4,4-tetraphenyl-1,3-butadiene (TPB) in the photon detection system in Section 2.2.3. Lastly, Section 2.2.4 provides a description of the data acquisition (DAQ) systems.

2.2.1 Acrylic Vessel and Inner Detector

The main component of the inner detector is the spherical AV with an 85 cm inner radius and 5 cm thick walls. Poly(methyl Methacrylate (MMA)) (PMMA) is the acrylic material of choice because it has favourable optical, mechanical, and thermal properties
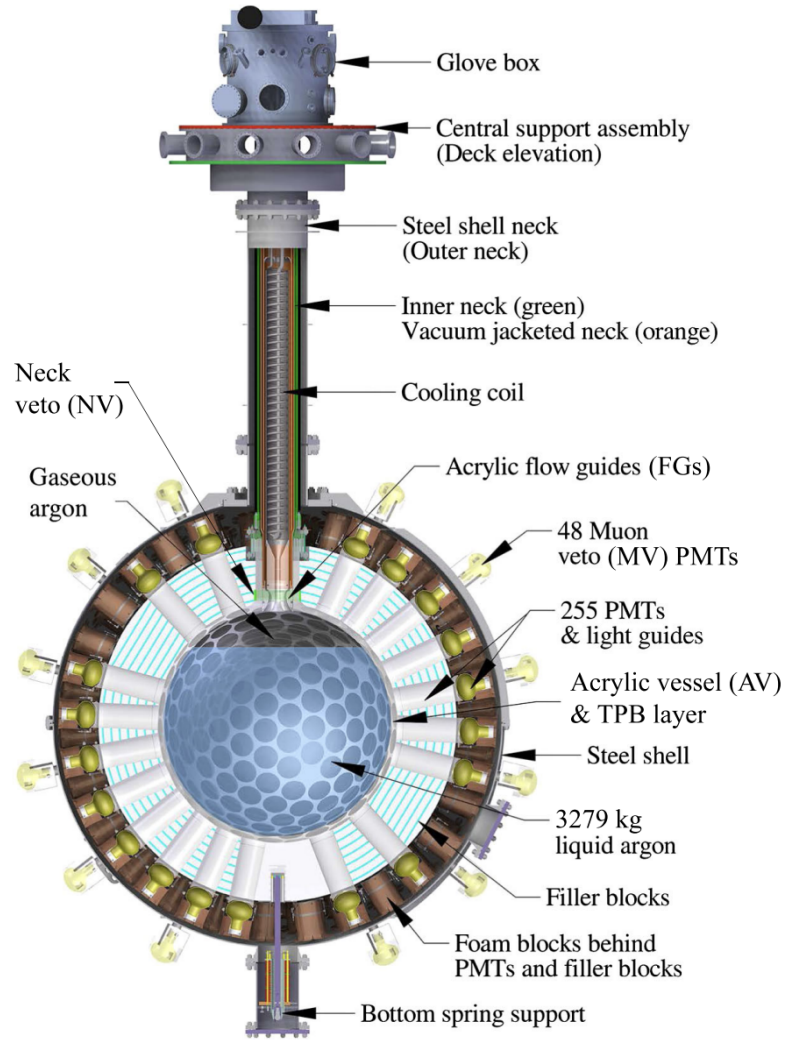
FIGURE 2.1: Schematic diagram of the DEAP-3600 detector, operated at SNOLAB in Sudbury, Ontario, Canada. Image taken from Ref [59]

for the purposes of DEAP-3600. Namely, it's strong enough to support the weight of the detector, it can withstand cryogenic temperatures, and it's optically transparent; 88.6% transmission efficiency for photon wavelengths of 420 nm [85], which as discussed in Section 2.2.3 is the mean wavelength of TPB fluorescence.

The inner detector is equipped with an array of 255 8-inch Hamamatsu R5912 High Quantum Efficiency (HQE) PMTs facing inward towards the LAr. Figure 2.2 shows the angular arrangement of these 255 PMTs which cover 81.3% of the inner detector surface. Each PMT is coupled to a 45 cm long acrylic light guide, which is directly bonded to the exterior wall of the AV. The material requirements of the light guides were based on optical transmission efficiency. The selected light guide acrylic has an attenuation length of 6.2±0.6 m for 440 nm photons. The light guides were annealed
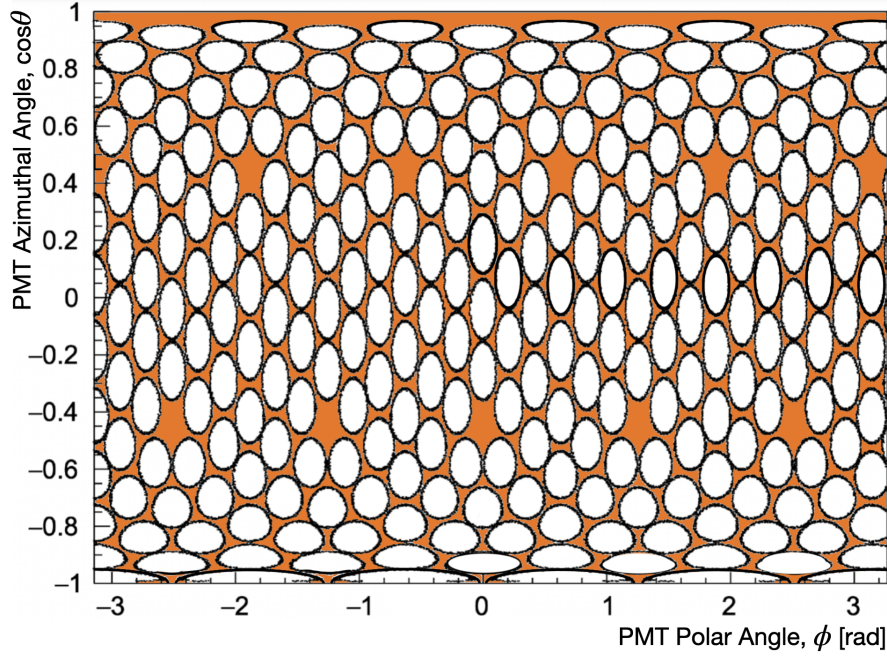
FIGURE 2.2: PMT footprints on the DEAP-3600 inner detector surface shown in angular position $(\cos(\theta)$ vs. $\phi)$. White areas represent the position of a PMT.

at $85\,^{\circ}$C in order to reduce Rayleigh scattering in the acrylic, and minimize optical transmission efficiency losses at the AV and light guide interface [84]. 80% of the photons entering the light guides are trapped by total internal reflection, but to increase collection efficiency, the light guides are also wrapped with a sheet of aluminized mylar foil. This material effectively traps the remaining 20% of optical photons in the light guides, and also optically isolates the light guides from each other. Similarly, the areas on the outer surface of the AV between light guides are covered in white Tyvek, which is 98% reflective and traps scintillation photons inside the detector in the event that they miss the light guides. Covering the layer of white Tyvek is a layer of black Tyvek followed by a layer of closed-cell polyethylene foam backing, which suppresses external photons from leaking into the detector. Filling the void between the light guides are blocks composed of alternating layers of high-density polyethylene and polystyrene. In addition to providing thermal insulation to the AV, the filler blocks serve as part of an ensemble of neutron shielding components. Hydrogenous materials like the acrylics of the light guides and the AV also serve as effective shielding materials from external neutron radiation, especially from the borosilicate glass of the PMTs. An order of magnitude

estimate for a neutron attenuation length[4] in the light guide acrylic and filler blocks is $l \sim 10$ cm [86], which means the probability of a neutron leaking into the LAr through the 50 cm of acrylic/filler blocks is 0.1%. In the absence of these components, the only other form of neutron shielding in the inner detector is the 5 cm thick AV wall, which has a neutron leakage probability of 51%. The assembly design coupling the PMTs to each
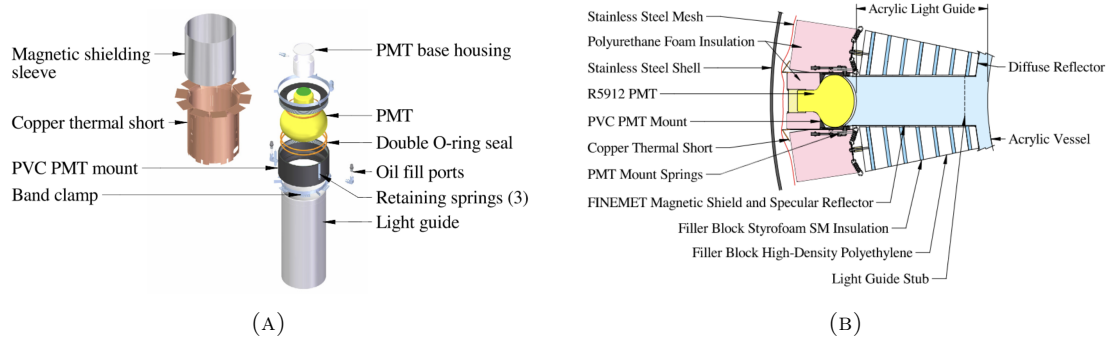
FIGURE 2.3: ((A) DEAP-3600 PMT assembly schematic shown in exploded view and (B) within a schematic of the inner detector. Images taken from Ref [84].

light guide are shown in Figure 2.3. Each PMT is connected to a light guide with a PVC mounting cylinder, with O-rings sealing the point of contact between the PMT and the PVC mount. The volume enclosed between the light guide, PVC cylinder, and PMT glass is then filled with silicone oil, which has a similar index of refraction to acrylic and glass.[5] The PMT and PVC mounts are surrounded by a metal sleeve with an inner layer of FINEMET [87] for magnetic shielding and an outer layer of copper in the metal sleeves acts as a thermal short. Sections of polyurethane foam fill up the remaining spaces between the PMT-PVC-metal sleeve assemblies, which provides further thermal insulation.

20 of the inner detector PMTs are equipped with an apparatus called an Aluminum coated Acrylic Reflector Fibre (AARF), shown in Figure 2.4a. The AARFs provide a means of injecting LED light into the inner detector for calibrating the PMTs, as well as monitoring the stability and gain of the inner detector PMTs over time. The 435 nm LED is controlled outside the detector and can be tuned in intensity from zero up to several hundred photons per pulse. The optical fibre component of each AARF then directs the LED light onto an aluminum coated acrylic reflector, which subsequently

---

[4]A more commonly cited quantity is the *macroscopic cross-section* for neutron interactions, reported in units of cm^{-1}. However, it can be equivalently expressed as an attenuation length where the probability of neutron transmission scales as $e^{-x/l}$, where x is the distance that the neutron travels into the shielding material.

[5]$n =1.495$ and 1.52, for acrylic and glass, respectively and $n =1.405$ for silicone oil.

reflects the light onto the glass of the AARF PMT. Most of the photons generate a signal in the AARF PMT, but 20–25% of the light reflects off the PMT glass and into the AV [88].
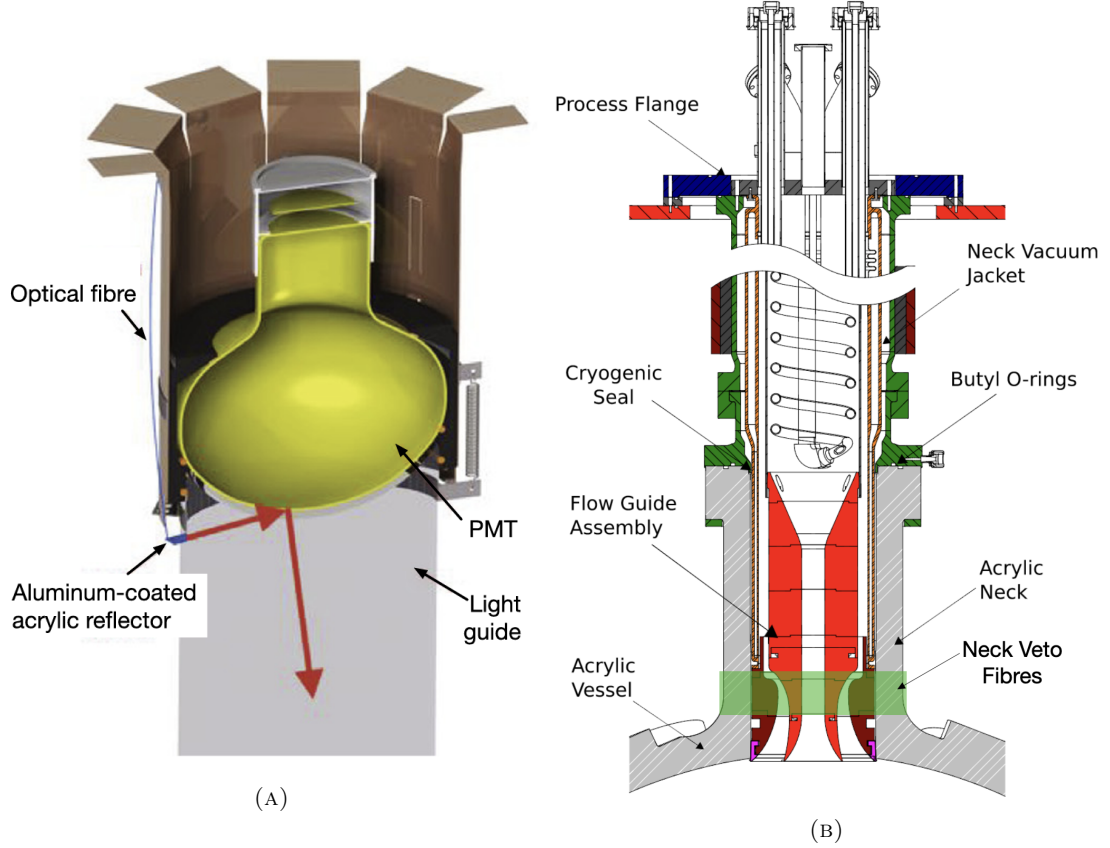
FIGURE 2.4: (A) Depiction of the AARF calibration apparatus on a PMT in the inner detector (image taken from Ref [88]). (B) Schematic diagram of the DEAP detector neck and neck veto system (image modified from Ref [84]).

In Figure 2.1, the spherical AV is connected to a long cylindrical neck structure through which the LAr enters the detector. The neck is not optically isolated from the AV, and due to the geometry of the components in the neck, events originating from this region are prohibitively difficult to characterize in energy and position. The schematic diagram in Figure 2.4b shows that the bottom 10 cm of the detector neck is wrapped in wavelength shifting optical fibres, which transport photons in the neck towards an additional set of four Hamamatsu HQE R7600-300 PMTs. These comprise the neck veto system for DEAP-3600, which make it possible to reject neck events. In particular, this system is intended to reject Čerenkov radiation or α scintillation in the neck.

The design of the inner detector was originally intended to hold 3600 kg of LAr in the AV and be filled up into the neck of the detector. However, on 17 August 2016, an

incident occurred during the filling of the AV whereby LAr leaked into a vapour space buffering the vacuum jacketed acrylic inner neck and stainless steel casing of the outer neck (see Figure 2.1). The acrylic-steel interface is sealed by two butyl O-rings, which failed when they rapidly cooled after coming into contact with LAr. When the O-rings failed, a pathway was created for radon-scrubbed nitrogen, intended for purging the detector, to enter the AV. The solution for this problem was to restart the filling process and stop when the LAr reached a level of approximately 550 mm above the centre of the AV, or 300 mm below the intersection of the neck with the AV. Stopping the filling of the detector at this level provided a greater safety margin for the butyl O-rings to function as intended. The trade-off for the greater safety margin is that the target mass of LAr in the detector dropped from 3600 kg to approximately 3300 kg.

2.2.2 Outer Detector
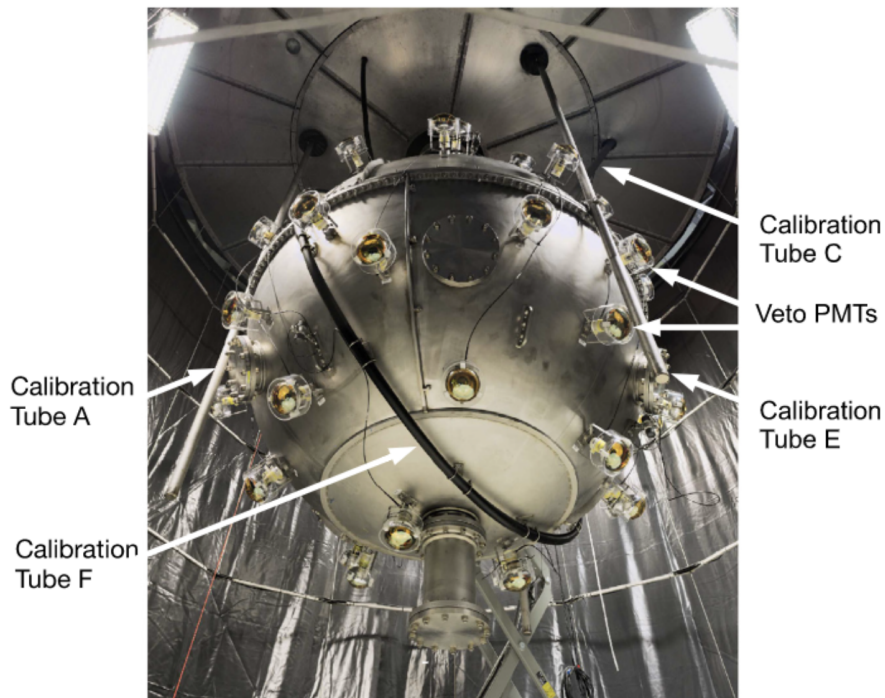
FIGURE 2.5: DEAP-3600 outer detector, showing the shielding water tank, muon veto PMTs, and radioactive calibration tubes. Image taken from Ref [84].

Shown in in Figure 2.5 is the outer detector of DEAP-3600. The inner detector described in Section 2.2.1 is encased in the steel shell of outer detector and placed in a 7.8×7.8 m cylindrical tank filled with ultra-pure water, which further shields the LAr target from neutron radiation emerging from the rock walls at SNOLAB. The outer detector also

has an additional set of 48 Hamamatsu R1408 PMTs facing outward from the steel shell as part of the muon veto system. The residual cosmic rays that pass the 2 km of norite granite overburden at SNOLAB can generate Čerenkov radiation in the water tank. The muon veto PMTs can then be used to reject events in coincidence with the Čerenkov light from cosmogenic muons and their decay products, which may include cosmogenic neutrons leaking into the inner detector. The rejection efficiency of the muon veto system depends on the muon energy, but for muons with energy $> 1\,\mathrm{GeV}$ (which is 99.56% of all muons at SNOLAB [89]), the rejection efficiency has been estimated to be $> 99\%$.[6]

The outer detector also contains DEAP's radioactive calibration systems, which includes:

i) Three vertical, stainless steel tubes hanging from the ceiling of the water shielding tank (Tubes A, B (not visible in Figure 2.5), and E).

ii) One stainless steel tube protruding out from the upper hemisphere of the steel shell (Tube C).

iii) One high density polyurethane tube wrapping around the lower hemisphere of the steel shell (Tube F).

Radioactive sources are lowered into position within these tubes using stepper motors, with position uncertainty of $\sim 1\,\mathrm{cm}$. The specific sources used for calibration are summarized in Table 2.2. ^{22}Na is a positron emitter with a half-life of 2.6 years. When a

Source	Emission Type	ER/NR	Mean Energy [MeV]	Activity [MBq]
^{22}Na	γ-ray	ER	1.275	1
AmBe	neutron	NR	4.2	74

TABLE 2.2: Summary of radioactive calibration sources used in DEAP-3600. Note that the items listed in this table are limited to the external calibration sources. DEAP-3600 also uses internal monoenergetic γ rays from the primordial radionuclide decay chains, such as ^{208}Tl and ^{40}K.

positron is emitted, it will soon after annihilate with a nearby electron, producing two $511\,\mathrm{keV}$ photons. The ^{22}Na nucleus typically decays to an excited ^{22}Ne* nucleus, which de-excites via the emission of a $1.275\,\mathrm{MeV}$ γ-ray in coincidence with two $511\,\mathrm{keV}$ annihilation photons. The ^{22}Na calibration source therefore uses the annihilation photons to tag the $1.275\,\mathrm{MeV}$ γ-ray in calibration studies. To do this, the ^{22}Na source is placed between two cerium-doped Lutetium Yttrium Orthosilicate (LYSO) crystals, which are

---

[6]Though the cosmogenic neutrons themselves don't produce Čerenkov in the water tank.

coupled to two compact Hamamatsu R9880U PMTs. The LYSO crystals scintillate when irradiated by the back-to-back annihilation photons, producing the tagging signal to be read out by the attached PMTs.

The AmBe (Americium-Beryllium) source is a compact mixture of AmO_2, beryllium-9. The neutron-producing reaction goes as follows [90]:

$$^{241}\text{Am} \rightarrow \,^{237}\text{Np} + \alpha \tag{2.18}$$

$$\alpha + \,^{9}\text{Be} \rightarrow \,^{12}\text{C} + n + h\nu, \tag{2.19}$$

where $h\nu$ is a γ-ray, with energy of 4.4 MeV, produced in the α absorption on ^{9}Be. Similar to the ^{22}Na source, the AmBe calibration source is placed between two NaI crystals and two ETL 9102 PMTs. The NaI crystals scintillate when irradiated by the 4.4 MeV γ-ray, which then constitutes the tagging signal for the emitted neutron.

2.2.3 Photon Detection

Photon Propagation in LAr

For LAr, the scintillation processes described in Section 2.1 produce the photon spectrum shown in Figure 2.6. The dominant feature of this spectrum—accounting for 99.8% of LAr scintillation photons—is the peak centred on 128±3.3 nm [91], which corresponds to a photon energy of 9.78 eV. The closest spectral line for neutral atomic argon has a photon energy of 11.62 eV [92] and the first ionization energy of argon is 15.749 eV [93]. Therefore LAr scintillation generally does not have enough energy to ionize argon or be absorbed in atomic transitions, effectively making LAr transparent to its own scintillation.

The most dominant interaction for scintillation photons as they propagate through the LAr is Rayleigh Scattering, which is when photons elastically scatter off of particles much smaller than their wavelength. The Rayleigh scattering length, L, is the mean distance that a photon with wavelength, λ, will propagate through a medium before scattering. This can be expressed as [95],

$$L^{-1} \simeq \frac{8\pi^3}{3\lambda^4}\left[kT\kappa_T\left(\frac{(n^2-1)(n^2+2)}{3}\right)^2\right], \tag{2.20}$$
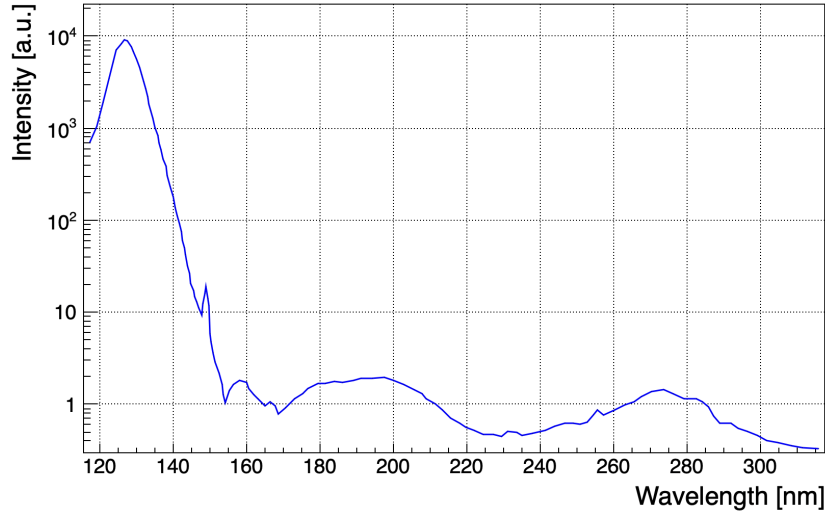
FIGURE 2.6: Measured LAr scintillation spectrum, showing a prominent peak at 128 nm with a full-width at half-maximum of 7.8 nm. The narrow feature at 149.1 nm is attributed to xenon impurities in the measurement apparatus used to obtain this spectrum. The scintillation mechanism thereof is outside the scope of this work, but is discussed in Refs [91, 94]. Plot reconstructed from data taken in Ref [91].

where k is the Boltzmann constant; T and κ_T are the temperature and isothermal compressibility of the medium, respectively; and $n = n(\lambda)$ is the index of refraction of the medium. Between interaction sites, scintillation photons will freely propagate through the LAr at a group velocity v_g given by

$$v_g = \frac{c}{n - \lambda_0 \frac{\partial n}{\partial \lambda_0}}, \tag{2.21}$$

where λ_0 is the vacuum wavelength of the photon.

Together, the optical parameters expressed in Equations 2.20 and 2.21 entirely govern how scintillation photons propagate through the LAr. Note that they are correlated through their mutual dependence on the index of refraction, n. The group velocity is also dependent on the differential index of refraction $\partial n / \partial \lambda_0$, which means $n(\lambda)$ in LAr is an important optical parameter to understand, in addition to Rayleigh scattering length and group velocity. The relationship between refractive index and photon wavelength in a medium is given by the *Sellmeier Equation* [96],

$$n^2(\lambda) = a_0 + \sum_i \frac{a_i \lambda^2}{\lambda^2 - \lambda_i^2}, \tag{2.22}$$

where a_0 and a_i are called Sellmeier coefficients, and λ_i represent wavelengths of resonant photon absorption in the medium. The LAr scintillation mean wavelength is between

two LAr resonant absorption wavelengths in the vacuum ultraviolet (VUV) and infrared (IR). Thus, for the purposes of DEAP-3600, Equation 2.22 can be simplified to

$$n^2(\lambda) = a_0 + \frac{a_{\mathrm{VUV}}\lambda^2}{\lambda^2 - \lambda_{\mathrm{VUV}}^2} + \frac{a_{\mathrm{IR}}\lambda^2}{\lambda^2 - \lambda_{\mathrm{IR}}^2}. \tag{2.23}$$

Equation 2.23 is used to quantify the Rayleigh scattering length and group velocity in the DEAP-3600 optical model. The discussion in Section 4.3.2 focuses on the use of Equation 2.23 to also quantify the systematic uncertainties of Rayleigh scattering length and group velocity, as well as their correlation for use in the DEAP-3600 Profile Likelihood WIMP search.

Wavelength Shifting

In commonly used PMT designs, including the R5912-HQE PMTs used in DEAP-3600, photons must pass through a borosilicate glass window in order to generate a signal. Most borosilicate glass compositions are opaque to photons of wavelengths shorter than $\sim 300\,\mathrm{nm}$, and this drives the quantum efficiency of PMTs to $< 0.01\%$ for $128\,\mathrm{nm}$ photons. To increase sensitivity to LAr scintillation, the inner surface of the AV is coated with a $3\,\mu\mathrm{m}$ thick layer of TPB, which can absorb VUV photons and re-emit them as visible photons. The fluorescence spectrum and efficiency of TPB are shown in Figure 2.7 [97]. The most probable re-emission wavelength of the TPB is $420\,\mathrm{nm}$, which is near the peak quantum efficiency wavelength for the R5912-HQE PMT design ($390\,\mathrm{nm}$, see Table 2.3). Furthermore, the total efficiency[7] of TPB fluorescence for $128\,\mathrm{nm}$ photons is approximately 1.2[8] [97], which means TPB does not negatively impact the observed scintillation yield in DEAP.

Once wavelength shifted from $128\,\mathrm{nm}$ to $420\,\mathrm{nm}$, the visible photons can undergo elastic scattering in the TPB, which has an impact on their angular distribution as they enter the acrylic. The TPB scattering length is an important systematic for position reconstruction, and is discussed more in Section 4.3.2. However, having traversed the TPB, propagation of the visible photons in the acrylic is virtually unhindered. Recall that at $440\,\mathrm{nm}$ the attenuation length of the light guide acrylic is $6.2\pm0.6\,\mathrm{m}$, therefore

---

[7]Integrated over all solid angles and assuming a Lambertian re-emission distribution.

[8]The down conversion of $128\,\mathrm{nm}$ photons to $420\,\mathrm{nm}$ corresponds to an energy differential of $\Delta E \approx -6.7\,\mathrm{eV}$, which means there is sufficient energy from the scintillation photon to generate multiple TPB re-emission photons. Therefore a mean re-emission efficiency greater than unity is not unphysical.
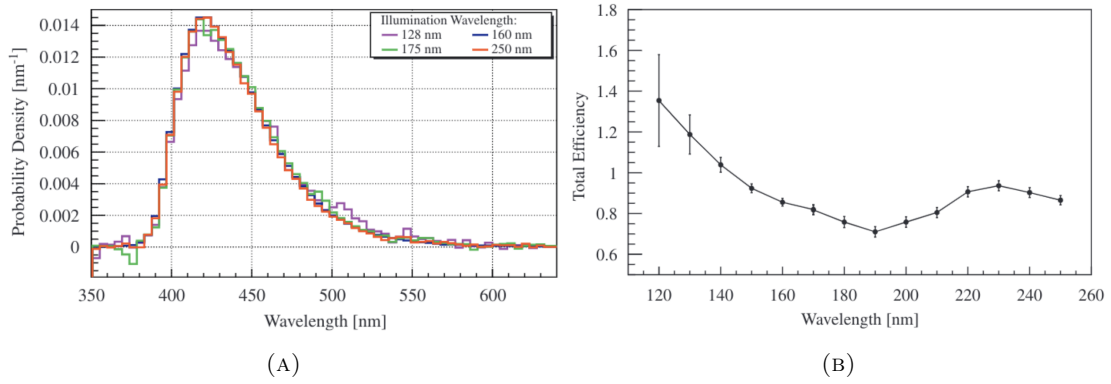
FIGURE 2.7: TPB fluorescence spectrum (A) and total fluorescence efficiency vs wavelength (B). Images taken from Ref [97]

a re-emitted photon from the TPB that travels through a 45 cm light guide has an 85.1–93.0% likelihood of reaching the PMT.[9]

Photomultiplier Tubes

PMTs generate a signal by converting incident light into photoelectrons (PEs) via the photoelectric effect. The component in the PMT which produces the initial photocurrent after being struck by incident photons is called the photocathode: a semitransparent layer of a compound semiconductor substrate with embedded alkali metals [98, 99] coating the inner surface of the PMT window. Alkali metals with especially low work functions, such as potassium, cesium, or rubidium, are favoured for use in photocathodes in order to maximize the spectral range of incident light that can yield a measurable signal. The spectral range of a PMT is typically bounded at longer wavelengths by the sensitivity of the photocathode, and at shorter wavelengths by the transmission efficiency of the window. For example, a Cs-I photocathode substrate is insensitive to photons with wavelengths longer than 200 nm, and a MgF_2 window is opaque to photons with wavelengths shorter than 115 nm, so the spectral range of a PMT with this combination would be 115–200 nm [98].

Figure 2.8 shows how a generic PMT converts a single photon into a measurable signal through a process often referred to as *avalanche multiplication*. The incident photons strike the photocathode and generate a population of PEs, which are then accelerated up to energies of several hundred eV by a large electric field towards a special set of

---

[9]Assuming that the attenuation length for 420 nm is equal to that of 440 nm in the light guide acrylic, and also assuming a maximum acceptance angle of 60°.
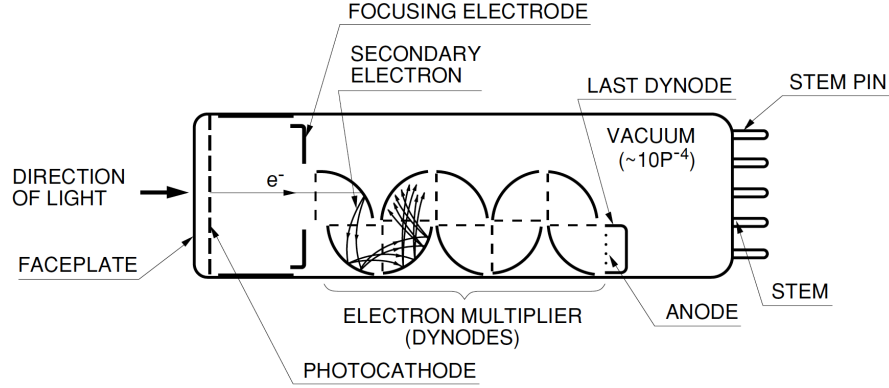
FIGURE 2.8: A generic PMT schematic diagram. Figure taken from Ref[98].

electrodes called *dynodes*. These are typically metal plates, such as nickel, stainless steel, or copper-beryllium alloy, coated in a thin layer of metal oxides or similar materials (e.g. beryllium oxide, magnesium oxide, gallium phosphide) [98]. A focusing electrode provides the source of this electric field, and also channels the PEs towards the first dynode. Upon impact at the dynode, each PE will transfer energy to the lattice structure of the coating material, generating secondary electrons in the process via ionization [100]. Therefore for larger accelerating fields, more secondary electrons can be generated. PMTs typically have 10-15 dynodes, fixed at successively larger voltages provided by a voltage divider. Thus the secondary electrons generated from one dynode become the primary electrons for the next one in the dynode chain. This results in an exponentially growing population of secondary electrons. This charge avalanche process amplifies the initial number of PEs at the photocathode by a factor of $\sim 10^7$, depending on the PMT supply voltage. Therefore even a single PE can generate a total avalanche charge on the order of pC. Finally, the accumulated charge in the avalanche is collected by the anode, and output to the DAQ systems (see Section 2.2.4).

The typical spectral, quantum efficiency, timing, and electrical characteristics of the R5912-HQE PMTs used in the DEAP-3600 inner detector are summarized in Table 2.3. The R5912-HQE design has a bialkali photocathode substrate, which employs two alkali metals instead of one. Compared to (mono)alkali photocathodes, the spectral range is typically extended to longer wavelengths—up to 650 nm for the R5912—and the quantum efficiency is increased from $\sim 15\%$ to 25% [98]. The window material of the R5912-HQE PMT design is borosilicate glass, which is opaque to photons with wavelengths shorter than 300 nm. Thus, the overall spectral range for the R5912-HQE PMTs used in DEAP is 300–650 nm. The dynode chain structure for the R5912-HQE PMT design is

known as a 'box-and-line' type. This is a hybrid of two other dynode structures, called 'box-and-grid' and 'linear-focused,' which are structures designed for optimizing signal gain and response time, respectively. The box-and-line type has a faster response time than the box-and-grid type, but also higher gain than the linear-focused type. This makes it a suitable choice for use in DEAP-3600, which requires both single photon sensitivity (i.e. high signal gain) and precise time resolution (fast response time) for the pulse shape discrimination technique. Sections 3.1 and 3.3 cover these topics in greater detail.

Quantity	Value
Spectral Range [nm]	300–650
Peak Efficiency Wavelength [nm]	390
Peak Quantum Efficiency [%]	42.2
Quantum Efficiency at 420 nm [%]	39
Rise Time [ns]	3.4
Electron Transit Time [ns]	54
Supply Voltage [V]	1500
Single PE Gain	10^7

TABLE 2.3: Typical spectral, timing, and electrical properties of R5912-HQE PMTs.

2.2.4 Data Acquisition System
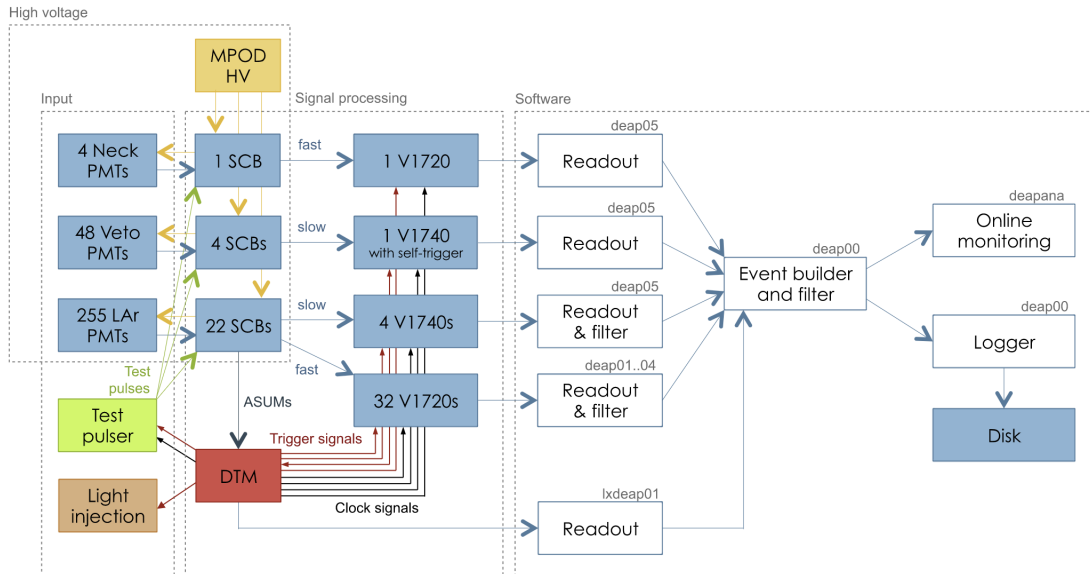
FIGURE 2.9: Flow chart of the DAQ infrastructure for DEAP-3600. Image taken from Ref [84]

The DAQ system for DEAP-3600 is given in a flow chart in Figure 2.9. The key hardware components of this infrastructure are the PMTs, the Digitizer and Trigger Module (DTM), the Signal Conditioning Boards (SCBs), and the CAEN V1720/V1740 digitizers. Signal propagation begins with the PMTs, for which a description of their operational principles was provided in Section 2.2.3. The output of each PMT is fed as input into one of 22 SCBs. Each SCB has 12 identical input channels for handling up to 12 PMTs at once. The purpose of the SCB is to supply the high voltage to operate the PMTs, decouple the high voltage from the PMT output signal, provide high voltage protection for the digitizers, and shape and amplify the PMT signal for analog-to-digital conversion (ADC). The output from the SCBs is then split into three outputs: a high gain readout channel, a low gain readout channel, and an analog sum (ASUM) channel.

The high gain readout channel is digitized by 32 CAEN V1720 modules; each module having 8 input channels with $2\,V_{pp}$ dynamic range, and sampling rate of 250 MHz (or 4 ns per sample). The V1720s convert analog voltage samples into digital levels with 12-bit resolution, i.e. $2^{12} = 4096$ digital voltage levels. The integer values corresponding to the digital voltage levels define an ADC unit system for input signals, which will hereafter be denoted as V_{ADC}. The V1720s process data in a format called Zero Length Encoding (ZLE), which limits the amount of computer memory devoted to signal fluctuations from electrical noise. A sample ZLE V1720 waveform is provided in Figure 2.10. When the input signal is on the level of DC noise (i.e. at baseline) the ZLE triggering mode will not record any data. In the high gain readout channel then noise fluctuations are usually at the amplitude level of $1.2\,V_{ADC}$, whereas pulses from single PEs reach amplitudes of approximately $50\,V_{ADC}$. Therefore the ZLE trigger threshold is nominally set at $5\,V_{ADC}$.

The low gain readout channel is digitized by 4 CAEN V1740 modules, which also have 12-bit resolution over a $2\,V_{pp}$ dynamic range, but have 64 input channels per module and a much lower sampling rate of 64.5 MHz compared to the V1720s. V1740 digitizers also do not have the ZLE functionality, so they save entire waveforms for every triggered event. The low gain channel is operated at 5% of the gain compared to the high gain channel for the purposes of extending the dynamic range of the detector for high energy analyses. High energy events ($\gtrsim 1\,MeV$) that are sufficiently close to the AV surface ($\lesssim 350\,mm$ away from the surface) can easily generate pulses that exceed the dynamic range of the V1720s, resulting in digitizer clipping. Due to the lower gain setting in the low gain channel, the V1740s are typically able to capture those same pulses without

clipping. However, because the low gain channel does not have ZLE capability, the low gain channel is only triggered when the high gain channel signal amplitude exceeds $3400\,\mathrm{V_{ADC}}$, which allows for backup signals to be recorded in the event of clipping, while minimizing unnecessary computer memory usage.
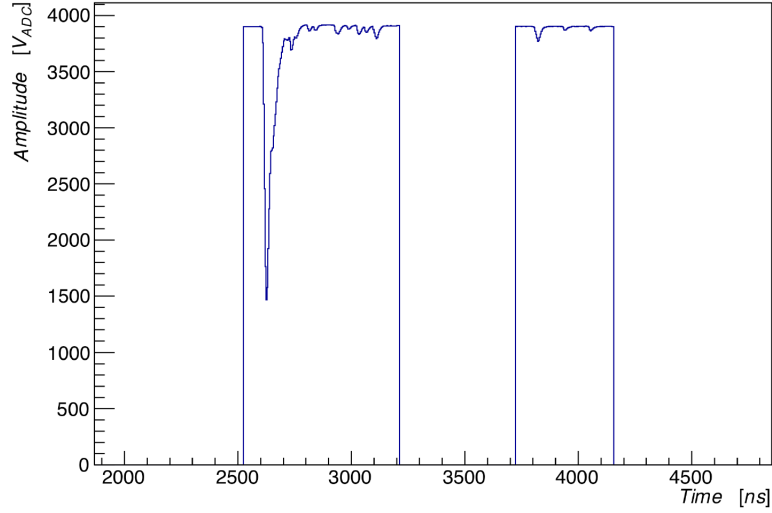
FIGURE 2.10: Example waveform with ZLE from the high gain readout channel in DEAP-3600 physics data.

The ASUM channel for each SCB outputs the summation of all 12 of its analog input signals, which is used by the DTM to trigger readout for any given event. Within the energy range relevant to the DEAP-3600 WIMP search, the trigger efficiency is virtually 100% [101]. The DTM also provides the master clock for trigger times and assigns a hexadecimal label to an event, called a *trigger source*. The trigger source can be classified as a calibration, random, or physics trigger. Calibration triggers are initiated by external hardware to the DAQ system, e.g. the R9880U PMTs used in the ^{22}Na calibration source, and random triggers are solely initiated by the DTM for detector monitoring purposes. Physics triggers are initiated by the SCB ASUM channels, and are also subcategorized based on the promptly arriving light (arriving within 150 ns of the triggered pulse's leading edge) and the fraction of prompt-to-total light. Once the DTM decides to trigger an event, the high gain channel is digitized for every PMT signal in which there was at least one observed PE. All triggering information and digitized waveforms are then packaged into a single $16\,\mu$s event object by DEAP's 'Event Builder' software before being saved in computer hard disk memory for processing and analysis.

2.3 Background Interactions

The sources of background in the DEAP-3600 detector are radiogenic in nature. For example, there are radioactive isotopes of otherwise stable elements in the detector which are created by cosmic rays. This is the source of the β-emitting ^{39}Ar in atmospheric argon, which is the most prominent background for DEAP-3600. This background is discussed in Section 2.3.1. Additionally, trace amounts of uranium and thorium, originally created in the formation of the solar system, exist in virtually all naturally sourced materials on Earth today. Neither uranium nor thorium have any stable isotopes, and the only remaining isotopes have half-lives that are comparable to the age of the solar system; i.e. $\sim 10^9$ years. These long-lived isotopes are called *primordial radionuclides*; they and their progeny are an ever present and irreducible source of radioactivity in the detector. The β emitters in the decay chains of the primordial radionuclides can produce excited daughter nuclei, which subsequently relax via the emission of γ-rays; these β and γ sources are also discussed in Section 2.3.1. ^{210}Po is an α emitter in the ^{238}U decay chain, which is often embedded at the surface of materials within or adjacent to the LAr bulk. It is therefore a source of α particles with degraded energy, which can appear as low energy NRs in the LAr. It can also result in misreconstructed event position if the surface has a nontrivial geometry. These backgrounds are described in more detail in Section 2.3.2. Radiogenic neutron backgrounds are a byproduct of the the primordial radionuclide decay chains via (α, n) reactions, which are discussed in Section 2.3.3. Lastly, Čerenkov radiation in the acrylic light guides is an indirect background correlated with the primordial decay chains, and this is briefly summarized in Section 2.3.4.

2.3.1 Electromagnetic Backgrounds

DEAP-3600 sources its LAr from atmospheric argon, which has naturally occurring isotope abundances of 99.6% ^{40}Ar, 0.337% ^{36}Ar, and 0.063% ^{38}Ar. However the ^{39}Ar isotope is maintained at an abundance of roughly (7.9 ± 0.3) parts in 10^{16} of atmospheric argon [102] by cosmic rays, through neutron knockout reactions, such as:

$$^{40}\text{Ar} + n \rightarrow \,^{39}\text{Ar} + 2n. \tag{2.24}$$
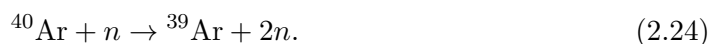
As previously mentioned in Section 2.1.4, ^{39}Ar is unstable and undergoes β decay in the following reaction:

$$^{39}\text{Ar} \rightarrow e^- + \bar{\nu}_e + {}^{39}\text{K} \qquad (2.25)$$

^{39}Ar β decay has a lifetime of 388 years (or a half-life of 269 years) [83], and the specific activity of ^{39}Ar in atmospheric argon has been measured at 1.01 ± 0.01 Bq/kg [103]. Therefore, given a total mass of atmospheric argon of 3300 kg, the activity of ^{39}Ar β decay in the DEAP detector is about 3.3 kBq. Furthermore, for an experiment like DEAP-3600 with a total run time of 3–5 years, this rate of ^{39}Ar β decay is approximately constant due its relatively long lifetime.

The Q-value of Equation 2.25 is 565 keV [83], and since β decays produce an accompanying $\bar{\nu}_e$ in the reaction, this means that the energy of the electron in Equation 2.25 has a broad spectrum with an endpoint at 565 keV and a mean energy of 220 keV, as shown in Figure 2.11. Approximately 55% of this energy spectrum directly overlaps with the recoil energy range for 100 GeV WIMP scattering events in a LAr target, which is 0–235 keV (see Figure 1.11). This makes ^{39}Ar β decays the most dominant background for DEAP-3600. However, since β decays predominantly induce ER events in LAr, the Pulse Shape Discrimination technique described in Section 3.3 is able to reach a rejection power against ^{39}Ar events of 10^{10} [104].
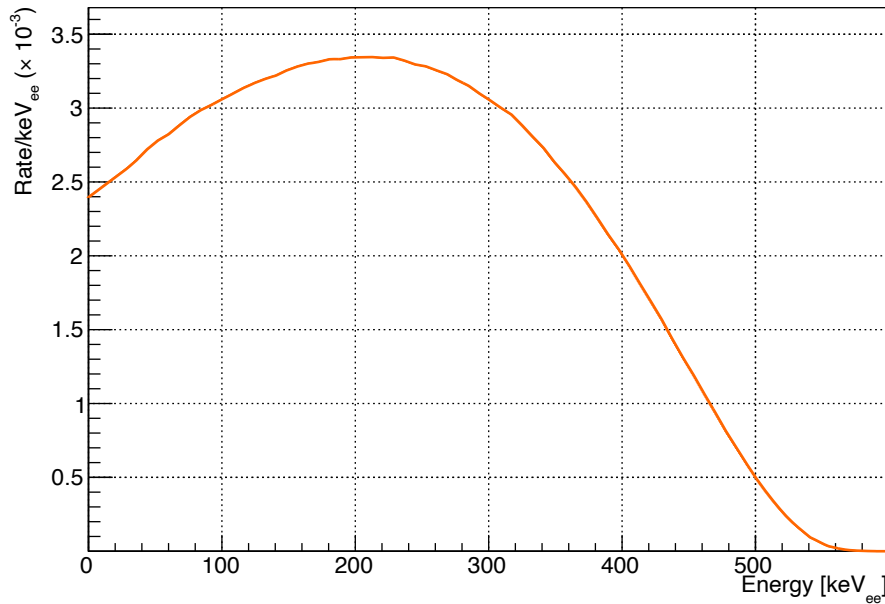
FIGURE 2.11: ^{39}Ar β spectrum as calculated for use in Ref [59].

^{39}Ar β decay is part of a suite of low energy electromagnetic backgrounds, which include γ-rays and other β decays from the primordial radionuclide decay chains. Figure 2.12 [105] indicates the locations and sources of the major electromagnetic backgrounds in DEAP. The locations range from the internal LAr bulk to external detector components all the way out to the steel shell.
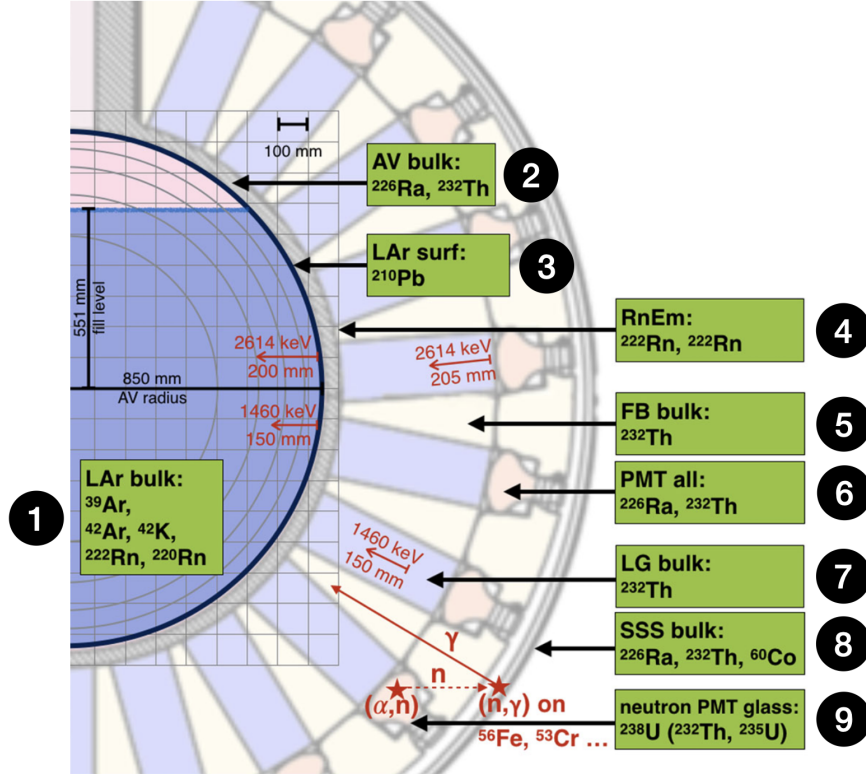
FIGURE 2.12: A schematic breakdown of the sources of electromagnetic backgrounds in DEAP-3600. Location labels indicate: (1) liquid argon bulk; (2) acrylic vessel bulk; (3) liquid argon-TPB-acrylic interfaces; (4) radon emanation from acrylic bulk; (5) filler blocks; (6) PMTs and all internal components; (7) light guides; (8) stainless steel shell; (9) radiogenic neutrons from PMT glass. Image modified from Ref [105].

The internal sources of electromagnetic background relevant to the WIMP NR energy range include β decays from ^{39}Ar, ^{42}Ar, and ^{42}K, as well as the β emitting daughters of ^{222}Rn and ^{220}Rn. Higher energy γ-rays in the LAr bulk, on the order of ~MeV, tend to transfer all their energy to the LAr. Since γs are emitted with well-defined energies, ones emitted in the LAr bulk can be easily rejected. However, when they are emitted in the AV or further out from the LAr bulk, they can lose energy non-radiatively to Compton scattering. This can result in ER events with degraded energy, from either the γ itself or the scattered electron entering the AV. Furthermore, β particles from the uranium and thorium decay chains emitted near the AV surface can similarly degrade

in energy before scintillating in the LAr or produce bremsstrahlung radiation directed into the LAr [105].

Aside from ^{39}Ar β decays, the next most prevalent electromagnetic backgrounds come from the decay chains of ^{232}Th, ^{226}Ra, and ^{40}K originating in the PMTs. However collectively, these account for 0.549% of the total background in the WIMP recoil energy range, with ^{39}Ar accounting for 99.45% and the remaining 0.001% coming from all other sources indicated in Figure 2.12 [105].

2.3.2 Radon Decay Chains

The uranium and thorium decay chains each have, as an intermediate step, a radioactive isotope of the noble gas, radon: ^{222}Rn and ^{220}Rn, respectively. Radon can emanate into the air from any material, or in the case of DEAP, into the LAr from the acrylic or other detector materials. Figure 2.13 shows the decay chain of both radon isotopes. The half-life of ^{222}Rn is 3.83 days, which is much longer compared to the 55.6 second half-life of ^{220}Rn. Therefore the activity of the former in the LAr is expected to be much larger than the latter, since ^{222}Rn can emanate from anywhere in the detector and end up in the LAr bulk, whereas ^{220}Rn is limited by its lifetime.
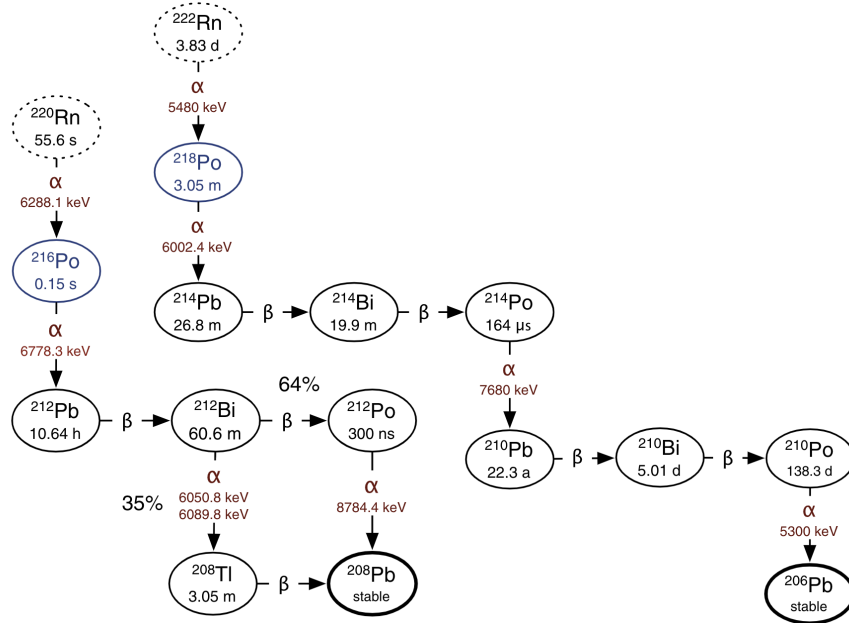
FIGURE 2.13: The decay chains of ^{222}Rn (from ^{238}U) and ^{220}Rn (from ^{232}Th). Image taken from Ref [106].

There are a combined total of eight α emitters among the progeny of ^{220}Rn and ^{222}Rn, including themselves. Since α particles are ^{4}He nuclei, the resulting signal of an α emitted in the LAr bulk will be a high energy NR event from 5–10 MeV. Similar to the high energy γ-rays, the radon chain αs emitted in the LAr bulk are easily rejected based on their energy scale. However, the relatively long-lived ^{210}Po isotope has a mean half-life of 138.3 days, and can circulate in the inner detector long enough to get embedded in surface materials, such as the inner surface of the AV or the inner detector neck. The depth to which ^{210}Po nuclei can penetrate into surface materials can range from 0 to $\sim 100\,\mu$m. Depending on the direction of emission, the ^{210}Po α can lose a virtually all of its kinetic energy non-radiatively (e.g. in the acrylic) and appear as a NR of $\lesssim$ 100 keV. The following subsections discuss the various contributions of ^{210}Po α decays to the total background in the DEAP-3600 WIMP search.

Inner Detector Surface Alphas
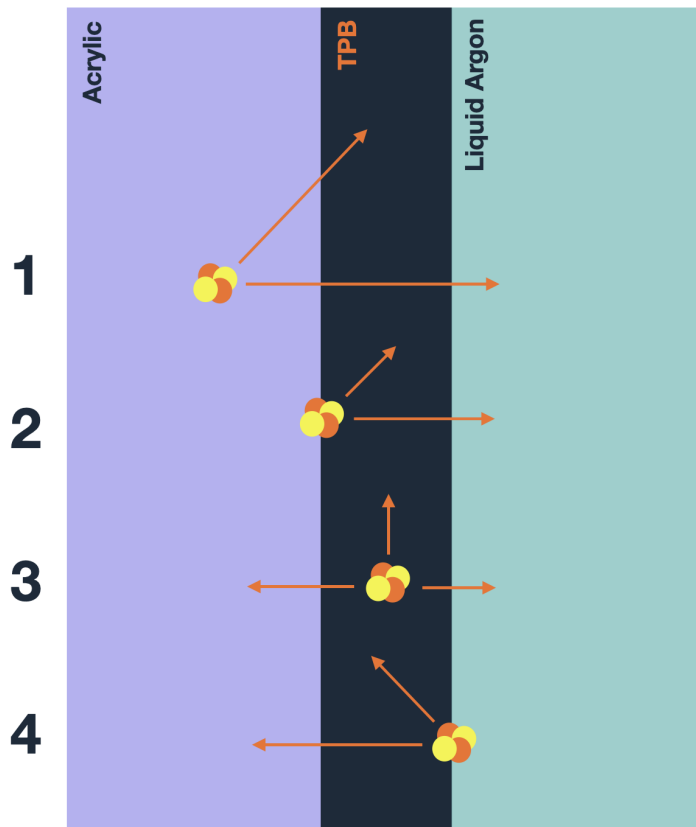
FIGURE 2.14: Cartoon diagram of energy degradation mechanisms for ^{210}Po α decays in the inner detector surface.

When a ^{210}Po nucleus diffuses into the detector inner surface, it can decay in four possible locations, as shown in Figure 2.14:

1. The AV acrylic bulk

2. The interface between the TPB and AV

3. The TPB bulk

4. The interface between the TPB and LAr

α particles traversing the AV lose energy non-radiatively according to their stopping power in acrylic. TPB will emit α-induced scintillation with an efficiency of 882 ± 210 photons per MeV of α energy loss [107], which is approximately 9.6% the efficiency of LAr for the NR events (calculated based on a 20% photon detection efficiency estimated in Ref [84], a reported light yield of 6.1 PE/keV$_{ee}$ in Ref [59] and keV-scale NR quenching factors measured in Ref [108]).

Situations 1 & 2 can therefore produce α events that look like keV-scale NRs, provided that either all of their kinetic energy goes to TPB scintillation or they lose sufficient kinetic energy to the AV before leaking into the TPB or LAr. On the other hand, situations 3 & 4 generally don't apply enough stopping power to α particles before reaching the LAr to result in an event that appears at the keV scale. However, they can be emitted towards (or parallel to) the AV surface and lose a portion of (or all) their kinetic energy to TPB scintillation. In situation 4, there is also the potential for the ^{206}Pb daughter nucleus to recoil into the LAr to produce a keV-scale NR event in the LAr. These events are discriminated against based on their reconstructed position in the detector (see Section 3.2). However, there is a $\sim 10^{-5}$ probability of ^{210}Po surface αs being accepted after position-based background rejection cuts (see Section 3.5.3) [59].

Neck Alphas

The detector neck was designed to promote convective flow of LAr during the filling of the AV and recirculation, while also blocking scintillation in the neck from entering the detector [84]. This is achieved with 'flow guides,' which are shown in Figure 2.15. With the current LAr fill level, the flow guides are entirely surrounded by gaseous argon,
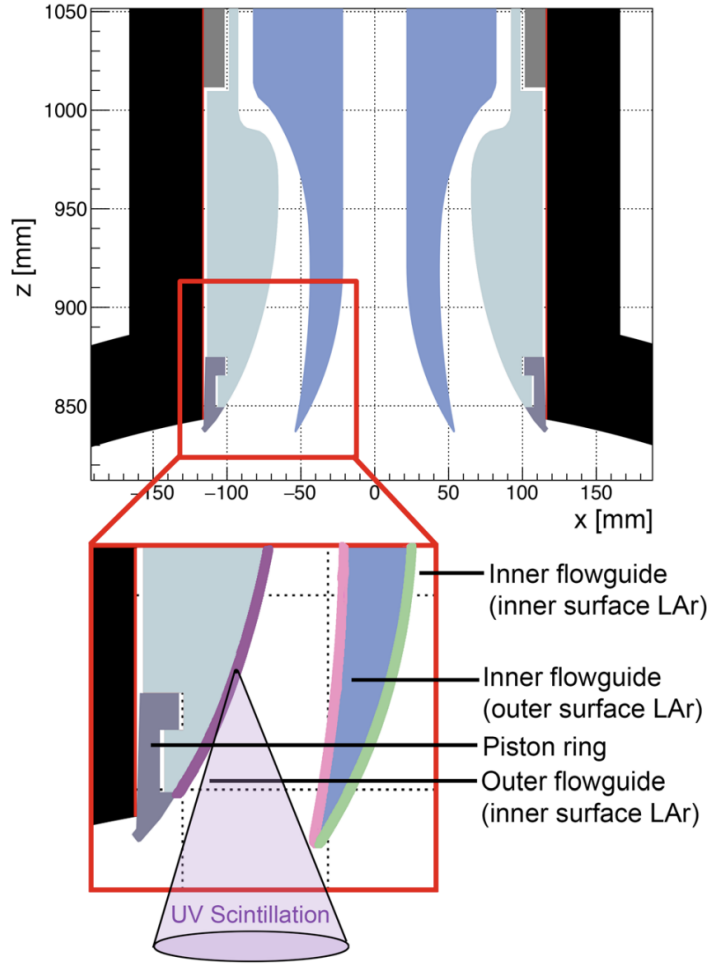
FIGURE 2.15: Diagram of shadowing effects for ^{210}Po α decays in the inner detector neck. Image taken from Ref [59].

however there is a significant background contribution observed in DEAP, which is consistent with NR scintillation coming from the detector neck. The hypothesis adopted by DEAP-3600 is that a thin film ($50\,\mu$m) of LAr condenses onto the flow guides; ^{210}Po α decays on the surface of the flow guides causes scintillation in the LAr film, which is shadowed by the flow guide geometry (as illustrated in Figure 2.15).

There are three surfaces of the flow guides which can contribute to this type of background. The inner flow guide's inner and outer surfaces, and the outer flow guide's inner surface. The flow guides are not coated in TPB, so the majority of observed energy loss comes from shadowing of the UV scintillation, as depicted in Figure 2.15. As will be discussed in Section 3.2, the default position reconstruction algorithm used in DEAP assumes an isotropic scintillation profile, which does not adequately describe the the angular distribution of α scintillation photons originating from the flow guides. In this

scenario, the PMTs at the bottom of the detector receive more photons than the top PMTs due to shadowing, resulting in the reconstructed position of neck αs being biased inward. Consequently, approximately 98% of these events are not rejected by fiducial radius cuts.

Alphas from Dust Particles

There exists a population of α-like events similar to those under the surface and neck ^{210}Po α hypotheses, but with a different angular scintillation distribution compared to neck αs and with greater frequency than can be attributed to the surface αs. The current working hypothesis is that these events are the result of ^{210}Po α decays originating in dust particulates in the LAr bulk. The origin of these dust particulates is proposed to be from a period of resurfacing of the AV inner surface [109], where approximately 10 tonnes of nitrogen gas were used to purge the AV to manage radon contamination in the detector. The nitrogen gas was introduced into the AV through a filter with pores of width $50\,\mu$m. Dust particulates smaller than $50\,\mu$m, likely from eroded pieces of metal (specifically copper) in the nitrogen cryogenic storage tanks, could have passed through this filter and into the AV. Samples of the dust present in the nitrogen stored in Cube Hall at SNOLAB (where DEAP-3600 is located) were taken by passing the nitrogen gas through filter paper. Analysis of these samples under an electron microscope support the hypothesis described here.

Figure 2.16 illustrates how an α decay in a dust particle can result in both energy degradation and shadowing. Energy degradation of the emitted α within the bulk of the dust particle is identical to that of an α emitted in the acrylic bulk of the AV. Significant shadowing of the LAr scintillation induced by the α can occur if the dust particle size is comparable to the track length of the α in the LAr. Since α particles have a very large stopping power, they typically travel a distance on the order of microns before stopping. Under the current dust hypothesis for DEAP-3600, the maximum size of the dust particulates is $\sim 50\,\mu$m in diameter, which was the size of the pores in the nitrogen purge filtration systems. Therefore geometrically, shadowing of scintillation from dust α events is a likely occurrence.
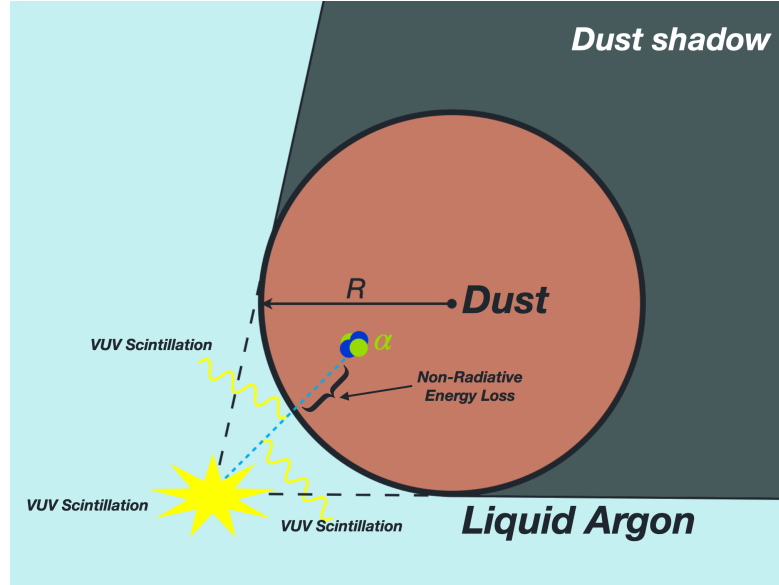
FIGURE 2.16: Cartoon diagram of energy degradation and shadowing effects for ^{210}Po α decays in dust particulates suspended in the LAr bulk.

Within the scope of the analysis presented in Chapter 4, the working hypothesis is that dust particles diffuse approximately uniformly throughout the detector.[10] Under this hypothesis, dust α events are not well rejected by fiducial volume cuts. This makes them similarly difficult to suppress as neck α events. High energy α events generally exhibit more quenching than lower energy NR events, which results in a slightly larger observed LAr singlet-to-triplet ratio. How this can be used to mitigate neck and dust α events in the DEAP-3600 WIMP search is discussed in Chapter 3, Section 3.5.

2.3.3 Radiogenic Neutrons

Radiogenic neutrons are generated by radioactive processes; specifically spontaneous fission and (α, n) reactions. Spontaneous fission refers to when a large nucleus (often with atomic mass number $A > 230$) spontaneously breaks apart into two or more smaller nuclei, usually ejecting some number of subatomic particles in the process. The only relevant fissile nucleus for DEAP-3600 is ^{238}U, which will undergo spontaneous fission in 5.4×10^{-5} % of all decays, and generate an average of 2.07 neutrons per fission reaction [110]. (α, n) reactions, like Equation 2.19, occur when an α particle collides with a reactant nucleus and is absorbed, resulting in a neutron being ejected from the product nucleus. This reaction is suppressed by a Coulomb barrier, since the α particle and the

---

[10]'Floating' and 'sinking' dust models have been considered in other analyses within DEAP-3600.

nucleus have the same electric charge. Therefore (α, n) reactions are rarer for nuclei with large atomic numbers Z, becoming negligible for nuclei heavier than copper [111].

Generally, the average number of neutrons generated per decay—i.e. the *neutron yield* [neutrons/sec/Bq]—from spontaneous fission reactions is a constant. In contrast, the neutron yield of (α, n) reactions depends on the energies of the emitted α particles, the Q-values of the (α, n) reactions, and the isotope-dependent (α, n) cross-sections for the reactant nuclei in the material [111]. In practice, (α, n) neutron yields for a given material are reported as the average over an entire primordial radionuclide decay chain.

In DEAP-3600, the total neutron background is dominated by (α, n) neutrons from the borosilicate glass of the 255 inner detector PMTs and the polyethylene filler blocks, followed by ceramic components in the PMTs, the PVC PMT mounts, polyurethane filler foam, and neck veto PMTs [59]. All of these components are beyond the LAr bulk volume, and can therefore be suppressed with fiducial volume cuts. However, unlike αs, neutrons are not highly ionizing particles and can travel much farther into the LAr bulk. The size of the fiducial volume is heavily constrained by radiogenic neutrons as a result.

2.3.4   Čerenkov Radiation

Čerenkov radiation occurs when a charged particle traversing a dielectric travels at a velocity, v_p, greater than the local speed of light, i.e.

$$v_p > \frac{c}{n},\qquad(2.26)$$

where c is the speed of light in vacuum and n is the refractive index of the dielectric. The charged particle generates an electric field which polarizes the nearest molecules, which then polarize their neighbours, and so on; this polarization wave travels through the dielectric at c/n. When the charged particle moves in the dielectric, the polarization direction of the nearest molecules changes accordingly, which is then communicated to their neighbours in another polarization wave traveling at c/n. If the charged particle is moving at $v_p > c/n$ successive polarization wavefronts will overlap and constructively interfere, producing photons. These photons are emitted in a cone-like distribution, resulting in a characteristic 'light ring' signature.

In DEAP-3600, this happens in the acrylic detector components and PMT glass. γ-rays can Compton scatter off of electrons, sending them recoiling away with kinetic energies up to the 100 keV or MeV scale. Similarly, there are β-emitters in both the uranium and thorium decay chains—e.g. ^{210}Bi—with endpoint energies $\gtrsim 1$ MeV, which are capable of emitting electrons on similar energy scales. When an electron produces a Čerenkov signal in a light guide or PMT glass window, a likely outcome (approximately 50% likelihood) is a large fraction of the total light being measured by a single PMT, which can be quantified and used as a discriminant against Čerenkov radiation (see Section 3.4). For the cases where this method of rejecting Čerenkov events fails, pulse shape discrimination can also be used, as the timescale for Čerenkov radiation is <1 ns [59].

Chapter 3

Event Reconstruction in DEAP-3600

The key observables for the dark matter analysis in DEAP-3600 are the energy and position of a scattering event in the LAr, and the species of the scattering particle. The event energy is determined by measuring the accumulated electric charge generated from the avalanche processes (described in Section 2.2.3) in the 255 signal PMTs in the DEAP detector. Section 3.1 provides a description of how the total electrical charge integrated over all PMT signals is measured and used as an estimator of event energy. For event position reconstruction, DEAP has developed an algorithm called `MBLikelihood`, which is discussed in Section 3.2. Particle species identification is primarily done with the Pulse-Shape Discrimination (PSD) technique, which is reviewed in Section 3.3. Supplementary knowledge of the distribution of scintillation photons among the 255 signal PMTs provides further topological information for identifying backgrounds like Čerenkov radiation and neck α decays. These topological identifiers are described in Section 3.4. Lastly, Section 3.5 describes how the Region of Interest (ROI) for the DEAP-3600 WIMP search was determined in Ref [59] over a 2.5 tonne-year exposure, and also provides the WIMP acceptance and sensitivity for this analysis.

This chapter is a description of the analysis work done collectively by the DEAP-3600 collaboration. My specific contributions to DEAP-3600 analysis is mostly contained within Chapter 4. However the collective DEAP-3600 analysis discussed here also makes use of my work summarized in Ref [112], which was done in the first year of my PhD

studies. The product of this work is a correction algorithm for PMT nonlinearities and digitizer saturation effects in signal readout, which is important for high energy analyses ($\sim$MeV) but not directly relevant to a WIMP search at the keV energy scale. Therefore it is not discussed in this thesis, but will be highlighted in discussions of analyses where it was used.

3.1 Energy Reconstruction

The DAQ and calibration components described in Section 2.2 are the detector systems which provide the necessary inputs for energy estimation in DEAP-3600. Energy estimation is done by integrating PMT pulses in a fixed time window and calculating the number of photoelectrons (PEs) detected for the observed scattering event in the LAr. DEAP-3600 has two main ways of determining the number of PEs detected:

(i) Measuring aggregate pulse integrals across all PMTs, normalized to the average charge generated by a single PE.

(ii) Extending method (i), using a Bayesian algorithm to remove sources of correlated noise originating from PMT artifacts.

Sections 3.1.1 and 3.1.2 summarize methods (i) and (ii), respectively. Section 3.1.3 then reviews how these charge measurements are converted to event recoil energies. Note that the signal saturation and nonlinearity correction algorithm [112] mentioned in the preamble of this chapter is applied prior to the calculations in items (i) and (ii), thereby removing signal saturation as a systematic effect in energy reconstruction. The same is true of all energy-dependent event reconstruction calculations.

3.1.1 Scaling to Single PE Charge

On average, the number of scintillation photons produced in a given scattering event varies linearly with recoil energy, and the number of PEs generated at the photocathodes of the PMTs—i.e. the total photocathode charge—also varies linearly with the total number of scintillation photons. Therefore the summed photocathode charges across all
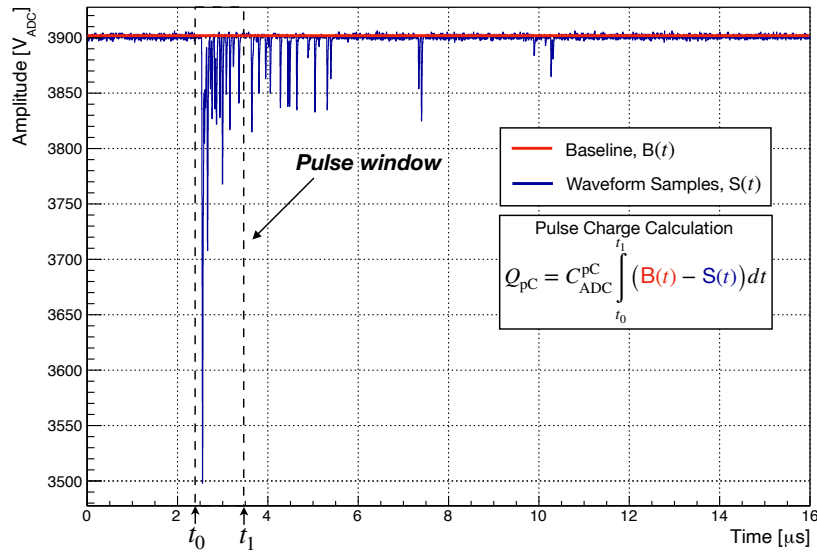
FIGURE 3.1: Sample DEAP-3600 PMT waveform with pulse charge calculation. Samples suppressed by ZLE have been interpolated in this example to indicate average baseline location. C_{ADC}^{pC} factor is defined in Equation 3.1.

255 signal PMTs in DEAP-3600 can be used as an estimator for the recoil energy of a scattering event in the LAr.

The analog output of each PMT signal is input into a CAEN V1720 digitizer readout channel and saved as a digitized waveform, as described in Section 2.2.4. Figure 3.1 demonstrates how to convert the digitized waveform samples into a measure of photo-cathode charge for a given pulse within a waveform. The first step is to convert raw digitizer units (V_{ADC}) to physical units; at this stage 'physical units' refers to a measure of the PMT anode charge. Recall that for the CAEN V1720 digitizers, $1\,V_{ADC}$ corresponds to an analog voltage $V_{ana} = 2\,[V_{pp}]/4096\,[bits]\,V$, and each digitized sample is $\Delta t = 4\,ns$ in duration. Given this information, and that the V1720 input impedance is $Z_{in} = 50\,\Omega$, the following conversion factor is used to transform $1\,V_{ADC}$ into an anode charge in picocoulombs,

$$C_{ADC}^{pC} = \frac{V_{ana}}{Z_{in}} \cdot \Delta t = \frac{2\,V_{pp}}{4096\,bits \cdot 50\,\Omega} \cdot 4 \times 10^{-9}\,s \cdot \frac{10^{12}\,pC}{1\,C} = \frac{80}{2048}\,pC. \qquad (3.1)$$

The next step is to sum the appropriately converted waveform samples (relative to the baseline level) over a time window relevant for the pulse. This time window is determined by a pulse-finding algorithm which defines the pre-pulse boundary at 8 ns before the leading edge of the pulse, and the post-pulse boundary at 8 ns after the point where the pulse amplitude drops below $3\,V_{ADC}$ below the baseline value. Here, the leading edge

of the pulse is defined to be where its first time derivative exceeds an absolute value of $0.75\,\mathrm{V_{ADC}/ns}$. These pre- and post-pulse boundaries ensure that the entirety of a given pulse is captured within the window, while minimizing overlap with neighbouring pulses. Integrating over this time window returns a pulse charge in picocoulombs, with the timestamp in nanoseconds of its observed leading edge. The total charge of an event is then taken to be the sum of all pulse charges in all PMT waveforms within $10\,\mu$s of the start of the event.

The last step is to calibrate each PMT for the average anode charge generated by a single PE. The set of observed pulse charges in each PMT are then normalized to their respective single PE charge. DEAP-3600 monitors the PMT single PE charges on a weekly basis using the AARF system described in Section 2.2.1. In Figure 3.2, PMT occupancy is defined as

$$\mathcal{O}_{\mathrm{PMT}\,j} = \frac{N^{\mathrm{obs}}_{\mathrm{PMT}\,j}}{N^{\mathrm{tot}}} \times 100\% \tag{3.2}$$

where,

$$N^{\mathrm{obs}}_{\mathrm{PMT}\,j} \equiv \text{Number of observed AARF flashes in PMT } j, \tag{3.3}$$

$$N^{\mathrm{tot}} \equiv \text{Total number of AARF flashes.} \tag{3.4}$$

Figure 3.2 shows that the LED light injected into the inner detector from the AARF
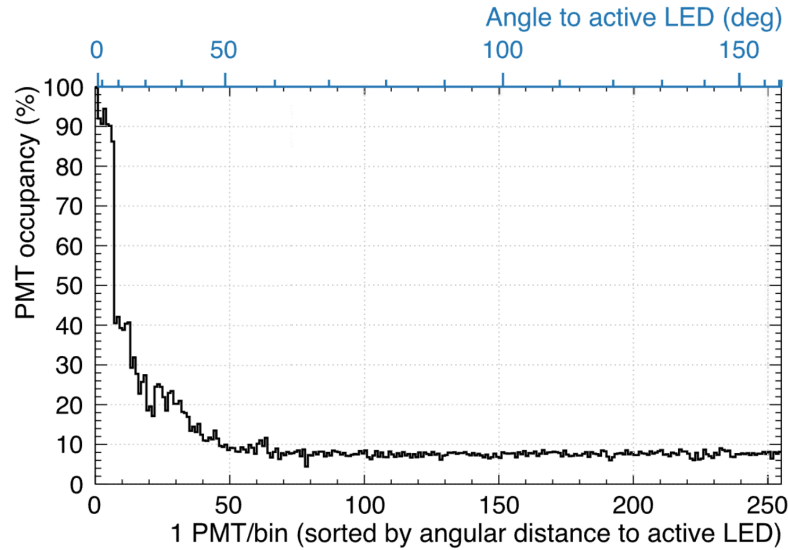
FIGURE 3.2: AARF occupancy vs angular separation from active LED location in the DEAP-3600 inner detector. Here, PMT occupancy is defined in Equation 3.2. Image taken from Ref [88].

system is uniformly distributed across PMTs separated by more than $50°$ from the active

AARF PMT. Furthermore, at 10% occupancy, the mean number of PEs detected per PMT (according to Poisson statistics) is

$$\langle n_{\mathrm{PE}} \rangle = -\ln(1 - \mathcal{O}_{\mathrm{PMT}\,j})$$
$$= -\ln(0.9)$$
$$\approx 0.105.$$

Therefore the AARF system is capable of providing a low intensity light source for simultaneously measuring the few-PE distribution of 205 signal PMTs.

An example of a few-PE distribution for one of the R5912-HQE PMTs used in DEAP is shown in Figure 3.3. A detailed overview of the fit model used in Figure 3.3 is given in Ref [88], but the components are briefly summarized here:

Pedestal Component

Represents the baseline noise or 0 PE component of the overall few-PE distribution. Modelled as a Gaussian.

1 PE Component

Represents the single PE component. Modelled as a Gamma distribution convolved with the pedestal. The total number of electrons, N_{elec} generated in the avalanche process in PMTs is the result of successive Poisson processes with varying mean parameters, which is described by a Polya distribution; in the limit of very large N_{elec}, the Polya distribution can be approximated as a Gamma distribution, which is given in Equation 3.5. Convolving this with the pedestal ensures that the baseline noise fluctuations are reflected in the single PE charge resolution.

n PE Components

Represent 2+ PE components. Modelled as n-fold convolutions of the 1 PE Gamma distribution with itself, plus a one-fold convolution with the pedestal.

$$\mathrm{Gamma}(q|\mu, b) = \frac{1}{b\mu\Gamma\left(1/b\right)} \left(\frac{q}{b\mu}\right)^{\frac{1}{b}-1} e^{-q/b\mu} \tag{3.5}$$

where,

$$q \equiv \text{Observed anode charge [pC]}$$

$$\Gamma \equiv \text{Bernoulli's Gamma function}$$

$$b \equiv \text{Arbitrary shape parameter}$$

$$\mu \equiv \text{Mean parameter [pC]}$$

This model is fit to a measured few-PE distribution, resulting in curves like the one shown in Figure 3.3. The single PE anode charge is then obtained from these fits by extracting the mean of the Gamma distribution in the 1 PE component separately from all other contributions. The number of photoelectrons detected in a PMT, calculated as its measured anode charge divided by the single PE anode charge, is hereafter labelled as qPE.
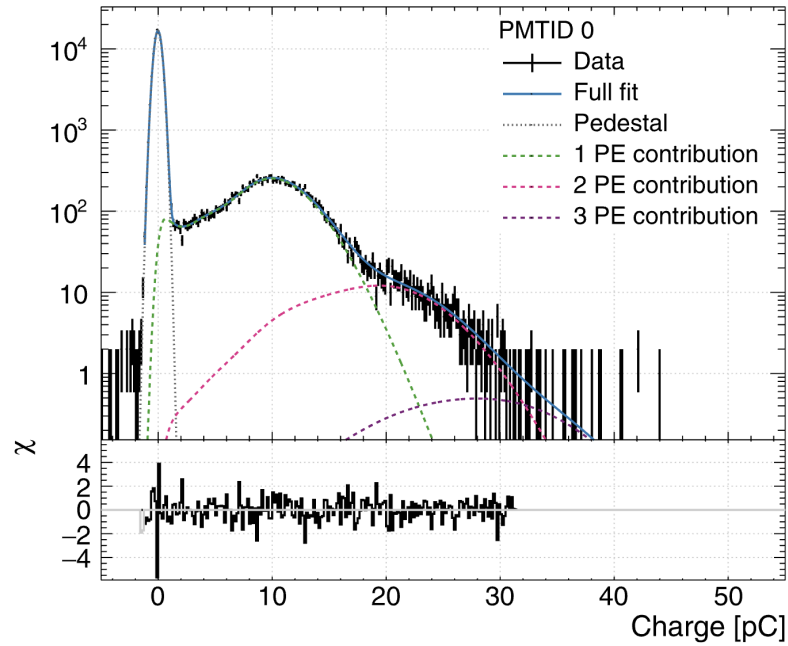
FIGURE 3.3: An example of a few-PE distribution for one of the 255 R5912-HQE PMTs used in DEAP-3600. Image taken from Ref [88].

3.1.2 Bayesian Charge Estimation

A well-documented source of correlated noise for PMTs, known as *afterpulsing*, occurs when a free streaming gas particle inside the PMT is struck by an accelerating PE from

the photocathode. The PE will ionize the gas particle, making it a positive ion which accelerates towards the photocathode. Upon impact at the photocathode, the ion can liberate more electrons, which proceed to generate a pulse as if they were ordinary PEs [88]. Depending on the mass of the ionized particle, the timescale of afterpulsing can range from ~ 100 ns to $\sim 10\,\mu$s, but for a given ion mass there is a characteristic afterpulsing timescale. Afterpulsing also biases observed scattering recoil energies towards higher charges, and as will be discussed in Section 3.3, this effect reduces the particle identification power of the PSD technique.

In DEAP-3600, the probability of a given pulse being an afterpulse is modelled as a time and charge dependent quantity. To measure this probability and its associated uncertainty, a method is described in Ref [113] whereby a low intensity light source is used to trigger single PE pulses in a PMT (which defines a reference time, $t = 0$), and a histogram of the Time-To-Next-Pulse (TTNP)—i.e. the time between the triggering (primary) pulse and the next observed (secondary) pulse—is obtained. In DEAP-3600, the low intensity light source used for monitoring afterpulsing is the AARF light injection system. Figure 3.4 shows the measured afterpulsing probability versus the TTNP and
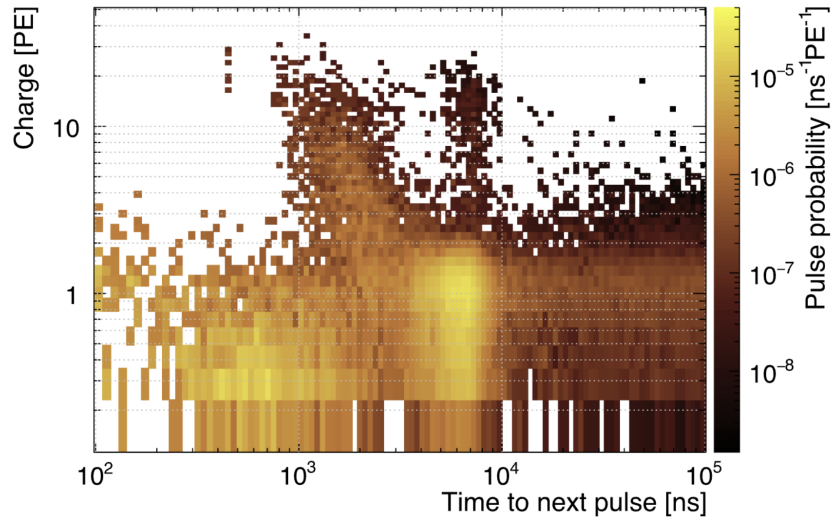
FIGURE 3.4: 2D histogram of the afterpulsing probability of a given pulse as a function of TTNP and secondary pulse charge. Image taken from Ref [88].

observed charge of secondary pulses from AARF flashes. Measurements like the one shown in Figure 3.4 inform one's choice of functional form to model afterpulsing. In

DEAP-3600, the model used is the sum of three Gaussian distributions [104],

$$I_{\mathrm{AP}}(t) = \sum_{i=1}^{3} \nu_{\mathrm{AP}i} \, \mathrm{Gaus}(t, \mu_{\mathrm{AP}i}, \sigma_{\mathrm{AP}i}), \tag{3.6}$$

where Gaus is a normalized Gaussian distribution, $\nu_{\mathrm{AP}i}$ are the total afterpulsing probabilities for each Gaussian term, with mean times of $\mu_{\mathrm{AP}i}$ and widths $\sigma_{\mathrm{AP}i}$. Equation 3.6 captures afterpulsing likelihoods in three different time regions: 300–1000 ns, 1000–3000 ns, and 3000–10000 ns.

The model in Equation 3.6 is part of a method for the removal of afterpulsing from energy estimation via a Bayesian likelihood approach. Consider an observed pulse with a total anode charge Q, generated by some number of PEs, n_{PE}, at the PMT photocathode. Knowing that the probability of afterpulsing is non-zero, the total number of PEs can be split between a contribution coming from scintillation, n_{Sc}, and another from afterpulsing n_{AP}. By definition, n_{Sc} is a better recoil energy estimator than n_{PE}, since it is decoupled from afterpulsing. To obtain a value for n_{PE}, DEAP uses Bayes' theorem:

$$P(n_{\mathrm{Sc}} + n_{\mathrm{AP}} = n_{\mathrm{PE}} | Q) = \left(\frac{P(Q | n_{\mathrm{PE}})}{P(Q)} \right) P(n_{\mathrm{Sc}}) P(n_{\mathrm{AP}}). \tag{3.7}$$

The LHS of Equation 3.7 is the posterior probability of n_{PE} given an observed pulse charge Q. On the RHS of Equation 3.7, the first factor is the 'support' that the observed data provides for a given value of n_{PE}, while the remaining two terms are the prior distributions for n_{Sc} and n_{AP}.

Precision measurements of both $P(n_{\mathrm{Sc}})$ and $P(n_{\mathrm{AP}})$ was the subject of Ref [60]. As shown in Figure 3.5, these were obtained in fits of observed pulse shapes with a model that includes a component for each of:

(i) LAr scintillation

(ii) TPB re-emission

(iii) Afterpulsing

(iv) 'Stray' light (i.e. dark noise + residual photons from preceding events)

The probabilities for the three afterpulsing components (ν_i parameters in Equation 3.6) were constrained in TTNP measurements like Figure 3.4. From these constraints, the model fits in Ref [104] finds afterpulsing probabilities summarized in Table 3.1

Parameter	Mean Time	Float/Fixed	Result
ν_{AP1}	520 ns	Fixed	0.2%
ν_{AP2}	1660 ns	Fixed	2.0%
ν_{AP3}	6300 ns	Float	6.8%

TABLE 3.1: Fit results for afterpulsing probabilities from Ref [104]. Parameters ν_{AP1} and ν_{AP2} were fixed in this fit due to these afterpulsing components being subdominant compared to TPB re-emission and LAr scintillation at the relevant times. The means and afterpulsing probabilities for these features were obtained in-situ with AARF calibrations.
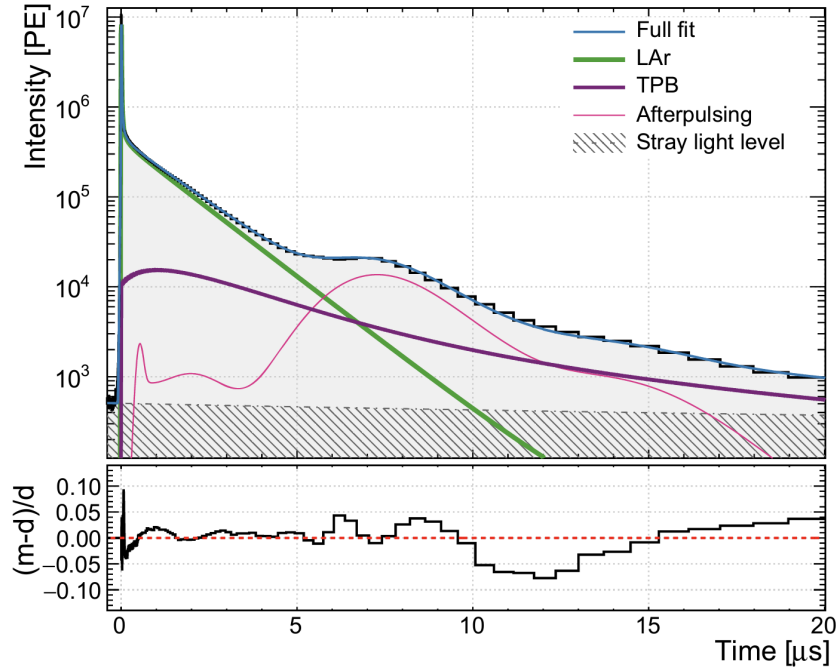
FIGURE 3.5: The LAr pulse shape from ^{39}Ar β decays in DEAP-3600, used to determine the priors $P((n_{\mathrm{AP}})$ and $P(n_{\mathrm{Sc}})$ in Equation 3.7. In the inset residual plot, the symbols m and d on the y-axis represent "model" and "data," respectively. Image taken from Ref [60].

Once a posterior distribution $P(n_{\mathrm{PE}}|Q)$ is found for the pulse with observed charge Q, the estimator for the number of PEs from scintillation photons, $\hat{n}_{\mathrm{Sc}}$, is obtained by averaging over the posterior, i.e.

$$\hat{n}_{\mathrm{Sc}} = \sum_{n_{\mathrm{PE}}=0}^{\infty} \sum_{n_{\mathrm{Sc}}}^{n_{\mathrm{PE}}} n_{\mathrm{Sc}} P(n_{\mathrm{Sc}} + n_{\mathrm{AP}} = n_{\mathrm{PE}}|Q). \tag{3.8}$$

Equation 3.8 represents a Bayesian estimator known as the Minimum-Mean-Square-Error (MMSE) for the number of scintillation PEs. The measure of photocathode charge obtained using Equation 3.8 will hereafter be denoted as `nSCBayes`. This is the currently used default recoil energy estimator used in DEAP analyses.

3.1.3 DEAP-3600 Energy Response

As shown in Figure 3.6, the DEAP-3600 detector was calibrated in energy using the ^{22}Na calibration source; γ-ray peaks from ^{40}K (1.46 MeV), ^{214}Bi (1.76 MeV), and ^{208}Tl (2.61 MeV); and the ^{39}Ar β spectrum. However, since it is a key topic in Chapter 4 the following discussion focuses on the β spectrum from ^{39}Ar decays in the LAr bulk. Ref [114] provides a theoretical energy spectrum for ^{39}Ar βs, where the energy units are in keV. The DEAP-3600 calibration analysis carried out in Ref [59] parameterized the theoretical spectral shape with the following:

$$\mu(E) = \langle N_{\mathrm{DN}} \rangle + Y_{\mathrm{PE}} \cdot E, \tag{3.9}$$

$$\sigma^2(E) = \sigma^2_{\mathrm{PE}} \cdot \mu(E) + \sigma^2_{\mathrm{rel,LY}} \cdot \mu^2(E), \tag{3.10}$$

where,

$\mu \equiv$ Mean number of scintillation PEs detected for total event energy, E [keV]

$$\tag{3.11}$$

$\sigma^2 \equiv$ Energy resolution $\tag{3.12}$

and,

(i) $\langle N_{\mathrm{DN}} \rangle \equiv$ Mean number of PEs from uncorrelated noise, or '*dark noise*'

(ii) $Y_{\mathrm{PE}} \equiv$ Detector light yield [PE/keV], mapping recoil energy in keV to detected PEs in `nSCBayes` (see Section 3.1.2)

(iii) $\sigma^2_{\mathrm{PE}} \equiv$ Fano factor and Poisson counting resolution term

(iv) $\sigma^2_{\mathrm{rel,LY}} \equiv$ Light yield variance resolution term (relative to mean)

For the energy response calibration of DEAP-3600, parameters (ii)–(iv) were allowed to float in a fit of a theoretical ^{39}Ar β `nSCBayes` spectrum, $S'(q)$, to the observed ^{39}Ar

nSCBayes spectrum (where q is nSCBayes). The theoretical spectrum was calculated by convolving the ^{39}Ar β energy spectrum shown in Figure 2.11, $S_{\mathrm{Ar}}(E)$, with a Gaussian kernel with a mean and variance determined by Equations 3.9 and 3.10; i.e.

$$S'(q\,;\,\mu(E),\sigma^2(E)) = \int\limits_0^\infty S_{\mathrm{Ar}}(E) \cdot \frac{1}{\sqrt{2\pi\sigma^2}} e^{-(q-\mu(E))^2/2\sigma^2(E)} dE, \qquad (3.13)$$

Parameter (i) was measured using PMT signals preceding scintillation events, and is an average value over all 255 PMTs [59]. The results of the fit reported in Ref [59] are provided in Table 3.2. The energy response function of DEAP-3600 with these parameters

Parameter	Value	Units
$\langle N_{\mathrm{DN}} \rangle$	(1.1 ± 0.2)	[PE]
Y_{PE}	(6.1 ± 0.4)	[PE/keV]
σ^2_{PE}	(1.4 ± 0.1)	[PE]
$\sigma^2_{\mathrm{rel,LY}}$	$0.0004^{+0.001}_{-0.0004}$	[#]

TABLE 3.2: Best fit values of the DEAP-3600 energy response parameters. The ^{22}Na low energy feature refers to a feature at $\sim 40\,\mathrm{keV}$ which comes from photo-absorption of the ^{22}Na 1.27 MeV γ-rays near the acrylic surface at [101].

is shown in Figure 3.6. For comparison with other ER event sources, the points from ^{22}Na calibration data, as well as the high energy γ-rays associated with ^{40}K, ^{214}Bi, and ^{208}Tl are overlaid.
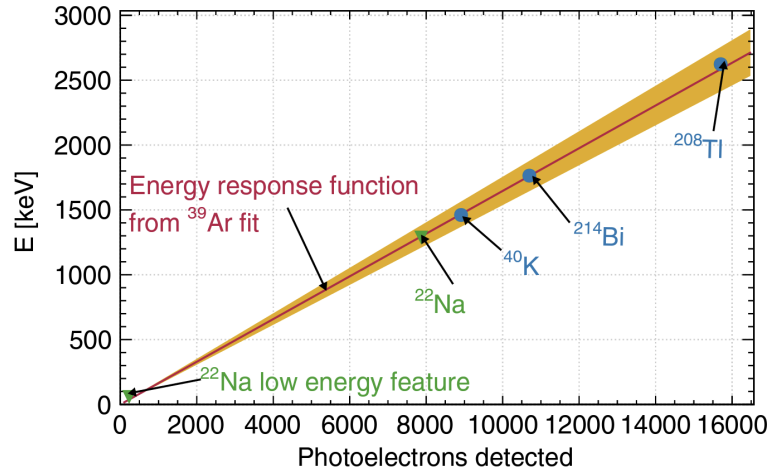
FIGURE 3.6: The DEAP-3600 energy response function extrapolated to high energy. Image taken from Ref [59].

3.2 Position Reconstruction

Assessing the location of a scattering event in the LAr is necessary for making the decision to accept or reject that event based on its proximity to the detector surface. Picking the decision boundary is the subject of Section 3.5.3. This section discusses the methods of position reconstruction in DEAP-3600 based on the information provided by the 255 signal PMTs. This can be done with two quantities as the basis of a maximum likelihood fit:

(i) The observed spatial distribution of PEs across all PMTs in the detector

(ii) The arrival times of observed photons in the scattering event

Item (i) is used by the `MBLikelihood` position reconstruction algorithm, which is the topic of Section 3.2.1, whereas item (ii) is used by the `TimeFit2` algorithm, discussed in Section 3.2.2. The output of both the `MBLikelihood` and `TimeFit2` algorithms is a 3D vector in Cartesian coordinates, where the Z-axis is collinear with the detector neck axis and the origin is located at the centre of the AV sphere.

3.2.1 `MBLikelihood` Position Fitter

The `MBLikelihood` position reconstruction algorithm determines the position of an event by finding the test position, $\vec{x}$, which maximizes the log-likelihood function defined as

$$\ln \mathcal{L}(\vec{x}) = \sum_{i}^{N_{\mathrm{PMTs}}} \ln \mathrm{Pois}(q_i; \lambda_i), \tag{3.14}$$

where

$$\lambda_i \equiv \lambda\left(|\vec{x}|, \frac{\vec{x} \cdot \vec{r_i}}{|\vec{x}||\vec{r_i}|}, q_{\mathrm{total}}\right)$$

$$q_{\mathrm{total}} \equiv \text{Total PEs detected in event}$$

$$r_i \equiv \text{Position of PMT } i$$

$$q_i \equiv \text{PEs detected in PMT } i$$

$$\mathrm{Pois} \equiv \text{Poisson distribution}$$

$$N_{\mathrm{PMTs}} \equiv \text{Number of PMTs} = 255$$

The Poisson mean parameters, λ_i, use the relative distance between the test position of the event and a given PMT to vary the mean of the Poisson distribution according to an inverse-square dependence of the light intensity coming from point-like interactions in the LAr. However, to fully account for systematic effects associated with optics and detector geometry, the mean PE values for each PMT, λ_i, are trained on MC simulations rather than defining an analytical function. The training procedure involves simulating events in the LAr along three axes: one collinear with the central axis of the detector neck, and two perpendicular axes along the equatorial plane of the AV. These simulations include the LAr scintillation and photon transport physics discussed in Sections 2.1.4 and 2.2.3. For all simulated event positions, the λ_i for each PMT are measured, and encoded in splines varying with event radius (i.e. $|\vec{x}|$) and angular separation from PMT i (i.e. $\frac{\vec{x}\cdot\vec{r_i}}{|\vec{x}||\vec{r_i}|}$). Assuming spherical symmetry allows for these splines to extend to all event positions in the LAr.

The `MBLikelihood` algorithm converges to a maximum likelihood estimate of the position via the Nelder-Mead minimization routine, or sometimes known as the *Simplex* Method. A simplex of order-n (or n-simplex) is the simplest possible geometric object in n-dimensional space, having $n+1$ faces and $n+1$ vertices. For example, the 2-simplex is a triangle, and the 3-simplex is a tetrahedron. The Simplex method begins with initializing a simplex of order-n in a space defined by the user, and assigns a numerical value to each vertex according to a minimization condition also defined by the user. In the case of the `MBLikelihood` position fitter, the space is 3D position space within the LAr, and the minimization condition is determined by the likelihood function in Equation 3.14. Once all the vertices $\vec{v_i}$ of the 3-simplex are defined and ascribed a likelihood value $\mathcal{L}(\vec{v_i})$, `MBLikelihood` iterates through the Simplex Method, which is described and provided in pseudo-code in Appendix B.1.

In summary, for every iteration, the vertex with the lowest likelihood is translated in 3-space in the direction of the centroid of the 3-simplex. This iteratively transforms the simplex until the true event position is contained within it, at which point the algorithm begins to shrink the volume of the simplex. Eventually this process converges until the simplex is essentially a point, which is returned as the maximum likelihood estimate of the event position.

3.2.2 `TimeFit2` Position Fitter

The alternative position fitter used in DEAP-3600 is called `TimeFit2`, and it computes an estimate for the position of an event by minimizing a quantity called the 'time residual,' t_{res}, for all detected pulses. To compute t_{res} for a pulse, `TimeFit2` initializes a test point $\vec{x}_0$ and event time t_0. The time residual is then defined as

$$t_{\text{res}} = (T_{\text{pulse}} - t_0) - T_{\text{flight}}(\vec{x}_0) \tag{3.15}$$

where T_{pulse} is the observed arrival time of the pulse and $T_{\text{flight}}(\vec{x}_0)$ is the time-of-flight of a photon travelling from $\vec{x}_0$ to the PMT which detected the pulse. This includes the photon propagation through the LAr, absorption and re-emission at the TPB, and propagation through the acrylic of the AV and light guide. However, the optical model used here neglects reflections and scattering of visible photons in the TPB, as well as Rayleigh scattering of VUV photons in the LAr [59]. Therefore only the prompt pulses are used in this method, as later pulses cannot be disentangled from photons that travelled along non-trivial trajectories, e.g. one or more reflections within the AV. Equation 3.15 is the difference between the observed and expected time-of-flight for the photons which generated a given pulse. It is used before position reconstruction with `TimeFit2` to get an estimate of the event time, $\hat{t}_0$, which minimizes $\sum t_{\text{res}}^2$, where the sum is over all pulses with $t_{\text{res}} < 8\,\text{ns}$.

Prior to fitting, `TimeFit2` calculates a look-up table defining the likelihood function, $\mathcal{L}^{\text{res}}(t_{\text{res}}; \vec{x}_j, \vec{r}_i)$ for a grid of test points, $\vec{x}_j$, connecting to all 255 signal PMTs at positions $\vec{r}_i$. Included in the calculation of $\mathcal{L}^{\text{res}}$ is a simplified optical model for the detector, where the group velocity of 128 nm photons in LAr is assumed to be 11 cm/ns and the group velocity of 420 nm photons is 24 cm/ns in TPB, and 20 cm/ns in the acrylic of the AV and light guides.

TimeFit2 returns an estimate of the event position by maximizing the log-likelihood function

$$\ln \mathcal{L}(t_0, \vec{x}_0) = \sum_{i=1}^{N} \ln \mathcal{L}^{\text{res}}(t_{\text{res}}; \vec{x}_0, \vec{r}(i)), \tag{3.16}$$

where N is the number of pulses arriving within 40 ns of the event time, and $\vec{r}(i)$ is the position of the PMT which detected pulse i. The output of this position reconstruction

algorithm is primarily used as a consistency check. This point is discussed in more detail in Section 3.5.1.

3.2.3   Validation and Performance

Both `MBLikelihood` and `TimeFit2` were validated using ^{39}Ar β decays, which are uniformly distributed throughout the LAr. Therefore, deviations from uniformity in the reconstructed radius distribution of ^{39}Ar events can be used as a measure of the fitter bias for both algorithms. Figure 3.7a shows the integrated LAr mass contained within a given reconstructed radius from both `MBLikelihood` and `TimeFit2`. The LAr mass is calculated by measuring the number of ^{39}Ar events per unit time within a reconstructed radius and dividing by the specific activity of ^{39}Ar β decay in LAr. For comparison, the same curve for a perfectly uniform distribution is overlaid. Both position fitters display agreement with the perfectly uniform event distribution to within 30%, but tend to have a clear outward bias, which results in negative residuals at low reconstructed radii ($\lesssim 680$ mm) and positive residuals at higher radii.

The reconstructed position resolution is shown in Figure 3.7b for the `MBLikelihood` fitter, which is the default algorithm for position reconstruction in DEAP-3600.[1] At the PE threshold for the WIMP search analysis in Ref [59] (i.e. 93 PE, see Section 3.5), the `MBLikelihood` fitter has a resolution of 30–40 mm for events reconstructed at the fiducial volume radius of 630 mm. For the Profile Likelihood WIMP search discussed in Chapter 4, the fiducial volume is expanded to 720 mm, and the resolution at threshold (90 PE) at this radius is 20–30 mm.

3.3   Pulse-Shape Discrimination

DEAP-3600 leverages the wide separation in scintillation time scales of singlet and triplet LAr excimers (see Table 2.1 in Section 2.1.4) for background rejection via PSD. This section will provide an overview of the PSD parameter, `Fprompt` (Section 3.3.1), how it can be used with energy as a scattering particle identifier (Section 3.3.2), and how powerful a discriminator it can be against ^{39}Ar β decay in atmospheric LAr (Section 3.3.3).

---

[1]At the time of publication for Ref [59], `TimeFit2` had a much larger bias and was thus reduced to a secondary fitting algorithm for cross-checking. The work in this thesis adopts `MBLikelihood` for backwards compatibility.

(A)

(B)
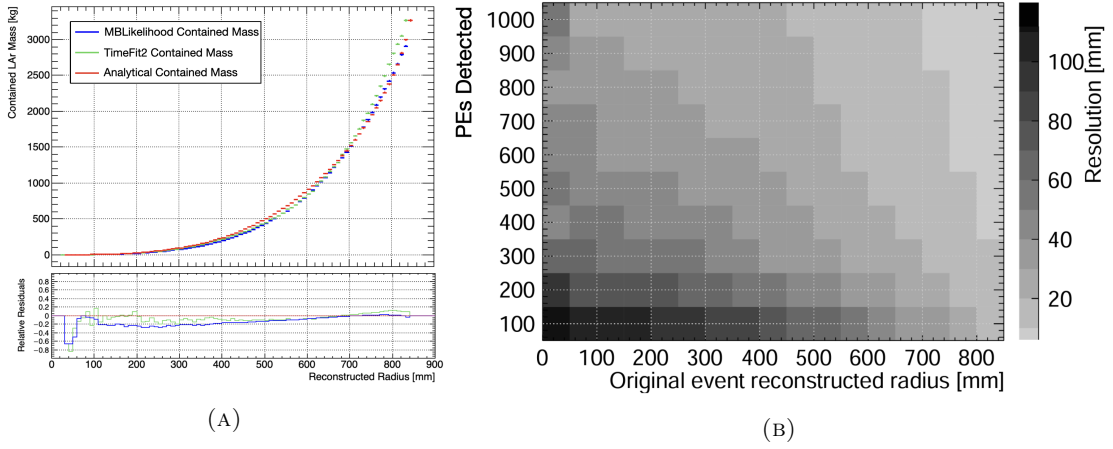
FIGURE 3.7: (A) Validation of the `MBLikelihood` and `TimeFit2` position fitters against an ideal uniform event distribution. Plotted is the contained LAr mass within a given reconstructed radius based on ^{39}Ar β decay rates. Residuals show that both fitters have a slight outward bias, which results in more events being reconstructed towards the AV surface. (B) Resolution of the `MBLikelihood` position fitter vs. reconstructed radius and PEs detected. At 630 mm events of equal radius tend to be within 30–40 mm of each other. At 720 mm the resolution improves to 20–30 mm. Image (B) taken from Ref [59].

3.3.1 Determination of `Fprompt`

The time profile of LAr scintillation emission, $S(t)$ can be modelled as the sum of two exponential distributions,

$$S(t) = \frac{\mathcal{R}}{\tau_S} e^{-t/\tau_S} + \frac{1}{\tau_T} e^{-t/\tau_T}, \qquad (3.17)$$

where $\tau_S = 7$ ns is the LAr singlet state mean de-excitation time, $\tau_T = 1.6\,\mu$s is LAr triplet state mean de-excitation time, and $\mathcal{R}$ represents the ratio of singlet to triplet excimer populations produced in a scattering event with an ^{40}Ar target. As discussed in Section 2.1.2, the ratio of excitons to ions produced in the track of a recoiling particle is highly correlated with $\mathcal{R}$; the exciton-to-ion ratio in LAr for ER and NR events has been measured at 0.21 and $\sim$1, respectively[2] [78, 108]. An observable which takes advantage of the large difference between τ_S and τ_T in LAr should be able to distinguish NR from ER interactions; i.e. potential WIMP events from ^{39}Ar β decays. This is the essence of PSD.

Figure 3.8 shows how the shape of the LAr scintillation time profile changes with $\mathcal{R}$. A boundary, t_{pr}, can be appropriately placed whereby the scintillation time profile is

---

[2]The NR exciton-to-ion ratio is dependent upon recoil energy, whereas Ref [78] takes the ratio of 0.21 to be a constant.

entirely dominated by the singlet contribution for $t \leq t_{\mathrm{pr}}$, and the triplet for $t > t_{\mathrm{pr}}$. The time intervals before and after t_{pr} are called the prompt and late windows, respectively. The integral of $S(t)$ within the prompt window contributes some fraction F_{pr} to the total integral between $[0, \infty)$, i.e.

$$F_{\mathrm{pr}} = \frac{\int_0^{t_{\mathrm{pr}}} S(t) dt}{\int_0^{\infty} S(t) dt},$$

or the 'fraction of prompt signal.' Based on Figure 3.8, larger values of $\mathcal{R}$ will produce larger values of F_{pr}.
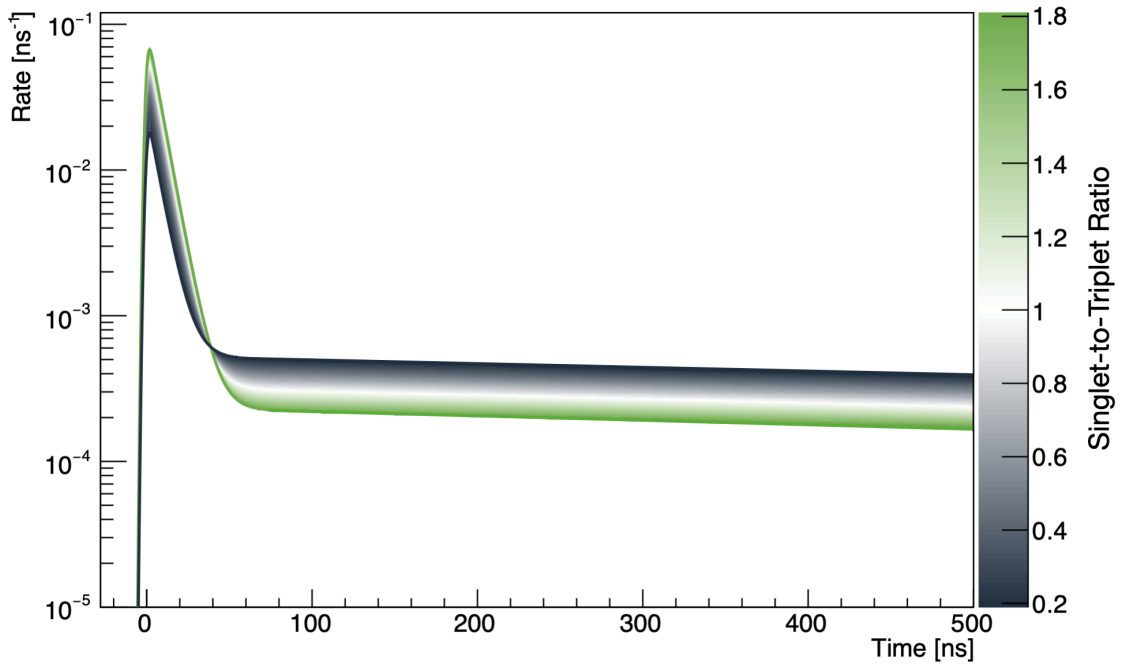
FIGURE 3.8: LAr scintillation time distribution as a function of the excimer singlet-to-triplet ratio.

The observable which quantifies PSD in DEAP-3600 is defined as:

$$\mathtt{Fprompt} = \frac{\sum_{t=-28\,\mathrm{ns}}^{60\,\mathrm{ns}} \mathrm{PE}(t)}{\sum_{t=-28\,\mathrm{ns}}^{10\,\mu\mathrm{s}} \mathrm{PE}(t)}, \tag{3.18}$$

where $\mathrm{PE}(t)$ refers to the photoelectrons detected at time t relative to the event start time, t_0. Here the default estimator of PE, $\mathtt{nSCBayes}$, is used, and t_0 is determined by minimizing the time residuals, as described in Section 3.2.2. The placement of t_{pr} for the 2.5 tonne-year analysis was set at 60 ns [59]. This was found to achieve maximal separation in $\mathtt{Fprompt}$ at the energy scale of WIMP interactions between ER and NR

events. A discussion of how the placement of t_{pr} affects the amount of bias in `Fprompt` of PSD is provided in Appendix A.2.

3.3.2 Particle Identification

Figure 3.9 demonstrates how `Fprompt` can be used to differentiate between a NR (the upper band in `Fprompt`) and ER (the lower band) scattering event in LAr. As discussed in Section 3.3.1, the low singlet-to-triplet ratio, $\mathcal{R}$ observed in ER events results in more of the long-lived scintillation dominating the pulse shape, resulting in a characteristically low value of `Fprompt`. In contrast, NR events not only have larger $\mathcal{R}$, but the quenching effects discussed in Section 2.1.2 disproportionately suppress the scintillation from triplet excimers over singlet excimers, which results in a significantly larger value of `Fprompt`.

Figure 3.9 also shows that scattering energy and PSD are enough to distinguish certain types of events; i.e. α and β decays, and γ-rays. For more granular background identification additional information, such as reconstructed position, is required. For example, an event with `nSCBayes` ~ 20000 PE, `Fprompt` ~ 0.7, is highly likely to be a ^{210}Po α decay, but radial information is required to further distinguish if it was in a dust particle or from the detector inner surface. A more detailed description of the background control regions used in the Profile Likelihood analysis is provided in Section 4.2.2.
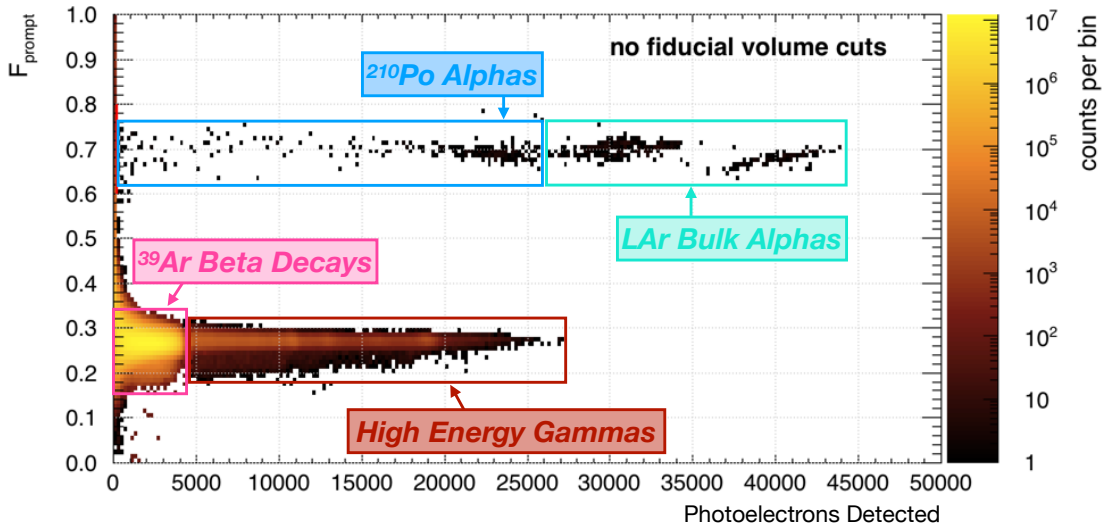
FIGURE 3.9: `Fprompt` vs. PE plane with labeled regions for ^{39}Ar, high energy γ-rays, α decays from the LAr bulk, and degraded/shadowed ^{210}Po α decays as discussed in Section 2.3.2. Neutrons are statistically limited in this plot, but would typically occupy a low energy region with charges $\lesssim 1000$ PE and `Fprompt` similar to low energy ^{210}Po αs.

3.3.3 Discrimination Power and Argon-39 Leakage Fraction

The power of pulse shape discrimination to select NRs over ERs in DEAP-3600 can be quantified with the same formalism as a generic hypothesis test comparing hypotheses $\mathcal{H}_0$ (null) and $\mathcal{H}_1$ (alternative). Consider some random variable f, where the null hypothesis predicts a distribution, $P(f|\mathcal{H}_0)$, and the alternative hypothesis predicts a distribution, $P(f|\mathcal{H}_1)$, such that

$$\int_{-\infty}^{\infty} f\, P(f|\mathcal{H}_0)\, df > \int_{-\infty}^{\infty} f\, P(f|\mathcal{H}_1)\, df.$$

A decision boundary F_{cut} can then be chosen for this test; if a data point $f_{\mathrm{obs}} > F_{\mathrm{cut}}$ ($f_{\mathrm{obs}} < F_{\mathrm{cut}}$), then f_{obs} favours the null (alternative) hypothesis. In this example, the discrimination power $\mathcal{M}$ of such a test is defined as [115]:

$$\mathcal{M} = 1 - \int_{F_{\mathrm{cut}}}^{\infty} P(f|\mathcal{H}_1)\, df, \tag{3.19}$$

i.e. the probability of accepting the alternative hypothesis, given that it is true.[3]

In the context of DEAP-3600 and PSD, discrimination power is used to describe the probability of correctly identifying an ^{39}Ar β decay using a measurement of `Fprompt`. The decision boundary, F_{cut}, delineates the regions in `Fprompt` which are dominated by ER and NR events. Letting $f \equiv$ `Fprompt` and $\mathcal{H}_1 \equiv {}^{39}$Ar, Equation 3.19 then returns the discrimination power of PSD in LAr,

$$\mathcal{M}_{\mathrm{PSD}} = 1 - \int_{F_{\mathrm{cut}}}^{1} P(f|^{39}\mathrm{Ar})\, df = 1 - P_{\mathrm{leak}}, \tag{3.20}$$

where P_{leak} is called the ^{39}Ar *leakage fraction*. The placement of the decision boundary F_{cut} is discussed in Section 3.5.

$P(f|^{39}\mathrm{Ar})$ was derived empirically in Ref [104], taking the form of a Gamma distribution convolved with a Gaussian, i.e.

$$P(f|^{39}\mathrm{Ar}) = I\, \mathrm{Gamma}(f|\mu_f, b_f) \circledast \mathrm{Gaus}(f|0, \sigma_f), \tag{3.21}$$

---

[3]The precise mathematical definition of discrimination power is dependent upon the hypotheses being considered, but this qualitative description is true in general

where,

$$I \equiv \text{Normalization constant} \tag{3.22}$$

$$\text{Gamma}(x|\mu, b) \equiv \text{As defined in Equation 3.5} \tag{3.23}$$

$$\text{Gaus}(x|\mu, \sigma) \equiv \frac{1}{\sqrt{2\pi}\sigma} e^{(x - \mu)^2/2\sigma^2} \tag{3.24}$$

and the parameters μ_f, b_f, and σ_f are all PE-dependent parameters defined as (letting `nSCBayes` $= q$) [104],

$$b_f = a_0 + \frac{a_1}{q} + \frac{a_2}{q^2}, \tag{3.25}$$

$$\sigma_f = a_3 + \frac{a_4}{q} + \frac{a_5}{q^2}, \tag{3.26}$$

$$\mu_f = a_6 + \frac{a_7}{q} + \frac{a_8}{q^2} + \frac{a_9}{q^3}. \tag{3.27}$$

The best-fit parameters $\hat{\mu}_f$, $\hat{b}_f$, and $\hat{\sigma}_f$ were obtained in χ^2 fits of Equation 3.21 to ^{39}Ar `Fprompt` distributions in `nSCBayes` bins with widths of 1 PE, and the coefficients $(a_0,\ldots,a_9)$ were subsequently found in χ^2 fits of $\hat{\mu}_f$, $\hat{b}_f$, and $\hat{\sigma}_f$ as a function of PE. Note that the parametrizations of μ_f, b_f, and σ_f in Equations 3.25–3.27 are entirely empirically driven, and the coefficients $(a_0,\ldots,a_9)$ have no physical meaning. These functional forms were chosen because they behave in a manner consistent with the mean and shape parameters of the `Fprompt` distribution for ^{39}Ar β decays: rapidly decreasing with `nSCBayes` at threshold while converging to constant as `nSCBayes` goes to positive infinity. Figure 3.10 shows the residuals ((model−data)/data) between the `Fprompt` model computed using this parametrization and ^{39}Ar data in the PE range of 100≤`nSCBayes`≤ 200 PE. This result shows that there is < 10% disagreement between the model and data (inside solid black contours), except for where statistics are limited (above upper contour), and where event pileup is a significant systematic effect (below lower contour). This `Fprompt` model parametrization is also adopted for characterizing the Profile Likelihood analysis background model, as discussed in Section 4.2.2.

The values of the ^{39}Ar leakage fraction, P_{leak}, and PSD discrimination power, $\mathcal{M}_{\text{PSD}}$, are dependent upon the placement of the decision boundary F_{cut}. Also dependent on F_{cut} is the probability of correctly identifying a NR event given NR hypothesis is true. This is called the '*Nuclear Recoil Acceptance*' (NRA). Figure 3.11a demonstrates this pictorially, with simulated NR events on ^{40}Ar nuclei as representing the `Fprompt` probability
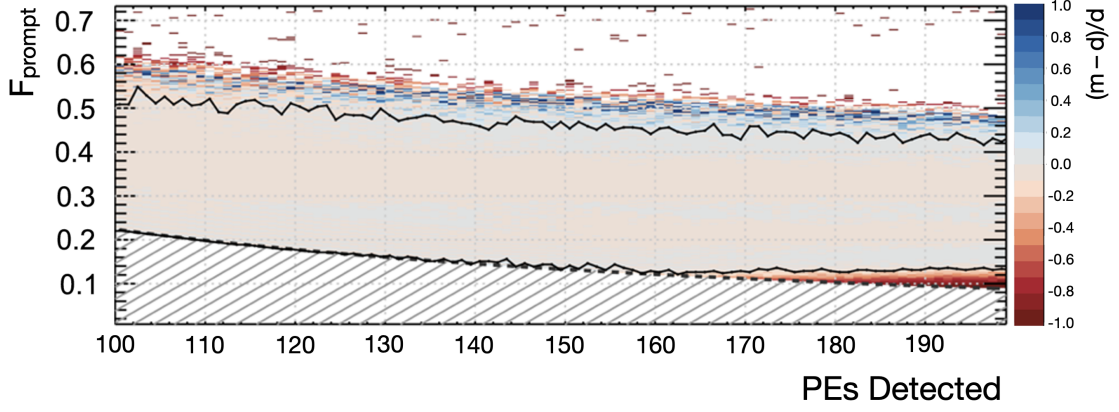
FIGURE 3.10: Relative residuals ((model−data)/data) vs. `Fprompt` and PEs detected (i.e. `nSCBayes`) between the `Fprompt` model described by Equations 3.21 and 3.25–3.27 and ^{39}Ar β decay data. The black dashed curve is the boundary above which the trigger efficiency is above 99.5%, and defines the lower fit boundary as a function of PE. The region enclosed within the black contours is where the residuals are bounded between ±10%. Above the upper contour, the deviations between model and data are dominated by statistical fluctuations. Below the lower contour, the deviations are dominated by event pileup. Image taken from Ref [104].

distribution for NRs [104]. Figure 3.11b then shows the P_{leak} and NRA dependences on F_{cut}. DEAP-3600 defines F_{cut} for measurements of discrimination power to be at the point where NRA = 50%, which returns $\mathcal{M}_{\text{PSD}} = 1 - 10^{-10}$ for `nSCBayes` = 110 PE. The PE-dependent placement of F_{cut} for the DEAP-3600 2.5 tonne-year WIMP search is explained in more detail in Section 3.5.4.
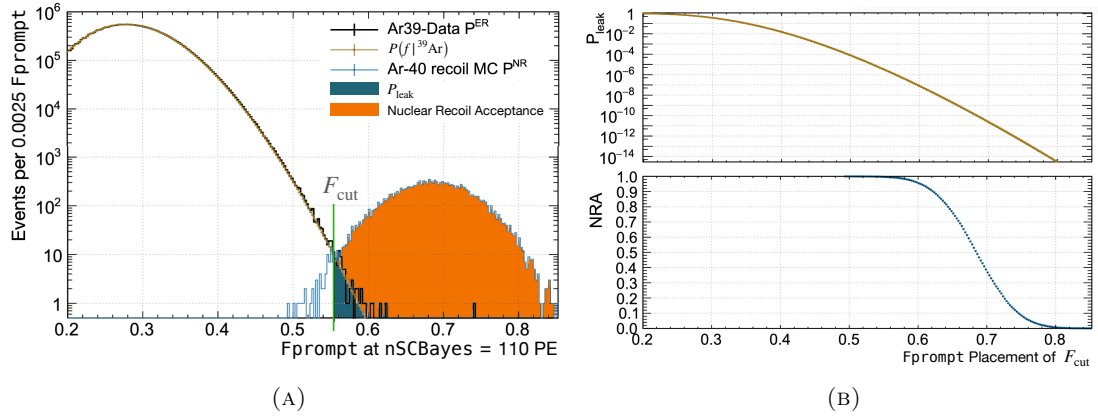
FIGURE 3.11: Pictorial representation of the P_{leak} and NRA dependence on F_{cut} (A); P_{leak} and NRA vs. the placement of F_{cut} (B). Images taken from Ref [104].

3.4   Event Topology

For the purposes of the discussion in this section, 'Event Topology' refers to the distribution of detected PEs among the 255 signal PMTs in both intensity and time. This information mainly supplements the rejection of Čerenkov, neck α, and dust α events. Section 3.4.1 motivates using the topological characterization of subsets of PMTs to these backgrounds, and Section 3.4.2 discusses the use of pulse timing as a means of discriminating against neck α events specifically.

3.4.1   Topological Characterization of Subsets of PMTs

DEAP-3600 utilizes three different `qPE`-based measurements of the photon distribution among the 255 signal PMTs:

   (i) Signal fraction in the PMT with the largest signal

  (ii) Signal fraction in the uppermost 10 PMTs in the detector

 (iii) Signal fraction in the lowermost 15 PMTs in the detector

In DEAP internal nomenclature, item (i) is called `fmaxpe`, and is evaluated as

$$\texttt{fmaxpe} = \frac{\text{`Brightest' PMT charge [qPE]}}{\text{Total event charge [qPE]}},\tag{3.28}$$

where, for a given event, the numerator of Equation 3.28 refers to the photocathode charge in the individual PMT which recorded the largest signal, and the denominator is the summed charge across all PMTs. This observable is mainly used as a discriminator against Čerenkov events in the light guides and PMT glass.

Recalling from Section 2.3.4 that Čerenkov radiation occurs commonly in these detector components, because of the presence of high energy βs and γ-rays from the primordial radionuclide decay chains, and the relatively large refractive indices in these detector components. Also recall that the relevant timescale for photon emission from Čerenkov radiation is $\tau < 1\,$ns. Therefore such an event is expected to be high in both `Fprompt` and `fmaxpe`. Figure 3.12 shows a 2D distribution of `fmaxpe` vs. `Fprompt` obtained from physics data in DEAP-3600. The Čerenkov population in the upper-right corner extends

down to `fmaxpe` ≈ 0.4, which is used as the cut boundary for rejecting this background.
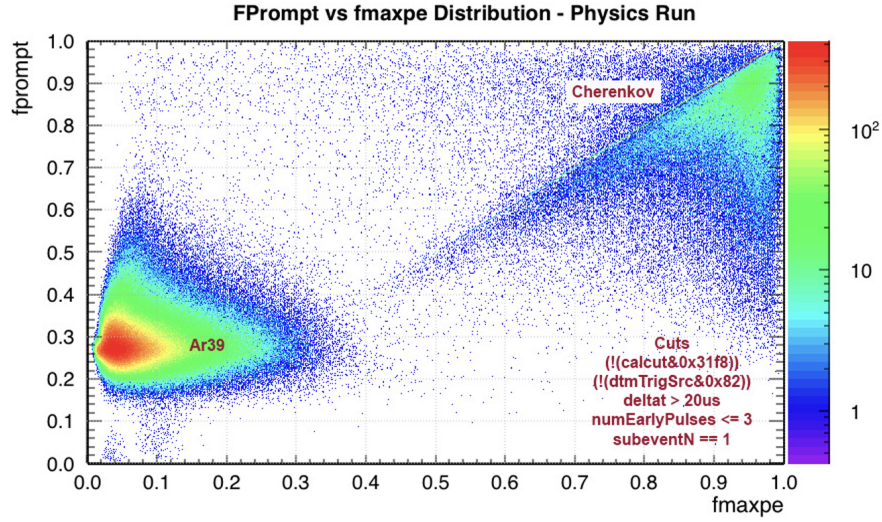
FIGURE 3.12: Plot of `fmaxpe` vs. `Fprompt` for ^{39}Ar β decay and Čerenkov populations labeled, for `nSCBayes` between 0–5000 PE and reconstructed radii from 0–850 mm. The 'cuts' labeled in the bottom-right corner are described in Section 3.5.1. Image taken from Ref [116].

Items (ii) and (iii), in DEAP nomenclature, are called the 'Charge Fraction Top 2 Rings' (`CFT2R`) and 'Charge Fraction Bottom 3 Rings' (`CFB3R`) variables, respectively. They are defined as:

$$\text{CFT2R} = \frac{\text{Total charge in 10 uppermost PMTs [qPE]}}{\text{Total event charge [qPE]}} \tag{3.29}$$

$$\text{CFB3R} = \frac{\text{Total charge in 15 lowermost PMTs [qPE]}}{\text{Total event charge [qPE]}} \tag{3.30}$$

`CFT2R` targets neck events, as photons originating from the neck components can reflect off the liquid-gas interface of the argon and produce a large signal in the uppermost PMTs. The `CFB3R` variable is motivated in Ref [117] as a means of rejecting the 'sinking dust' hypothesis. Events observed in DEAP-3600, which are consistent with the dust α background (see dust selection criteria in Table 3.3), are routinely reconstructed at the bottom of the detector. Such behaviour is not observed in ^{222}Rn α decays uniformly distributed throughout the LAr bulk. Figure 3.13 demonstrates that `CFB3R` is sensitive to this excess of dust α decays, and is therefore an effective discriminator against this background.
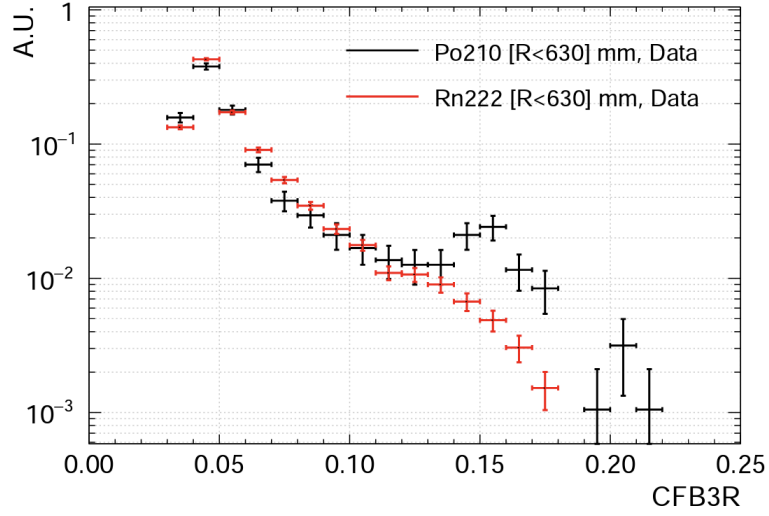
FIGURE 3.13: Distributions in `CFB3R` for events in a ^{222}Rn LAr bulk α decay control region (red) and ^{210}Po dust α control region (black). Image taken from Ref [117]

Variable	^{210}Po	^{222}Rn
`MBlikelihood` Radius	$< 630\,\text{mm}$	$< 630\,\text{mm}$
`MBlikelihood` Z	$< 500\,\text{mm}$	$< 500\,\text{mm}$
`fmaxpe`	< 0.75	< 0.75
`nSCBayes`	$[10000, 20000]\,\text{PE}$	$[25000, 32000]\,\text{PE}$

TABLE 3.3: Event selection criteria for the ^{210}Po dust α and the ^{222}Rn LAr bulk α control regions for the data shown in Figure 3.13.

3.4.2 Time-Ordered Pulse Index as Neck Alpha Discriminator

Similar to the motivation for `CFT2R` as a neck α discriminator, a discriminator based on the arrival time of pulses in the uppermost PMTs can be used to reject neck α events. This discriminator, hereafter referred to as T_0^{GAr}, is defined as:

- $\text{T}_0^{\text{GAr}} \equiv$ Time-ordered index of the first pulse recorded in a PMT coupled to the gaseous argon (GAr) volume of the detector

Recall from Section 2.3.2 that neck α decays generate scintillation in above the LAr fill level. Therefore any photons travelling towards the LAr-GAr interface can reflect back upwards towards the PMTs in the GAr region, which will trigger pulses earlier than PMTs coupled to the LAr. Figure 3.14 is a plot of the neck α rejection percentage as well as NRA (both from MC simulations) as a function of a rejection cut placement $\text{T}_0^{\text{GAr}} < X$. This shows that rejecting events where $\text{T}_0^{\text{GAr}} < 2$ (i.e. the first pulse observed in the GAr region was either 1st or 2nd overall) can remove approximately 85% of neck

α events. However, this same cut can reject $\sim 40\%$ of potential WIMP events. This will be an important detail for Section 4.2 which motivates the model structure used for the Profile Likelihood WIMP search.
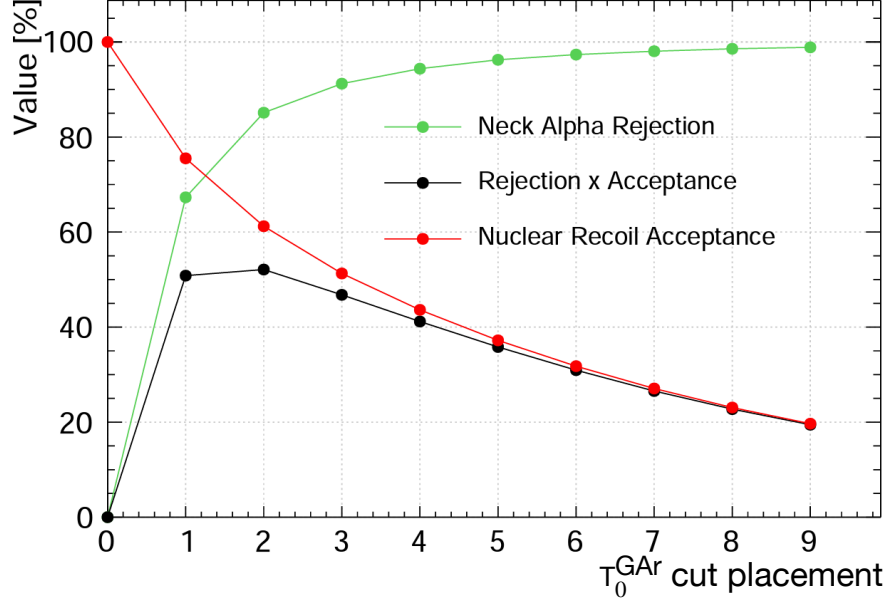
FIGURE 3.14: Neck α rejection vs. the placement of the background rejection cut $\mathtt{T_0^{GAr}} < X$. Image taken from Ref [117].

3.5 WIMP Search Event Selection Criteria

The DEAP-3600 WIMP search with a 2.5 tonne-year exposure [59] followed a general procedure called a 'cut-and-count' analysis, where a series of data quality, background removal, and event selection cuts are applied to observed data in order to achieve a background-free ROI. This section provides a brief description of how this is done in DEAP-3600.

3.5.1 Data Cleaning Cuts

The first set of applied cuts in the 2.5 tonne-year WIMP search cut flow remove low quality data. These data are generally related to instrumental effects; e.g. an event timestamp mismatch, or an event occurring when the DAQ system was overloaded and suppressing output. The DTM flags these events with a variable called '`calcut`' so they can be removed later for the WIMP search. Other types of events removed at this stage

are calibration and detector monitoring data, such as the AmBe/^{22}Na/AARF[4] events. These are also flagged by the DTM with another variable called 'dtmTrigSrc.' Cuts made based on these variables are done via bitwise comparisons, i.e.

$$\text{if (calcut \& 0x31f8) Reject Event} \tag{3.31}$$

$$\text{if (dtmTrigSrc \& 0x82) Reject Event} \tag{3.32}$$

where & is the bitwise AND operator,[5] and the 0x prefix denotes a quantity in hexadecimal representation. The hexadecimal values used for the comparison in Cuts 3.31 and 3.32 are simply compact representations of the binary values which encode all of the flags discussed above.

The next set of data cleaning cuts remove 'pileup' events; i.e. pairs of events which occur too closely to each other in time for accurate calculation of key observables, such as Fprompt or reconstructed position. There are four pileup cut variables, defined as follows:

(i) eventTime – Time-of-flight corrected event time relative to the DTM trigger time in nanoseconds (see Section 3.2.2). The DTM keeps waveform samples in a $2.5\,\mu$s pre-event time window, therefore the event time should be close to 2500 ns.

(ii) subeventN – Number of events occurring within a triggered event time window of 16μs, including the original triggered event. In order to isolate single-scatter events, which is the type of interaction expected for WIMP scatters in LAr, this variable should not be greater than one.

(iii) numEarlyPulses – Number of pulses in all PMTs occurring in a time window of 0–1600 ns relative to the start of a given PMT waveform. Accepting events with only a small number of early pulses limits the probability of contamination by the preceding event in the prompt time window of the triggered event.

---

[4]Also in this category are artificial events triggered by a pulse pattern generator, which are used to monitor detector electronics.

[5]The bitwise AND operator iteratively compares the ith binary bits of both operands, returning TRUE if the ith pair of bits are both 1 and FALSE otherwise. Therefore if the binary representation of the operands each have a 1 in the same bit placement for any bit, then the bitwise comparison returns TRUE overall. This can effectively consolidate many true-or-false checks into one line of code.

(iv) `deltat` – Time elapsed between successive triggered events in nanoseconds. Similar to `numEarlyPulses`, only accepting events where the previous event is separated by more than $20\,\mu$s limits the probability of contamination in the triggered event.

The cuts made based on these variables are

$$\text{if (eventTime < 2250 || eventTime > 2700) Reject Event} \qquad (3.33)$$

$$\text{if (subeventN != 1) Reject Event} \qquad (3.34)$$

$$\text{if (numEarlyPulses > 3) Reject Event} \qquad (3.35)$$

$$\text{if (deltat <= 20000) Reject Event} \qquad (3.36)$$

3.5.2   Cuts Based On Event Topology

Section 3.4 introduced two variables which are used to reject Čerenkov, dust α, and neck α backgrounds with the following cuts:

$$\text{if (fmaxpe > 0.4) Reject Event} \qquad (3.37)$$

$$\text{if (T}_0^{\text{GAr}} \text{ <= 2) Reject Event} \qquad (3.38)$$

There is an additional background rejection cut that utilizes the neck veto system, which was briefly discussed in Section,2.2.1. Any event which occurs in coincidence with a trigger in the neck veto system is removed from the WIMP search analysis. This cut is made with a variable called `neckVetoN`, and is defined as

$$\text{if (neckVetoN > 0) Reject Event,} \qquad (3.39)$$

where `neckVetoN` is the number of triggered neck veto PMTs in coincidence with the triggered event. Further background rejection cuts based on position reconstruction and observed energy are also made to eliminate radiogenic neutrons and degraded α decays, but these are covered in Sections 3.5.3 and 3.5.4, respectively.

3.5.3 Position Cuts and Fiducialization

Position-based cuts are applied for three main reasons:

(i) To ensure all accepted events occur within a *fiducial volume* (FV) containing a target mass of LAr of approximately 1 ton

(ii) Rejection of surface backgrounds; i.e. radiogenic neutrons and ^{210}Po α decays from the detector inner surface

(iii) To ensure consistency between the MBLikelihood and TimeFit2 position reconstruction algorithms

For item (iii), the criteria for sufficient consistency between the two position reconstruction algorithms were determined statistically using a sample of ^{39}Ar data passing Cuts 3.31–3.37, 3.39, 3.42, and 3.43. This sample of ^{39}Ar was used to construct the distributions, $P_z(Z)$ and $P_r(R)$. Here, the variables Z and R defined as

- $Z \equiv |\texttt{TimeFit2Z} - \texttt{MBLikelihoodZ}|$

- $R \equiv |\texttt{TimeFit2R} - \texttt{MBLikelihoodR}|$

where the Z suffix denotes the Z-component of the reconstructed position vector and the R suffix denotes the vector magnitude, or event radius. Therefore $P_z(Z)$ and $P_r(R)$ describe the statistical behaviours of disagreement between TimeFit2 and MBLikelihood in these quantities. The goal is then to reject events with,

$$Z > \texttt{CZ}$$

$$\text{and/or } R > \texttt{CR}$$

where CZ and CR are cut boundaries which satisfy

$$\int_{\texttt{CZ}}^{\infty} P_z(Z)\, dZ = 10\%,$$
$$\text{and } \int_{\texttt{CR}}^{\infty} P_r(R)\, dR = 10\%.$$

The locations of CZ and CR were evaluated as a function the number of prompt PEs (i.e. the numerator of Equation 3.18), producing the plots in Figure 3.15. Letting
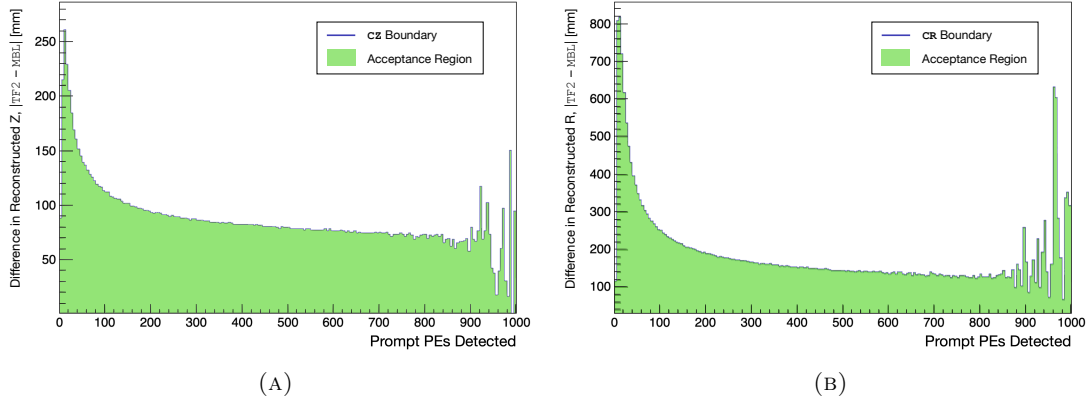
FIGURE 3.15: Consistency cut boundaries `CZ` (A) and `CR` (B) versus number of prompt PEs. The areas shaded in green indicate the acceptance regions for these cut variables.

`PromptPE = nSCBayes*Fprompt` (i.e. the x-axes in Figures 3.15a & 3.15b), `CZ` represent the distribution in Figure 3.15a and `CR` represent the distribution in Figure 3.15b, the DEAP-3600 consistency cuts can then be defined as

$$\text{if } (|\text{TimeFit2Z} - \text{MBLikelihoodZ}| > \text{CZ(PromptPE)}) \text{ Reject Event,} \qquad (3.40)$$

$$\text{if } (|\text{TimeFit2R} - \text{MBLikelihoodR}| > \text{CR(PromptPE)}) \text{ Reject Event.} \qquad (3.41)$$

The FV is intended to enclose the centre-most 1 tonne of LAr for the specific purpose of eliminating surface backgrounds, so items (i) and (ii)—referred to as fiducialization cuts—are complementary to each other. The fiducialization cuts used in the DEAP-3600 2.5 tonne-year WIMP search were defined as follows:

$$\text{if } (\text{CFT2R} > 0.04) \text{ Reject Event} \qquad (3.42)$$

$$\text{if } (\text{CFB3R} > 0.1) \text{ Reject Event} \qquad (3.43)$$

$$\text{if } (\text{MBLikelihoodR} > 630) \text{ Reject Event} \qquad (3.44)$$

$$\text{if } (\text{MBLikelihoodZ} > 550) \text{ Reject Event,} \qquad (3.45)$$

where `MBLikelihoodR` and `MBLikelihoodZ` are in millimetres. Note that the topological variables `CFT2R` and `CFB3R` are designated as fiducialization cuts because of their correlation with `MBLikelihoodZ`. The `MBLikelihoodZ` cut removes events which are reconstructed above the LAr fill level, in the GAr region of the detector, while the `MBLikelihoodR` cut primarily reduces the impact of radiogenic neutrons on the WIMP search. Together, `MBLikelihoodR` = 630 mm and `MBLikelihoodZ` = 550 mm define the

boundaries of the FV.

The FV radius of 630 mm was chosen based on eliminating surface background leakage in the ROI. With the other fiducialization cuts of the 2.5 tonne-year WIMP search, the fiducial mass of LAr is estimated to be 824 ± 25 kg and resulted in < 1 surface background event in the ROI in this analysis [59].

3.5.4 Determining the ROI
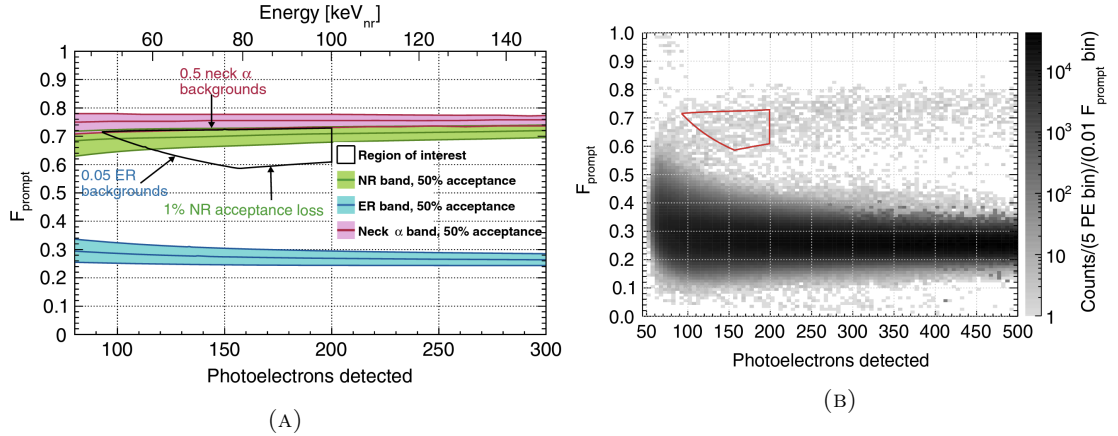
FIGURE 3.16: WIMP ROI boundary definitions for the DEAP-3600 2.5 tonne-year search (A) and WIMP ROI overlaid on AmBe calibration data (B) in PE vs. Fprompt plane. The low Fprompt band in (B) is from ^{39}Ar β decays. Images taken from Ref [59].

The DEAP-3600 ROI is a region in the PE [nSCBayes] vs. Fprompt plane wherein candidate WIMP signals are expected to be found, after the fiducialization cuts (Cuts 3.42–3.45) and topological background rejection criteria (Cuts 3.37–3.39). The exact boundaries for the WIMP ROI are determined to maximize NRA with the criterion that the expected background contribution in the ROI is $N_{\text{ROI}}^{\text{Bkg}} < 1$ event.

Figure 3.16a briefly summarizes the decisions behind the placement of the ROI upper and lower boundaries vs. PEs detected. The pink, green, and blue bands represent the Fprompt bounds (as a function of detected PEs) wherein 50% of neck α decays, WIMP-like NRs, and ERs would be accepted. The upper Fprompt boundary traces a contour such that a mean of 0.5 neck α events would reconstruct inside ROI over the 231-day exposure time in Ref [59]. This was assessed via analysis of neck α MC. Similarly the lower-left boundary was picked such that a mean of 0.05 events from ^{39}Ar would leak into the ROI. This was assessed using the model introduced in Section 3.3.3. Lastly, the lower-right boundary was determined based on a 99% NRA criteria, estimated using

AmBe calibration data (see Figure 3.16b). Note that neutrons can also produce multiple scatters in the LAr or be captured and produce gamma rays, generate signals with higher PE and lower Fprompt than what is expected for WIMPs. However, after eliminating multiple scatters with pileup cuts and eliminating capture gammas by selecting events within the ROI, the remaining AmBe neutron events are keV-scale, single scatter NRs, which are good proxy for WIMP scattering events.

The right-most boundary selects events with `nSCBayes`≤ 200 PE, which eliminates any remaining surface and dust α events from the ROI. At the time of publication, Ref[59] had not yet implemented a model for dust α backgrounds. As will be explained in greater detail in Chapter 4, the overall rate of dust alpha events were obtained in a comparison between a weighted summation of MC histograms with data in a high energy control region (8000–20000 PE), where the histogram weights were allowed to float in a χ^2 minimization. Based on this fit, it was found that the dust α rate in the ROI is equally significant as neck αs. Dust αs are therefore a key component in both the cut-and-count, as well as the Profile Likelihood WIMP search in Chapter 4.

3.5.5 WIMP Acceptance and Sensitivity

With the data cleaning, background rejection, and fiducialization cuts described in this section an estimate of the WIMP acceptance can be obtained using a combination of ^{39}Ar data and AmBe calibration data. ^{39}Ar β decays are point-like events which are uniformly distributed in the LAr bulk, just as WIMP NR events would be. Therefore all `Fprompt`-independent cuts should behave similarly between WIMPs and ^{39}Ar data. All `Fprompt`-dependent cuts—i.e. the ROI boundaries discussed in Section 3.5.4—can then be assessed independently using AmBe calibration data.

The upper `Fprompt` boundary cut corresponding to the 0.5 neck α event criterion, as estimated using AmBe calibration data, reduces WIMP acceptance to a maximum of $(69.2\pm5.3)\%$. This is given by the grey curve in Figure 3.17. Based on ^{39}Ar data, the data cleaning and background rejection cuts described in Cuts 3.31–3.41 are estimated to reduce WIMP acceptance down to $(35.4^{+2.9}_{-0.8})\%$, as indicated by the green curve in Figure 3.17. An estimate of the overall WIMP acceptance as a function of detected PEs (within the FV) can be taken as the product of these two curves, resulting in the light brown curve.
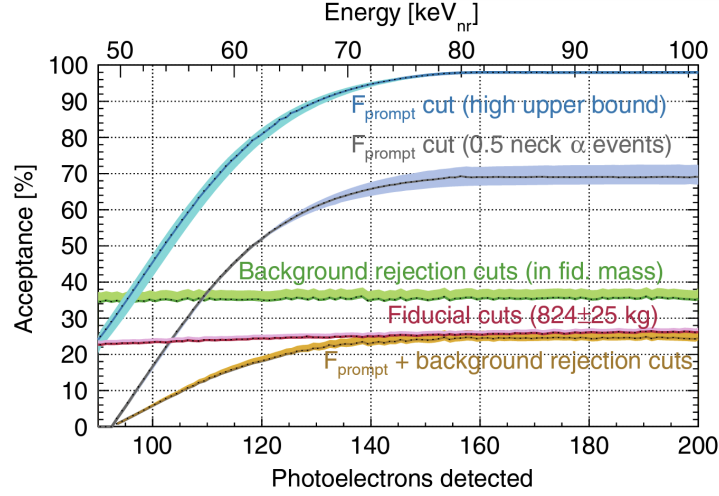
FIGURE 3.17: WIMP acceptance vs. PEs detected and cuts applied. Image taken from
Ref [59].

The sensitivity of a cut-and-count analysis comes from a comparison of the observed number of events in the ROI with the expected events under the background-only hypothesis, $N_{\mathrm{ROI}}^{\mathrm{Bkg}}$. Assuming the number of events in the ROI is Poisson distributed, an observed number of events in the ROI $N_{\mathrm{ROI}}^{\mathrm{obs}}$ is consistent with the background-only hypothesis at 90% confidence if

$$\int_{N_{\mathrm{ROI}}^{\mathrm{obs}}}^{\infty} \mathrm{Poisson}\big(x | N_{\mathrm{ROI}}^{\mathrm{Bkg}}\big)\, dx \geq 0.1,$$

where $\mathrm{Poisson}(x|\lambda)$ is the Poisson distribution with a mean parameter of λ. Given the mass contained in the FV and the exposure time of the search, the estimated number of WIMP events in the ROI comes from evaluating Equation 1.50 for an assumed WIMP mass and WIMP-nucleon elastic scattering cross-section, with the integrand appropriately weighted by the WIMP acceptance; i.e.

$$N_{\mathrm{ROI}}^{\mathrm{WIMP}} = m_T\, t_E \int_{E_{\mathrm{min}}}^{E_{\mathrm{max}}} A_{\mathrm{WIMP}}\big(E_r\big)\, \frac{dR}{dE_r}\, dE_r, \tag{3.46}$$

where E_r is the true WIMP recoil energy, $A_{\mathrm{WIMP}}\big(E_r\big)$ is the light-brown WIMP acceptance curve in Figure 3.17 and recall that $\frac{dR}{dE_r}$ depends on the WIMP mass m_χ and WIMP-nucleon scattering cross-section σ_χ. If the evaluation of Equation 3.46 for the assumed is greater than $N_{\mathrm{ROI}}^{\mathrm{obs}}$, then the combination of (m_χ, σ_χ) is excluded by the

analysis from the viable WIMP parameter space with 90% confidence.[6]

Herein lies the main disadvantage of a cut-and-count analysis: the same cuts that produce a background-free ROI also reduce WIMP acceptance—in the case of Ref [59], to a maximum of $(24.64^{+1.03}_{-1.66})\%$. With such a low acceptance, there is limited statistical power in the cut-and-count analysis when comparing an hypothesis of low σ_χ at any WIMP mass and the background-only hypothesis. Therefore, an alternative analysis methodology that does not reject events as efficiently can potentially test a much larger region of WIMP parameter space with the same set of data. It is for this reason that this work focuses on a different approach to the WIMP search analysis; namely the Profile Likelihood Ratio. This, and a more detailed discussion of handling systematic effects in DEAP-3600, are the subject of Chapter 4.

---

[6]This is a very brief summary of a much more complicated analysis, but the explanation given here is sufficient for the scope of this work.

Chapter 4

The Profile Likelihood Dark Matter Search in DEAP-3600

In this chapter, the focus will shift towards using the Profile Likelihood Ratio (PLR) approach, which is a statistical method of setting confidence intervals or claiming discoveries from experimental data, based on the Likelihood Ratio hypothesis test [118]. Compared to a cut-and-count analysis, the PLR method has the advantages of including information the expected probability distribution shapes of the dark matter signal and relevant backgrounds, as well as lifting the requirement for a background-free ROI leading to a larger fiducial volume (FV) and greater WIMP acceptance. Section 4.1 explains the important details of the PLR method in a general sense, and Section 4.2 discusses the construction of the likelihood model in the context of DEAP-3600. An important component of the PLR analysis is the concept of nuisance parameters, which are the manifestation of experimental systematic effects in the likelihood model. The relevant nuisance parameters for DEAP-3600 describe systematics which broadly fall into two categories: detector systematics and background/signal systematics. These topics are covered in Sections 4.3 and 4.4, respectively. Section 4.5 provides validation of the background model implementation via comparison with Monte Carlo (MC) simulations, as well as validation of using the asymptotic approximation (see Section 4.1) in this analysis. Lastly, Section 4.6 provides the culminating result from the PLR analysis in DEAP-3600, with a data set corresponding to an exposure of 3.5 tonne-years.

This chapter presents the combined work of myself and Dr. Ashlea Kemp, which was a continuation of ground work done by Dr. Navin Seeburn, and Dr. Alistair Butcher. The entire DEAP-3600 PLR analysis was supervised by Dr. Jocelyn Monroe. My specific contributions to the profile likelihood analysis include the construction and implementation of the radiogenic neutron (Section 4.2.2), ^{210}Po surface α (Section 4.2.2), and ^{210}Po dust α (Section 4.2.2) background models. Additionally, I designed the final version of the class structure in the analysis code which produced the results of the validation tests in Section 4.5 and the analysis results in Section 4.6.

4.1 The Profile Likelihood Method

The PLR method leverages the power of the likelihood ratio hypothesis test, which constitutes a "uniformly most powerful test" of a null hypothesis against an alternative. The premise of the PLR analysis is to compare two versions of a signal-plus-background model: the version which best describes the observed data (alternative) and another which best fits the data for an hypothesized signal normalization (null). Built into the model is a set of nuisance parameters, which parameterize the mean values and variations of experimental systematics: e.g. background rates, optical model parameters, etc. The PLR method therefore aims to determine how compatible the null hypothesis is with the alternative, given the variability afforded by systematic uncertainties. This section reviews the mathematical formalism of the method (Section 4.1.1) and the procedures followed in this specific analysis for setting a spin-independent WIMP cross-section limit (Sections 4.1.2 and 4.1.3).

4.1.1 Review of PLR Formalism

To claim a discovery or set an upper limit on WIMP-nucleon elastic scattering cross-sections using the PLR method, one needs a model that describes the probability of observing a distribution of events in data, given a signal hypothesis plus the expected background probability distributions. The form of the signal-plus-background probability density function (PDF) is,

$$f\left(x|\mu_s, \mu_b, \theta_s, \theta_b\right) = \mu_s\, S\left(x|\theta_s\right) + \mu_b\, B\left(x|\theta_b\right), \tag{4.1}$$

where x is a data point in an arbitrary observable space; μ_s and μ_b are parameters describing the signal and background normalizations; and θ_s and θ_b represent sets of parameters that may vary the shape of the signal and background PDFs, S and B, respectively. The parameter μ_s is a general representation for the 'parameter of interest'—for example, an interaction cross-section—while μ_b, θ_s, and θ_b represent the nuisance parameters. These are the manifestation in the model of systematic effects from measurements and analysis that, when varied, can change the shape of Equation 4.1. Hereafter, the nuisance parameters will be denoted with the shorthand $\boldsymbol{\theta}$. For a set of n observed data points, symbolized by the vector $\mathbf{x} = (x_1, x_2, \ldots, x_n)$, the likelihood of observing such a set of data is then given by the likelihood function,

$$\mathcal{L}\big(\mathbf{x}|\mu_s, \boldsymbol{\theta}\big) = \prod_{i=1}^{n} f\big(x_i|\mu_s, \boldsymbol{\theta}\big). \tag{4.2}$$

With a likelihood function such as the one in Equation 4.2, one can test a range of *null* hypotheses, $\mathcal{H}_0$, with varying values of μ_s and $\boldsymbol{\theta}$. Typically, this is done in reference to an *alternative* hypothesis, $\mathcal{H}_1$, which assumes the same model as $\mathcal{H}_0$ but with different values of μ_s and $\boldsymbol{\theta}$. The point of such a test is to either accept or reject $\mathcal{H}_0$ at a predetermined significance level, α, which quantifies the probability of rejecting $\mathcal{H}_0$ when $\mathcal{H}_0$ is true. For the chosen α, the hypothesis test which maximizes statistical power—i.e. maximizes separation between $\mathcal{H}_0$ and $\mathcal{H}_1$ (recall from Section 3.3.3)—is the *likelihood ratio test* [115]. This fact is formally stated in the Neyman-Pearson Lemma [118], for which a proof is given in Appendix A.3.

The likelihood ratio is defined as

$$\lambda = \frac{\mathcal{L}\big(\mathbf{x}|\mathcal{H}_0\big)}{\mathcal{L}\big(\mathbf{x}|\mathcal{H}_1\big)}, \tag{4.3}$$

where

$$\mathcal{H}_0 \text{ assumes } \begin{cases} \mu_s = \nu_0 \\ \boldsymbol{\theta} = \boldsymbol{\theta}_0 \end{cases} \quad \text{and} \quad \mathcal{H}_1 \text{ assumes } \begin{cases} \mu_s = \nu_1 \\ \boldsymbol{\theta} = \boldsymbol{\theta}_1 \end{cases}$$

The goal of the PLR method is then to use Equation 4.3 to either claim a discovery of a signal process, or set a limit on the strength of the signal process. For DEAP-3600, the 'signal process' refers to a WIMP-nucleus elastic scattering event; the signal strength would then be the WIMP-nucleon elastic scattering cross-section, σ_χ. In both cases,

two separate maximum likelihood fits of Equation 4.1 to the data stored in vector $\mathbf{x}$ are performed:

1. One where μ_s is fixed to some hypothesized value ν, while $\boldsymbol{\theta}$ is allowed to vary freely; i.e. a *conditional* maximum likelihood fit, $\mathcal{L}\big(\mathbf{x}|\mu_s = \nu, \hat{\hat{\boldsymbol{\theta}}}\big)$. The 'double-hat' parameter, $\hat{\hat{\boldsymbol{\theta}}}$, is the set of maximum-likelihood estimators for the nuisance parameters under the assumption that $\mu_s = \nu$ is true.

2. One where μ_s and $\boldsymbol{\theta}$ are both allowed to vary freely; i.e. an *unconditional* maximum likelihood fit, $\mathcal{L}\big(\mathbf{x}|\hat{\mu}_s, \hat{\boldsymbol{\theta}}\big)$. Parameters denoted with a 'single-hat' are their respective maximum-likelihood estimator values, regardless of assumptions about the signal strength.

Fit (1) takes the place of $\mathcal{H}_0$ in Equation 4.3, while Fit (2) takes the place of $\mathcal{H}_1$. Therefore Equation 4.3 can be recast as a function of the hypothesized signal strength,

$$\lambda(\nu) = \frac{\mathcal{L}\big(\mathbf{x}|\nu, \hat{\hat{\boldsymbol{\theta}}}\big)}{\mathcal{L}\big(\mathbf{x}|\hat{\mu}_s, \hat{\boldsymbol{\theta}}\big)}. \tag{4.4}$$

Determining $\hat{\hat{\boldsymbol{\theta}}}$ is typically referred to as 'profiling' over the systematic effects. Thus, Equation 4.4 is called the *Profile Likelihood Ratio* [119].

Note that, as it's written in Equation 4.4, the likelihood ratio is bounded by $0 \leq \lambda(\nu) \leq 1$. Since the denominator of Equation 4.4 is determined entirely by the observed data, $\lambda(\nu) = 1$ implies maximal agreement between data and the signal-plus-background model under the null hypothesis, $\mathcal{H}_0$. Therefore it's possible to use $\lambda(\nu)$ to quantify the hypothesis test directly. It is conventional to convert $\lambda(\nu)$ into a test statistic given by,

$$q_\nu = -2\ln\big(\lambda(\nu)\big). \tag{4.5}$$

This test statistic has a domain of $0 \leq q_\nu < \infty$, where increasing q_ν implies increasing *in*compatibility between the null hypothesis and observed data.

The probability that the best fit signal-plus-background model accurately describes the data is quantified as follows. Suppose q_ν, as it is defined in Equation 4.5, is a random variable distributed according to a known PDF $g(q_\nu|\mu_s)$, where the subscript ν refers to the hypothesized signal normalization, and μ_s is the true signal normalization in

the data set. From the data in $\mathbf{x}$, an observed value of the test statistic, q_ν^{obs}, can be obtained by performing the conditional and unconditional maximum likelihood fits described above. The PLR method then quantifies the overall level of agreement between the null hypothesis (which assumes $\mu_s = \nu$) and data via a p-value given by,

$$p_\nu = \int_{q_\nu^{\mathrm{obs}}}^{\infty} g(q_\nu | \mu_s = \nu) \, dq_\nu. \tag{4.6}$$

Equation 4.6 gives the probability that the model with hypothesized signal strength ν would have equal or greater incompatibility with the observed data, in a universe where $\mu_s = \nu$. The PLR method uses Equation 4.6 to make the final decision of rejecting or accepting $\mathcal{H}_0$ based on the predetermined value of α, i.e.

If $p_\nu < \alpha$, then reject $\mathcal{H}_0$ with $(1 - \alpha) \times 100\%$ confidence.

Else, do not reject $\mathcal{H}_0$.

Two important details to note at this point are:

(i) In practice, determining the PDF $g(q_\nu | \mu_s)$ requires detailed knowledge of the shapes of distributions of observables for both signal and background—knowing their integral over a given range is insufficient.

(ii) The exact form of the test statistic q_ν is different if the intent of the analysis is to claim a discovery vs. set an upper limit

Item (i) is the main topic of Section 4.1.2. Item (ii) points to a difference in the nature of the null hypothesis being tested. Specifically, when one wants to claim a discovery, the null hypothesis is the background-only version of Equation 4.1 (i.e. $\mu_s = 0$). The PLR method can then be used to reject the background-only hypothesis in favour of an alternative with an observed signal normalization of $\hat{\mu}_s$. The test statistic is then modified to

$$q_0 = \begin{cases} -2\ln\big(\lambda(0)\big) & \hat{\mu}_s \geq 0 \\ 0 & \text{else} \end{cases}. \tag{4.7}$$

If a limit is being set instead, the null hypothesis varies across the entire (not already excluded) μ_s parameter space. The test statistic in this case is

$$q_\nu = \begin{cases} -2\ln(\lambda(\nu)) & \hat{\mu}_s \leq \nu \\ 0 & \text{else} \end{cases}. \tag{4.8}$$

The objective in both cases is to assess how well the null hypothesis can agree with data with the 'wiggle room' provided by the nuisance parameters. Therefore, it is crucial to minimize the associated systematic uncertainties in order to maximize the sensitivity of a search for new physics with the PLR approach. Allowing $\boldsymbol{\theta}$ to float freely with no constraints may result in physically unreasonable values of $\hat{\hat{\boldsymbol{\theta}}}$ that artificially inflate the perceived agreement between a given hypothesis and the observed data. This can lead to an erroneous rejection of a discovery, or an underestimated size of the excluded μ_s parameter space. Constraining the nuisance parameters can be done with auxiliary measurements designed to probe specific systematics. This will be discussed in greater detail in Sections 4.3 and 4.4.

4.1.2 Asymptotic Approximation

Determining the sampling distribution of the test statistic $g(q_\nu|\mu_s = \nu)$ can be done via brute force with the use of pseudo-experiments. Using the PDF in Equation 4.1 and explicitly setting $\mu_s = \nu$ and $\boldsymbol{\theta}$ to nominal values, one can randomly generate a set of simulated data points and perform the PLR analysis described in Section 4.1.1. Storing the resulting q_ν value in a histogram and repeating this process many times returns an approximation of the true sampling distribution of q_ν.

However, this approach is both computationally expensive and time consuming. There is an alternative way of determining $g(q_\nu|\nu)$ which follows from results in Refs [120, 121]. Consider a case where an hypothesized signal normalization ν is being tested and a set of N_{pts} observed/simulated data points is distributed according to a signal normalization $\mu_s = \nu$. Provided there is only one parameter of interest in the analysis—that being the assumed signal normalization, ν—the test statistic q_ν (as it appears in Equation 4.5 for

now) can be written as

$$q_\nu = -2\ln\big(\lambda(\nu)\big) = \frac{(\nu - \hat{\mu}_s)^2}{\sigma^2} + \mathcal{O}\left(\frac{1}{\sqrt{N_{\text{pts}}}}\right),\tag{4.9}$$

where $\hat{\mu}_s$ follows a normal distribution of mean ν and variance σ^2. In practice, $\hat{\mu}_s$ is obtained from the unconditional maximum likelihood fit in Equation 4.4, and σ^2 is obtained from the covariance matrix $V_{i,j} = \text{cov}(\theta_i, \theta_j)$ obtained from the fit. If N_{pts} is sufficiently large, the $\mathcal{O}\big(1/\sqrt{N_{\text{pts}}}\big)$ term vanishes and the distribution of q_ν converges to a χ^2 distribution with one degree of freedom,

$$g(q_\nu|\nu) = \frac{1}{\sqrt{2\pi q_\nu}} \exp\left(-\frac{q_\nu}{2}\right)\tag{4.10}$$

This result is called the *Asymptotic Approximation*. To check its validity for a given model and number of observed data points, the brute force method is typically invoked to produce the sampling distribution for direct comparison. For the DEAP-3600 model, this is shown in Section 4.5.

The form of the test statistics used for claiming a signal discovery or setting an upper limit differ from that used in Equation 4.9, and this subtly changes the general form of the test statistic distribution. In the case of a discovery, the test statistic can be recast using the asymptotic approximation as

$$q_0 = \begin{cases} \frac{\hat{\mu}_s^2}{\sigma^2} & \hat{\mu}_s > 0 \\ 0 & \text{else} \end{cases}\tag{4.11}$$

and in the case of an upper limit, it becomes

$$q_\nu = \begin{cases} \frac{(\nu - \hat{\mu}_s)^2}{\sigma^2} & \hat{\mu}_s < \nu \\ 0 & \text{else} \end{cases}\tag{4.12}$$

The corresponding sampling distributions of these test statistics take the form of a *half* χ^2 distribution, i.e.

$$\text{Discovery: } g(q_0|0) = \frac{1}{2}\left(\delta(q_0) + \frac{1}{\sqrt{2\pi q_0}}e^{-q_0/2}\right), \tag{4.13}$$

$$\text{Upper Limit: } g(q_\nu|\nu) = \frac{1}{2}\left(\delta(q_\nu) + \frac{1}{\sqrt{2\pi q_\nu}}e^{-q_\nu/2}\right), \tag{4.14}$$

where $\delta(x)$ is the Dirac delta function. For the half χ^2 PDF, the cumulative distribution takes the form,

$$G(q_\nu|\nu) = \Phi\left(\sqrt{q_\nu}\right), \tag{4.15}$$

$$\text{and } p_\nu = 1 - G(q_\nu|\nu), \tag{4.16}$$

where $\Phi(x)$ is the cumulative distribution of a standard Gaussian, with a mean of 0 and standard deviation of 1. Using Equations 4.15 and 4.16, a simple formula can be derived for setting upper limits on the signal normalization without needing to run a large number of pseudo-experiments. Recall that in setting an upper limit, a set of hypothesized signal strengths are rejected when $p_\nu < \alpha$. Therefore, the value of ν corresponding to $p_\nu = \alpha$—say, ν_{up}—sets the upper limit of acceptable signal hypotheses. Solving for ν_{up} directly yields

$$p_\nu = \alpha = 1 - G(q_\nu|\nu) \tag{4.17}$$

$$= 1 - \Phi\left(\sqrt{q_\nu}\right) \tag{4.18}$$

$$\sqrt{q_\nu} = \Phi^{-1}\left(1 - \alpha\right) \tag{4.19}$$

$$\sqrt{\frac{(\nu_{\text{up}} - \hat{\mu}_s)^2}{\sigma^2}} = \Phi^{-1}\left(1 - \alpha\right) \tag{4.20}$$

$$\therefore \nu_{\text{up}} = \hat{\mu}_s + \sigma\,\Phi^{-1}\left(1 - \alpha\right). \tag{4.21}$$

For the DEAP-3600 PLR WIMP search analysis no discovery is being claimed, and therefore an upper limit on the WIMP-nucleon scattering cross-section, as determined by Equation 4.21, will be the end result. The chosen significance level for this analysis is $\alpha = 0.1$, corresponding to a 90% confidence limit (CL).

4.1.3 Power Constrained Limits

For a PLR analysis where an upper limit is being drawn, an important caveat is that the resulting upper limit is only meaningful when there is sufficient experimental sensitivity to the hypothesized signal. In other words, the separation between the signal hypothesis and background-only hypothesis cannot be negligible; alternatively, there should be a minimum allowable statistical power (see the discussion surrounding Equation 4.22) of the hypothesis test. The consequence of a small power is that the sampling distribution $g(q_\nu|\nu)$ would be similar to that where $\mu_s = \nu$ is hypothesized but $\mu_s = 0$ is true; i.e. $g(q_\nu|0)$. This might yield a situation where,

$$\alpha > \int_{q_\nu^{\mathrm{obs}}}^{\infty} g(q_\nu|\nu) \, dq_\nu \approx \int_{q_\nu^{\mathrm{obs}}}^{\infty} g(q_\nu|0) \, dq_\nu,$$

leading to a rejection of a signal hypothesis which was always going to be virtually indistinguishable from background because of the sensitivity of the experiment, and not the strength of the signal.

Ref [122] prescribes a method to address this situation. They first define a function M, called a *power function*. This describes the statistical power of an hypothesis test as a function of the chosen critical region w; i.e. the region of a given space where the data disfavour the null hypothesis. In general, the choice of critical region is dependent upon the signal normalization in both the null and alternative hypotheses. Therefore the power function for the PLR analysis can be written as,

$$M_\mu(\nu) = P(p_\nu < \alpha|\mu), \tag{4.22}$$

where the subscript μ is the signal normalization under the alternative (and assumed true) hypothesis, ν is that of the null hypothesis, and P is the probability of observing a p-value, p_ν (Equation 4.6) below the significance level α of the hypothesis test. For the purposes of addressing the issue raised in this section, one uses Equation 4.22 under the assumption of $\mu = 0$, which returns the power of a test comparing a null hypothesis with $\mu_s = \nu$ and a background-only alternative. The convention adopted in Ref [122] is to consider a signal hypothesis 'testable' if it satisfies

$$M_0(\nu) = P\big(p_\nu < \alpha|0\big) \geq \Phi(-1) \approx 0.16, \tag{4.23}$$

where $\Phi(x)$ is the cumulative distribution of a standard Gaussian (mean = 0, standard deviation = 1).

With this convention, the PLR analysis is unable to reject signal hypotheses which are *not* testable according to Equation 4.23. The resulting upper limit with this restriction is called a *Power Constrained Limit* (PCL), defined as

$$\nu_{\text{up}}^* = \max(\nu_{\text{up}}, \nu_{\text{min}}), \tag{4.24}$$

where

$$\nu_{\text{up}} \equiv \text{ as in Equation } 4.21 \tag{4.25}$$

$$\nu_{\text{min}} \equiv M_0^{-1}(0.16) \tag{4.26}$$

4.2 Constructing the DEAP Likelihood Model

The likelihood function constructed for the DEAP-3600 PLR WIMP search is defined as follows:

$$\mathcal{L}(\sigma_\chi | \vec{\mathbf{x}}, \boldsymbol{\theta}) = \mathcal{L}_{\text{PDF}}(\sigma_\chi | \vec{\mathbf{x}}, \boldsymbol{\theta}) \cdot \mathcal{L}_{\text{SB}}(\boldsymbol{\theta}) \cdot \mathcal{L}_{\text{Con}}(\boldsymbol{\theta}), \tag{4.27}$$

where the parameter of interest, σ_χ, is the spin-independent WIMP-nucleon elastic scattering cross-section; $\vec{\mathbf{x}} = \{\vec{x}_1, \vec{x}_2, \ldots, \vec{x}_{N_{\text{obs}}}\}$ is a vector of N_{obs} data points; and $\boldsymbol{\theta} = \{\theta_1, \theta_2 \ldots, \theta_{N_\theta}\}$ is a vector of N_θ nuisance parameters pertaining to the systematic effects discussed in Sections 4.3 and 4.4. Each data point $\vec{x}_i$ exists within the domain,

$$\begin{aligned}
\big\{ \vec{x}_i \in \mathbb{R}^4 \mid\ & 90 \leq q \leq 200, \\
& g_-(q) \leq f \leq g_+(q), \\
& 0 \leq r \leq 720, \\
& 0 \leq t \leq \infty \big\},
\end{aligned} \tag{4.28}$$

where $q \equiv$ nSCbayes [PE], $f \equiv$ Fprompt, $r \equiv$ MBLikelihood Radius [mm] (hereafter denoted as Rrec), $t \equiv \text{T}_0^{\text{GAr}}$, and $g_\pm(q)$ are PE dependant upper and lower bounds on Fprompt (see Figure 4.14a). The three terms on the right-hand side of Equation 4.27 are

defined as,

$$\mathcal{L}_{\text{PDF}}(\sigma_\chi | \vec{\mathbf{x}}, \boldsymbol{\theta}) = \text{Pois}\big(N_{\text{obs}}; N_{\text{exp}}(\sigma_\chi | \boldsymbol{\theta})\big) \cdot \prod_{j=1}^{N_{\text{obs}}} \left(\mathcal{P}_{\text{Sig}}(\vec{x}_j | \sigma_\chi, \boldsymbol{\theta}) + \sum_{i=1}^{N_{\text{Bkgs.}}} \mathcal{P}_i(\vec{x}_j | \boldsymbol{\theta}) \right), \quad (4.29)$$

$$\mathcal{L}_{\text{SB}}(\boldsymbol{\theta}) = \prod_{i}^{N_{\text{Bkgs.}}} \text{Pois}\big(N_{\text{obs},i}^{\text{SB}}; N_{\text{exp},i}^{\text{SB}}(\boldsymbol{\theta})\big), \quad (4.30)$$

$$\mathcal{L}_{\text{Con}}(\boldsymbol{\theta}) = \prod_{i=1}^{N_\theta} \text{Gaus}\big(\theta_i; \mu_i, \sigma_i\big), \quad (4.31)$$

where $\text{Pois}(N; \lambda)$ is a Poisson distribution of mean λ, and $\text{Gaus}(x; \mu, \sigma)$ is a Normal distribution of mean μ and standard deviation σ. Equation 4.29 is the 'PDF term' of the likelihood function, which contains the probability distributions of the WIMP signal, $\mathcal{P}_{\text{Sig}}(\vec{x}; \sigma_\chi, \boldsymbol{\theta})$, and $N_{\text{Bkgs.}}$ number of backgrounds, $\mathcal{P}_i(\vec{x}; \boldsymbol{\theta})$. Equation 4.30 is the 'Side Band' (SB) term, which constrains the nuisance parameters based on how each background probability distribution extrapolates immediately outside of the domain in Equation 4.28. Here $N_{\text{obs},i}^{\text{SB}}$ is the observed number of events in a side band pertaining to the ith background and $N_{\text{exp},i}^{\text{SB}}(\boldsymbol{\theta})$ is the expected number of events in the side band given an input set of nuisance parameters. Equation 4.31 is the 'Constraint' term of the likelihood model. This also constrains the nuisance parameters to reasonable values based on external analyses, which are described in Sections 4.3 and 4.4.

In the following, Sections 4.2.1 and 4.2.2 will describe the mathematical structures of each probability distribution in Equation 4.29 in greater detail, while Section 4.2.3 focuses on the side band and constraint terms.

Note that the background models for ^{210}Po α decays and radiogenic neutrons require the construction of PDF templates via extensive simulation work, which was all done with the Reactor Analysis Tool (RAT) [123] software package. RAT is a merger of ROOT analysis libraries with the GEANT4 simulation toolkit. The DEAP-3600 RAT installation used for building the models in this section was based on ROOT v5.34.36 and GEANT4 v9.6.02, specifically. The GEANT4 models describing the detector geometry and hardware include the full detector design described in Section 2.2.1, as well as the front end electronics and DAQ systems in Section 2.2.4.

4.2.1 WIMP Model

The signal probability distribution $\mathcal{P}_{\text{Sig}}(\vec{x}|\sigma_\chi, \boldsymbol{\theta})$, in Equation 4.29 describes the WIMP hypothesis introduced in Section 1.4.2. In the space of Equation 4.28, $\mathcal{P}_{\text{Sig}}$ can be written as

$$\mathcal{P}_{\text{Sig}}(\vec{x}|\sigma_\chi, \boldsymbol{\theta}) = Q(q|\sigma_\chi, \boldsymbol{\theta})\, F(f, q|\sigma_\chi, \boldsymbol{\theta})\, R(r, q|\sigma_\chi, \boldsymbol{\theta})\, T(t|\sigma_\chi, \boldsymbol{\theta}), \qquad (4.32)$$

where $Q(q|\sigma_\chi, \boldsymbol{\theta})$ is the PE PDF, $F(f, q|\sigma_\chi, \boldsymbol{\theta})$ is the `Fprompt` PDF, $R(r, q|\sigma_\chi, \boldsymbol{\theta})$ is the radial PDF, and $T(t|\sigma_\chi, \boldsymbol{\theta})$ is the `T0`$^{\text{GAr}}$ PDF. Note that the same model structure will be used for the backgrounds discussed in Sections 4.2.2, but without a dependence on σ_χ. The following discussion of the WIMP signal model is an appropriately modified version of the in Ref [124].

The PE PDF of the WIMP model, $Q(q|\sigma_\chi, \boldsymbol{\theta})$, is the convolution of the theoretical WIMP differential recoil rate, $\frac{dR}{dE_r}$ (Equation 1.37) with a Gaussian kernel, which represents the detector response:

$$Q(q|\sigma_\chi, \boldsymbol{\theta}) = \int_0^\infty q_f(E_r) \frac{dR}{dE_r}(\sigma_\chi) \cdot \frac{1}{\sqrt{2\pi\sigma^2}} e^{-(q-\mu)^2/2\sigma^2} dE_r, \qquad (4.33)$$

where,

$$\mu = \langle N_{\text{DN}} \rangle + Y_{\text{PE}} \cdot E_r \qquad \text{(As in Eq.3.9)}$$

$$\sigma^2 = \sigma_{\text{PE}}^2 \cdot \mu + \sigma_{\text{rel,LY}}^2 \cdot \mu^2 \qquad \text{(As in Eq.3.10)}$$

$$q_f(E_r) \equiv \text{Nuclear Recoil Quenching Factor (see Sec. 4.3.1)}.$$

The five parameters $\langle N_{\text{DN}} \rangle$ (dark noise mean charge [PE]), Y_{PE} (light yield [PE/keV$_{\text{ee}}$]), σ_{PE}^2 (Poisson/Fano energy resolution [PE]), $\sigma_{\text{rel,LY}}^2$ (light yield variance resolution), and $q_f(E_r)$ are contained within $\boldsymbol{\theta}$.

Recall from Section 1.4.2 that the WIMP differential recoil rate dR/dE_R describes the expected energy distribution of WIMPs as a function of their recoil energy, E_r [keV]. However, due to the quenching effects described in Section 4.3.1, only $\sim 30\%$ of nuclear recoil (NR) energy is converted into scintillation. Therefore the WIMP recoil energy is translated into its electron-equivalent energy in the detector [keV$_{\text{ee}}$] using the energy-dependent quenching factor $q_f(E_r)$. This conversion is necessary because the light yield

Y_{PE} is calibrated on electronic recoil (ER) events where quenching effects are negligible. Once in electron-equivalent energy, the distribution is convolved with the detector response model described by Equation 4.33. An example `nSCBayes` distribution for a 100 GeV/c^2 WIMP with a WIMP-nucleon cross-section of 10^{-44} cm^2 is shown in Figure 4.1, drawn using the nominal values for $\langle N_{\mathrm{DN}} \rangle$, Y_{PE}, σ^2_{PE}, and $\sigma^2_{\mathrm{rel,LY}}$ listed in Table 3.2; and $q_f(E_r)$ shown in Figure 4.11a.
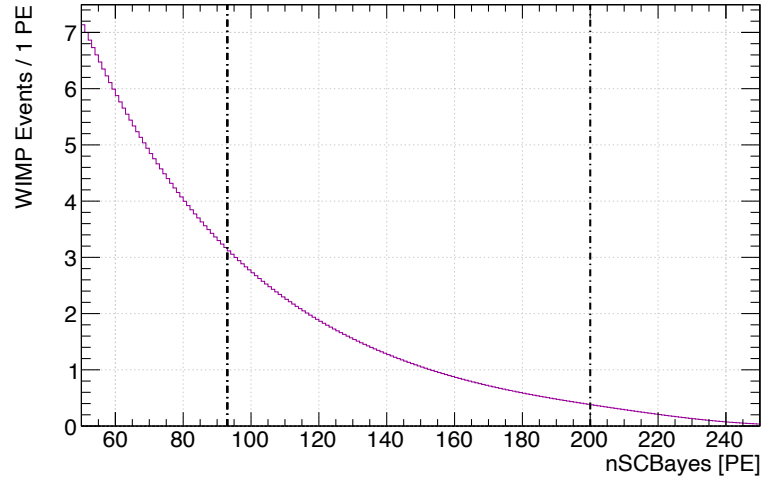
FIGURE 4.1: Number of events [PE^{-1}] for a 100 GeV WIMP as a function of `nSCBayes` [PE], for a WIMP-nucleon cross-section of 10^{-44}cm^2 (purple). The WIMP ROI is enclosed inside the two vertical dashed lines (black), between 93 PE - 200 PE. Image taken from Ref [124].

The WIMP `Fprompt` PDF, $F(f, q | \sigma_\chi, \boldsymbol{\theta})$, has a mean and width that vary with recoil energy, which was propagated through the detector response as follows. Measurements of the NR singlet-to-triplet ratio as a function of recoil energy were taken from the SCENE collaboration [108] and implemented into GEANT4 simulations of NR events in the DEAP-3600 detector. ^{40}Ar recoils from WIMP elastic scattering interactions were then simulated uniformly within the detector, and the resulting data was used to construct a 2D distribution of `Fprompt` vs. recoil energy. This distribution was used to assess the nominal mean `Fprompt` value for NRs, $\langle f^{\mathrm{NR}} \rangle$, and the width σ_f^{NR} for each energy bin.

The width in `Fprompt` is quantified as a function of `nSCBayes`, which was assessed based on fits of the `Fprompt` distribution in ER events. A 2D empirical model for the `Fprompt` distribution of ^{39}Ar β decays is presented in Ref [104], which is adopted for the DEAP-3600 WIMP likelihood model. For a given number of detected PEs in an ER event,

the probability of observing a given `Fprompt` value f is described by the convolution of a Gamma function (Equation 3.5) with mean of $\langle f^{\mathrm{ER}} \rangle$ and shape parameter b, with a Gaussian distribution centred at zero and having a standard deviation of σ_f^{ER},

$$F^{\mathrm{ER}} = \mathrm{Gamma}(f; \langle f^{\mathrm{ER}} \rangle, b) \circledast \mathrm{Gaus}(f; 0, \sigma_f^{\mathrm{ER}}). \tag{4.34}$$

where $\langle f^{\mathrm{ER}} \rangle$, b, and σ_f^{ER} are all dependent upon `nSCBayes`, i.e.,

$$\langle f^{\mathrm{ER}} \rangle \to \langle f^{\mathrm{ER}} \rangle(q) = m_0 + \frac{m_1}{q} + \frac{m_2}{q^2} + \frac{m_3}{q^3}, \tag{4.35}$$

$$b \to b(q) = b_0 + \frac{b_1}{q} + \frac{b_2}{q^2}, \tag{4.36}$$

$$\sigma_f^{\mathrm{ER}} \to \sigma_f^{\mathrm{ER}}(q) = s_0 + \frac{s_1}{q} + \frac{s_2}{q^2}. \tag{4.37}$$

To convert Equation 4.34 into an equivalent model for NRs, the mean and width parameters are substituted with their NR counterparts, i.e. $\langle f^{\mathrm{ER}} \rangle \to \langle f^{\mathrm{NR}} \rangle$ and $\sigma_f^{\mathrm{ER}} \to \sigma_f^{\mathrm{NR}}$. It is assumed that the shape parameter b are the same for ERs and NRs, but their skewnesses should be inverted relative to each other. This is achieved with the following NR `Fprompt` model:

$$F(f, q|\sigma_\chi, \boldsymbol{\theta}) = \mathrm{Gamma}(1 - f; 1 - \langle f^{\mathrm{NR}} \rangle, b) \circledast \mathrm{Gaus}(1 - f; 0, \sigma_f^{\mathrm{NR}}). \tag{4.38}$$

In position space, WIMP interactions are expected to be uniformly distributed throughout the liquid argon (LAr) in the detector. Therefore the number of WIMP interaction events contained within a sphere of radius, r, should scale with r^3, and a suitable WIMP radial PDF, $R(r, q|\sigma_\chi, \boldsymbol{\theta})$, should satisfy

$$R \propto \frac{3r^2}{R_0^3} \tag{4.39}$$

where R_0 is the inner radius of the AV, $R_0 = 850\,\mathrm{mm}$. The input value of the radial PDF is not a true radius, rather a reconstructed radius from the `MBLikelihood` position reconstruction algorithm, `Rrec`. To account for finite resolution and bias in position reconstruction, Equation 4.39 is convolved with a Gaussian resolution model, with `nSCBayes` and `Rrec` dependent model parameters. This is obtained via GEANT4 simulations, by comparing the true radial positions of events, R_{tr}, with their reconstructed

radial positions, $r = $`Rrec`. For a fixed value of R_{tr}, the cubic reconstructed radial distribution can be described by a Gaussian; i.e. $(r/R_0)^3 \sim \text{Gaus}((r/R_0)^3; \mu_C, \sigma_C)$, where μ_C is the mean reconstructed cubed-radius and σ_C is the cubed radial resolution. For simplicity, μ_C and σ_C are normalized to R_0. The radial bias is then given by,

$$\frac{\mu_{\text{B}}}{R_0} = (\mu_C)^{1/3} - \frac{R_{\text{tr}}}{R_0}., \tag{4.40}$$

and the radial resolution can be expressed as,

$$\frac{\sigma_{\text{B}}}{R_0} = \left((\mu_C + \sigma_C)^{1/3} - \mu_C^{1/3}\right). \tag{4.41}$$

The final form of the WIMP radial PDF is then expressed as,

$$R(r, q|\sigma_\chi, \boldsymbol{\theta}) = \frac{3R_{\text{tr}}^2}{R_0^3} \circledast \text{Gaus}\left(\left(\frac{r}{R_0}\right)^3; \frac{\mu_{\text{B}}}{R_0}, \frac{\sigma_{\text{B}}}{R_0}\right). \tag{4.42}$$

The PE-dependent, Gaussian radial resolution function is obtained by studying how the radial bias (Equation 4.40) and resolution (Equation 4.41) vary as a function of both `Rrec` and `nSCBayes`. To do this, ^{39}Ar events were simulated at 18 different radii in the LAr, which correspond to values of $(R_{\text{tr}}/R_0)^3$ between 0.05 and 0.95, equally spaced. An example fit of the radial resolution distribution to a Gaussian model is shown in Figure 4.2 between 250-450 PE.
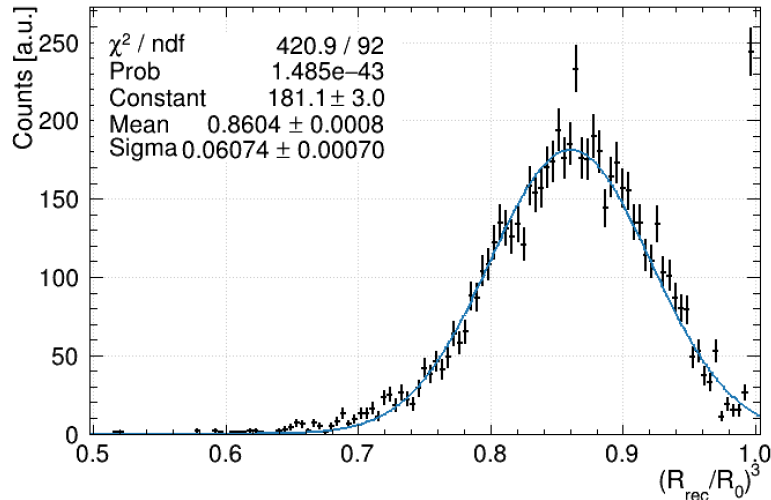
FIGURE 4.2: Gaussian fit to the $(r/R_0)^3$ distribution for $R_{\text{tr}} = 821.63$ mm in the 200–400 PE bin. Image taken from Ref [124].

The distributions of μ/R_0 and σ/R_0 as a function of $(r/R_0)^3$ were each fit with 5th order polynomials, which describe how the bias and resolution change as a function of `Rrec`. In order to account for the PE dependence of the radial resolution, this process is repeated for 15 `nSCBayes` bins, spanning from 0–3000 PE. The evolution with `nSCBayes` of each of the `Rrec` polynomial coefficients were also described with 5th order polynomials in PE. Example polynomial fits of the linear bias and resolution parameters as a function of $(r/R_0)^3$ for two `nSCBayes` bins are shown in Figure 4.3.
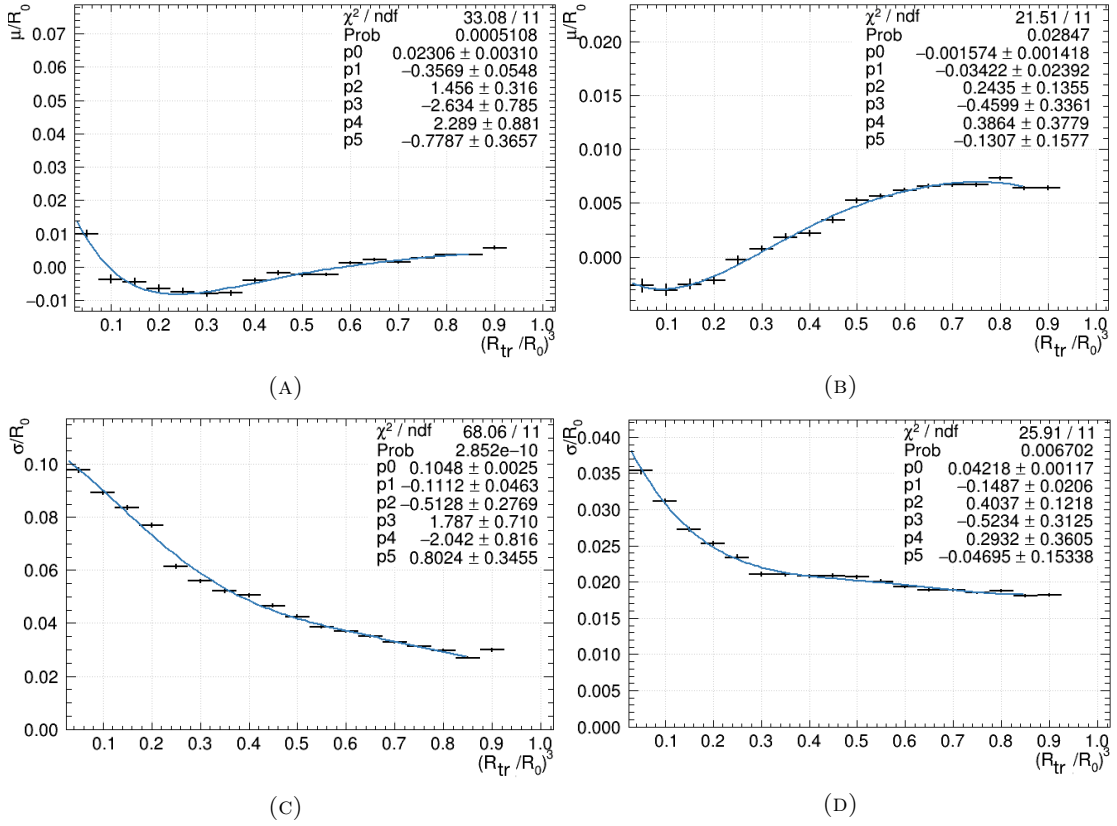
FIGURE 4.3: Radial bias as a function of $(r/R_0)^3$ for (A) $200\,\text{PE}{\leq}$`nSCBayes`${\leq}400\,\text{PE}$ and (B) $2800\,\text{PE}{\leq}$`nSCBayes`${\leq}3000\,\text{PE}$. Radial resolution as a function of $(r/R_0)^3$ for (C) $200\,\text{PE}{\leq}$`nSCBayes`${\leq}400\,\text{PE}$ and (D) $2800\,\text{PE}{\leq}$`nSCBayes`${\leq}3000\,\text{PE}$. Images taken from Ref [124].

Note that ^{39}Ar β decays are also uniformly distributed throughout the LAr volume, and so the radial model of this background is constructed in exactly the same way as WIMPs. Furthermore, since T_0^{GAr} is highly correlated with `Rrec`, the WIMP and ^{39}Ar T_0^{GAr} PDFs were also constructed in the same way as each other. The T_0^{GAr} PDF for WIMPs and ^{39}Ar β decays was observed directly from real ^{39}Ar data (see Figure 4.4a).

An important caveat to note about Equations 4.33, 4.38, and 4.42 is that these are functions independent of—and therefore uncorrelated with—T_0^{GAr}. To address this, additional

functions $G_Q(t, q)$, $G_F(t, f)$, and $G_R(t, r)$ (see Figures 4.4b–4.4d) were calculated in order to capture the correlations of `nSCBayes`, `Fprompt`, and `Rrec`, respectively, with $T_0^{\texttt{GAr}}$; this was done as follows. Histograms of real ^{39}Ar data in `nSCBayes`, `Fprompt`, and `Rrec` were built under 3 conditions: accepting events with any $T_0^{\texttt{GAr}}$ (H_{all}), accepting events with $T_0^{\texttt{GAr}} \leq 2$ ($H_{\leq 2}$), and accepting events with $T_0^{\texttt{GAr}} > 2$ ($H_{>2}$). Bin-by-bin ratios of these histograms were then computed for $H_{\leq 2}/H_{\text{all}}$ and $H_{>2}/H_{\text{all}}$ in `nSCBayes`, `Fprompt`, and `Rrec`. These ratios of spectra with different $T_0^{\texttt{GAr}}$ acceptance regions were then fit to cubic polynomials, as shown in Figures 4.4b–4.4d, which were then used in the WIMP and ^{39}Ar β background models to modify PDFs Q (Equation 4.33), F (Equation 4.38), and R (Equation 4.42); i.e.

$$Q(q|\sigma_\chi, \boldsymbol{\theta}) \rightarrow Q(q|\sigma_\chi, \boldsymbol{\theta}) \cdot G_Q(t, q) \tag{4.43}$$

$$F(f, q|\sigma_\chi, \boldsymbol{\theta}) \rightarrow F(f, q|\sigma_\chi, \boldsymbol{\theta}) \cdot G_F(t, f) \tag{4.44}$$

$$R(f, q|\sigma_\chi, \boldsymbol{\theta}) \rightarrow R(f, q|\sigma_\chi, \boldsymbol{\theta}) \cdot G_R(t, r) \tag{4.45}$$
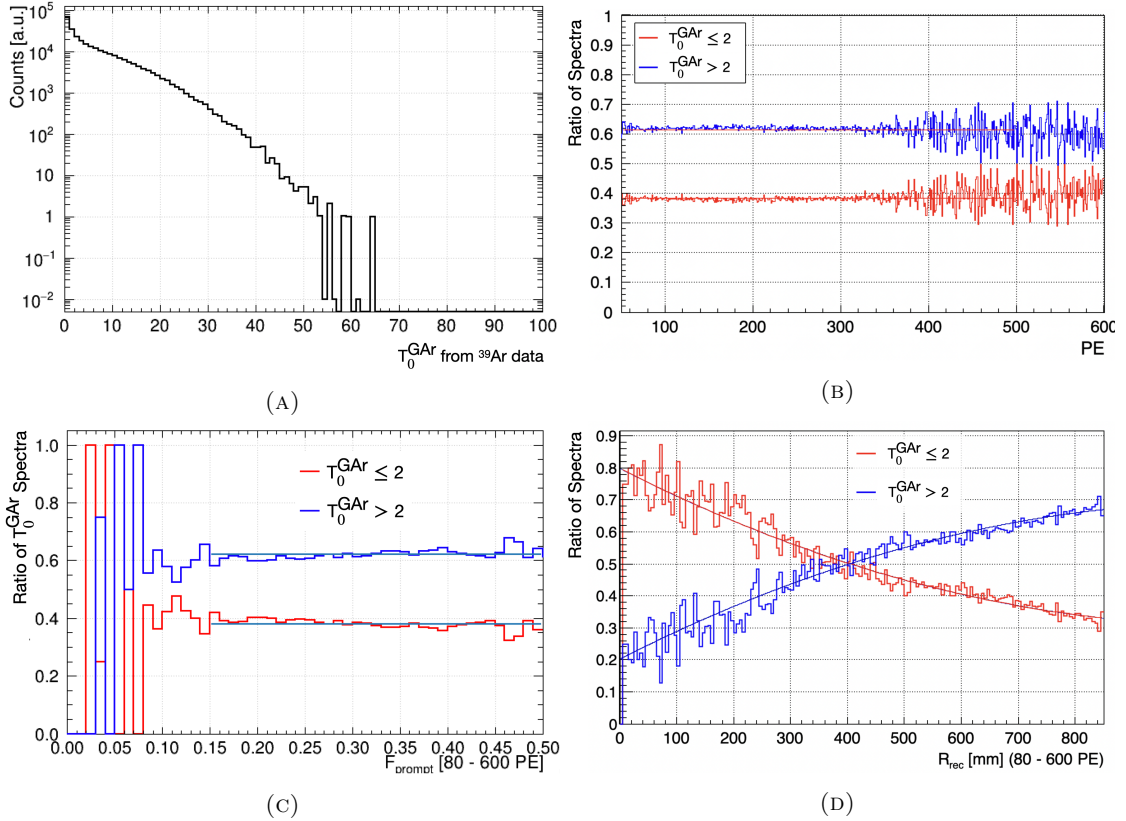
FIGURE 4.4: (A) The $T_0^{\texttt{GAr}}$ distribution as determined from ^{39}Ar data. The $T_0^{\texttt{GAr}}$ distribution for WIMP events is assumed to take the same shape. Also included are bin-by-bin histogram ratios for both $H_{\leq 2}/H_{\text{all}}$ and $H_{>2}/H_{\text{all}}$ in (B) `nSCBayes`, (C) `Fprompt`, and (D) `Rrec` spaces. Images taken from Ref [124].

4.2.2 Background Models

The backgrounds considered in the PLR WIMP search analysis include those discussed in Sections 2.3.1, 2.3.2, and 2.3.3 which are:

(i) ^{39}Ar β decays [124]

(ii) ^{210}Po α decays in the AV surface [125]

(iii) ^{210}Po α decays in the detector neck [126]

(iv) ^{210}Po α decays in copper dust particulates circulated within the LAr [127]

(v) Radiogenic neutrons [128]

The references cited in items (i)–(v) indicate the work done by other members of the DEAP-3600 collaboration in the amassing of critical information needed to build the background models discussed here.

^{39}Ar β Decays

The ^{39}Ar β background model was constructed in a similar fashion as the WIMP model. The only differences are in the `nSCBayes` and `Fprompt` PDFs, while the `Rrec` and `T`$_0^{\mathtt{GAr}}$ PDFs are identical. In the ^{39}Ar `nSCBayes`, the WIMP differential scattering rate is replaced with the ^{39}Ar β spectrum like the one shown in Figure 2.11, and the quenching factor is set equal to unity for all energies. The exact ^{39}Ar β spectrum used has been fit to DEAP-3600 data in the same way used to obtain the energy response model (see Section 3.1). Instead of Equation 4.38, the ^{39}Ar `Fprompt` PDF is taken directly from Ref [104] and thus follows Equation 4.34.

^{210}Po α Decays

As it is currently implemented, ^{39}Ar is unique in the DEAP-3600 likelihood model in that it is entirely determined by real data. Backgrounds (ii)–(v) are not as active as ^{39}Ar in the vicinity of the ROI, and therefore obtaining a clean sample of each one such that a data driven model could be built is infeasible. Therefore, these background models

were built upon MC simulations with a GEANT4 model encapsulating the DEAP-3600 detector and the systematics discussed in Section 4.3.

For the various ^{210}Po α backgrounds in items (ii)–(iv), there are several sub-components for each that combine to make up their whole MC data sets. Recall from Section 2.3.2 that surface α decays can originate from the bulk of the AV acrylic, the AV-TPB interface, the TPB bulk, or the TPB-LAr interface (see Figure 2.14). The relative weights of these components were determined in a fit of data in a high energy control region of $10000 \leq \text{PE} \leq 35000$, `Rrec`>845 mm, and `Fprompt`>0.5, which is expected to be dominated by ^{210}Po surface αs. The fit adds together simulated PE spectra of each of the mentioned surface components according to a weight which is allowed to float such that the χ^2 per degree of freedom is minimized. The result of this fit is shown in Figure 4.5a and the resulting trigger rates are given in Table 4.1. When appropriately weighted according to these trigger rates, the surface α MC data set can be looked at with event selection criteria similar to that outlined in Section 3.5.1, which produces the distribution in Figure 4.5b. This and the equivalent distributions in `Fprompt`, `Rrec`, and T_0^{GAr} can then be described by empirical functional forms (see Equations 4.46–4.55) which are used to describe PDFs Q, F, R, and T, as in the WIMP model.
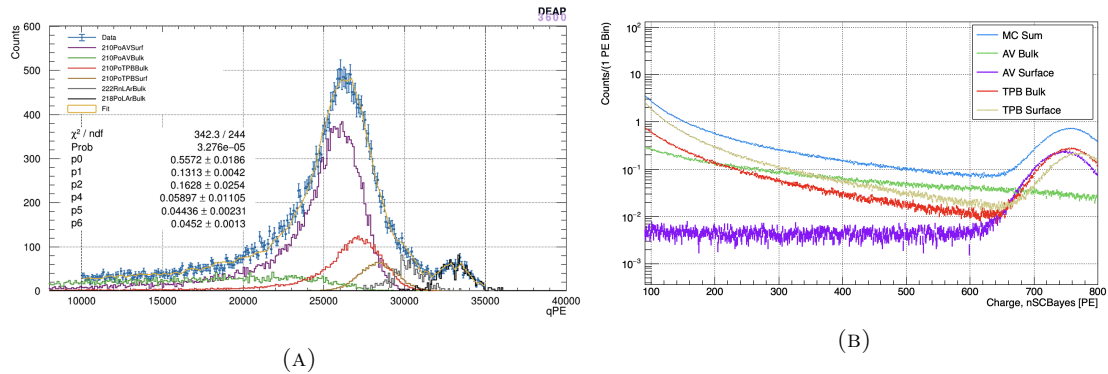
FIGURE 4.5: (A) Fit of MC surface α component weights (parameters p_0–p_6) to data in surface α control region of $10000 \leq \text{PE} \leq 35000$, `Rrec`>845 mm, and `Fprompt`>0.5. (B) Extrapolation of surface α MC components and their weighted sum to the ROI energy range. Figure (A) courtesy of Dr. Fred Schuckman.

A similar procedure was followed for items (iii) and (iv). The neck α control region applies the same event selection criteria as those listed in Section 3.5.1, but with the T_0^{GAr} cut removed, `nSCBayes` within $300 \leq \text{PE} \leq 3900$, and `Rrec` < 700 mm. The neck components simulated for the MC data set correspond to the different surfaces of the neck shown in Figure 2.15, i.e. the inner flow guide inner surface (IFIS), the inner flow

guide outer surface (IFOS), and the outer flow guide inner surface (OFIS). The Dust α control region is similar to that of surface αs, but with a different `Rrec` selection criteria of `Rrec` < 630 mm. The dust α components considered for the MC data set correspond to spherical copper dust particulates with different ranges of radii: 5–10 μm, 10–15 μm, 15–20 μm, and 20–25 μm. The corresponding fit results and ROI extrapolations for the neck and dust αs are provided in Appendix C and the estimated rate of triggers for each component in the surface, neck, and dust α models in the detector are provided in Table 4.1.

Background (χ^2/NDF)	Component	Rate [10^{-5} Hz]	Uncertainty [10^{-5} Hz]
^{210}Po Surface α (342.3/244)	AV Bulk	41.8	0.8
	AV Surface	50.8	3.4
	TPB Bulk	9.5	4.6
	TPB Surface	12.0	1.7
^{210}Po Neck α (449.1/172)	IFIS	1.41	0.13
	IFOS	1.98	0.13
	OFIS	2.35	0.14
^{210}Po Dust α (94.45/35)	5–10 μm	1.78	0.56
	10–15 μm	2.80	0.88
	15–20 μm	3.54	1.12
	20–25 μm	4.20	1.26

TABLE 4.1: Trigger rates of the various components in the Surface α [125], Neck α [126], and Dust α [127] backgrounds. Rate calculations were made using information from fits of weighted-sum spectra of each component in the control region for the corresponding background.

An important detail for the dust α background is that the hypothesis for the PLR model assumes 58% of the total dust particulate surface area has a 3 μm thick coating of TPB. Recall from Section 2.3.2 that the origin of the dust particulates in the AV is proposed to be from the period of resurfacing during detector construction, which occurred before the TPB layer was deposited onto the AV inner surface. Particulates that leaked in during this time would have been coated with TPB at the same time as the AV. To assess the fraction of total TPB coverage on dust particulates, another MC data set of dust αs with a 100% coverage, 3 μm layer of TPB coating was simulated. Comparing this data set with real data in the `nSCBayes` range of $500 \leq$ PE ≤ 1000 allows for another weighted-sum fit to indicate the percentage of dust particulate surface area that should be coated in TPB, and by extension the percentage that should be left 'naked'. This fit is provided in Figure 4.6. The dust component trigger rates provided in Table 4.1 are

the combined rates of both TPB-coated and naked dust, so the component rate of, say 5–$10\,\mu$m dust with a TPB coating would be $(1.78 \times 10^{-5}\,\text{Hz}) \cdot 0.58 = 1.01 \times 10^{-5}\,\text{Hz}$.

In the 3.5 tonne-year PLR WIMP search described in Section 4.6, the coverage fraction of TPB on the dust particulates was implemented as a nuisance parameter with a flat prior probability distribution bounded between 0–100%. Unlike the other nuisance parameters discussed in Sections 4.3 and 4.4, which have Gaussian prior distributions, the dust TPB coverage fraction is poorly constrained from the fit in Figure 4.6. Therefore assigning a flat prior from 0–100% for the dust TPB coverage fraction is a conservative approach to describe the systematic uncertainty on this effect.
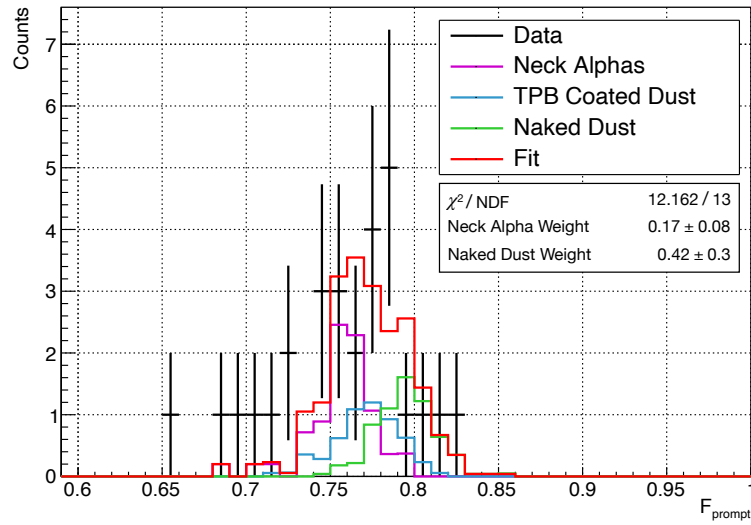
FIGURE 4.6: Fit of weighted-sum dust+neck α MC data set to real data in `Fprompt` for $500 \leq \text{PE} \leq 1000$. The Naked Dust Weight parameter is the fraction of all dust particulates in the data set with no TPB coating, and therefore the fraction of all dust that have a TPB-coating is $(1 - 0.42) \times 100\% = 58\%$. Image reconstructed from data in Ref [127].

As with the WIMP and ^{39}Ar models, the ^{210}Po α background models use a histogram from their MC data sets instead of an empirical fit function for describing the $\texttt{T}_0^{\texttt{GAr}}$ PDF. The empirical functional forms for Q, F, and R used to describe the `nSCBayes`, `Fprompt`, and `Rrec` PDFs for each of the ^{210}Po α backgrounds are as follows:

Surface α:

$$Q(q|\boldsymbol{\theta}) = \frac{\sum_{j=1}^{2} N_j \text{Lan}(q; \mu_j, \sigma_j)}{1 - e^{(q-W)/T}} \tag{4.46}$$

$$F(f, q|\boldsymbol{\theta}) = N_{\text{TPB}}\text{Gaus}(f; \mu_{\text{TPB}}, \sigma_{\text{TPB}}) + N_{\text{LAr}}\text{SkewGaus}(f; \mu_{\text{LAr}}, \sigma_{\text{LAr}}, \alpha) \tag{4.47}$$

$$R(r, q|\boldsymbol{\theta}) = \sum_{k=1}^{2} \frac{N_k}{\tau_k} e^{-(R_0 - r)/\tau_k} + N_G \text{Gaus}(R_0 - r; \mu_R, \sigma_R) \tag{4.48}$$

where $R_0 = 850\,\text{mm}$; $\text{Lan}(x; \mu, \sigma)$ is a Landau distribution with a most probable value μ and width parameter σ; the skewed Gaussian function (with skewness parameter α) is

$$\text{SkewGaus}(x; \mu, \sigma, \alpha) = \text{Gaus}(x; \mu, \sigma) \cdot \frac{1}{2}\left(1 - \text{Erf}\left(\frac{\alpha(x - \mu)}{\sqrt{2}\sigma}\right)\right); \tag{4.49}$$

and $\text{Erf}(x)$ is the standard Error Function.

Neck α:

$$Q(q|\boldsymbol{\theta}) = \sum_{n=0}^{3} p_n q^n + \sum_{m=1}^{2} N_m \text{Gaus}(q; \mu_m, \sigma_m) \tag{4.50}$$

$$F(f, q|\boldsymbol{\theta}) = \text{Gamma}(1 - f; 1 - \langle f^{\text{Neck}}\rangle, b^{\text{Neck}}) \circledast \text{Gaus}(1 - f; 0, \sigma_f^{\text{Neck}}) \tag{4.51}$$

$$R(r, q|\boldsymbol{\theta}) = \sum_{\ell=1}^{2} N_\ell \text{Gaus}(r; \mu_\ell, \sigma_\ell) \tag{4.52}$$

Dust α:

$$Q(q|\boldsymbol{\theta}) = B_0 + \sum_{i=0}^{2} \frac{1}{\tau_i} e^{-q/\tau_i} \tag{4.53}$$

$$F(f, q|\boldsymbol{\theta}) = N_{\text{TPB}}\text{Gaus}(f; \mu_{\text{TPB}}, \sigma_{\text{TPB}}) + N_{\text{LAr}}\text{Gaus}(f; \mu_{\text{LAr}}, \sigma_{\text{LAr}}) \tag{4.54}$$

$$R(r, q|\boldsymbol{\theta}) = N_R^{\text{Dust}}\left(e^{r/\rho} - 1\right) \tag{4.55}$$

Note that in Equations 4.47, 4.48, 4.51, 4.52, 4.54, and 4.55, all function parameters are implied to have a dependence on PE; i.e. $N_{\text{LAr}} \Rightarrow N_{\text{LAr}}(q)$, and $\mu_R \Rightarrow \mu_R(q)$, etc. Furthermore, as with the WIMP signal and ^{39}Ar background models, the same approach to ensure the correlations with $\texttt{T}_0^{\texttt{GAr}}$ are included is taken with the surface and dust α backgrounds. However the PDF shapes for the neck α background model are much more sensitive to changes in $\texttt{T}_0^{\texttt{GAr}}$. Therefore with neck αs, the MC data sets were sorted into

bins with $T_0^{GAr} \leq 2$ and $T_0^{GAr} > 2$, and Equations 4.50–4.52 were fit to these distributions directly, as shown in Figure 4.7 for `nSCBayes`. Further details regarding the fits of these functions to their respective MC data sets are provided in Section 4.5. Plots showing fit results are provided in Appendix C.1.

(A) (B)
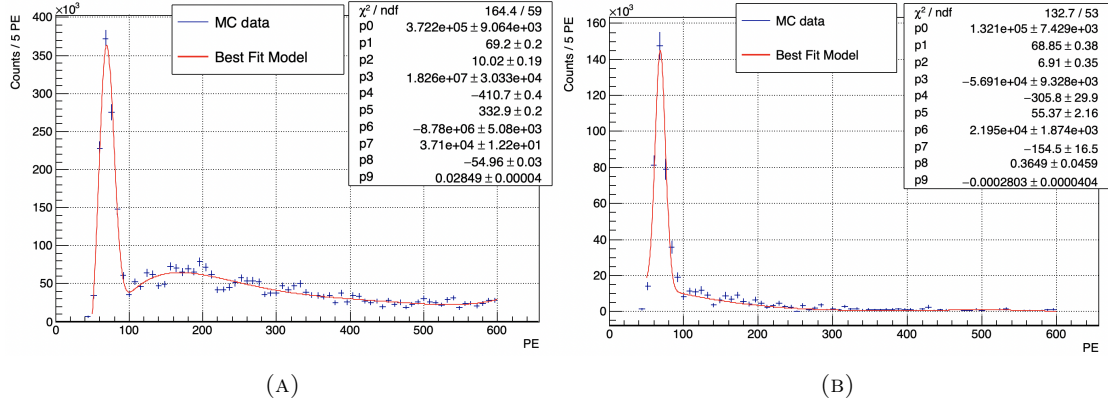
FIGURE 4.7: `nSCBayes` distributions of the neck α decay PDF from MC simulations for the $T_0^{GAr} \leq 2$ bin (A) and $T_0^{GAr} > 2$ bin (B), where the three individual IFIS, IFOS and OFIS sources are summed together. The distributions were fit with the empirical model, described by Equation 4.50.

Radiogenic Neutrons

The radiogenic neutron background model was constructed in a similar fashion as the ^{210}Po α backgrounds: MC data sets were simulated for the neutron components listed below, and the weighted-sum distributions in `nSCBayes`, `Fprompt`, and `Rrec` were used in a χ^2 minimization fit with empirical functions.

The neutron components considered here are (α, n) neutrons generated by the various α sources in the ^{238}U, ^{235}U, and ^{232}Th decay chains. Note that secular equilibrium is assumed in all chains, except for ^{238}U where equilibrium is broken upon reaching ^{226}Ra.[1] For this reason ^{238}U$_{upper}$ will hereafter denote the ^{238}U chain up to ^{226}Ra and ^{238}U$_{lower}$ will denote the ^{238}U chain from ^{226}Ra onward. Secular equilibrium is assumed within the upper and lower sub-chains. The specific (α, n) components in the radiogenic neutron background model are as follows:

---

[1]The rationale for this assumption is that barium, which is commonly used in PMT glass, is in the same periodic group as radium. Therefore since radium can form the same chemical bonds as barium, there could be a small radium content within the PMT glass and the extra ^{226}Ra could be introduced into the detector materials in this way. Since the lifetime of ^{226}Ra is $\sim 10^3$ years, it could stay out of equilibrium with ^{238}U for the whole duration of the DEAP-3600 WIMP search. The breaking of secular equilibrium in the ^{238}U chain at ^{226}Ra is supported by radiometric assays performed for the 231 live-day WIMP search analysis in Ref [59].

(i) (α, n) neutrons originating in the 255 AV PMTs

(ii) (α, n) neutrons originating in the four neck veto PMTs

(iii) (α, n) neutrons originating in the polyethylene+polystyrene filler blocks

(iv) (α, n) neutrons originating in the polyurethane filler foam insulation

Spontaneous fission is expected to be a subdominant source of neutrons compared to items (i)–(iv) above ($\mathcal{O}(10^{-6})$ n/s/Bq compared to $\mathcal{O}(10^{-4})$ n/s/Bq, respectively), and therefore it is neglected in the radiogenic neutron background model here.

To generate the MC data sets, neutron energy spectra were calculated using the Neutron Calculator Based On TALYS (NeuCBOT) code repository [129]. NeuCBOT calculates the energy spectra based user input of the decay chains (or list of α energies) and material in which an α is emitted. For the relevant materials, NeuCBOT then loads look-up tables for stopping powers generated by SRIM [130] and (α, n) cross-sections generated by the TALYS nuclear reaction simulation code [131] and calculates neutron yields and outgoing kinetic energies. These kinetic energy spectra are given in units of [n/s/Bq], and therefore material assays were required to obtain the activity of each primordial decay chain in items (i)–(iv). These assays were performed by γ-ray spectroscopy with the SNOLAB PGT and germanium well detectors. Samples of acrylic were also α-counted to measure ^{210}Pb contamination. The assay results are provided in Table 4.2. A plot of the summed energy spectra calculated by NeuCBOT for each component (scaled according to measured activities) is shown in Figure 4.8.

Component	^{238}U$_{\text{upper}}$	^{238}U$_{\text{lower}}$	^{235}U	^{232}Th	Mass [kg]
AV PMTs	18300 ± 4500	3100 ± 200	600 ± 100	840 ± 70	496.8
Neck Veto PMTs	2500 ± 1500	166 ± 15	110 ± 70	300 ± 20	1.4
Filler Blocks	14.4 ± 3.5	0.30 ± 0.27	0.15 ± 0.15	0.16 ± 0.16	2650.0
Filler Foam	115.8 ± 63	33 ± 3	1.43 ± 1.0	1.49 ± 0.16	32.0

TABLE 4.2: Specific activities in [mBq/kg] of primordial radionuclide decay chains in the various detector components which contribute to the radiogenic neutron model.

The empirical functions used to describe the radiogenic neutron MC PDFs in `nSCBayes`, `Fprompt`, and `Rrec` are provided in Equations 4.56–4.58. Similar to the α backgrounds, it is implied that all function parameters in Equations 4.57 and 4.58 are PE dependent. Details regarding the fits of these functions to the MC data set are provided in
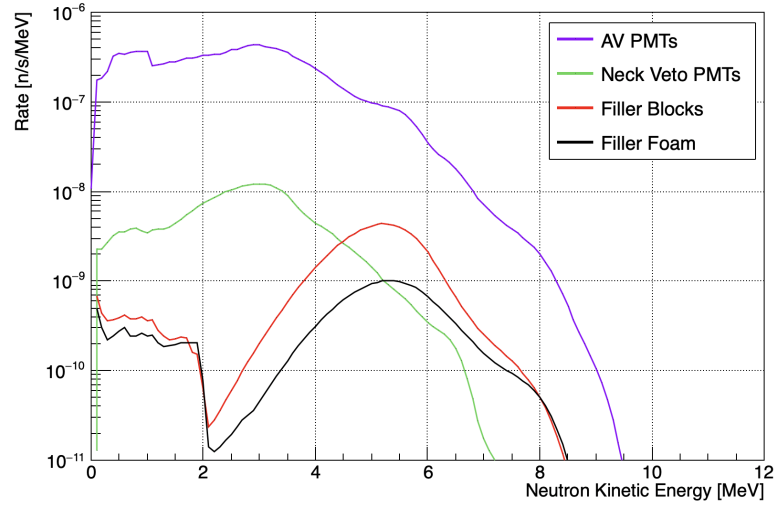
FIGURE 4.8: Radiogenic neutron energy spectra calculated by NeuCBOT for the AV PMTs, neck veto PMTs, filler blocks, and filler foam. Rates shown here are normalized according to measured activities reported in Table 4.2.

Section 4.5. Plots showing fit results are provided in Appendix C.2.

$$Q(q|\boldsymbol{\theta}) = \frac{1}{1 - e^{(q-W)/T}} \frac{N_\Omega}{\Omega} e^{-q/\Omega} \tag{4.56}$$

$$F(f, q|\boldsymbol{\theta}) = \mathrm{Gamma}(1 - f; 1 - \langle f^{\mathrm{neut}} \rangle, b^{\mathrm{neut}}) \circledast \mathrm{Gaus}(1 - f; 0, \sigma_f^{\mathrm{neut}}) \tag{4.57}$$

$$R(r, q|\boldsymbol{\theta}) = \frac{N_\eta}{\eta} e^{-r/\eta} \tag{4.58}$$

4.2.3 Side Band and Constraint Terms

For every nuisance parameter in the DEAP-3600 likelihood model (with the exception of the dust TPB coating coverage fraction, see Section 4.2.2), there is a constraint term that prevents the conditional and unconditional maximum likelihood fits in Equation 4.4 from converging towards unreasonable values for the nuisance parameters. Each constraint term takes the form of a Gaussian such as in Figure 4.9a. The mean of the Gaussian is set to a nominal value for the associated systematic, and the standard deviation is set to its estimated systematic uncertainty. Therefore, reducing the systematic uncertainties also reduces the level variability in the likelihood model, which is crucial for maximizing the sensitivity of the analysis. Section 4.3 is a summary of the studies undertaken in DEAP-3600 to understand experimental systematics.

Side bands refer to regions immediately adjacent to the ROI, as depicted in Figure 4.9b.

In principle, there could be a side band term for each background included in the likelihood model. However in practice, the only background that can produce a usable side band is ^{39}Ar β decay, which is used to constrain the detector energy response (Equation 3.9). The ^{39}Ar side band term applies a penalty to the likelihood model based on the observed number of events, $N_{\mathrm{obs}}^{\mathrm{SB}}$, between 90–200 PE and below the lower bound in `Fprompt` of the red ROI in Figure 4.9b. The ^{39}Ar background model is then extrapolated into the side band region and integrated to get the expected number of events $N_{\mathrm{exp}}^{\mathrm{SB}}(\boldsymbol{\theta})$ assuming a set of nuisance parameters $\boldsymbol{\theta}$. The side band term assumes the number of side band events is Poisson distributed about a mean of $N_{\mathrm{exp}}^{\mathrm{SB}}(\boldsymbol{\theta})$, and therefore, is maximized when the nuisance parameters result in $N_{\mathrm{exp}}^{\mathrm{SB}}(\boldsymbol{\theta}) \approx N_{\mathrm{obs}}^{\mathrm{SB}}$.
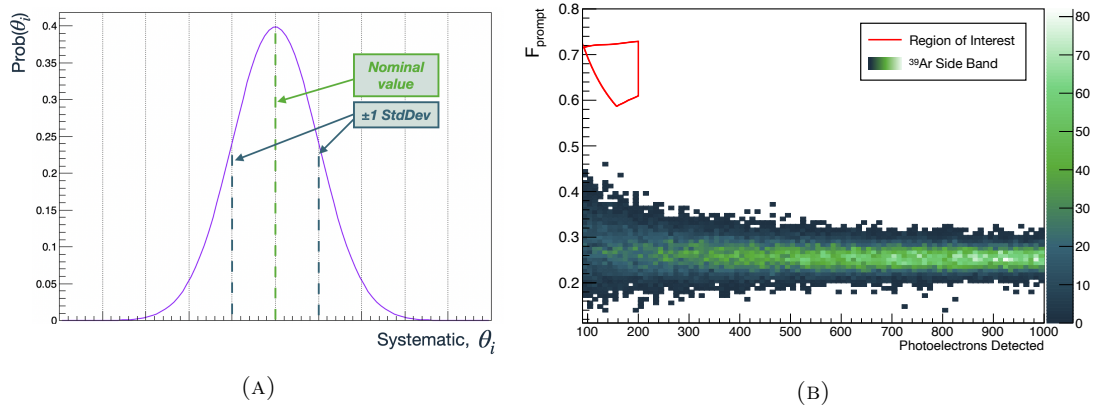
FIGURE 4.9: (A) Generic nuisance parameter constraint PDF taking the form of a Gaussian centred at a nominal value and with a standard deviation (StdDev) determined by the $\pm 1\sigma$ uncertainty of the associated systematic. (B) ^{39}Ar side band next to the ROI from Ref [59] in PE-`Fprompt` space.

4.2.4 Constraint Implementation

Constraints on the nuisance parameters are implemented in the likelihood model in two different ways:

MC Method

Recall from Section 4.2.2 that the nominal background models for the ^{210}Po αs and radiogenic neutrons were built upon MC data sets, with empirical fit functions describing their PDFs. Following this approach, MC data sets were also generated with individual systematic parameters in the GEANT4 detector model varied by $\pm 1\sigma$, resulting in two additional MC data sets per nuisance parameter. Each of these data sets was used to

build an analogous PDF structure to Equation 4.32 with one nuisance parameter, say θ_k, set to either its $+1\sigma$ or -1σ variation, i.e.

$$\mathcal{P}^{\pm k}_{\text{Sig/Bkg}} = \mathcal{P}_{\text{Sig/Bkg}}(\vec{\mathbf{x}}|\sigma_\chi, \boldsymbol{\theta} \pm \boldsymbol{\sigma}_k), \tag{4.59}$$

where,

Recalling that $\boldsymbol{\theta} = \{\theta_1, \theta_2, \ldots \theta_k, \ldots, \theta_{N_\theta}\}$

and in similar fashion $\boldsymbol{\sigma}_k = \{0, 0, \ldots, \sigma_k, \ldots, 0\}$

Analytical Method

For some of the nuisance parameters, it was determined that the effect of their associated systematics can be modelled by using the nominal PDF and applying simple analytical transformations to the `nSCBayes` dimension of the data, $\vec{\mathbf{x}}$. In this case, the equivalent statement of Equation 4.59 would be

$$\mathcal{P}^{\pm k}_{\text{Sig/Bkg}} = \mathcal{P}^{\text{nom}}_{\text{Sig/Bkg}}(\vec{\mathbf{x}}^{\pm k}), \tag{4.60}$$

and the vector $\vec{\mathbf{x}}^{\pm k}$ contains data points, where $\mathcal{P}^{\text{nom}}_{\text{Sig/Bkg}}$ refers to the Signal+Background model with all nuisance parameters set to their nominal values, and $\vec{\mathbf{x}}^{\pm k}$ contains data points, $\vec{x}_i$, that have been transformed in `nSCBayes` according to the variation of nuisance parameter θ_k, i.e.

$$\vec{x}_i \rightarrow \big\{ q(1 \pm S_q \sigma_k), \ f, \ r, \ t \big\}.$$

Here, the coefficient S_q is a scaling factor for the systematic uncertainty. For example, the effect of the $\pm 1\sigma$ variation on the PMT efficiency (see Section 4.3.3) results in a scaling of all observed values of `nSCBayes` by approximately 5%. Therefore $S_q = 0.05$ and $0 \leq \sigma_k \leq 1$.

In order to achieve a smooth transition in the shape of the Signal+Backgrounds model between nominal values and the $\pm 1\sigma$ variations, each nuisance parameter discussed in Sections 4.3, θ_k, is recast as a floating parameter, A_k, where $-1 \leq A_k \leq 1$. The

Signal+Background model can then freely vary these parameters by evaluating,

$$\mathcal{P}_{\text{Sig/Bkg}} = \mathcal{P}_{\text{Sig/Bkg}}^{\text{nom}} + \begin{cases} |A_k|(\mathcal{P}_{\text{Sig/Bkg}}^{+k} - \mathcal{P}_{\text{Sig/Bkg}}^{\text{nom}}) & A_k \geq 0 \\ |A_k|(\mathcal{P}_{\text{Sig/Bkg}}^{-k} - \mathcal{P}_{\text{Sig/Bkg}}^{\text{nom}}) & A_k < 0 \end{cases}, \qquad (4.61)$$

Table 4.3 summarizes the set of nuisance parameters discussed in Sections 4.3 and 4.4. The nominal values are input as the priors for the likelihood fits discussed in Section 4.6.

Nuisance Parameter	Nominal	$\pm 1\sigma$ Uncertainty	Method
Mean Light Yield [PE/keV]	6.1	0.4	Analytical
NR Quenching Factor [108]		See Figure 4.11	Analytical
α Quenching Factor		See Figure 4.11	Analytical
LAr Refractive Index	1.369	0.005	MC
TPB Scattering Length [μm]	2.25	$^{+2.25}_{-1.13}$	MC
PMT Afterpulsing Probability	6.8%	1%	Analytical
Relative PMT Efficiency	—	4.5%	Analytical
Dust TPB Coverage Fraction	50%	50%	MC

TABLE 4.3: Summary table of the nuisance parameters implemented in the PLR software, shown with their respective nominal values, uncertainties, and implementation methods.

4.3 Detector Systematics

The pathway from a scintillation event to a detectable signal in DEAP-3600 contains several stages where systematic effects are introduced. These broadly fall under three categories: liquid argon (LAr) scintillation, optical, and instrumental. Here, these are covered in Section 4.3.1, Section 4.3.2, and Section 4.3.3, respectively. Included in the discussion of LAr scintillation systematics is the time dependent variation in light yield and the LAr quenching factor. The optical systematics discussed include the LAr refractive index and the TPB scattering length. Lastly, the topics included in the instrumentation subsection include PMT efficiency and afterpulsing.

4.3.1 Liquid Argon Scintillation Systematics

Light Yield Variations

The light yield, Y_{PE} (see Equation 3.9), is implemented in the likelihood model as a nuisance parameter as described in Table 4.3. However, an important fact to note is that Y_{PE} is not perfectly stable over long periods of time. Figure 4.10 [132] shows that a small drift of $0.25\pm0.05\,\mathrm{PE/keV}$ is detectable over a four year span. To account for this, the drift is corrected in the data before being input into the likelihood model. This is done by rescaling the `nSCBayes` component in all data points via the transformation,

$$q' = q\,\frac{Y_{\mathrm{PE}}(0)}{Y_{\mathrm{PE}}(t)}, \tag{4.62}$$

where q is the observed PE count in `nSCBayes` at time, t; q' is the rescaled PE count in `nSCBayes`; $Y_{\mathrm{PE}}(0) = 6.1\,\mathrm{PE/keV}$ is the observed light yield in Ref [59]; and $Y_{\mathrm{PE}}(t)$ is the observed light yield at time t, taken from Figure 4.10. This correction effectively removes any time dependence from the data, allowing the light yield nuisance parameter to vary about a constant mean value, constrained by its systematic uncertainty in Table 3.2, in the conditional and unconditional maximum likelihood fits.
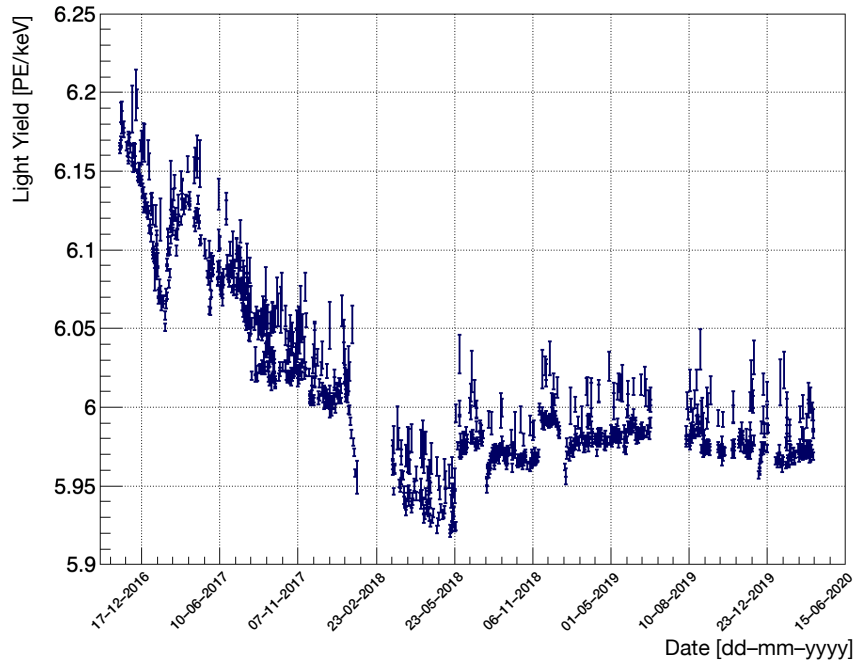
FIGURE 4.10: Drift of the light yield parameter, Y_{PE}, over time as measured in ^{39}Ar. Image made from data obtained for study in Ref [132]

Nuclear Recoil and Alpha Quenching Factors

Recall from Sections 2.1.1 and 2.1.2 that in LAr, the scintillation efficiency for nuclear recoils (NRs) is lower compared to electronic recoils (ERs) through quenching processes. These processes are described in Lindhard theory [76] and Birks' Saturation Law [81], and culminate in a total quenching factor given in Equation 2.15.

To measure the quenching factor, one simply takes the ratio of observed energy E_m (calibrated to physical units, e.g. keV) to a known deposited energy E_d, say from a monoenergetic α decay. With a series of such measurements at various recoil energies, Equation 2.15 can be fit to that data, and the A and kB parameters obtained in the process. In order to do this fit, one also needs information about the nuclear and electronic stopping power of a given particle in LAr. This is generally non-trivial to determine, however there exist several treatments of this problem in literature [133–135]. The stopping powers calculated in the SRIM (Stopping and Range of Ions in Matter) software package [130] are used in DEAP analyses.

In DEAP-3600, the quenching factors for ^{40}Ar NR events (e.g. from neutron or WIMP scattering events) and αs were assessed independently. The former was obtained by using measurements from the SCENE collaboration [108], where a LAr time projection chamber was exposed to a low energy (0.510–1.773 MeV) neutron beam, which provided a sample of ^{40}Ar NRs ranging in recoil energy from $\sim$ 10–50 keV. The fit and systematic uncertainties for this measurement are provided in Figure 4.11a. Similarly, a fit of the quenching factor for high energy α decays ($\sim$5–8 MeV) was determined using a measurement from Doke et al. [136] for the quenching factor of ^{210}Po α decay at 5.30 MeV. Three additional data points were created from DEAP-3600 data via the α decays of ^{222}Rn (5.49 MeV), ^{218}Po (6.00 MeV), and ^{214}Po (7.69 MeV). The fit of Equation 2.15 to these four data points and calculation of the systematic uncertainties are shown in Figure 4.11b [137].
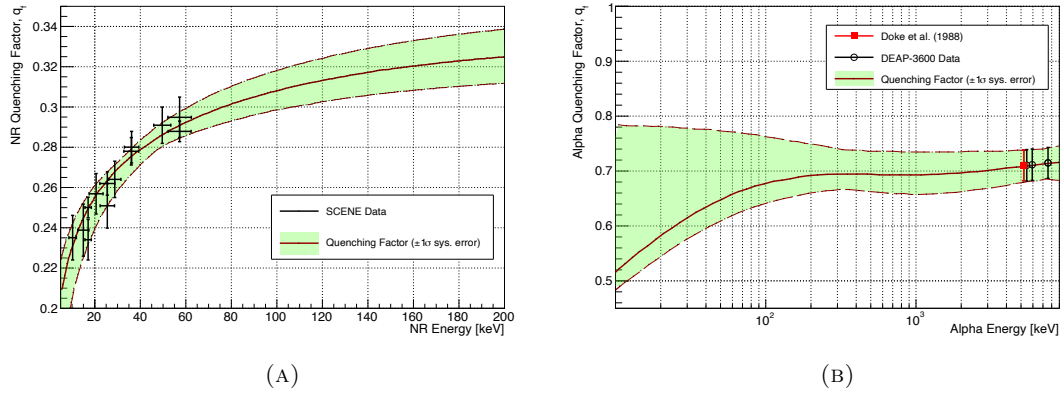
FIGURE 4.11: (A) Quenching factor vs. recoil energy for NR events scattering off ^{40}Ar with data from Ref [108]. (B) Quenching factor vs. recoil energy for α particles determined in Ref [137] based off of measurement from Ref [136].

4.3.2 Optical Systematics

LAr Refractive Index

Recall from Section 2.2.3 that the quantities that govern photon transport through the LAr are the Rayleigh scattering length (Equation 2.20) and the photon group velocity (Equation 2.21), and that both of these quantities are correlated by their mutual dependence on the LAr refractive index. This fact is used to constrain the DEAP-3600 LAr optical model parameters based on measurements of the LAr refractive index vs. wavelength. These measurements are those done by Sinnock and Smith [138] and Babicz et al. [139], which are shown in Figure 4.12.
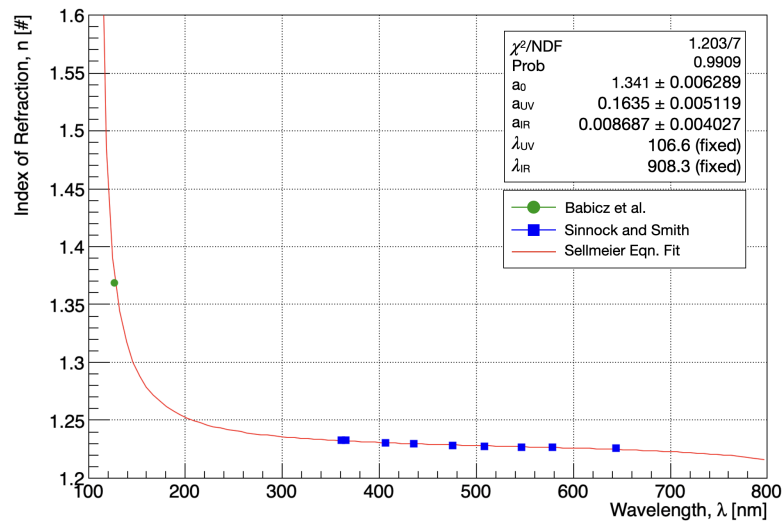
FIGURE 4.12: Fit of the Sellmeier Equation (2.23) to data from Sinnock and Smith [138] (blue squares) and Babicz et al. [139] (green circles).

The LAr optical parameters used in DEAP-3600 are based on the fit shown in Figure 4.12 [140], and are summarized in Table 4.4. These values are for a LAr temperature of 86 ± 2 K and for a LAr scintillation wavelength of $\lambda = 127 \pm 0.2$ nm. For the Sellmeier equation fit, $\lambda_{\mathrm{UV}} = 106.6$ nm and $\lambda_{\mathrm{IR}} = 908.3$ nm are fixed parameters, which is similar to the treatment in Ref [96].

Parameter	Nominal	$\pm 1\sigma$ Sys. Error
Refractive Index [#]	1.369	0.005
Rayleigh Scattering Length [cm]	92.0	6.0
Group Velocity [cm/ns]	13.33	0.27

TABLE 4.4: DEAP-3600 optical model parameters based on a fit of the Sellmeier equation to data from Sinnock and Smith [138] and Babicz et al. [139]. Anlysis of the fit in question was performed in Ref [140].

TPB Scattering Length

The photon scattering length for the tetraphenyl butadiene (TPB) wavelength shifter adopted in the DEAP-3600 optical model is $2.25^{+2.25}_{-1.13}\,\mu$m. This estimate is consistent with a measurement of the TPB scattering length of 440 nm photons in Ref [141], which reports $2.75^{+0.25}_{-0.75}\,\mu$m. The measurement involved recording the intensity of re-emitted photons from TPB into a solid angle of $\mathcal{O}(10^{-3})$ str as a function of TPB thickness, which was varied from 50–1000 nm. A UV lamp outputting photons of wavelength $\lambda = 254$ nm was used to stimulate the TPB fluorescence. The observed re-emission intensity vs TPB thickness data was compared to GEANT4 simulations of their setup, in which a mean free path parameter for the 420 nm re-emitted photons was varied. Simulated data with a mean free path parameter set between 2–3 μm had a χ^2 per degree of freedom of 1.46–1.58 in comparison to observations [141].

4.3.3 Instrumentation Systematics

Relative PMT Efficiency

As it is implemented in the PLR analysis, the 'PMT efficiency' is actually a consolidation of several effects into one systematic parameter. They are:

(i) PMT quantum efficiency at 420 nm

(ii) Light guide collection efficiency

(iii) Optical transmission of photons through light guides

(iv) Drift in PMT gain

(v) Drift in the gain of the signal conditioning boards (SCBs)

Items (i)–(iii) are examples of systematic effects which can vary between PMTs, but are otherwise assumed to be constants in time. Together they amount to a photon detection efficiency for each PMT. Items (iv) and (v) affect the probability of a detected photon not being recorded because of the zero length encoding (ZLE) function in the digitizers. These effects are time dependent, however, they are also inseparable from the time dependence in light yield (see Section 4.3.1). Since the variations in light yield over time are divided out in the PLR analysis when using Equation 4.62, items (iv) and (v) can also be treated as constants in time with statistical variations between PMTs.

There is no exact value for the PMT efficiency, as it is described here. Rather it is left as an emergent property in MC simulations for each PMT, where the light guide acrylic has a nominal attenuation length of 6.2 ± 0.6 m (see Section 2.2.1) and the Hamamatsu R5912-HQE PMTs have nominal properties listed in Table 2.3.[2] Systematic variations of the PMT efficiency are accounted for with a global scaling factor which shifts the PMT efficiencies of all PMTs in the detector by $\pm4.5\%$. This scaling variation was determined by comparison of relative PMT efficiencies measured using detector monitoring systems, like the AARFs described in Section 2.2.2, and similar measurements using ^{39}Ar data. These independently measured relative PMT efficiency measurements were in agreement to within 4.5% on average.

PMT Afterpulsing

As discussed in Section 3.1.2, correlated noise in PMTs, called afterpulsing (AP), was measured in ^{39}Ar scintillation events in Ref [104] using Equation 3.6 as the AP model. The nominal values for AP probabilities are summarized in Table 3.1. The systematic

---

[2]In other words, there is no variable in the GEANT4 DEAP-3600 detector model where an overall 'PMT efficiency' can be set to a known nominal value. The PMT efficiency as it is described here emerges from the known detector physics, such as the geometry, light guide attenuation length, PMT quantum efficiency and gain, etc.

uncertainty on the AP probabilities was assessed via MC simulations of ^{39}Ar β scintillation pulse shapes, like the one shown in Figure 3.5. Pulse shapes were simulated with the following random variations:

(i) TPB re-emission time constants randomly sampled from a Gaussian of mean 3550 ns and standard deviation of 1000 ns, per Ref[142][3]

(ii) Dark noise counts sampled from a Poisson distribution with a mean of 2×10^{-4} (assuming ~ 1 kHz dark noise rate and a pre-event window of 160 ns)

(iii) The number of prompt scintillation photons sampled from a Poisson distribution with the mean of $(220 \text{ keV})(6.1 \text{ PE/keV})(0.3) = 400 \text{ PE}$ (product of the mean ^{39}Ar β energy, measured light yield, and mean `Fprompt` of ER events in LAr scintillation)

For each PMT the pulse shape was simulated 1000 times with random variations outlined in items (i)–(iii). For each simulated pulse shape, the fit described in Section 3.1.2 and Ref[104] was performed with the lower and upper fit boundaries sampled from uniform distributions ranging from 500–1000 ns and 3000–4000 ns, respectively. The resulting AP probabilities were then stored in histograms like that in Figure 4.13a. The means and standard deviations of these histograms were then plotted against PMT ID number as in Figure 4.13b. Note in Figure 4.13b, the mean values are offset by the predicted AP probability of 0.068. The observed AP probabilities and standard deviations are approximately constant ($\lesssim 1\%$ AP probability variation) in all PMTs. The relative systematic uncertainty of the AP probability obtained using the fit methodology is taken to be the mean standard deviation divided by the prediction, i.e. $\delta_{\text{AP}} = 0.01/0.068 \approx \pm 15\%$.

---

[3]This reference characterizes four time constants for TPB re-emission, which are from the Short, Intermediate, Long, and Spurious components of TPB fluorescence. The short, intermediate, and spurious components are not relevant for the AP systematic uncertainty analysis because they are too short lived; i.e. $\lesssim 300$ ns. Therefore the long component, with a time constant of 3550 ns is the only one considered here.
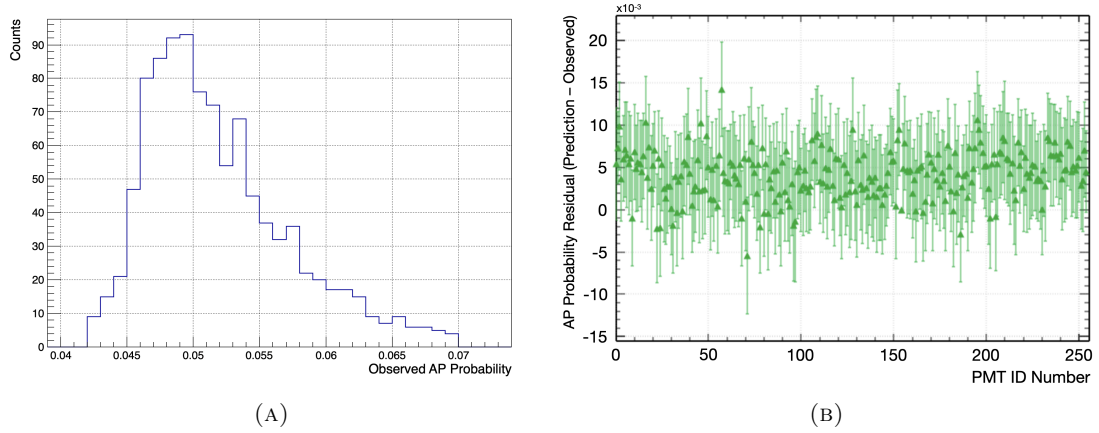
FIGURE 4.13: (A) Distribution of the observed AP probabilities from the pulse shape fits of simulated ^{39}Ar β event pulses. (B) Measurement of the AP probability residuals (where the predicted AP probability is 6.8%) for each PMT in DEAP-3600 after 1000 MC simulations.

4.4 Event Selection Criteria and Background Predictions

The event selection criteria for the DEAP-3600 PLR WIMP search are provided in Table 4.5. This set of criteria is similar to that of the cut-and-count analysis described in Ref [59], but with the omission of the cuts $\text{T}_0^{\text{GAr}} \geq 2$ and `Rrec` $< 630\,\text{mm}$.

Variable	Acceptance Range	Defined In
calcut	!(calcut & 0x31f8)	Cut 3.31
dtmTrigSrc	!(dtmTrigSrc & 0x82)	Cut 3.32
eventTime	(2250, 2700) ns	Cut 3.33
subeventN	≤ 1	Cut 3.34
numEarlyPulses	≤ 3	Cut 3.35
deltat	$(20000, \infty)$ ns	Cut 3.36
fmaxpe	≤ 0.4	Cut 3.37
neckVetoN	< 1	Cut 3.39
CFT2R	≤ 0.04	Cut 3.42
CFB3R	≤ 0.1	Cut 3.43
CZ(PromptPE)	See Fig 3.15	Cut 3.40
CR(PromptPE)	See Fig 3.15	Cut 3.41
MBLikelihoodZ	$\leq 550\,\text{mm}$	Cut 3.45
ROI	See Fig. 4.14a	—
Rrec	See Fig. 4.14b	—

TABLE 4.5: Selection criteria for accepting data in the PLR WIMP search.

The fiducial volume (FV) radius and ROI contour in the PE-`Fprompt` plane were both expanded for the PLR WIMP search compared to the cut-and-count analysis, as shown in Figure 4.14. The upper boundary in `Fprompt` of the PLR ROI was drawn to limit the NR acceptance loss to 10%. The reason why the upper boundary does not go up

to `Fprompt = 1` is because Čerenkov backgrounds become prevalent at `Fprompt` $\gtrsim 0.8$ and a Čerenkov background model is not included in the PLR likelihood function of Equation 4.29. The FV radius for the PLR WIMP search was expanded from 630 mm in Ref [59] to 720 mm, which increases the fiducial target mass by $\sim 50\%$.
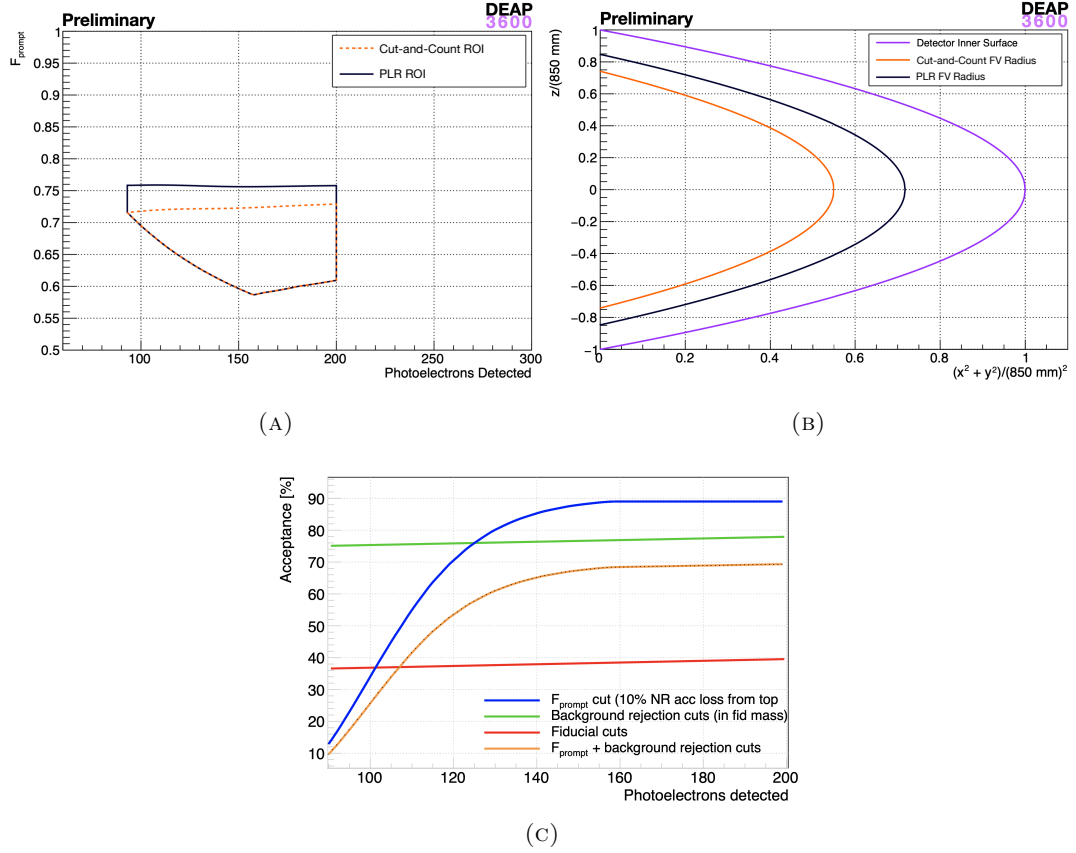
FIGURE 4.14: (A) ROI and (B) FV radius of the DEAP-3600 PLR WIMP search compared with the ROI and FV radius of the cut-and-count analysis in Ref [59]. (C) NR acceptance in the DEAP-3600 PLR WIMP search broken down by types of event selection criteria.

Combining the selection criteria in Table 4.5; the MC data sets used to create the background models; and the trigger rates and neutron yields given in Table 4.1 and Figure 4.8, a prediction of the number of events from each background in the PLR ROI can be computed. This is done by taking the product of the total live-time[4] of the exposure, the trigger rate of the background, and the acceptance fraction of that background given the event selection in Table 4.5:

$$N_{\exp} = T_{\text{Live}} \cdot \sum_{n=1}^{N_{\text{Bkgs.}}} \int_{90}^{200} \frac{d}{dq} R_n(q) \cdot F_n(q) dq,$$

---

[4]This refers to the aggregate time that the detector was recording data

where T_{Live} is the live-time, $\frac{d}{dq}R_n(q)$ is the differential trigger rate versus `nSCBayes` of the nth background, and $F_n(q)$ is its acceptance fraction versus `nSCBayes`. The NR acceptance fraction used for WIMPs (shown in Figure 4.14c) was calculated in the same manner as in Ref [59]; based on comparison with Figure 3.17, the overall improvement in WIMP acceptance for the PLR analysis over cut-and-count (inclusive of `Fprompt`, background rejection, and fiducial cuts) is by a factor of approximately four.

The acceptance fraction for each background was assessed using their respective MC data sets. The predicted background event rates in the PLR ROI are summarized in Table 4.6.

Background	Predicted Events	Uncertainty
^{39}Ar β decays	0.18	$\pm$ 0.01
Neck α decays	5.9	± 2.7
Surface α decays	0.001	$\pm$ 0.001
Dust α decays	5.2	± 5.2
Radiogenic Neutrons	1.1	$\pm$ 0.9
Total	12.4	± 5.9 (syst.)

TABLE 4.6: Summary of the number of predicted number of ROI events in the 3.5 tonne-year exposure from each background source included in the DEAP-3600 PLR likelihood model, after applying all event selection criteria in Table 4.5.

4.5 Model Validation

To validate the implementation of the likelihood model described in Section 4.2, a comparison of the background model prediction and the MC data sets is shown in Figure 4.15. Each sub-figure shows the marginalization of the model and MC data sets over all but one of the dimensions listed in Equation 4.28; i.e. a projection onto either the `nSCBayes` (Figure 4.15a), `Fprompt` (Figure 4.15b), or `Rrec` 'axis.' The marginalization was done with the event selection criteria in Table 4.5, and the following acceptance region:

- $90 \leq$ `nSCBayes` ≤ 550 PE

- $0.575 \leq$ `Fprompt` ≤ 0.8

- $0 \leq$ `Rrec` ≤ 800 mm

- $0 \leq$ `T`$_0^{\text{GAr}}$ $< \infty$

These extensions were made so that the validation could include more background domi-nated regions, thus allowing contributions of all backgrounds to be more noticeable than if the test was limited to the ROI. Note that this test was not done with $\mathtt{T}_0^{\mathtt{GAr}}$ because the likelihood model uses the MC histograms in this space for all backgrounds rather than an empirical fit function. Also note that $^{39}\mathrm{Ar}$ is omitted from this test because this background model is entirely data driven.

(A)

(B)

(C)
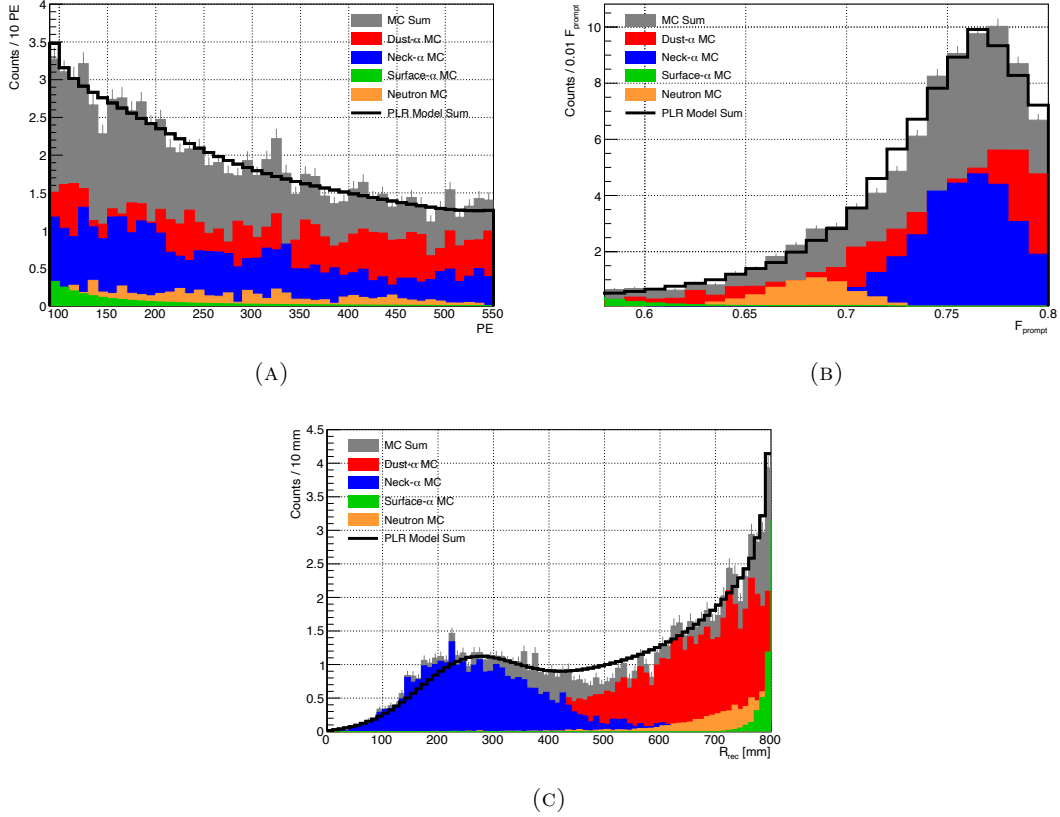
FIGURE 4.15: Validation of the DEAP-3600 likelihood model by comparison with MC data sets. (A) is the marginalization over all but `nSCBayes`, (B) is the marginalization over all but `Fprompt`, and (C) is the marginalization over all but `Rrec`.

Recall from Section 4.1.2 that the asymptotic approximation allows the PLR analysis to circumvent the need to generate a sample of pseudo-experiments in order to assess the p-value for a cross-section hypothesis. To demonstrate that the asymptotic approx-imation holds given the model constructed and the number of observed events in the ROI, the analysis was carried out for a test WIMP hypothesis of $m_\chi = 100\,\mathrm{GeV}$ and the interaction cross-section $\sigma_\chi = 10^{-45}\,\mathrm{cm}^2$. 1250 pseudo-experiments were run to gener-ate the distribution $g(q_\nu | \nu)$ of the test statistic q_ν defined in Equation 4.8. Figure 4.16

shows that the distribution of q_ν from the pseudo-experiments is described by the half-χ^2 distribution (Equation 4.14) with a χ^2 per degree of freedom of $60.71/61 \approx 0.9952$. This result justified the use of the asymptotic approximation in lieu of generating $\sim 10^3$ pseudo-experiments per signal hypothesis.
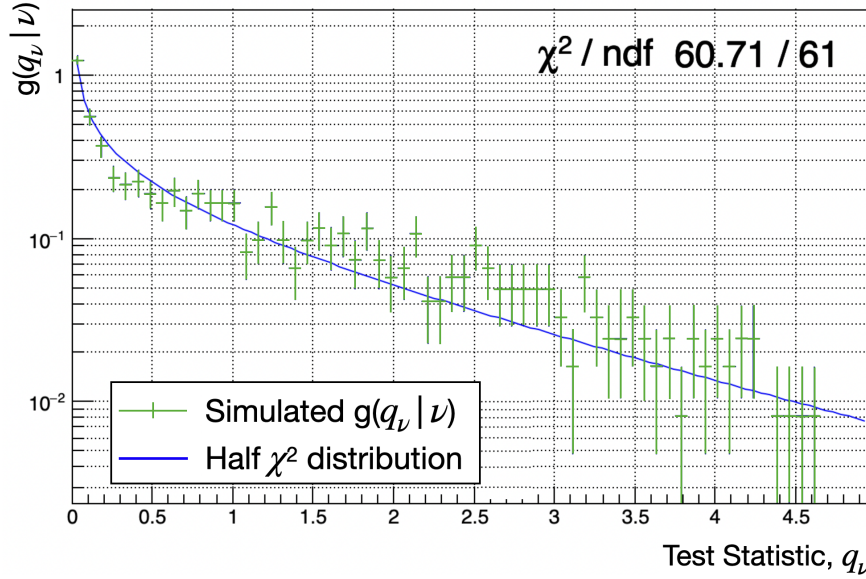
FIGURE 4.16: Distribution of $g(q_\nu|\nu)$ as obtained from fitting 1250 pseudo-experiments in the PLR analysis, with a signal model of $[m_\chi = 100 \text{ GeV}/c^2, \sigma_\chi = 10^{-45} \text{ cm}^2]$. The half chi-square distribution given by the asymptotic approximation (Equation 4.14) is overlaid.

4.6 Results

4.6.1 3.5 Tonne-Year Exposure

Over an observation period of roughly 3 calendar years, DEAP-3600 has collected a total of 879.79 days worth of WIMP search data. 47.1% of the data set was left open for this analysis, and the remaining 52.9% was blinded for future analysis. Approximately 7–8% of total live-time is lost to data cleaning and event pileup cuts, which results in a total live-time of 388.24 days. The LAr target mass in the detector throughout this time was 3269 ± 24 kg, giving an exposure of 3.5 tonne-years. After applying event selection criteria and correcting the data to account for the drift in light yield as prescribed in Section 4.3.1, 23 events remain inside ROI defined for the PLR WIMP search. The distribution of these events inside the ROI is shown in Figure 4.17. Also shown in

Figure 4.17 is the nominal background-only model prediction within the ROI, integrated from 0–720 mm in `Rrec` and summed over all `T₀ᴳᴬʳ`. For a given WIMP mass, these events were fit to the signal+background model presented in Section 4.2 using the PLR method described in Section 4.1, assuming signal hypotheses with a range of cross-sections. Based on the results of these fits, the observed 90% CL upper limit was determined using asymptotic approximation.
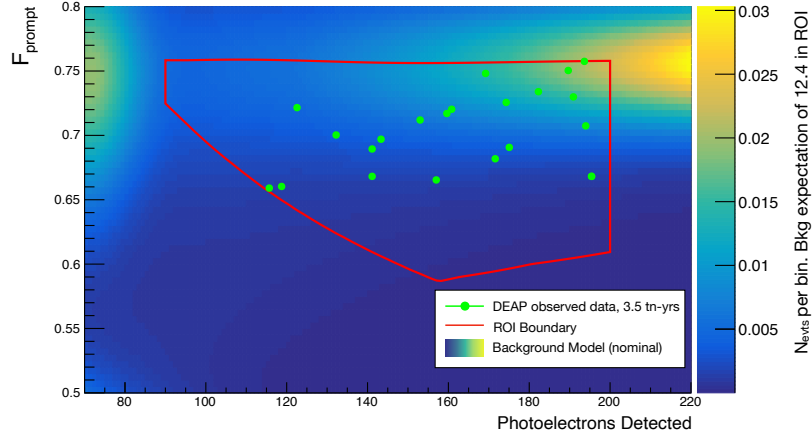
FIGURE 4.17: ROI used for the PLR analysis in `nSCBayes-Fprompt` space. There are 23 surviving events in the full three-year open data set inside this ROI. These data are what were fit in the PLR framework. The data are overlaid on the predicted background model in the `nSCBayes-Fprompt` space integrated from 0–720 mm in `Rrec` and summed over all `T₀ᴳᴬʳ`. The background model peaks along the high `Fprompt` boundary because of the neck and dust α backgrounds.

The posterior normalizations for the background-only case are given in Table 4.7 and the posterior nuisance parameters are given in Table 4.8. In the signal+background unconditional maximum likelihood fit, the signal normalization converges to a negative value and is therefore consistent with zero. Consequently, the final results come from the background-only case. The ^{39}Ar β and ^{210}Po surface α background component normalizations were fixed in the background-only fit. In the case of ^{39}Ar, this model is entirely data driven, and is well constrained by calibration data (see Section 3.1.3). Surface α decays contribute negligibly to the expected background rate in the ROI, and are therefore a subdominant effect in this analysis. The Dust α normalization increases by 1.98σ, or a factor of 2.98 from the nominal case, whereas the radiogenic neutrons and neck α backgrounds converge to posterior values within 1σ of their priors. The overall posterior background normalization was found to be $22.0^{+3.7}_{-13.2}$(syst.)± 4.5(stat.), which is in agreement with the 23 observed events. The large negative systematic uncertainty is driven primarily by the dust α normalization uncertainty.

Figures 4.18a, 4.18b, and 4.18c show the prior and posterior background-only model compared to the observed data, projected onto the `nSCBayes`, `Fprompt`, and `Rrec` dimensions, respectively. These plots demonstrate that the posterior background distribution shapes are also in agreement with the observed data.

Source	Prior	Posterior (bkg-only)
^{39}Ar β	0.18 ± 0.01	0.18 ± 0.01
Radiogenic n	1.1 ± 0.9	1.0 ± 0.9
Surface α	$10^{-3} \pm 10^{-3}$	$10^{-3} \pm 10^{-3}$
Neck α	5.9 ± 2.7	5.3 ± 2.2
Dust α	5.2 ± 5.2	$15.5 \, ^{+2.8}_{-13.0}$
Total Bkg	12.4 ± 5.9 (syst.) ± 3.5 (stat.)	$22.0 \, ^{+3.7}_{-13.2}$ (syst.) ± 4.5 (stat.)
$m_\chi = 100$ GeV/c^2, $\sigma_\chi = 10^{-45}$ cm^2	4.5 ± 0.5 (syst.) $^{+3.2}_{-2.0}$ (stat.)	$-$

TABLE 4.7: Summary table of the expected number of ROI events from each background source in the prior background model, and the posterior model in the background-only hypothesis. Also given are the expected number of WIMP signal events at the same benchmark mass value and $\sigma_\chi = 10^{-45}$ cm^2. In the data, 23 events are observed in the ROI.

Nuisance Parameter	Prior	Posterior (bkg-only)
Mean Light Yield [PE/keV]	6.1 ± 0.4	6.081 ± 0.001
NR Quenching Factor	nom.$+(0 \pm 1)\sigma$	nom.$+(0.001 \pm 0.98)\sigma$
α Quenching Factor	nom.$+(0 \pm 1)\sigma$	nom.$+(-1.24 \pm 0.76)\sigma$
LAr Refractive Index	1.369 ± 0.005	1.368 ± 0.006
TPB Scattering Length [μm]	$2.25^{+2.25}_{-1.13}$	2.19 ± 0.97
PMT Afterpulsing Probability	$(6.8 \pm 1)\%$	$(6.801 \pm 0.98)\%$
Relative PMT Efficiency	nom.$+(0 \pm 4.5)\%$	nom.$+(-1.48 \pm 4.4)\%$
Dust TPB Coverage Fraction	$(50 \pm 50)\%$	$(100 \pm 94)\%$

TABLE 4.8: Summary table of nuisance parameters and systematic uncertainties in the prior model, and the posterior model in the background-only hypothesis.

It is also important to determine the expected median sensitivity of the experiment, with its $\pm 1\sigma$ and 2σ contours, and show this alongside the observed upper limit. The median sensitivity provides a sanity check on the observed limit from the data, which is necessary for making the decision to apply a power constraint. The expected median sensitivity is determined for a given WIMP mass by simulating an ensemble of pseudo-experiments with zero signal; i.e. background-only. The number of events from each background in a given simulated data set is randomly generated from a Poisson

(A)

(B)

(C)
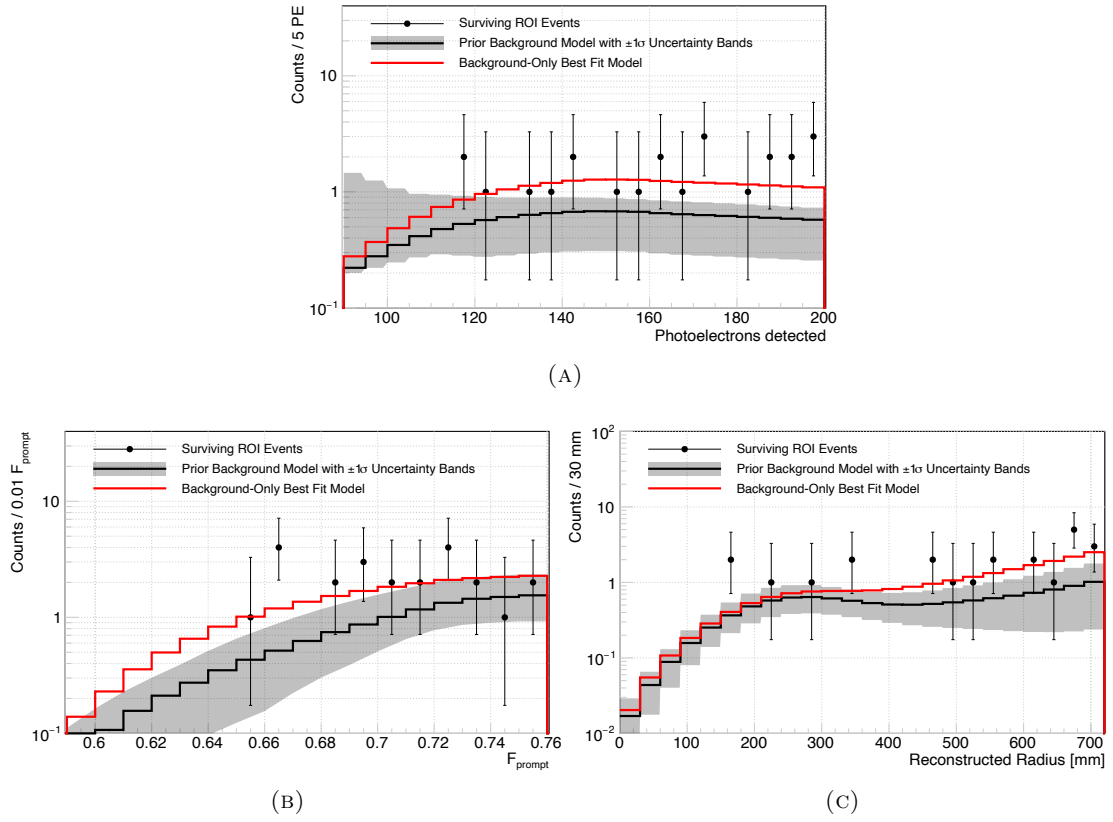
FIGURE 4.18: Projected distributions in `nSCBayes` (A), `Fprompt` (B) and `Rrec` (C) of the observed data, the prior background model with $\pm 1\sigma$ systematic uncertainties, and the best-fit background-only model. Error bars shown on the data points are the 68% confidence intervals around the bin contents using the Pearson χ^2 distribution. Images taken from Ref [124].

distribution with the mean equal its corresponding normalization in Table 4.6. Additionally, the values of each nuisance parameter are randomized according to their prior constraint terms summarized in Table 4.3. In this way, the systematic uncertainties are propagated into the median sensitivity and the $\pm 1\sigma, 2\sigma$ error bands. For each of these experiments, the 90% CL upper limit cross-section is determined using the asymptotic approximation. An histogram of the cross-section upper limits is then populated by the resulting cross-section upper limits from these pseudo-experiments. The cross-section which corresponds to a quantile of 0.5 is the median sensitivity at the given WIMP mass. The $\pm 1\sigma$ limits at that WIMP mass are the cross-sections which return quantiles of 0.16 and 0.84, and the $\pm 2\sigma$ limits correspond to quantiles of 0.025 and 0.975.

Figure 4.19 shows the distribution of upper-limit cross-sections for an ensemble of 500 pseudo-experiments for a 10 TeV WIMP mass, and the quantiles of the distribution. Figure 4.20 shows the final exclusion curves. The blue line corresponds to the observed

limit as determined from the fit to the 23 data events. The black dotted line corresponds to the expected median sensitivity as calculated from the method described above. The green and yellow error bands corresponds to the $\pm 1\sigma$ and $\pm 2\sigma$ bands, respectively, about the median sensitivity. For comparison, the red line corresponds to the WIMP-nucleon cross-section exclusion upper limit reported in Ref [59].
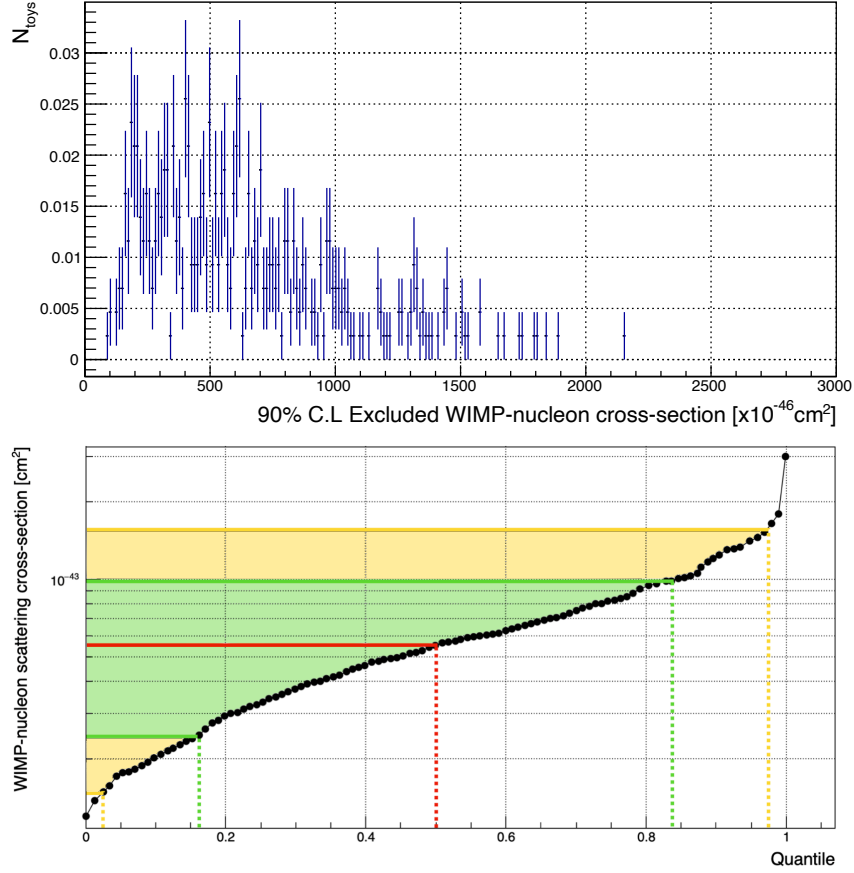
FIGURE 4.19: Top: Distribution of excluded WIMP-nucleon cross-sections $[\times 10^{-46}\,\mathrm{cm}^2]$ for a 10 TeV WIMP as determined from an ensemble of 500 toy experiments fitted with the PLR framework. Bottom: Quantiles of the distribution used to calculated the median sensitivity (red line), as well as the $\pm 1\sigma$ (green region) and $\pm 2\sigma$ (yellow region) bands for a 10 TeV WIMP mass.

4.6.2 Discussion

In the case of low WIMP masses, $m_\chi \lesssim 90\,\mathrm{GeV}$, the PCL (Equation 4.24) was applied, resulting in the reported cross-section upper limit from this analysis to conform to the -1σ bound of the median sensitivity curve. Recall from Section 4.1.3, that the PCL is a treatment of the PLR method that accounts for a lack of separation between the signal+background and background-only hypotheses. This situation can be realized in
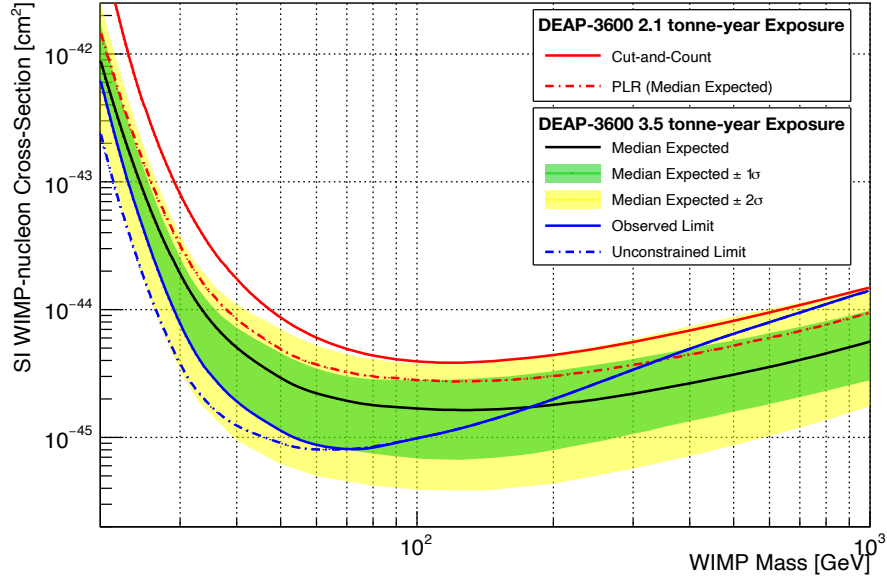
FIGURE 4.20: Observed 90% CL upper limit on the WIMP-nucleon spin-independent (SI) cross-section as a function of WIMP mass for the 3.5 tonne-year exposure, with power constraint (solid blue) and unconstrained (dashed blue). Also shown for the 3.5 tonne-year exposure are the median expected limit (black line) with $\pm 1\sigma$ and $\pm 2\sigma$ quantile bands (green and yellow respectively). For comparison, the median expected limit using the PLR approach for an exposure of 2.1 tonne-years (dashed red), and the previous observed result from DEAP with a 2.1 tonne-year exposure (solid red) [59] are also provided.

the case where there is a statistical downward fluctuation in observed data compared to the model predictions. Consider Figure 4.21, which shows the observed 23 data points in the ROI overlaid on the signal-only model of a 20 GeV WIMP (Figure 4.21a) and 10 TeV (Figure 4.21b). For the 10 TeV WIMP case, there are several data points which can be used to constrain signal model strength (i.e. the WIMP-nucleon scattering cross-section) in the unconditional fit of the DEAP-3600 likelihood model to the data. However in the case of the 20 GeV WIMP, there is virtually no data to constrain the scattering cross-section in the fit. Therefore if background rate prediction in the region of $90 \le$ `nSCBayes` ≤ 110 is greater than zero, and there are zero observed events in this region, then there is no way for the PLR analysis to separate signal+background and background-only hypotheses. The conditional fit will then converge towards lower bound in background normalizations and a minimal WIMP-nucleon scattering cross-section, resulting in artificially high sensitivity. Therefore the PCL regularizes the results of this analysis due to the reduced sensitivity at low WIMP masses. This behaviour was seen almost identically by LZ, which also applied a PCL in Ref [61].
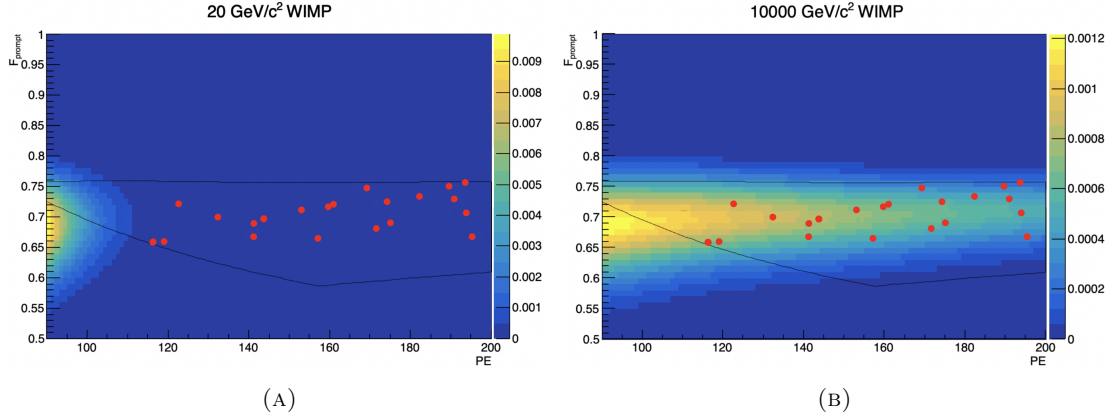
FIGURE 4.21: WIMP signal model in `nSCBayes-Fprompt` space for two WIMP masses, 20 GeV (A) and 10 TeV (B), both shown with the 23 observed data points overlaid.

With power constraints applied, the DEAP-3600 PLR WIMP search is sets an upper limit on the spin-independent (SI) WIMP-nucleon elastic scattering cross-section of $9.8 \times 10^{-46}\,\mathrm{cm}^2$ ($1.4 \times 10^{-44}\,\mathrm{cm}^2$) for WIMPs with mass of 100 GeV (1 TeV). This is approximately $4\times$ better than the previous best WIMP sensitivity among experiments using a LAr target, set by DEAP-3600 in the 2.1 tonne-year cut-and-count analysis, which was $3.9 \times 10^{-45}\,\mathrm{cm}^2$ for 100 GeV WIMPs [59]. The best sensitivity occurs for WIMPs at a mass of 72.9 GeV, where the cross-section upper limit is $8.1 \times 10^{-46}\,\mathrm{cm}^2$.

Note that at WIMP masses greater than 178.2 GeV, the observed limit begins to increase above the median expected limit. This is due to the fact that an excess of backgrounds above the nominal background prediction was observed. At the time of writing, the origin of the discrepancy between the background model and the observed data is not known conclusively. Based on comparison of the data with individual background distributions, the likeliest explanation is an underestimation of the dust α background contribution, however investigation into this matter is still ongoing.

Also provided in Figure 4.20 are the median expected sensitivities for both the 3.5 tonne-year (black line) and the 2.1 tonne-year (dashed red line) exposures using the PLR analysis method, as well as the observed limit in Ref [59] (solid red line) which uses cut-and-count approach. The dashed red line shows that, for the same exposure, the PLR analysis performs 36.02% better than cut-and-count on average. This is a direct consequence of relaxing event selection criteria, thereby increasing the WIMP acceptance and the fiducial target mass. The solid black line then shows that, when using the PLR

analysis, the expected improvement that can be attributed solely to the increase in exposure is an additional 40.47%.

DEAP-3600 has finished collecting a larger blinded data set spanning 813 live-days, for a total exposure of 7.3 tonne-years. Unblinding and analysis of this data set is expected to proceed while hardware upgrades take place, which are aimed at fixing the neck seal failure described in Section 2.2. These upgrades will allow for the entire AV to be filled with LAr as originally designed. This will enable DEAP-3600 to use the neck veto system more efficiently to target neck events, as well as enable the LAr circulation systems to purify the LAr, which will mitigate the presence of dust. However, pushing further into untested WIMP parameter space with higher discovery potential (see Figure 1.12) is the aim of future experiments, such as DarkSide-20k. This is discussed more in Chapter 5.

Chapter 5

Photosensors for Next-Generation Astroparticle Physics Detectors

The analyses in Chapter 4, as well as those in Refs [61, 143], did not observe sufficiently large WIMP signals to warrant claiming a discovery of new physics. In order to improve the likelihood of making a discovery, or exclude more of the WIMP parameter space, next-generation astroparticle detectors are being designed with larger targets and various technological advances to reduce backgrounds, and improve energy resolution and position reconstruction capabilities. An example of a technological advancement, which will be the focus of this chapter, is the use of Silicon Photomultipliers (SiPMs) over PMTs as the primary photosensing hardware for noble liquid scintillation experiments. A full description of silicon-based photon detectors will be given in Section 5.1. The basic properties of SiPMs, with two specific examples from the Hamamatsu Photonics K.K. and Fondazione Bruno Kessler manufacturers, will also be discussed in Section 5.1. Following this, Section 5.2 describes the major systematics associated with using SiPMs. Lastly, Sections 5.3, 5.4, and 5.5 briefly discuss the nEXO, DUNE, and DarkSide-20k experiments, all of which are being built with SiPMs as their light detector of choice.

5.1 Silicon Based Photo-Sensors

PMTs have been in use since the mid 1930s, and have become a well-established form of technology for physics experiments. However, there are characteristics of PMTs that

can be improved upon for low background astroparticle physics experiments. In the case of DEAP-3600, there are the following examples.

(i) **Radiopurity**:

As previously stated in Section 2.3.3, the borosilicate glass of PMTs is a large source of radiogenic neutrons from (α, n) reactions, which ultimately limit the size of the fiducial volume in DEAP-3600.

(ii) **Physical Size**:

The R5912-HQE PMTs used in DEAP-3600 have a photocathode diameter of 8 inches (20.2 cm). Figure 2.2 shows the angular position and size of the PMTs projected onto the detector inner surface via the light guides. Arranged as they are, the 255 signal PMTs only cover 81.3% of the inner detector surface, which leaves 19.7% of the surface unable to transport scintillation photons towards the PMTs.

(iii) **Single Photoelectron Resolution**:

A typical PMT low charge distribution, for example in Figure 3.3, has a measurable single photoelectron (PE) peak, which is heavily overlapping with higher PE features. Reducing this overlap would improve energy resolution, which is a systematic effect that drives, e.g. leakage of background events into the energy region of interest (ROI) from just outside the ROI, or surface event leakage into the fiducial volume for low PE background events.

(iv) **High voltage**:

PMTs require voltages of order $\mathcal{O}(\mathrm{kV})$, which is a significant source of heat for a cryogenic experiment like DEAP-3600, and requires cabling that is an additional source of radiogenic backgrounds at the level of mBq/kg [84].

(v) **Quantum Efficiency**:

The quantum efficiency (QE) of PMTs is typically significantly reduced at cryogenic temperatures.

SiPMs have emerged as compelling photo-sensor candidates for next-generation experiments in astroparticle physics and high energy physics. Relative to PMTs, SiPMs provide significant improvements in all five of these categories. Radio-assays of SiPMs done

in Ref [144] show that specific activities of ^{238}U, ^{40}K, and ^{232}Th are all $\lesssim 10^{-1}$ mBq/kg, which is much lower than the $\mathcal{O}(10^2)$ mBq/kg observed in the R5912-HQE PMTs used in DEAP. SiPMs typically have dimensions of 3–6 millimetres and are square in shape, which means each unit occupies a much smaller footprint than a single PMT, and can tile a plane more efficiently than a round PMT. Therefore, SiPMs offer greater coverage of the inner detector surface than PMTs. The SiPM low-light distribution in Figure 5.1 shows the greatly improved charge resolution of SiPMs, where single- and multi-PE peaks are well defined up to at least 5 PE. As will be discussed in Sections 5.1.2 and 5.1.3, SiPMs require supply voltages on the order of 50 V, and lastly, they can have photon detection efficiencies for 128 nm photons as high as 15% [145, 146]. At 420 nm, which is relevant for detectors like DUNE and DarkSide-20k that use TPB, SiPMs can have photon detection efficiencies varying between 25–45% [147]. For these reasons, SiPMs are the baseline solution in the DUNE experiment [148], aiming at precise neutrino oscillation measurements, the DarkSide-20k experiment searching for dark matter [62, 149], and the nEXO neutrinoless double-beta decay search experiment [150].
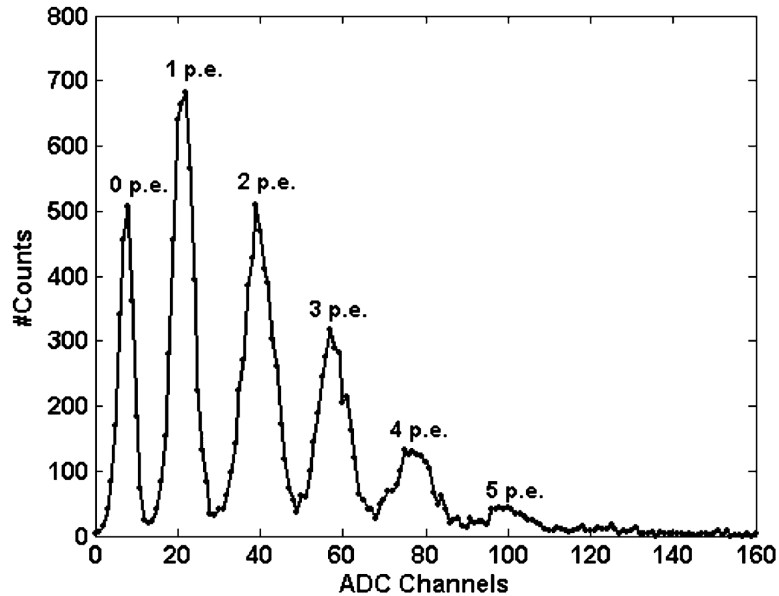
FIGURE 5.1: Low light distribution of a SiPM, with single- and multi-PE peaks labeled. Image taken from Ref [151].

This section explains the operational mechanisms of SiPMs by building upon those of similar silicon-based photo sensors, starting with avalanche photodiodes (APDs) in Section 5.1.1 and single photon avalanche diodes (SPADs) in Section 5.1.2. This is followed by Section 5.1.3, which explains how these components are put together to form a SiPM.

5.1.1 Avalanche Photodiodes

APDs and SPADs (and ultimately SiPMs) detect photons in two steps

(i) Conversion of photons into charge carriers in the silicon via the photoelectric effect

(ii) Multiplication of the charge carriers through a process called *avalanche breakdown*

For step (i), the photon must have sufficient energy to promote an electron in the valence band of the silicon crystal lattice to the conduction band. In the band structure of pure silicon, the energy gap between the valence and conduction bands (i.e. the *band-gap*) is 1.12 eV [152], which corresponds to a maximum photon wavelength of $\sim$ 1100 nm. However, silicon semiconductors used in diodes are doped with either positively or negatively charged impurities—i.e. P-type or N-type semiconductors, respectively— which reduce the band-gap relative to pure silicon (depending on the concentration of the dopants). In typical silicon semiconductors, the dopant concentration is between 10^{13}–10^{18} cm^{-3}, which can narrow the band-gap by roughly 50 meV [153]. This can increase the spectral sensitivity range in silicon-based sensors to as high as 1150 nm. Once a photon promotes an electron to the conduction band, it leaves behind a hole in the valence band, which responds to an external electric field like a positive charge carrier with electric charge $q_e = 1.602 \times 10^{-19}$ C.

Like all diodes, APDs comprise a P-type semiconductor bonded to an N-type, resulting in a P-N junction. In the vicinity of the junction, the excess of electrons in the N-type fill the excess of holes in the P-type, forming an electrically neutral 'depletion zone.' Once the depletion zone is sufficiently wide, it becomes a potential barrier that stops the flow of more electrical current, unless an external electric field—i.e. a bias voltage—is applied across the P-N junction. Figure 5.2 shows a cartoon representation of a typical I-V curve for a silicon P-N junction. The forward and reverse bias regimes describe the ordinary function of electrical diodes, where current is only allowed to flow when a forward bias is applied. A sufficiently large forward bias (typically 0.7 V) generates an electric field directed from P-type to N-type, which narrows the depletion zone enough for current to flow, and the diode acts like a conductor. A reverse bias does the opposite, resulting in the diode acting like an insulator. However, when a sufficiently large reverse bias voltage is applied across the P-N junction, it stops behaving like an

electrical insulator and instead a large current is produced. This regime is referred to as avalanche breakdown. In this regime, a single charge carrier in the depletion zone will gain sufficient kinetic energy from the external electric field to generate secondary electron-hole pairs via impact ionization. Similar to the avalanche process in PMTs (see Section 2.2.3), this process repeats for each charge carrier in the depletion zone, creating an exponentially growing charge avalanche, resulting in a large current.
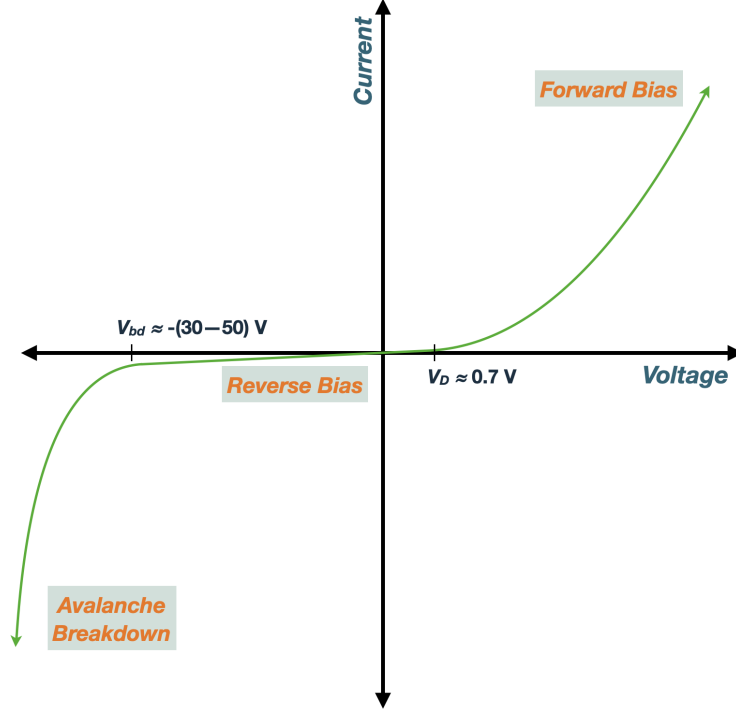
FIGURE 5.2: Cartoon diagram of a typical diode I-V curve with the voltage regimes of forward bias, reverse bias, and avalanche breakdown labeled. V_D is the typical diode "turn-on" voltage, which is typically around $0.7\,\mathrm{V}$ for silicon, and V_{bd} is the "breakdown voltage," beyond which the P-N junction will be in avalanche breakdown.

A photodiode is a silicon P-N junction with an applied reverse bias voltage[1] of $\sim 10\,\mathrm{V}$, which is well below the point of avalanche breakdown. Under these conditions, current passing through the P-N junction would be $\lesssim \mathcal{O}(\mathrm{nA})$. However, if a light source irradiates the depletion zone, the incident photons can generate electron-hole pairs via the photoelectric effect, which results in a current through the photodiode proportional to the light source intensity. The electrons moving through the depletion zone are unable to generate more charge carriers, so the charge gain is of order unity and therefore photodiodes are insensitive to single photons.

---

[1]Note that reverse bias voltage is defined as the negative of supply voltage, so that it can be reported as a positive value.

APDs operate on a similar premise as photodiodes, only with the applied reverse bias voltage at or near the voltage where the avalanche breakdown regime begins: i.e. the *breakdown voltage*, V_{bd}. At the breakdown voltage, a single photon can create an electron-hole pair which initiates an avalanche, as described above. APDs are manufactured to have breakdown voltages on the order of $100\,\text{V}$. A higher breakdown voltage for APDs translates into higher gain. Typical APDs have gains of ~ 100–1000, making them more applicable in low light applications than ordinary photodiodes.

In the voltage regime at or near breakdown, only the electrons reach sufficient kinetic energies to generate secondary charge carriers. The holes have a relatively larger effective mass than electrons in the silicon band structure, and therefore require larger electric fields to reach the same kinetic energy as electrons. Consequently, the avalanche ceases once all the electrons have cleared the depletion zone.

5.1.2 Single Photon Avalanche Diodes

A SPAD is an extension of the APD where the reverse bias voltage exceeds the breakdown voltage; where $V_{\text{bd}} \sim 30$–$50\,\text{V}$ in most cases [145]. In this regime, the holes gain enough kinetic energy to generate secondary electron-hole pairs in the depletion zone. So for each electron that clears the depletion zone, it will create a hole which will go the opposite direction and create another electron 'upstream' in the depletion zone, as depicted in Figure 5.3. When this process repeats itself, the current passing through the P-N junction continues growing indefinitely and diverges in a self-sustaining avalanche. The gain in this case is infinite and no distinction can be made between a single photon and several photons impinging on the SPAD. In other words, the output of a SPAD is binary: it's either conducting a current or it isn't. This is often referred to as operating an APD in *Geiger Mode*, and SPADs are also called Geiger Mode APDs (GM-APDs).

The probability of a photon being detected in a SPAD (and by extension, a SiPM) is called *Photon Detection Efficiency* (PDE), which is defined as [154]:

$$\text{PDE}(\lambda, V_{\text{ov}}) = \text{QE}(\lambda) \cdot P_{\text{Av}}(\lambda, V_{\text{ov}}) \cdot \text{FF} \qquad (5.1)$$

where $\text{QE}(\lambda)$ is the quantum efficiency of a photon with wavelength λ generating an electron-hole pair in the SPAD; $P_{\text{Av}}(\lambda, V_{\text{ov}})$ is the avalanche triggering probability as a
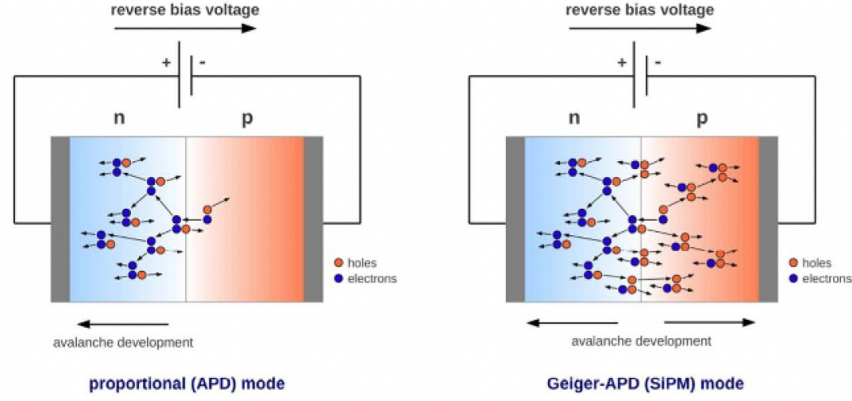
FIGURE 5.3: Avalanche development in APDs (left) and in SPADs (right). For APDs, holes do not have sufficient kinetic energy to generate secondary electron-hole pairs, and the avalanche only develops in one direction. For SPADs, the holes do generate secondary electron-hole pairs. The generated electrons then accelerate in the opposite direction as the holes and create more electron-hole pairs, and so on.

function of λ and over-voltage; and FF is the geometric fill factor, which quantifies the proportion of surface area that is sensitive to incident photons. QE(λ) describes the probability of a successful photoelectric conversion of an incident photon into a charge carrier in the SPAD. This primarily depends on optical parameters such as reflectivity at the SPAD surface and optical absorption depth of photons with wavelength λ in silicon, but also on material properties like the silicon band-gap energy, which varies with conditions like the concentration of dopants, temperature, electric field strength, etc. Once a photon has been converted into an electron-hole pair, it will have a probability, $P_{\mathrm{Av}}(\lambda, V_{\mathrm{ov}})$, of resulting in a self-sustaining avalanche. Recall from Section 5.1.1 that electrons are kinematically more likely to generate secondary charge carriers than holes, and that due to the bias direction electrons move from P-type to N-type. Therefore, the probability of a self-sustaining avalanche being triggered is maximized when electron-hole pairs are generated in the P-type semiconductor, so that the electrons travel the greatest distance in the depletion zone, where the electric field strength is greatest. Lastly, the geometric fill factor is the proportion of the SPAD (or SiPM) surface area that is sensitive to photons, which is discussed more in Section 5.1.3.

Recall from Section 5.1.1 that the avalanche in APDs has a natural endpoint when all the charge carriers clear depletion zone; this process is called *quenching*. In SPADs, there is no such self-quenching mechanism, which means a triggered avalanche would render the SPAD unable to detect photons unless the process is quenched by some other means. In practice, SPADs are built with a *quenching circuit*, which is a quenching resistor

R_q placed in series with the P-N junction. When a photon triggers an avalanche, a large current suddenly starts to flow through the junction and the resistor. This results in an increasing voltage drop across the resistor, which reduces the voltage across the junction. On the timescale of ~ps, the voltage across the junction will drop down to the breakdown voltage and the holes are no longer able to reach sufficient kinetic energy to generate secondary charge carriers. At this point, the avalanche is no longer able to sustain itself, thus quenching the SPAD.

Figure 5.4 shows an equivalent electrical circuit model for a SPAD. Here the SPAD is represented as a diode in series with the quenching circuit. The diode is modelled by its equivalent diode resistance and capacitance, R_d and C_d, in parallel with each other, and a switch that closes upon the photoelectric conversion of a photon. Within the diode is also a fixed voltage supply set at V_{bd}. The quenching circuit is modelled with a quenching resistor, with resistance $R_q \gg R_d$, in parallel with a parasitic capacitor, having a capacitance C_q.[2] The SPAD is also being biased at a voltage $V_{bias} > V_{bd}$, and therefore the voltage across the diode capacitor is $V = V_{bias} - V_{bd}$; a quantity called *over-voltage*, V_{ov}.

In this model, when a photon is "detected"—i.e. the photon generating an electron-hole pair, which subsequently triggers an avalanche—the switch closes allowing current to flow through the diode resistor. Once the switch is closed, the diode capacitor begins to discharge, and this represents the avalanche traversing the depletion zone of the P-N junction. The time constant of the discharge (i.e. the avalanche duration) is given by

$$\tau_{av} = R_d \cdot (C_d + C_q). \tag{5.2}$$

As the current passing through the quenching resistor from the avalanche rises, the voltage drop across the quenching resistor also rises proportionally due to Ohm's Law. Consequently, the bias voltage across the diode reduces until it reaches V_{bd}, at which point the avalanche is quenched. In the model of Figure 5.4, this is represented as the switch re-opening. The remaining charge in the depletion zone is then extracted as the current flows towards the anode. This is modelled as the diode capacitor recharging until its voltage drop goes back up to V_{ov}. This is a 'recovery period' over which the SPAD is less sensitive to single photons because of reduced gain. The recovery period

---

[2]Parasitic capacitance is an unavoidable build-up of charge on surfaces of electronic components in a circuit, usually due to the electric fields in nearby components of the circuit.
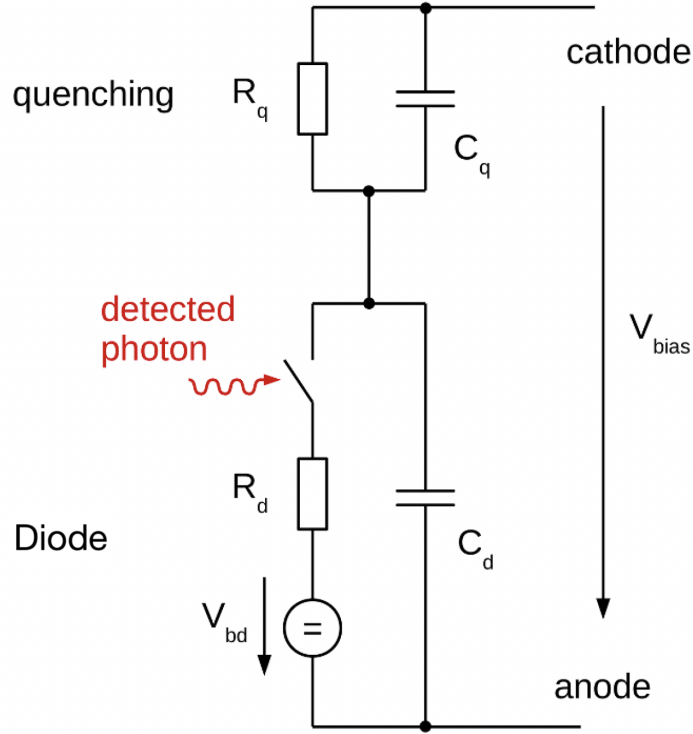
FIGURE 5.4: Model circuit diagram of SPAD with parallel quenching circuitry. In this model, the photon detection closes the switch, allowing the diode capacitor to discharge, which signifies avalanche breakdown in the SPAD. As the capacitor voltage drops down to V_{bd}, the avalanche ceases and the switch opens. Image taken from Ref [154].

has a time constant,

$$\tau_{\mathrm{rec}} = R_q \cdot (C_d + C_q), \tag{5.3}$$

which varies depending on the size of the SPAD and the value of R_q, but can range from 10s of nanoseconds to a few microseconds [62, 155]. Once fully recharged, the SPAD sensitivity is completely recovered. Ultimately a characteristic total charge generated in this avalanche quenching cycle, Q_{SPAD} is collected at the anode for signal readout. This is given by

$$Q_{\mathrm{SPAD}} = V_{\mathrm{ov}} \cdot (C_d + C_q). \tag{5.4}$$

The single-photon detection capabilities of SiPMs stems from the extremely high gain of SPADs, as a single electron-hole pair created in the depletion zone can generate a charge avalanche on the order of 10^5–10^7 electrons [156, 157].

5.1.3 Silicon Photomultipliers

A SiPM consists of an array of thousands to several millions of tightly packed SPADs connected in parallel, all sharing a common P- or N-type substrate. In Chapter 6, the focus will be on two specific SiPM technologies: The Fondazione Bruno Kessler (FBK) VUV-HD3, and the Hamamatsu Photonics K.K. (HPK) VUV4, which are both depicted in Figure 5.5. The HPK VUV4 has a total area of $3\times3\,\mathrm{mm}^2$ and SPADs of dimensions $50\times50\,\mu\mathrm{m}^2$, while the FBK VUV-HD3 is $6\times6\,\mathrm{mm}^2$ in area and has SPADs of dimensions $35\times35\,\mu\mathrm{m}^2$. Because the SPADs are connected in parallel, SiPMs can be powered at 3–6 V above the breakdown voltage of a single SPAD, which is much lower than the kilovolts required to power PMTs, and achieve comparable gains of $\sim 10^6$.

The breakdown voltage of a given SiPM is measured by finding the maximum derivative of a characteristic IV curve for the unit. As seen in Figure 5.5 the FBK VUV-HD3 has $V_{\mathrm{bd}} =32\pm1\,\mathrm{V}$, and for the HPK VUV4, $V_{\mathrm{bd}} =52\pm1\,\mathrm{V}$.
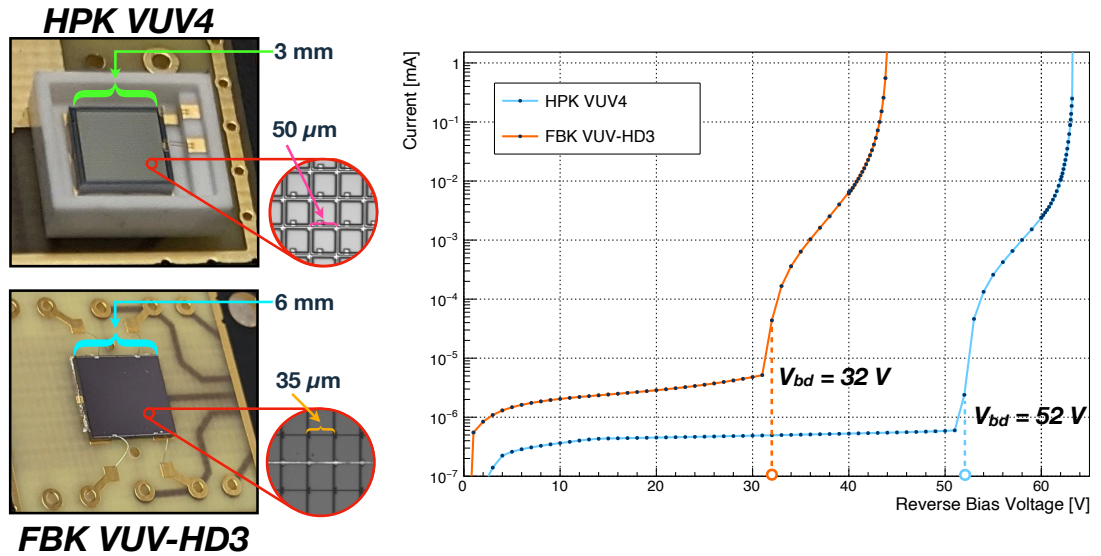
FIGURE 5.5: Physical dimensions (left) and characteristic I-V curves (right) for the HPK VUV4 and FBK VUV-HD3 and the HPK VUV4 SiPMs tested in Chapter 6.

Each SPAD in a SiPM operates as an individual photo-sensing cell, often called a pixel. All pixels are electrically and optically isolated from each other by *trenches*, which are physical borders separating SPADs, typically $\sim 5\,\mu\mathrm{m}$ in width. The trenches are completely insensitive to impinging photons, and comprise 'dead zones' on the SiPM surface. When a single photon impinges on a SiPM in an active area, it can generate an avalanche within a pixel, which subsequently generates a total charge given by Equation 5.4. That

charge flows towards the common substrate and is collected by an anode for readout. If n photons irradiate the SiPM at the same time, assuming all of them hit different pixels, there will be n avalanches generating a total charge of nQ_{SPAD}.

The dynamic range of the SiPM is therefore set by the number of pixels, making more pixels an advantageous design feature. This requires the pixel dimensions to be smaller, which also reduces the intrinsic capacitance of the SPAD and leads to a quicker recovery time for all pixels. However, lower capacitance that comes with smaller pixels also reduces Q_{SPAD} (see Equation 5.4). Furthermore, smaller pixel sizes typically translate to a smaller geometric fill factor. This is because the trench width is key to suppressing correlated noise between SPADs. Therefore when scaling down the pixel size the trench width usually stays the same, thereby increasing the proportion of the SiPM surface area in the dead zones. This trade-off between fill factor and correlated noise suppression is discussed in more detail in Section 5.2.2.

There are two basic configurations for SiPMs, which are

(a) N-on-P; i.e. an N-type semiconductor layer on top of a P-type substrate

(b) P-on-N

The important distinction between these two configurations is that (a) is more efficient in detecting red and infrared photons, while (b) is more efficient in the blue and UV range. The reason for this is illustrated by, Figure 5.6, which shows a simulation of the avalanche triggering probability vs depth in a SPAD with a P-on-N configuration, as well as the charge carrier concentration (both electrons and holes) and electric field strength. The absorption depth in silicon for UV photons is $\sim 0.5 \mu m$ [158], which means that virtually all UV photons will be absorbed in the green region of Figure 5.6 labelled with P^+. The electrons would then traverse the entire high field region, which maximizes P_{Av}. For the N-on-P configuration, all curves in Figure 5.6 would be reflected about the vertical line labelled with X_{PN} which marks the location of the P-N junction. In this case, the electron-hole pairs generated by UV photons would be created in the N-type semiconductor; the electrons would travel a short distance in the high field region, and P_{Av} would be low. In contrast, photons in the red and infrared regions have and absorption depth of order mm, and they can penetrated deeper into the silicon before getting absorbed. Therefore the N-on-P configuration is ideal for longer wavelengths.

The FBK VUV-HD3 and HPK VUV4 are both P-on-N SiPMs, and are suitable candidate designs for use in next generation noble liquid scintillation experiments, which will be discussed in Sections 5.3–5.5.
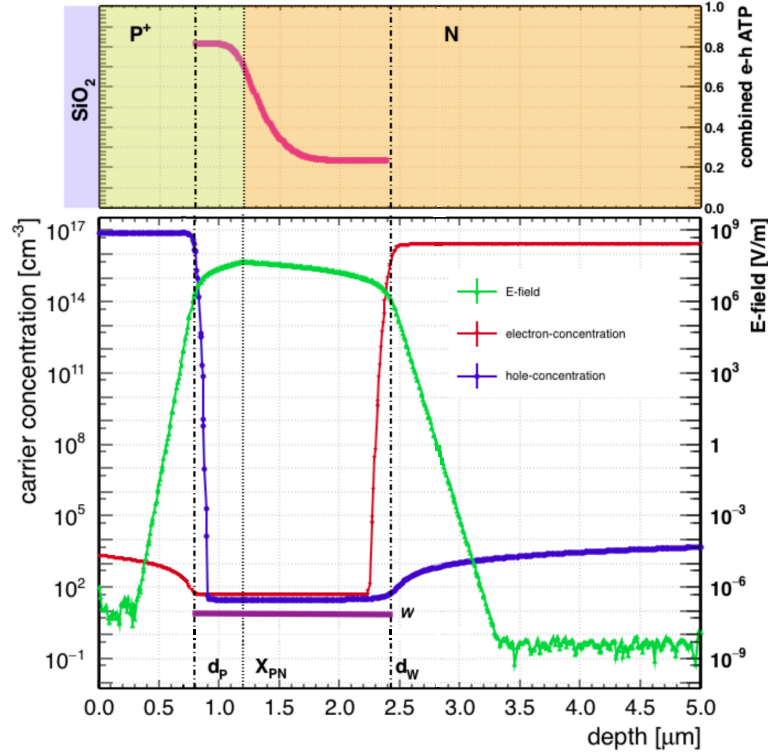
FIGURE 5.6: Simulation of avalanche triggering probability in a P-on-N SPAD taken from Ref [159]. In a N-on-P configuration, all of the above curves would be reflected about the vertical line labelled with x_{PN}. (Top) Avalanche triggering probability (ATP) as a function of photon absorption depth, with regions labelled for the P-type and N-type semiconductors. Note that "+" superscripts indicate "heavy" doping. The P^+ layer has a dopant concentration of 7.5×10^{16} cm^{-3}, and the N layer has a concentration of 2.5×10^{16} cm^{-3}. (Bottom) charge carrier (electrons and holes) concentration and electric field strength as a function of depth in the silicon. d_P and d_W mark the edges of the depletion zone; x_{PN} is the position of maximum electric field; and $W = d_W - d_P$ is the width of the depletion zone.

5.2 Sources of Noise Associated With SiPMs

5.2.1 Dark Count Rate

One of the limitations of SiPMs is the fact that operating a P-N junction beyond the breakdown voltage introduces a high Dark Count Rate (DCR). For example the HPK VUV4 has a DCR of 1 MHz at a temperature of 298 K and $V_{ov} = 4$ V [145], while the R5912-HQE PMTs used in DEAP-3600 have a DCR of 4 kHz in equivalent conditions.
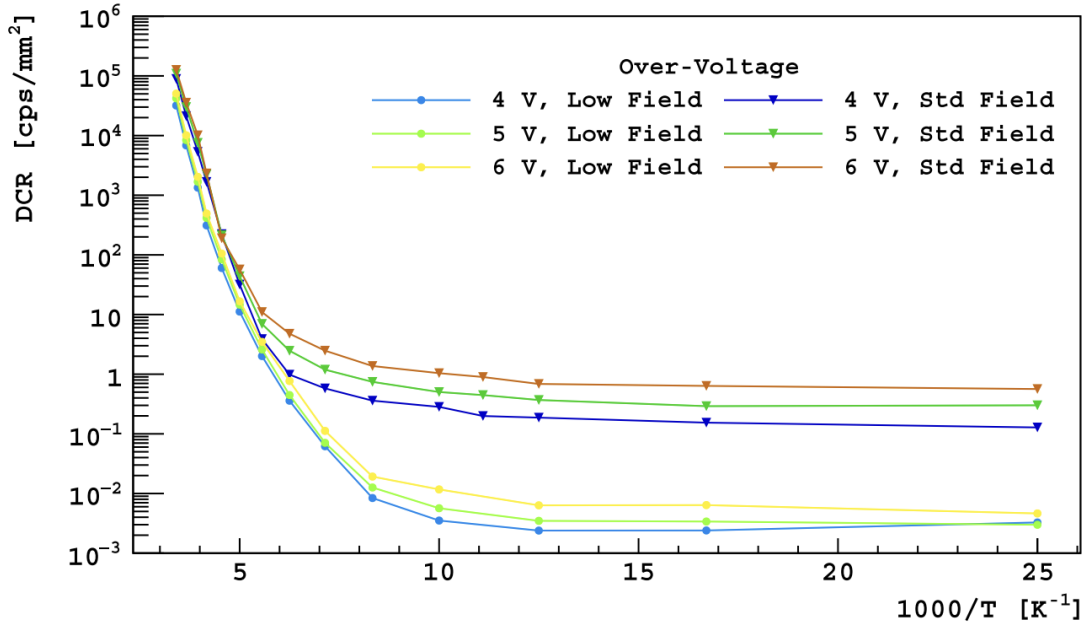
FIGURE 5.7: DCR as a function of over-voltage and inverse temperature in the FBK NUV-HD-SF SiPM (std. field) and the FBK NUV-HD-LF SiPM (low field). Image taken from Ref[161].

Dark counts or dark noise in SiPMs are avalanches triggered by thermally induced electron-hole pairs in the silicon. There are two main ways that these charge carriers can be spontaneously generated [160],

(i) Electrons gaining sufficient energy via thermal processes to transition from the valence to conduction band

(ii) Electrons tunnelling through the band gap potential wall.

The first mechanism generally depends on the strength of the electric field in the SiPM pixels and the SiPM temperature, and can be understood intuitively. Larger electric fields reduce the band gap energy in the silicon, which allows electrons to transition between bands with less thermal agitation than with lower electric fields. At higher temperatures, there is more thermal energy available for electrons to absorb and transition between bands. Thermodynamically, the probability of an electron transitioning between bands is proportional to $\exp(-\Delta E/kT)$, where ΔE is the band gap energy, k is the Boltzmann constant, and T is the temperature. An example observation of exponentially decreasing DCR with T^{-1} and increasing with over-voltage (and therefore electric field strength) is shown in Figure 5.7.

The reduction of DCR via cooling is effective when $T > 150\,\mathrm{K}$, after which point the DCR becomes dominated by mechanism (ii) over (i). Tunnelling of electrons between bands is facilitated by the presence of defects in the crystal structure brought on by impurities in the silicon or nonuniformities in the semiconductor doping profile. In the Shockley-Read-Hall model [162], such defects locally introduce intermediate energy states between the conduction and valence bands, often called 'traps.' The tunnelling of electrons between bands via traps is called a 'trap assisted band transition.' Reduction of the DCR at cryogenic temperatures is therefore only achieved through improved manufacturing techniques to either limit the number of trap sites in the silicon or reduce the strength of the internal electric field at a given over-voltage, as shown in Figure 5.7.

5.2.2 Correlated Cross-Talk

A byproduct of semiconductors undergoing avalanche breakdown is the emission of secondary photons [163], which can lead to sources of noise called *correlated cross-talk* [164, 165]. Though an exhaustive list of production mechanisms is not known conclusively at present, secondary photon emission in silicon has been previously modeled as a combination of direct and indirect interband transitions; direct intraband transitions; and intraband Bremsstrahlung processes [166–168]. Shown in Figure 5.8b is a set of band structure cartoon diagrams describing these mechanisms. Direct interband transitions are when electrons in the conduction band recombine with a hole in the silicon such that there is zero momentum transfer to the lattice structure, and the emitted photon has energy equal to the band-gap. Conversely, an indirect interband transition occurs when there is a non-zero momentum transfer to the lattice, resulting in the emission of a photon and a phonon. Bremsstrahlung or "stopping radiation" occurs when an electron in the conduction band rapidly decelerates in a collision, generating a photon and transferring momentum to the lattice. Lastly, intraband hole recombination occurs when a hole is created with a vacancy in a lower energy level than the valence band, and an electron in the valence band emits a photon as it transitions to fill the vacancy.

Each mechanism is responsible for light emission in a different spectral region, i.e. at certain wavelengths, as shown in Figure 5.8a. In this model, avalanche emission below $2\,\mathrm{eV}$ is dominated by indirect interband transitions, between $2\,\mathrm{eV}$ and $2.3\,\mathrm{eV}$ by intraband Bremsstrahlung and above $2.3\,\mathrm{eV}$ by direct interband [166–168]. While such attempts

to model the secondary photon emission spectrum of avalanche breakdown in silicon are able to loosely agree with data, modelling the systematic effect of cross-talk photons in next-generation physics experiments is expected to be more reliably done with measured spectra for specific SiPM designs. This is the main motivation for conducting the measurements discussed in Chapter 6.

(A)

(B)
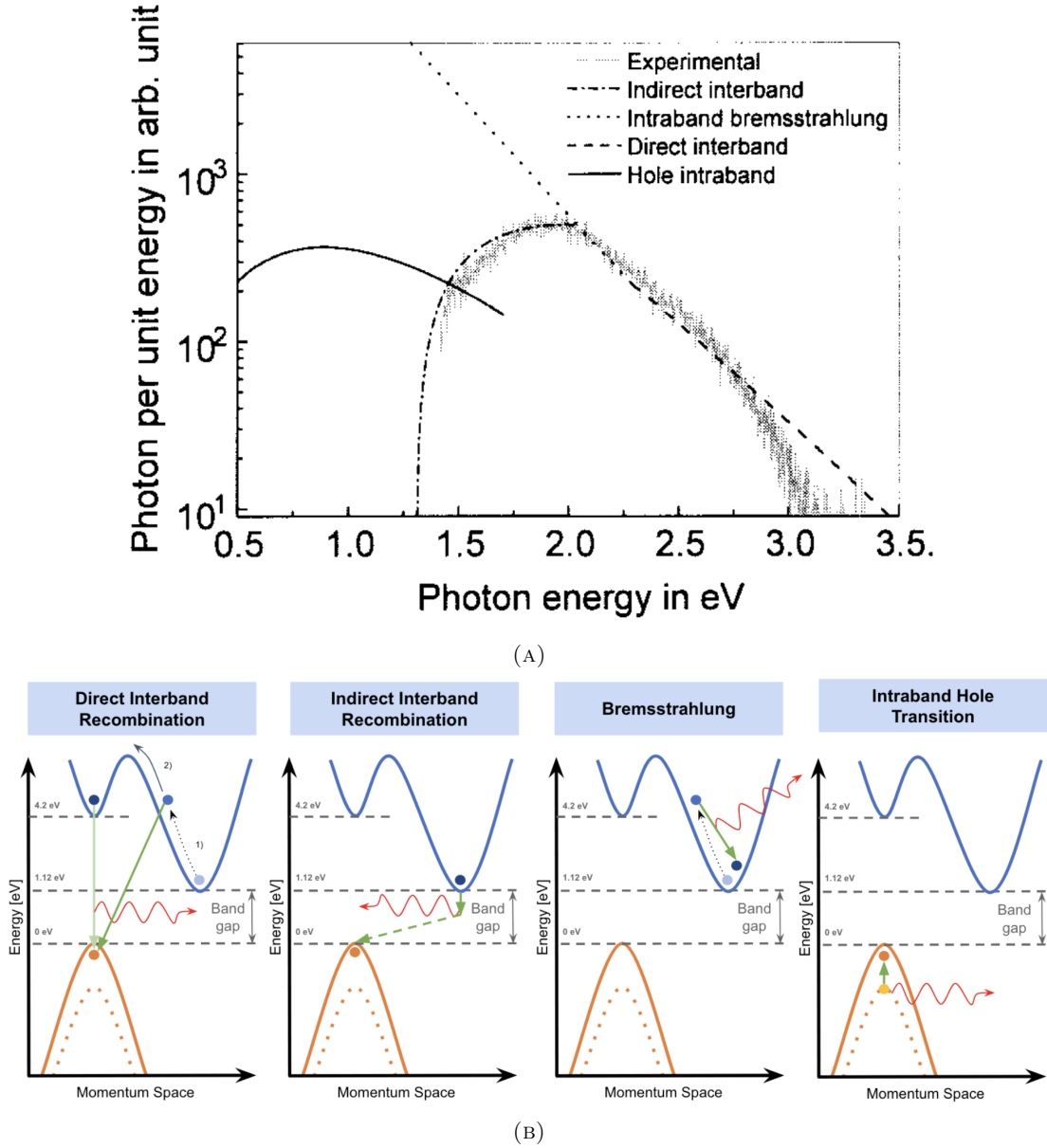
FIGURE 5.8: A model-data comparison of secondary photon emission in silicon under avalanche breakdown (A) [166] and cartoon diagrams of the band structure describing each mechanism (B). See text for more details.

Correlated cross-talk in SiPMs is generally sub-categorized into three distinct processes (depicted in Figure 5.9):

(i) **External Cross-Talk**[3]:

Avalanche breakdown produces secondary photons that escape the SiPM and leak into the detector, potentially triggering avalanches in neighbouring SiPMs or SiPMs on the opposite side of the detector.

(ii) **Internal Direct Cross-Talk (DiCT)**:

Avalanche breakdown produces secondary photons that propagate into the high field region of a neighbouring pixel, triggering a second avalanche in the same SiPM. This can occur either directly, via reflection off the backside of the SiPM, or via reflection off of the thin film of SiO_2 on the SiPM surface.[4] The timescale of DiCT is of order picoseconds [169].

(iii) **Internal Delayed Cross-Talk (DeCT)**:

Avalanche breakdown produces secondary photons that are absorbed in the substrate of a neighbouring pixel, triggering a second avalanche in the same SiPM after the generated charge carrier drifts into the high field region. The timescale of DeCT is of order nanoseconds [170].

DiCT and DeCT contribute to the total number of correlated avalanches per pulse [169]. A common design element of modern SiPMs that reduces the rates of both DiCT and DeCT is optically opaque trenches which isolate each pixel. The trenches limit the available paths for secondary photons to propagate into neighbouring pixels. A comparison of the 'thick' trenches used in the HPK VUV4 design and the relatively thinner trenches used in the FBK VUV-HD3 is provided in Chapter 6.

---

[3]At the time of writing this work, there is some debate about the definition of external cross-talk among researchers. There is the one given here, where external cross-talk is limited to photons exiting the SiPM entirely, and there is the alternative where it also includes photons reflecting back towards a neighbouring SPAD in the SiPM of origin. In the former case, external cross-talk exclusively describes the process of one SiPM detecting the secondary emission of a different SiPM, and internal cross-talk describes a SiPM detecting its own secondary emission. In this sense, the latter definition somewhat conflates external and internal cross-talk because external cross-talk can also describe a SiPM detecting its own secondary emission. In this work, the former definition is used, as it is more useful in the context of particle detectors.

[4]SiO_2 spontaneously forms on the surface of pure silicon exposed to oxygen in the atmosphere. Though some companies like FBK will control this process to create a protective coating for their units, the formation of the SiO_2 layer is virtually unavoidable.
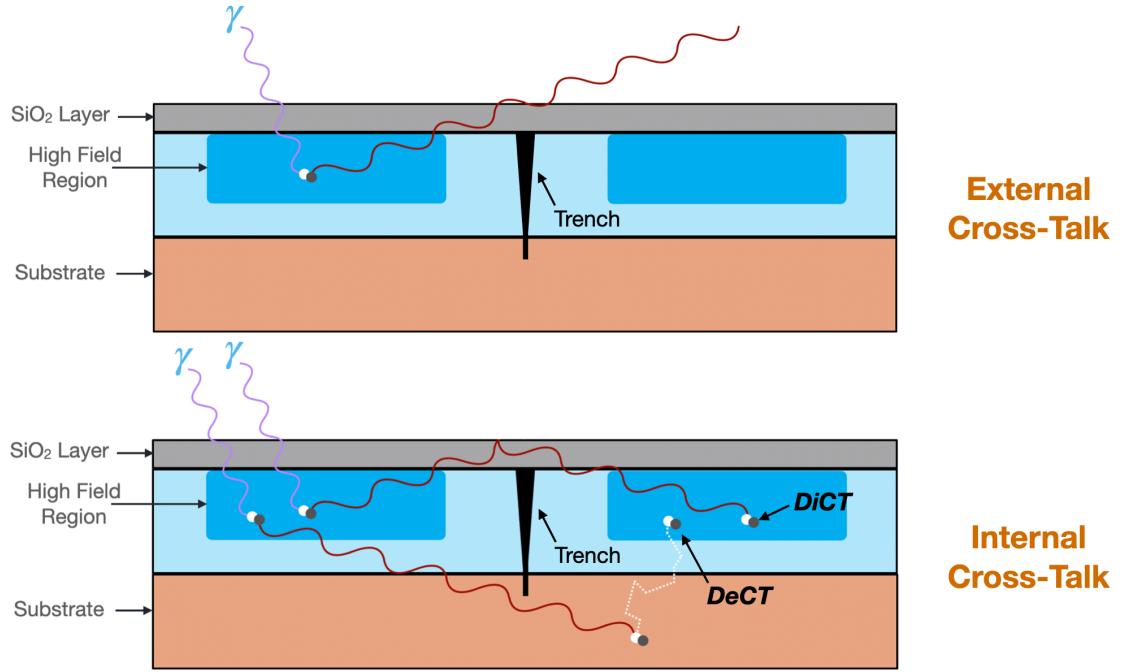
FIGURE 5.9: Diagram of correlated cross-talk variations. (Top) External cross-talk. (Bottom) Internal delayed and direct cross-talk.

5.2.3 Afterpulsing

Unlike cross-talk, which affects neighbouring pixels and SiPMs, afterpulsing is a source of correlated noise in the same pixel where the original avalanche was triggered. Afterpulsing in a SiPM can be induced in two ways: from the secondary photon emission of the avalanche (i.e. optically induced) and from trapped and released charge carriers in the high field region (trap induced). In the case of optically induced afterpulsing, a secondary photon from the avalanche process is absorbed somewhere in the low field region of the pixel. In this way a charge carrier can be generated which then must drift into the high field region and trigger another avalanche. Trap induced afterpulsing involves charge carriers in the avalanche itself falling into a Shockley-Read-Hall trap in the high field region and subsequently escaping to produce a second avalanche. If the time delay between the initial avalanche and the injection of the secondary charge carriers into the high field region is less than the full recovery time of the pixel, the secondary avalanches induced this way will not be self-sustaining, and thus of lower charge than an ordinary avalanche. Furthermore, if the secondary avalanche is generated at the beginning of the recovery period, the gain will be lower than at the end of the cycle. Therefore afterpulses typically look like pulses with charge $Q_{\mathrm{AP}} \leq Q_{\mathrm{SPAD}} \equiv 1\,\mathrm{PE}$, but $Q_{\mathrm{AP}} \to Q_{\mathrm{SPAD}}$ as the time delay approaches the SPAD recovery time (see Equation 5.3).
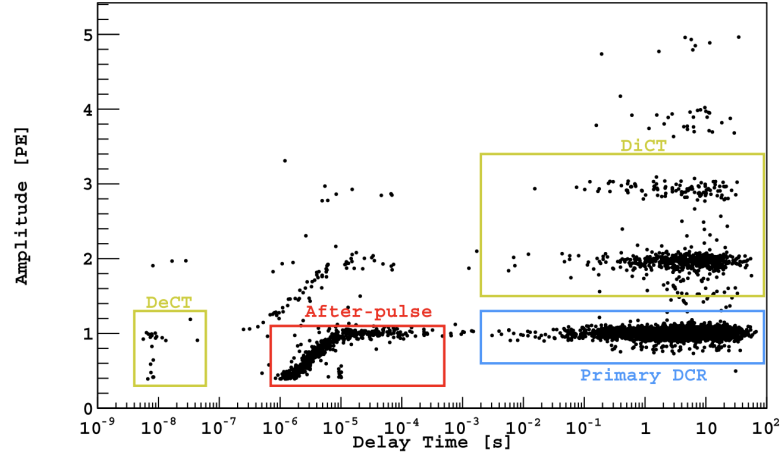
FIGURE 5.10: Plot demonstrating the pulse counting techniques for characterization of DiCT and DeCT in SiPMs. Image taken from Ref [161].

5.2.4 SiPM Noise Characterization

DiCT and DeCT are extensively studied in literature with both measurements [171] and simulation [165]. Different pulse-counting techniques are used to discriminate against or study these processes as in Refs [161, 171, 172], though they all utilize a space defined by pulse charge [PE] vs. time delay between consecutive pulses [s] as in Figure 5.10. Afterpulsing, DiCT, and DeCT each populate different regions in this space, which can be used to measure their rates per detected scintillation photon. Afterpulsing appears in the red box of Figure 5.10. Here, the pulse charge is positively correlated with the time interval, which is due to the fact that afterpulses are mostly generated within the recovery time of SPAD when the gain is reduced. DeCT tends to appear as a full avalanche (i.e. an integer number of PE) occurring $\sim 10\,\mathrm{ns}$ after the detected photon. Therefore measuring the DeCT rate per detected avalanche can be done by counting the number of pulses that reconstruct inside the bottom-left region in Figure 5.10.

The average additional charge from DiCT, DeCT, and afterpulsing is characterized by the *excess charge factor* (ECF) of the SiPM, and is defined as [154]

$$\mathrm{ECF} = \frac{\langle Q \rangle}{\langle Q_N \rangle}, \tag{5.5}$$

where if a SiPM receives N photons, $\langle Q \rangle$ would be the average observed pulse charge, and $\langle Q_N \rangle$ is N times the average single photon charge. The average single photon charge is obtained from low-light SiPM charge distributions like that of Figure 5.1, and removing the correlated noise with the same pulse counting technique used to make Figure 5.10.

The presence of correlated noise also degrades the charge resolution, resulting in an *excess noise factor* (ENF), which is defined as [154]

$$\text{ENF} = \frac{(\sigma_Q/\langle Q \rangle)^2}{(\sigma_{Q_N}/\langle Q_N \rangle)^2}, \tag{5.6}$$

where σ_Q is the standard deviation of the observed pulse charge distribution about $\langle Q \rangle$, and σ_{Q_N} is the standard deviation of the single photon SiPM charge distribution. An ideal SiPM would have zero likelihood of DiCT, DeCT, or afterpulsing, and therefore ECF = ENF = 1 in this case. The ECF and ENF for realistic devices is dependent on a variety of factors, such as over-voltage, temperature, and trench structure. The typical values for ECF and ENF in the most recent SiPM designs are of order unity [173].

In similar fashion, external cross-talk is a source of excess noise for detectors, especially those with large surface areas tiled by SiPMs which are facing each other. This is the case for nEXO, DUNE, and DarkSide-20k detector designs, which are discussed in Sections 5.3, 5.4, and 5.5. Characterizing the impact of external cross-talk on detector performance is difficult to do precisely without accurate simulation of secondary photon emission in SiPMs, which is the primary motivation for the measurements described in Chapter 6. These measurements characterize the external cross-talk photon spectra of SiPMs induced by dark noise with varying over-voltage. The observed spectra can be used in detector simulation software as empirical sampling distributions for external cross-talk photon energies. Combining this with PDE (Equation 5.1) in a detector simulation can be used to quantify the impact of external cross-talk on various detector performance parameters, e.g. energy response and resolution, position reconstruction resolution, pulse-shape discrimination, etc.

5.3 nEXO

The nEXO experiment [174] is the next generation version of EXO-200, which is a search for neutrinoless double β-decay ($0\nu\beta\beta$) using a single-phase LXe TPC enriched with the xenon isotope ^{136}Xe. nEXO is proposed to use a $5000\,\text{kg}$ target of LXe enriched to 90% ^{136}Xe and has a projected sensitivity to the $0\nu\beta\beta$ half-life of 10^{28} years. This section briefly motivates the search for $0\nu\beta\beta$ (Section 5.3.1) and summarizes how nEXO stands to benefit from the use of SiPMs in its experimental design (Section 5.3.2).

5.3.1 Neutrinoless Double Beta Decay

The discovery of neutrino oscillations [175] proves that at least two of the active neutrino flavours have non-zero mass. With that fact being established conclusively, an ambiguity arises regarding the nature of the neutrino; i.e. whether the neutrino is a Dirac or Majorana fermion. If the neutrino is a Dirac fermion, then it has a distinct antineutrino. On the other hand, Majorana neutrinos would be identical to their antiparticle counterparts. The theoretical underpinnings of Dirac and Majorana neutrinos, and how they manifest in Standard Model Lagrangian formalism is outside the scope of this work, but are summarized briefly in Ref [174] and in more detail in Ref [176]. The important potential consequences of neutrinos being Majorana fermions are:

(i) The existence of heavy, right-handed, sterile neutrinos[5], with masses coupled to those of the active neutrinos via the *see-saw mechanism* [174, 176, 177]

(ii) The possibility of lepton number violating processes

These consequences can provide answers for currently unanswered questions in neutrino physics, such as why the neutrino mass is at least 10^6 times smaller than the mass of the electron [177]. They also have interesting ramifications for early universe cosmology, as lepton flavour symmetry violation in leptogenesis could have contributed to the baryon-antibaryon asymmetry [177].

One such lepton number violating process which might be observed in experiments like nEXO is $0\nu\beta\beta$, which is the simultaneous emission of two electrons from a nucleus, X (having Z protons and N neutrons), with no accompanying neutrinos, i.e.

$$_N^Z\text{X} \rightarrow 2e^- + _{N-2}^{Z+2}\text{X}. \tag{5.7}$$

The rare, but experimentally verified reaction of two-neutrino double beta decay ($2\nu\beta\beta$),

$$_N^Z\text{X} \rightarrow 2e^- + 2\bar{\nu}_e + _{N-2}^{Z+2}\text{X}, \tag{5.8}$$

has been observed in a catalogue of nuclides, including ^{136}Xe (with half-life $\tau_{1/2} = 2.11 \times 10^{21}$ years), which was first detected by EXO-200 [178]. In the Majorana picture of

---

[5]The handedness of the neutrino in this context refers to the *chirality* of the particle, which is discussed in Ref [176]. The weak force couples to fermions of left-handed chirality, and therefore the right-handed Majorana neutrino would be sterile according to Standard Model physics.

neutrinos, any double beta decaying nuclide can undergo both $2\nu\beta\beta$ and $0\nu\beta\beta$, where the latter is 'mediated' by the lighter left-handed neutrino (see Figure 5.11). In the case of $0\nu\beta\beta$, the Majorana neutrino is 'absorbed' by one of the W^- bosons which subsequently becomes the 2nd electron emitted in the decay.[6] Note that this can only proceed if the neutrino is indeed its own antiparticle. Otherwise lepton number must be conserved, and would be violated at the absorption vertex.
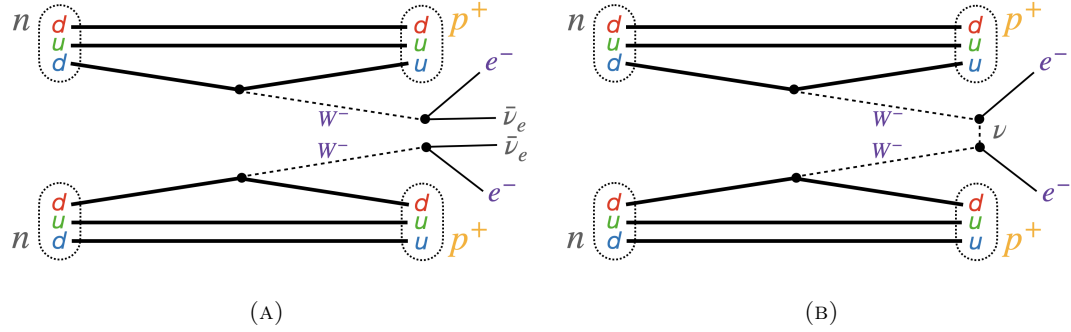
FIGURE 5.11: Feynman diagrams for (A) $2\nu\beta\beta$ and (B) $0\nu\beta\beta$. The neutrons, n, and protons p^+ exist within a double beta decaying parent nucleus and its daughter, respectively.

Similar to single beta decay, $2\nu\beta\beta$ has a broad energy spectrum with an endpoint determined by the Q-value of the reaction. Since $0\nu\beta\beta$ has no neutrinos which can carry away any kinetic energy, virtually all of the energy is given to the electrons, which would interact nearly simultaneously in a particle detector, such as the LXe TPC of nEXO. The two simultaneous electron interactions would then appear as one event with total energy equal to the Q-value of the double beta decay. Therefore if $0\nu\beta\beta$ is a physically realizable process, a double beta decay energy spectrum would look like the one depicted in Figure 5.12. A prominent $2\nu\beta\beta$ spectrum would span an energy range from zero up to the Q-value of the double beta decay, $Q_{\beta\beta}$, and a small energy peak centred at $Q_{\beta\beta}$ would be visible from the relatively rare $0\nu\beta\beta$ events. In an ideal detector, the $0\nu\beta\beta$ peak would be described by a delta function, $\delta(E - Q_{\beta\beta})$, where E is the observed event energy. However, a realistic detector has finite energy resolution, and therefore the tail of the $2\nu\beta\beta$ spectrum would overlap with the $0\nu\beta\beta$ peak, resulting in the green and red curves in Figure 5.12. As a result, the quality of an experiment's energy resolution plays a major role in its sensitivity to $0\nu\beta\beta$. Improving detector energy resolution is the main motivation for using SiPMs in nEXO over large area APDs or PMTs.

---

[6]This is a tremendously simplified reduction of the physics involved in $0\nu\beta\beta$. For a more detailed description, see Refs [176, 177].
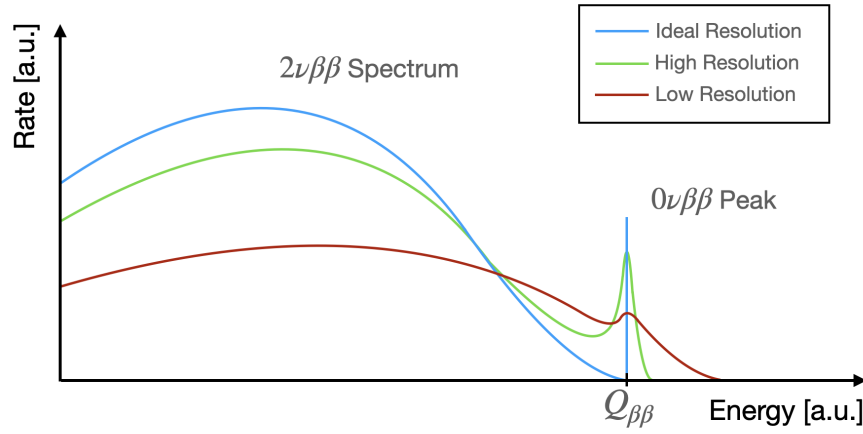
FIGURE 5.12: Cartoon depiction of a double beta spectrum, as a function of detector energy resolution.

5.3.2 SiPMs in nEXO

The nEXO detector (shown in Figure 5.13a [174]) is planned to be a LXe TPC which measures event energy by adding the light signal from scintillation in LXe and the charge signal from ionization. Any charge carriers generated in a scattering event can either recombine to produce scintillation or drift towards the TPC electrodes, and therefore the ionization and photon yields will be anti-correlated with each other; this can be exploited to enhance energy resolution of the detector by projecting the sum of the ionization and scintillation signals onto a 'rotated' energy axis, as seen in Figure 5.13b [179].

The energy (Equation 5.9) and energy resolution (Equation 5.10) of nEXO can be modelled as [174],

$$\langle E \rangle = W(N_Q + N_S), \tag{5.9}$$

$$\sigma^2_{\langle E \rangle} = W^2(\sigma_Q^2 + \sigma_S^2 + \lambda_N), \tag{5.10}$$

where N_Q and N_S are the number of ions and scintillation photons produced in a scattering event; W is the average energy per quanta in both the ionization and scintillation channels; σ_Q^2 and σ_S^2 are the variances in the ionization and scintillation signals; and λ_N is an excess noise factor which accounts for additional sources of noise like those discussed in Section 5.2. The dominant term in Equation 5.10 is the scintillation signal variance, σ_S^2. There are two main contributors to this:

(A)

(B)
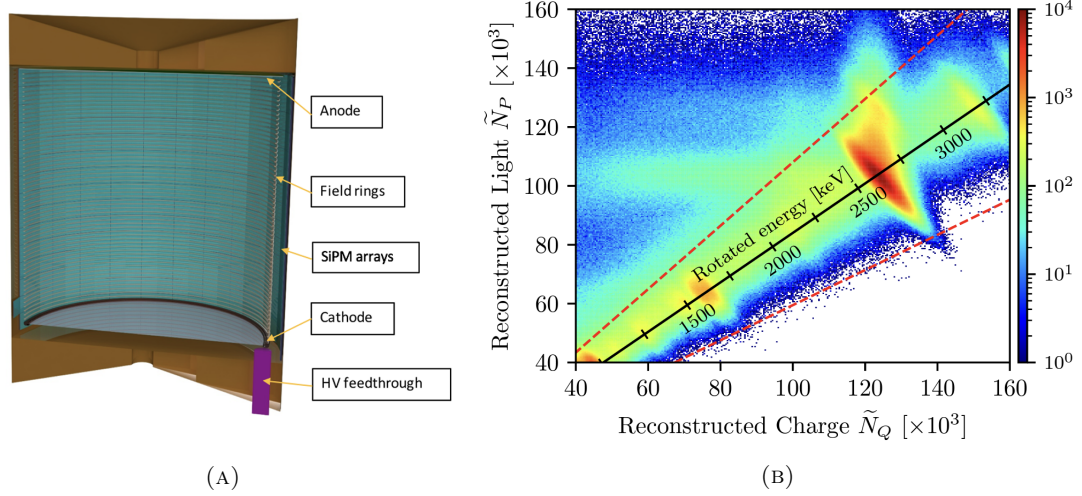
FIGURE 5.13: (A) The nEXO pre-conceptual TPC design [174]. SiPMs are planned to line vertical walls of the cylindrical TPC vessel for maximal light collection efficiency while charge collection will occur at the anode at the top of the drift field. (B) Charge vs. light signal in nEXO for simulated ^{232}Th decays in the TPC. Dashed red lines indicate event selection cut boundaries for analysis in the 'rotated' energy space. Figure (B) taken from Ref [179].

(i) Electronic readout noise

(ii) Photon detection efficiency

Large area APDs (LAAPDs) were used in EXO-200 for their low radioactivity and high QE ($\sim$ 100% [180]) for VUV photons. However the overall signal gain for LAAPDs is $\simeq$200, which is 4–6 orders of magnitude lower than in PMTs or SiPMs; the ratio of signal amplitude to the RMS of readout noise for SiPMs in similar operating conditions can be up to 5 orders of magnitude greater than LAAPDs as a result. Additionally, the circular shape of LAAPDs limited the photo-sensitive area of the EXO-200 detector to 48% of the total detector surface [181], which limits the overall photon detection efficiency.

For nEXO, switching to SiPMs improves the scintillation signal variance by addressing both of these items. As previously discussed in this chapter, SiPMs have far superior single PE charge resolution compared to PMTs and APDs, because of the binary nature of the SPAD signal output. Additionally, with the development of P-on-N SiPM designs like the FBK VUV-HD3 and HPK VUV4, SiPMs can now be made with PDE at 178 nm of >15%, which was reported as a minimum requirement for nEXO [174]. The size and shape of SiPMs also makes them able to cover approximately 100% of the nEXO detector, which greatly improves on the 48% packing efficiency of the LAAPDs in EXO-200.

These improvements contribute to an expected overall energy resolution improvement for nEXO from $\sigma_E/E = 1.2\%$ to 0.8% [179].

5.4 DUNE

The Deep Underground Neutrino Experiment (DUNE) [182, 183] will be a next-generation, long baseline neutrino oscillation experiment using LAr TPCs, and will be jointly run out of Fermi National Accelerator Laboratory (Fermilab) near Chicago, Illinois, and the Sanford Underground Research Facility (SURF) in Lead, South Dakota. This section will briefly summarize and motivate the DUNE physics program (Section 5.4.1) and highlight the use of SiPMs in pursuit of DUNE's scientific goals (Section 5.4.2).

5.4.1 DUNE Physics

Two key physics goals for DUNE are searching for CP violation in the neutrino sector to probe their contribution to the matter-antimatter asymmetry and determining the hierarchy of neutrino mass eigenstates. Both of these goals can be achieved with precision measurements of neutrino flavour oscillations [184]. The model which describes flavour oscillations has seven parameters [185]:

○ 3 mixing angles coupling mass eigenstates (labeled with subscripts $1, 2, 3$); θ_{12}, θ_{23}, and θ_{13}

○ 3 squared-mass splittings; Δm_{12}^2, Δm_{23}^2, and Δm_{13}^2, where $\Delta m_{ij}^2 = m_i^2 - m_j^2$

○ A phase parameter, δ_{CP}, which allows neutrino oscillations to violate CP symmetry

Of these parameters, five have been independently measured in various experiments [185]:

○ θ_{12} and Δm_{12}^2 from solar neutrino oscillation measurements

○ θ_{13} from the Daya Bay, Double Chooz, and RENO experiments

○ θ_{23} and $|\Delta m_{23}^2|$ from atmospheric neutrino oscillation measurements

Note that only the magnitude of Δm_{23}^2 has been determined, and its sign remains unknown. This leaves the possibility of two mass hierarchies: Normal Hierarchy, where $m_1 < m_2 < m_3$, and Inverted Hierarchy, where $m_3 < m_1 < m_2$. The true neutrino mass hierarchy remains as a key question in neutrino physics [185]. Additionally, having a precision measurement of the CP violation phase parameter, δ_{CP}, will indicate whether there is any CP violation in the neutrino sector, which could have contributed to the matter-antimatter asymmetry of the early universe.

DUNE aims to measure these two parameters with a controlled, high intensity muon-neutrino beam originating at Fermilab [182]. The expected energy range of the beam goes from the sub-GeV level up to as high as $10\,\text{GeV}$, with the peak flux occurring at $\sim 2.5\,\text{GeV}$. Over such a broad range, several oscillations in the neutrino energy spectrum can be observed, making DUNE sensitive to the Δm_{23}^2 mass splitting parameter. The energy scale of this neutrino beam and the ability to change its content from (predominantly) ν_μ to $\bar{\nu}_\mu$ will also make DUNE sensitive to the δ_{CP} parameter [184]. The former is important in this context because matter-antimatter asymmetry in neutrino oscillations can arise due to the fact that the neutrino beam passes through matter-dominated rock and soil en route to the detector(s). At higher energies, the asymmetries arising from this effect are enhanced, which will help disentangle the asymmetries arising from CP violation. Changing the content of the beam from neutrinos to anti-neutrinos will result in a phase inversion from the CP-violation parameter; i.e. $\delta_{CP} \to -\delta_{CP}$. This will change the shape of the neutrino energy spectrum, as shown in Figure 5.14, and can thus be used to constrain δ_{CP}.

In addition to precision neutrino oscillation measurements, DUNE will be sensitive to proton decay, particularly via the channel $p \to K^+ \bar{\nu}$; and ν_e flux from core-collapse supernovae within our galaxy. Observing proton decay would be a crucial experimental development for probing physics beyond the Standard Model. The signal in the DUNE detector from $p \to K^+ \bar{\nu}$ would be a virtually monoenergetic peak centred at the proton rest mass of $\sim 1\,\text{GeV}$. DUNE is expected to be sensitive to proton decay partial lifetimes at the level of $\tau/B \approx 3 \times 10^{34}$ years after a 10–12 year search for the $p \to K^+ \bar{\nu}$ signal (where τ is the proton lifetime and B is the branching fraction for this channel) [183]. Neutrinos from core-collapse supernovae in our galaxy would generate a large number of ν_e events in DUNE in a short period of time: roughly 1500 events in the span of $\sim 1\,\text{s}$ for a supernova $10\,\text{kpc}$ away from Earth [183]. Through charged current interactions
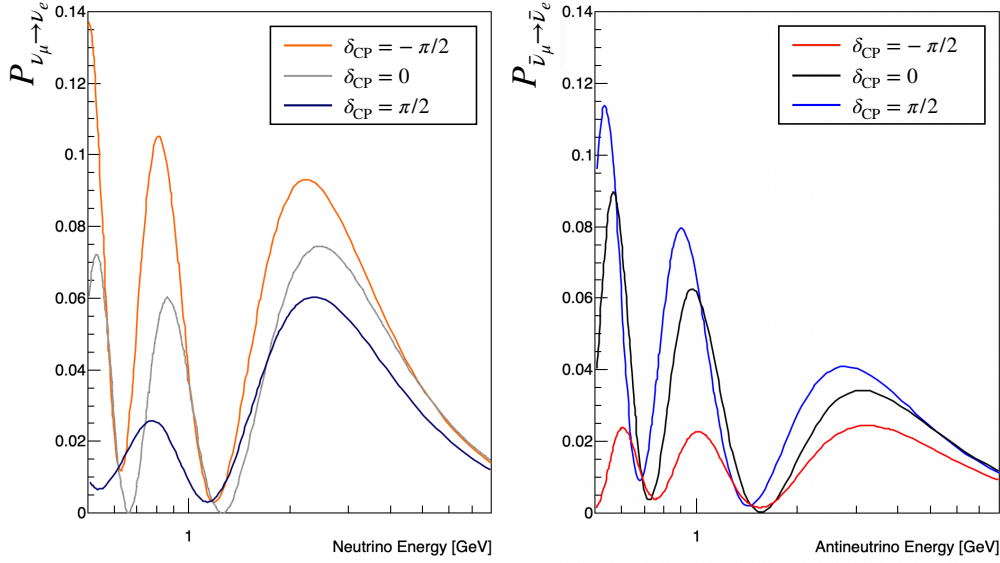
FIGURE 5.14: Neutrino oscillation probability as a function of beam energy and δ_{CP}, for (left) neutrinos and (right) antineutrinos. Images recreated from Ref [184].

with ^{40}Ar, i.e.

$$^{40}\mathrm{Ar} + \nu_e \rightarrow e^- + {}^{40}\mathrm{K}^*, \tag{5.11}$$

the coincidence of electrons and γ-rays from ^{40}K* can be used to tag ν_e in the energy range of 5-50 MeV, which is the relevant energy range for core-collapse supernova neutrinos.

5.4.2 SiPMs in DUNE

The DUNE experimental design [182] consists of three major components:

(i) A high-intensity ν_μ and/or $\bar{\nu}_\mu$ beam with an expected peak flux of $\sim 3 \times 10^{10} \, \nu/\mathrm{m}^2$ [184]

(ii) A closely situated 'Near Detector,' 574 m downstream from the neutrino beam source

(iii) A larger 'Far Detector' located 1285 km away at SURF

The Far Detector will consist of four LAr TPC detector modules, each equipped with cryostats that can hold 17.5 kilotons of LAr; the fiducial mass of LAr in each cryostat will be 10 kilotons. When a neutrino deposits energy in the LAr through interactions like $\nu_\mu + n \rightarrow \mu^- + p^+$, the recoiling lepton will create a track of ions, free electrons,

and excitons (recall from Section 2.1). This results in a charge signal, as a subset of the electrons drift towards the TPC anodes for collection; and a scintillation signal from argon excimer de-excitation. Given the dimensions of the Far Detector are of order 10s of metres, the scintillation signal can be detected as promptly as 10s of nanoseconds. Therefore the scintillation signal will be used as an event trigger for the charge signal, which drifts through the LAr over a timescale $\mathcal{O}(\text{ms})$ [186].

The DUNE Photon Detection System (PDS) will measure the LAr scintillation from each event, which will provide its trigger time and a portion of the deposited energy from neutrino interactions. For this reason, maximizing PDE of the PDS is an important design goal for the DUNE Far Detector. Increasing PDE decreases the relative uncertainty of energy measurements in the scintillation signal, thereby leading to finer energy resolution, and it also maximizes the likelihood of detecting the most prompt photons from an event, leading to better trigger time estimates. Optimal estimation of the trigger time will translate to accurate position reconstruction in the direction of the TPC drift direction, which is critical for fiducialization. Additionally, this is important energy estimation as the charge signal falls exponentially with drift time due to a finite electron lifetime. Another key detector parameter is the trigger efficiency, which will be an important systematic for low energy measurements, e.g. for core-collapse supernova neutrinos.

The DUNE PDS will utilize X-ARAPUCA [187] photon trap modules, which rely on SiPMs for photon detection. As shown in Figure 5.15, the X-ARAPUCA is designed to transmit VUV photons into the module through an input window, which comprises a dichroic filter coated with a layer of para-Terphenyl (pTP) wavelength shifter. The pTP downshifts the VUV photons from LAr scintillation to 350 nm, which transmit through the dichoric filter with a cutoff wavelength at 400 nm. Once inside the module, the photons are downshifted again by a wavelength shifter (WLS) plate to 430 nm, and guided towards a set of SiPMs via total internal reflection. SiPMs with high sensitivity to near UV and visible photons will therefore be used in the X-ARAPUCA. The FBK NUV-HD-SF SiPM design is one recently considered for the DUNE PDS, which has peak sensitivity to photons of 420 nm and can reach PDEs of >50% for over-voltage levels above $V_{\text{ov}} = 4\,\text{V}$ [188]. Other technologies considered are the HPK S14160 series SiPMs, which also have PDE > 50% for $V_{\text{ov}} > 2.5\,\text{V}$ [189]. PMTs are a comparable technology which are capable of single photon detection, and typically have quantum efficiencies at
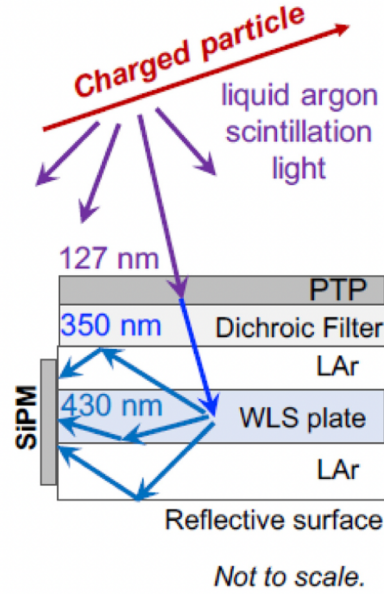
FIGURE 5.15: Illustration of the working principle for the X-ARAPUCA light trap modules to be used in DUNE. Figure taken from Ref [148].

the level of $\sim 20\%$ for 430 nm photons. Therefore SiPMs can offer a $\gtrsim 2.5\times$ better PDE in the DUNE PDS over alternative technologies.

5.5 DarkSide-20k

Chapter 4 discussed the upper limits placed on the spin-independent WIMP-nucleon elastic scattering cross-section from the 3.5 tonne-year exposure in DEAP-3600. With no discovery signal being claimed by DEAP-3600 or any other major direct detection experiment, a global programme of noble liquid experiments will proceed in searching the dark matter parameter space beyond current constraints, in the GeV–TeV mass range. The future of the LAr dark matter program, specifically, will be with the Global Argon Dark Matter Collaboration, which is a consortium of the DEAP-3600, DarkSide, ArDM, and MiniClean collaborations. The next generation LAr dark matter detector will be a 50 tonne (20 tonne fiducial mass) dual phase LAr TPC called DarkSide-20k [62]. Similar to other noble liquid TPC detectors, DarkSide-20k will make use of both scintillation and ionization signals for event reconstruction, and similar to DEAP, it will utilize PSD for particle identification. The effectiveness of combining these techniques in LAr technology has been demonstrated in DarkSide-50, which achieved a WIMP-nucleon cross-section upper limit of $1.14\times10^{-44}\,\mathrm{cm}^2$ for over a 16.7 ± 0.27 tonne·day exposure [63].

The projected sensitivity of the DarkSide-20k detector for a $\sim$200 tonne-year exposure is expected to be to 1.5×10^{-48} cm^2 (7.4×10^{-48} cm^2) for a 100 GeV (1 TeV) WIMP mass, as shown in Figure 5.16 [190].
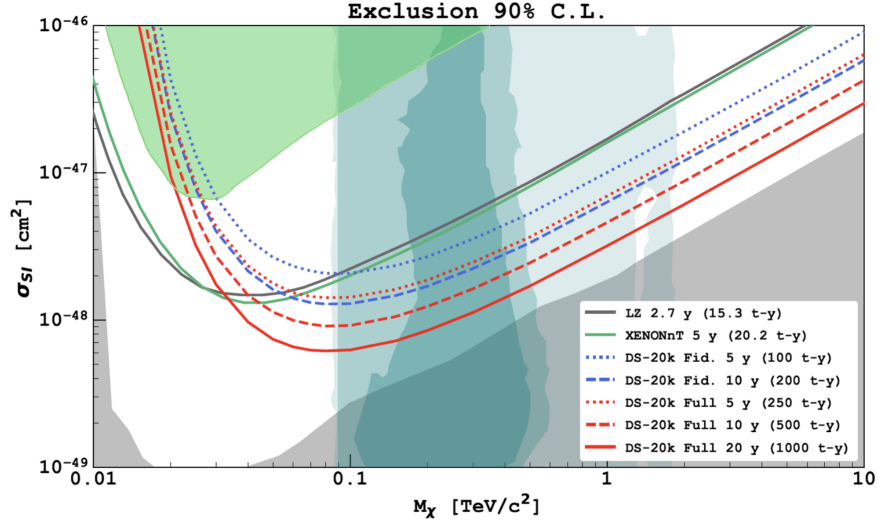
FIGURE 5.16: Projected sensitivity of the DarkSide-20k detector for various exposures, with projected exclusion curves from XENONnT (20.2 tonne-years) [191] and LZ (15.3 tonne-years) [192]. The green shaded region is the region of WIMP parameter space already excluded by LZ [61]; the grey shaded region represents the neutrino floor; and the turquoise filled contours represent the 1σ, 2σ, and 3σ regions from the pMSSM11[7] model as yet not excluded by astrophysical constraints and LHC data. Image modified from Ref [190].

5.5.1 SiPMs in DarkSide-20k

Aside from a much larger target mass than DEAP-3600 and DarkSide-50, DarkSide-20k will include other design features that will increase WIMP sensitivity; e.g. using argon sourced from deep underground rather than from the atmosphere, which will reduce the impact of ^{39}Ar β decays [62]. However, a key detector performance parameter for DarkSide-20k is PDE since WIMP signals are expected to be low energy single scatter events. Achieving maximal PDE is crucial for increasing energy resolution and sensitivity to low energy interactions, which would allow DarkSide-20k to lower the minimum energy threshold for its WIMP search. Recall from Figure 1.11 that the WIMP differential scattering rate falls rapidly with recoil energy, and thus reducing the energy threshold would increase WIMP acceptance significantly. In DarkSide-20k, increasing

---

[7]phenomenological Minimal SuperSymmetric Model with 11 free parameters

PDE from that which has been achieved in experiments like DEAP-3600 or DarkSide-50 will primarily be the result of using SiPMs over PMTs.

Aside from the reasons listed in Section 5.1, SiPMs are the photo-sensor of choice for DarkSide-20k because their high PDE in the visible photon wavelength range. As previously discussed in Section 5.4.2, various SiPM technologies have PDE > 50% in the visible wavelength range, which is more than 2.5× better than the quantum efficiency of the R5912-HQE PMTs used in DEAP-3600. In addition to their superior PDE, SiPMs also have a square profile, which allows them to be more efficiently packed in the photo-sensitive areas of the DarkSide-20k cryostat, as depicted in Figure 5.17. SiPMs will be deployed in DarkSide-20k in photosensing units called a PhotoDetector Modules (PDMs), which are $50 \times 50 \, \text{mm}^2$ tiles of SiPMs, and each PDM will be equipped with 24 $8 \times 12 \, \text{mm}^2$ SiPMs. The PDMs will then be coupled to $20 \times 20 \, \text{cm}^2$ motherboards and attached onto PDM arrays the top and bottom surfaces of the cryostat. In both the anode and cathode arrays, there will be a total of approximately 8200 PDMs [193], covering nearly 100% of each surface.
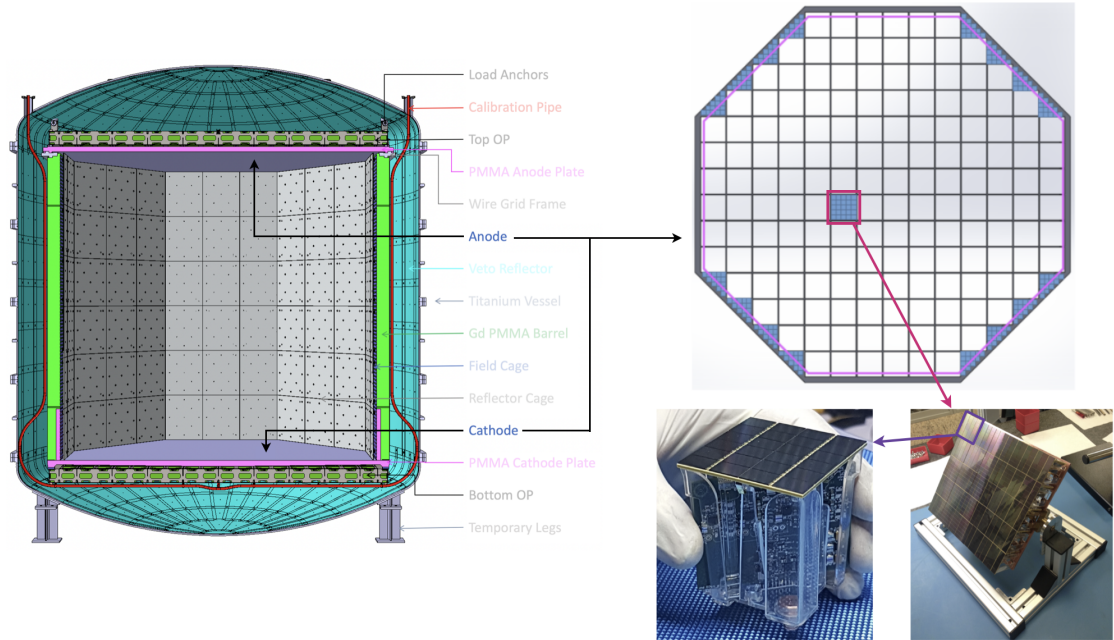
FIGURE 5.17: Depiction of the PhotoDetector Module (PDM) structure in the DarkSide-20k TPC. (Left) Cross-sectional 3D rendering of the DarkSide-20k TPC and cryostat. (Top-right) Top view of the TPC cathode/anode highlighting the grid of PDM tiles. (Bottom-right) Lab pictures of a PDM tile and individual PDM. Images from Ref [193].

5.6   Summary and Outlook

SiPMs are a key feature in future detectors—such as those discussed in Sections 5.3–5.5—primarily because of their superior PDE and energy resolution compared to PMTs and APDs, but also for the benefits listed in Section 5.1. However the future analyses in experiments like nEXO, DUNE, and DarkSide-20k will rely on in-depth external characterization of the dark noise, afterpulsing, and correlated cross-talk discussed in Section 5.2. This is the primary motivation for the MIEL experiment, which is the subject of Chapter 6.

Chapter 6

Microscopy with Injected and Emitted Light

In the previous chapter, the central focus was the future of astroparticle physics experiments with SiPMs as a key component in experimental designs. One challenge associated with using SiPMs is characterizing their various sources of correlated noise: afterpulsing; prompt and delayed internal cross-talk; and external cross-talk. This chapter gives a detailed overview of the measurement of optical cross-talk performed in Ref [194]. Section 6.1, reviews the central experiment of Ref [194]—the Microscopy with Injected and Emitted Light (MIEL) experiment—with its data acquisition operations detailed in Section 6.2, background removal techniques in Section 6.3, and calibration in Section 6.4. Imaging measurements are described in Section 6.5, along with emission microscopy images of the SiPMs used in this experiment. The data taking procedures and analysis which yields spectral measurements of the SiPMs are reviewed in Sections 6.6 and 6.7. Lastly, experimental uncertainties and the discussion of final results follows in Sections 6.9 and 6.10.

This chapter presents work done by Dr. Giacomo Gallina and me, supervised by Dr. Fabrice Retière. Giacomo performed the commissioning work in the construction of the MIEL apparatus prior to my arrival at the TRIUMF research facility, with the final iteration of the MIEL apparatus was built in equal parts by Giacomo and me. The data taking procedures were formulated by Fabrice and me, and I was responsible for all data acquisitions and analysis.

6.1 The MIEL Experiment

6.1.1 Experimental Design Considerations

The MIEL experimental apparatus was designed to characterize the emission spectrum and photon yield of secondary photons generated by silicon undergoing avalanche breakdown; this is a dim light source, emitting $\mathcal{O}(1\text{--}10)$ photons per charge avalanche (see results in Section 6.10). In this context, silicon is known to primarily emit in visible and near-infrared (NIR) [163, 166, 195], which is the photon energy region of interest for MIEL. At higher photon energies—e.g. in the UV and VUV ranges—the attenuation length in silicon varies between $10^{-6}\text{--}10^{-5}$ cm [196], which suppresses SiPM emission of photons with $\lambda \lesssim 400$ nm. Secondary photon emission in this range has indeed been observed to be vanishingly small in previous measurements [197], which are shown in Figure 6.1a. At lower energies, i.e. $\lambda > 1107.6$ nm, silicon-based detectors typically have limited sensitivity to photons due to the silicon band-gap[1] [198]. Figure 6.1b demonstrates this with rapidly decreasing sensitivity of NIR-sensitive silicon-based photosensors as the incident photon wavelength approaches 1100 nm. Photons with wavelengths as long as 1600 nm are still produced in avalanche breakdown of silicon (see Figure 6.1a), but this spectral range is ignored for the purposes of MIEL, due to lack of expected sensitivity. The upper bound of MIEL's wavelength range is in fact limited to 1020 nm because of the limited sensitivity to NIR photons of the CCD camera described in Section 6.1.4.

These signal qualities—i.e. a dim source of visible-to-NIR photons—call for components that are efficient in the transmission and detection of NIR photons, as well as mechanically and electrically stable over long periods of time for photon collection. Between photon collection and detection efficiencies, and attenuation, less than 1 in 10^8 photons emitted by the investigated SiPMs end up contributing to the measured signal; therefore exposure times from 2–8 hours are required to build spectra with adequate statistics. More details on these losses are given in Sections 6.4, 6.5, and 6.6. Additionally, heavy suppression of background photons is required to obtain a good signal-to-noise (S/N) ratio. Note that here, the 'signal' is the secondary photon emission from the SiPM, which in most other contexts would be considered as noise. For MIEL, S/N is defined

---

[1]Recall from Section 5.1.1 that doped silicon has a comparatively smaller band-gap than pure silicon, depending on the concentration of the charge carriers.

(A)

(B)
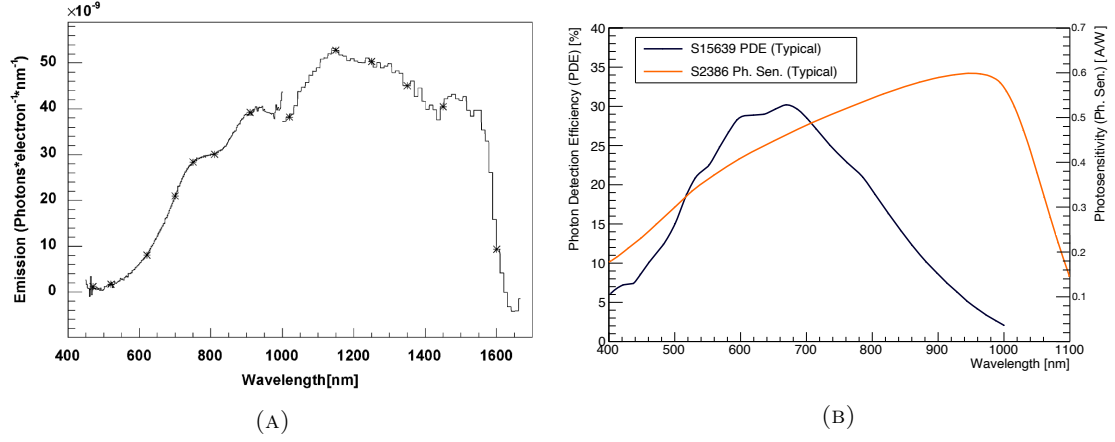
FIGURE 6.1: (A) Results of Ref [197] showing suppressed secondary photon emission of UV photons in silicon undergoing avalanche breakdown. (B) The Photon Detection Efficiency (PDE) and Photosensitivity (Ph. Sen.) of the Hamamatsu S15639 MPPC and S2386 Avalanche Photodiode, respectively.

as

$$\text{S/N} = \frac{S(\lambda) - \text{E}[B]}{\text{RMS}[B]},\tag{6.1}$$

where

$$S(\lambda) = \text{SiPM Emission Spectrum Amplitude vs wavelength, } \lambda,$$

$$\text{E}[B] = \text{Baseline mean after background removal,}$$

$$\text{RMS}[B] = \text{Baseline root-mean-square after background removal.}$$

The microscopy setup depicted in Figure 6.2 was designed and built at TRIUMF in order to accommodate spectral and imaging measurements for the physical size of SiPMs, which is typically 10s of mm^2. This apparatus, dubbed as *MIEL*, includes instruments with spatial precision down to the micron scale. The MIEL setup comprises:

(i) Olympus IX83 microscope

(ii) Princeton Instruments (PI) HRS 300-MS SpectraPro Spectrometer

(iii) PI PyLoN 400BR_eXcelon CCD camera

The SiPM is affixed to a translation stage above the microscope, with motorized position adjustment in the XY-plane of Figure 6.2. The SiPM position is controlled and measured using a ThorLabs Kinesis K-Cube stepper motor, with precision down to 0.1 μm. The
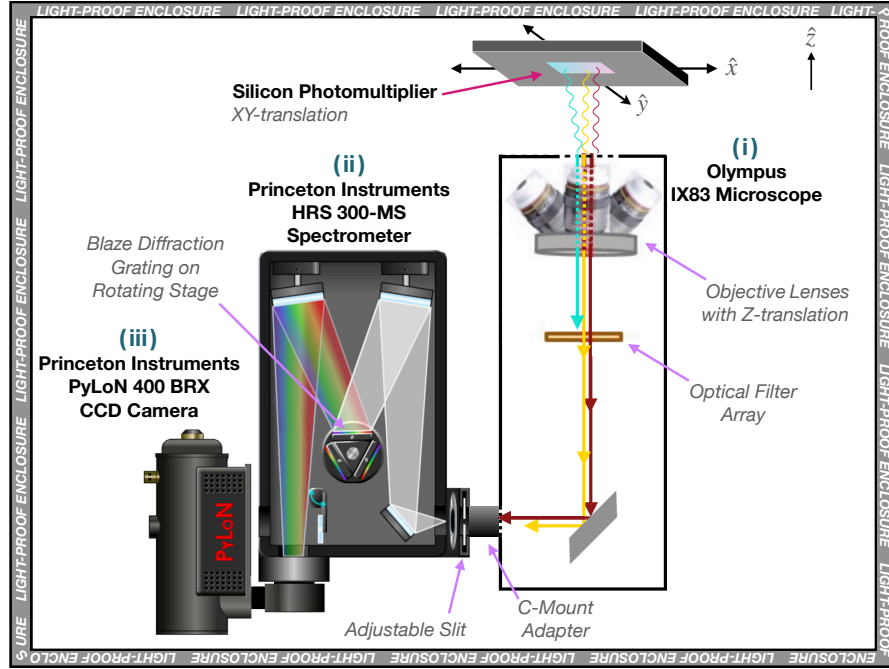
FIGURE 6.2: Schematic diagram of the MIEL apparatus used for SiPM imaging and spectroscopic measurements.

SiPM is biased by a Keithley 6487 Picoammeter, which is also used to monitor the current flowing through the SiPM over time. Note that the SiPM is the light *source* for the measurements described here. The over-voltages used (see Section 6.2) are 2–3× larger than typical operating conditions, which drive steady currents of $\mathcal{O}(0.01$–$1)$ mA through the SiPM. In the absence of light, current in the SiPM is primarily from avalanches induced by dark noise/dark counts. For currents on the mA scale, this corresponds to a dark count rate of >50 MHz.[2] For comparison, the maximum dark count rate for the Hamamatsu VUV4 SiPM is 3 MHz, when operated at the recommended over-voltage [145]. Therefore, the SiPM signal itself is far too noisy to obtain any useful or interesting information.

The entire apparatus is contained within a steel, light-proof enclosure, with all components controlled externally. The spectrometer is controlled by the PI LightField software (see Section 6.1.5), while the microscope is controlled by a combination of Olympus software and hardware.

---

[2]Assuming charge avalanches contain $\sim 10^6$ charge carriers

6.1.2   IX83 Microscope

The main functions of the Olympus IX83 microscope are imaging of the SiPM and photon collection for spectral measurements. There are three components within the microscope pertinent to the analysis contained in this chapter: a filter array, used to insert a 550 nm long-pass filter in the light path; an array of objective lenses; and the side port of the microscope coupling to the input of the spectrometer.

The long-pass optical filter (transmission efficiency curve shown in Figure 6.4b) only transmits photons with wavelengths, $\lambda \gtrsim 550$ nm. Its sole function is to suppress the 2nd order diffraction features from the $\lambda < 550$ nm spectral range when measuring $\lambda \geq 900$ nm. This point is explained in greater detail in Section 6.1.3.

The MIEL setup uses three objective lenses: one for imaging and two for spectroscopy in the visible and NIR portions of SiPM emission spectra. This is done to maximize the sensitivity of MIEL to photons with $450 \leq \lambda \leq 1020$ nm. Table 6.1 provides a list of the objective lenses installed in MIEL along with their usage, as explained in Section 6.2. Additionally, it provides their magnifications and numerical apertures, the latter of which is an important quantity to note for Section 6.7.3. Numerical aperture, NA, is defined using Snell's Law as,

$$\text{NA} = n_{\text{loc}} \sin(\theta_{\text{acc}}), \tag{6.2}$$

where n_{loc} is the local index of refraction between the source and the objective lens, θ_{acc} is the maximal acceptance angle as depicted in Figure 6.3. Figure 6.4a shows the transmission efficiencies of the LMPLFLN20X and LCPLN20XIR objectives.

Lens Model	Magnification	Numerical Aperture	Primary Use
PLCN4X-1-7	4×	0.1	Imaging
LMPLFLN20X	20×	0.4	Visible Spectroscopy
LCPLN20XIR	20×	0.45	NIR Spectroscopy

TABLE 6.1:   List of Olympus objective lenses used in MIEL, with their numerical apertures, magnifications, and primary purposes.

The side port of the microscope is a one of three image outputs (the other two being the eyepiece, and an auxiliary camera attachment); it directly couples and passes the image to the input of the spectrometer. The microscope controls the output using an internal
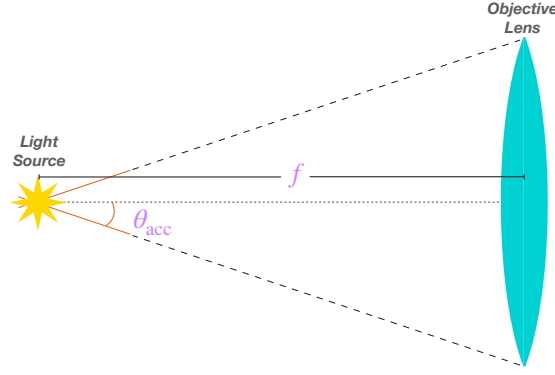
FIGURE 6.3: Depiction of the numerical aperture of an objective lens, defined mathematically in Equation 6.2. θ_{acc} is the maximal photon acceptance angle of the objective lens with a light source at the focal point, a distance f away from the lens.
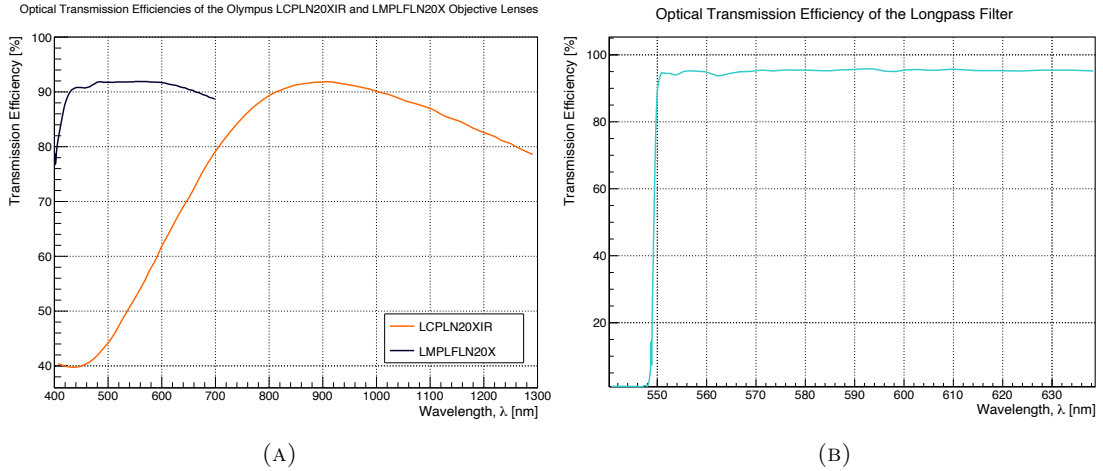
FIGURE 6.4: Optical transmission efficiencies of the LMPLFLN20X and LCPLN20XIR objective lenses (A), and the long-pass filter (B). The long-pass filter is used to suppress 2nd order diffraction features for NIR spectroscopy (see Section 6.2). This data was provided by Olympus and ThorLabs, respectively, via hardware specifications.

mirror and the side port has collimating hardware to maintain image quality, both of which have wavelength dependent reflection and transmission efficiencies. Olympus was able to provide 6 data points for the purposes of calibrating MIEL, which are provided in Table 6.2.

In lieu of the IX83 sample translation stage, a custom built SiPM translation apparatus was designed for MIEL, which included an aluminum mounting structure—designed and machined on-site at TRIUMF—and a 2D translation stage driven by two Kinesis K-Cube DC stepper motors. This apparatus, shown in Figure 6.5, gives MIEL the ability to control the SiPM position relative to the objective lenses with a precision of $0.1\,\mu\mathrm{m}$, in the X-Y plane. For the Z-direction, the IX83 microscope has DC motor driven

Wavelength [nm]	Transmission Efficiency [%]
300	0
400	86
500	95
700	95
950	87
1200	70

TABLE 6.2: Olympus IX83 microscope side port transmission efficiency data points provided by Olympus for the microscope used in MIEL.

control over the vertical distance between the objective lens and the SiPM, with $0.01\,\mu$m precision.
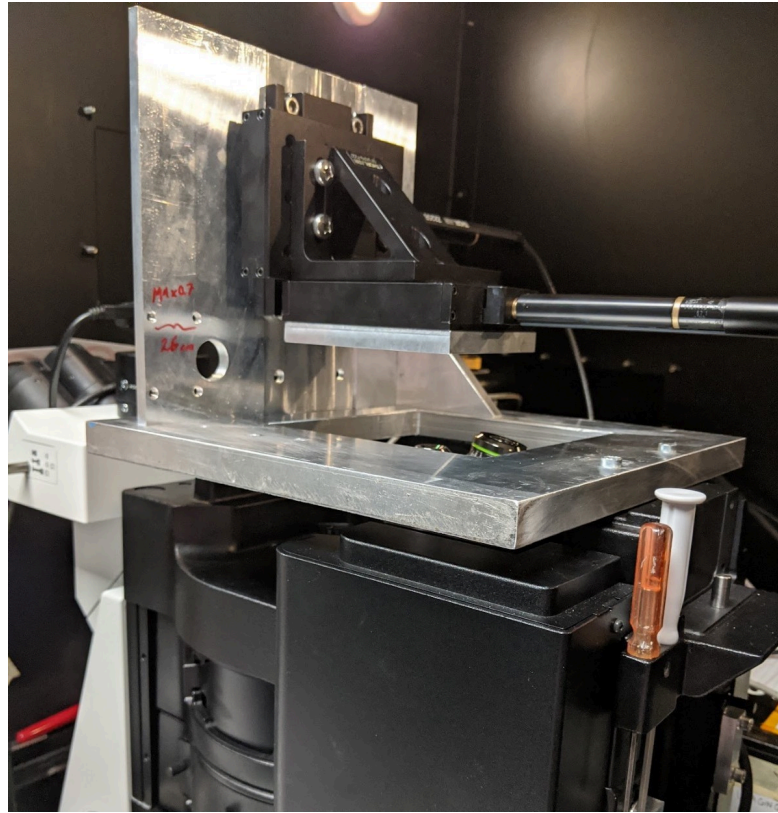
FIGURE 6.5: SiPM translation stage mounted on the IX83 microscope at TRIUMF.

6.1.3   HRS 300-MS SpectraPro Spectrometer

The PI HRS 300-MS SpectraPro spectrometer is the component which disperses the spectral components of input image. It is attached to the microscope side port via a C-mount adapter. At the input of the spectrometer is a slit with an adjustable width, which can be used to control the wavelength resolution of the experiment. A thinner slit results in better wavelength resolution, but it also comes at the cost of photon collection

efficiency, which reduces the S/N ratio. A slit width of $200\,\mu$m was chosen and fixed in place. This was wide enough to produce measurable spectra in less than 9 hours (the maximum allowable exposure time in LightField for a single exposure), and sufficiently narrow for accurate wavelength calibrations using the IntelliCal system. The slit can also be removed entirely from the optical path; the use of this feature is explained in Section 6.2.

Internally, the spectrometer has the following components:

  (i) a 300 lines/mm blazed diffraction grating with peak efficiency at 300 nm

 (ii) a 150 lines/mm blazed diffraction grating with peak efficiency at 800 nm

(iii) three high-reflectivity mirrors with Acton #1900 Al+MgF$_2$ coating
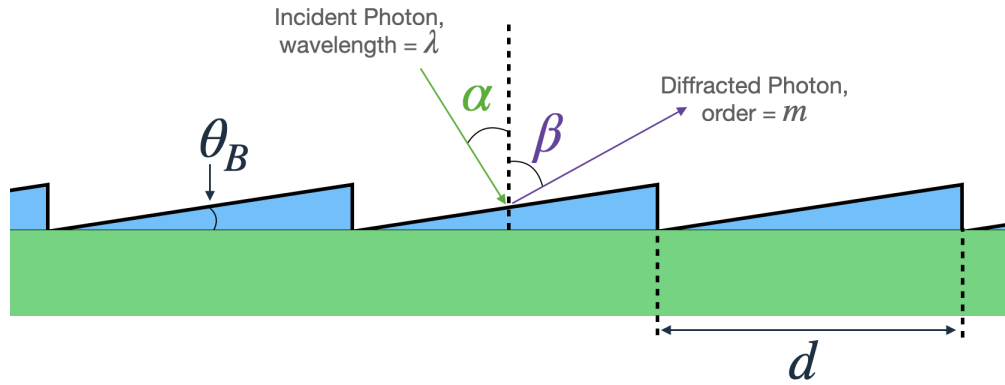
FIGURE 6.6: Schematic diagram of a blazed reflective diffraction grating, with labels for the blaze angle θ_B and the parameters appearing in Equation 6.3.

Generating photon spectra in MIEL is achieved using *blazed* reflective diffraction gratings. Figure 6.6 shows a schematic diagram of a typical blazed grating, with a characteristic saw-tooth profile. Since these are reflective gratings, they can also be used as mirrors for imaging as well as spectral measurements. To illustrate this, consider the grating equation:

$$m\lambda = d\big(\sin(\alpha) + \sin(\beta)\big), \tag{6.3}$$

where m is the diffraction order, λ is the incident photon wavelength, d is the spacing between adjacent grooves in the grating, α is the angle of incidence, and β is the angle of diffraction (note: α and β are signed angles). If $m = 0$, the only solutions for α and β are $\alpha = \beta = 0$ and $\alpha = -\beta$, which are consistent with specular reflection and

independent of λ. Therefore at 0th order, no separation of the image into its spectral components occurs—i.e. a pure reflection of the image—whereas the locations of higher order diffraction peaks are wavelength dependent.

Note that if α is fixed, there will be cases where two wavelengths at different diffraction orders will diffract into the same angle β, i.e.

$$m_1\,\lambda_1 = d\big(\sin(\alpha) + \sin(\beta)\big) = m_2\lambda_2, \tag{6.4}$$

$$\therefore \quad \frac{m_1}{m_2} = \frac{\lambda_2}{\lambda_1}, \tag{6.5}$$

where m_i is the diffraction order of photons with wavelength λ_i, and Equation 6.5 is a general condition for overlapping diffraction orders. Since MIEL measures SiPM emission spectra from 450–1020 nm, it's possible for the 2nd order features of wavelengths $450 \leq \lambda_2 \leq 510$ nm to overlap with the 1st order features of wavelengths $900 \leq \lambda_1 \leq 1020$ nm. The 550 nm long-pass filter used in the microscope filter array removes these 2nd order diffraction features up to 1100 nm, which eliminates any spectral overlapping in MIEL.

In a blazed grating, the angle of the saw-tooth relative to the substrate is called the *blaze angle*, θ_B. The value of θ_B is the parameter that determines which wavelength is diffracted with the highest efficiency; i.e. the blaze wavelength, λ_B. The gratings in components (i) and (ii) have θ_B such that λ_B are 300 nm and 800 nm, respectively. These gratings were chosen to maximize the spectrometer efficiency over the wavelength range of 450–1020 nm, and were used in spectral measurements as described in Section 6.2. The mirrors were designed to focus the light onto the diffraction gratings, and then again onto the CCD camera pixels. Figure 6.7 shows the transmission and reflection efficiencies of all components inside the spectrometer. The 300 nm blazed grating has better efficiency than the 800 nm blazed grating for $\lambda < 490$ nm, and the maximum efficiency between both of them never falls below 44% over the 450–1020 nm wavelength range. The reflectivity of the mirrors varies between 83–95% over that same wavelength range.

Switching between the two types of gratings and adjusting the central wavelength for a spectral measurement are done to optimize the sensitivity of the MIEL apparatus to different wavelength regimes. These are both done using PI's AccuDrive scanning
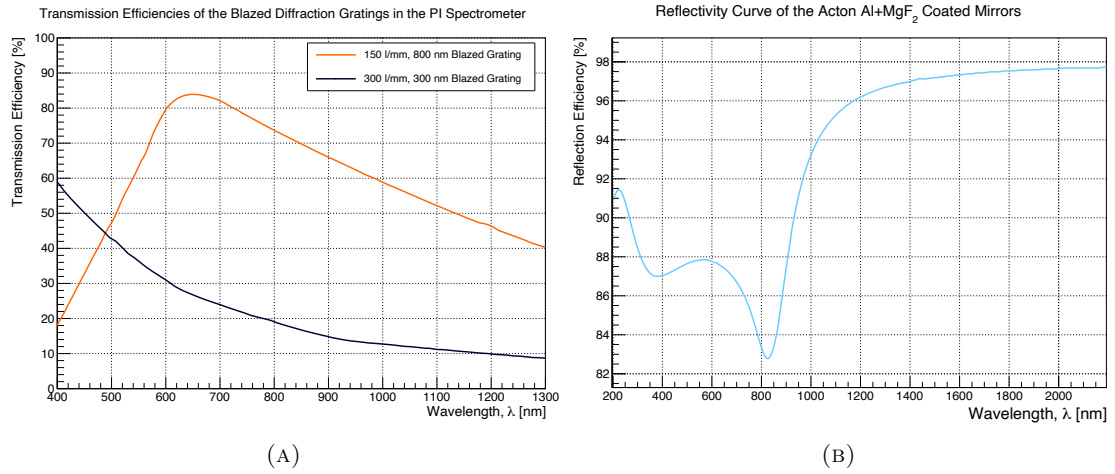
FIGURE 6.7: Optical transmission efficiencies of the 300 nm and 800 nm blazed diffraction gratings (A), and the reflectivity curve of the Acton Al+MgF$_2$ coated mirrors (B). This data was provided by PI via hardware specifications.

system. This system uses a DC motor driven turret to rotate a mounting stage, which can hold up to three diffraction gratings. The orientation of the stage determines which of the gratings is being used for a given measurement, and which photon wavelength is focused onto the centre of the CCD camera. The AccuDrive system was tested by PI and shown to be able to reproduce wavelength positioning on the CCD to within ± 0.52 camera pixels, or $\pm 10.4\,\mu$m.

6.1.4 PyLoN 400BR_eXcelon CCD Camera

The PI PyLoN 400BR_eXcelon CCD camera is coupled directly to the output of the spectrometer. It is a silicon-based CCD with a 1340×400 pixel array, where each pixel is a square of side length $20\,\mu$m. To maintain data quality over the duration of hours-long exposure times, this CCD camera is equipped with a 4 L dewar for holding liquid nitrogen (LN2). The LN2 keeps the pixel array temperature fixed at $(-120 \pm 1)\,^\circ$C, suppressing dark current in the pixels which would make measurements unstable over long periods of time.

As the PyLoN 400BR_eXcelon CCD is a silicon-based device, its quantum efficiency (QE) begins to drop significantly with photon wavelengths approaching the band-gap energy of silicon ($\lambda = 1107.6\,$nm). Figure 6.8 shows the QE curve of a typical PyLoN 400BR_eXcelon camera. The QE drops below 10% at $\sim$1020 nm, which was the main reason for setting the upper limit of the spectral range in MIEL at this wavelength.
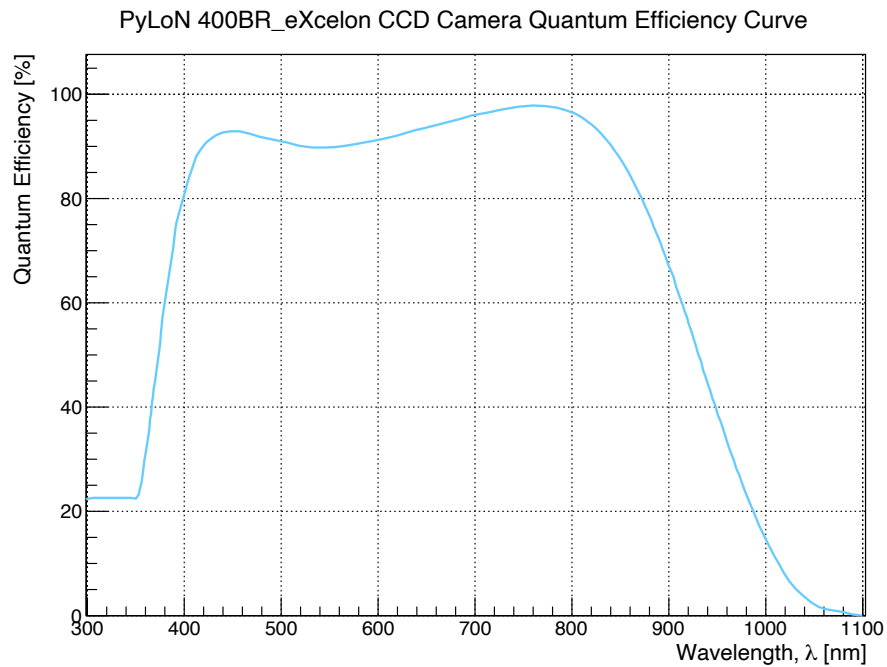
FIGURE 6.8: The PI PyLoN 400BR_eXcelon CCD camera QE curve. This data was provided by PI via hardware specifications.

6.1.5   LightField Software

LightField is software designed by PI to interface with their hardware. For the HRS 300-MS SpectraPro Spectrometer and the PyLoN 400BR_eXcelon CCD camera, LightField is able to control the following parameters:

HRS 300-MS SpectraPro Spectrometer

(i)   Choice of diffraction grating

(ii)   Spectrum central wavelength

(iii)   Wavelength calibration light source, method and wavelength range

(iv)   Intensity calibration light source and wavelength range

PyLoN 400BR_eXcelon CCD Camera

(i)   Exposure time

(ii)   Acquisition time background subtraction

(iii)   Acquisition time cosmic ray removal

(iv)   Pixel well capacitance (low noise, high capacitance)

(v) Analog gain (low, mid, high)

(vi) Digitization rate (50 kHz–4 MHz)

(vii) Operating temperature (fixed at $-120\,^{\circ}$C)

Items (i) and (ii) for the spectrometer are entirely dependent on the mode of measurement (see Section 6.2) and the part of the spectrum being measured for a given acquisition. Items (iii) and (iv) pertain to a premium extension of LightField, which is designed for wavelength and relative light intensity calibrations. This software extension, called IntelliCal [199], comes with NIST traceable light sources for both the wavelength and intensity calibrations. Note that the intensity calibration done by IntelliCal is a *relative* calibration, which was deemed insufficient for spectral measurements where the results were to be reported in absolute quantities. This being the case, it was decided that a separate photon detection efficiency (PDE) analysis would be done in lieu of using IntelliCal. A general overview of this point is given in Section 6.4.

Items (i)–(iii) in the list of CCD camera parameters were determined at acquisition time based on the requirements of a given measurement. For example, a bright source of light would require a small exposure, whereas a dim source would need a longer one. Both of these would need background subtraction, and some degree of cosmic ray removal (see Section 6.3.1) depending on the duration of the exposure. The remaining CCD camera parameters were set in order to maximize the S/N ratio (recall Equation 6.1). The pixel well capacitance can be set to a higher value for brighter sources of light so that signals don't get clipped in digitization, or to a lower value for dimmer sources so that high frequency Johnson noise[3] is suppressed. These are labeled as "high capacitance" and "low noise," respectively, the latter of which was chosen for spectral measurements in MIEL. The analog gain scales the voltage generated by a detected photon in a pixel. The settings are simply "low," "mid," and "high;" given that the expected photon flux from a SiPM is low, the highest gain setting was chosen. The digitization rate determines how often the pixel wells are emptied, their contents sampled, and then stored in memory. Slower digitization rates integrate a signal over a longer period of time and effectively suppress noise via averaging. Lastly the operating temperature was fixed at the minimum allowable by LightField ($-120\,^{\circ}$C), which minimizes dark current and readout noise.

---

[3]Johnson (or Johnson-Nyquist) noise refers to electrical noise generated by thermal motion of charge carriers in a conductor [200, 201].

Analysis of raw CCD data requires knowledge of the readout noise (reported here as a RMS value in units of electron charge, e^-) and analog-to-digital unit (ADU) conversion (e^-/ADU). These quantities will vary based on the choice of CCD operating parameters (iv)–(vii). Table 6.3 summarizes how these quantities change with digitization rate[4] with items (iv), (v), and (vii) held at the aforementioned settings.

Digitization Rate [MHz]	0.05	0.10	0.20	0.50	1.00	2.00	4.00
Readout noise [e^- (RMS)]	3.26	3.30	3.69	4.37	5.40	13.5	19.5
ADU Conversion [e^-/ADU]	0.7	0.7	0.7	0.7	0.7	0.89	0.89

TABLE 6.3: Readout noise and ADC conversion factors for digitization rates ranging from 50 kHz to 4 MHz, measured by the manufacturer. These values are for the chosen CCD operating parameters in MIEL: analog gain = "high", pixel well capacitance = "low noise," and operating temperature = $-120\,°$C.

6.2   Modes of Measurement

While the primary function of the MIEL apparatus is to measure secondary photon emission spectra from SiPMs, the analysis described in Section 6.7.2 requires imaging data in order to estimate the total emission over the entire SiPM surface. For this reason, the MIEL apparatus has two basic modes of operation, which utilize different combinations of objective lenses, filters, and gratings, summarized as follows.

Imaging mode

Imaging mode is used to record microscopic images of the biased SiPM in dark conditions. One of the the PLCN4X-1-7 or LMPLFLN20X objectives was used (depending on the desired field of view) with no optical filters along the light path. The adjustable slit of the PI spectrometer was disengaged and the 300 nm blazed grating was selected and aligned with its 0th order peak centred on the CCD camera. At 0th order, a blazed grating effectively acts as a mirror, and the 300 nm blazed grating (300 lines/mm) has a higher line density than the 800 nm blazed grating (150 lines/mm), which provides better separation from the 1st order diffraction features.

---

[4]The digitization rate is a parameter that was slightly more free to vary throughout the development of measurement procedures in MIEL, but all measurements reported here were digitized at 50 kHz.

Spectroscopy mode

Spectroscopy mode is used to measure the spectral components of the secondary photons emitted by the biased SiPM, also under dark conditions. To maximize the transmission of the PI spectrometer and the IX83 microscope in the wavelength range spanning 450–1020 nm, two combinations of gratings, filters, and microscope objectives were used. Within the 450–550 nm range, the LMPLFLN20X objective lens was used with no optical filters, in combination with the 300 nm blazed grating centring the 1st order diffraction feature of 500 nm photons on the CCD pixel array (this configuration is hereafter called *Visible Spectroscopy mode*). Wavelengths between 550–1020 nm were measured using the LCPLN20XIR objective, and the 800 nm blazed grating with the 1st order feature of 800 nm centred on the CCD. Additionally, the 550 nm long-pass filter was inserted into the IX83 light path to cut any 2nd order diffraction features from wavelengths below 550 nm (this configuration is hereafter called *NIR Spectroscopy mode*). As previously mentioned in Section 6.1.3, the spectrometer adjustable slit was set to a width of approximately 200 μm, corresponding to a wavelength width in Full Width at Half Maximum (FWHM) of 0.6 nm for the 300 nm blazed grating, and 1.4 nm for the 800 nm blazed grating. These values were obtained by imaging the slit and measuring the its FWHM in CCD pixels, then converting to nanometres using the wavelength calibration described in Section 6.4.1.

In either measurement mode, the applied over-voltage to the SiPMs was between 10–12 V. Based on the I-V curves shown in Figure 5.5, these over-voltages correspond to SiPM currents between 75 μA–2 mA, which is well beyond currents at typical operating conditions. Since the number of photons emitted per charge carrier is rather low (on the order of 10^{-6} γ/e^-, see Section 6.10) and this chapter focuses on SiPM photon emission driven by dark noise induced avalanches, the high over-voltages were needed to generate a large number of avalanches in the SiPMs. With the over-voltages reported in Table 6.4 the S/N ratio at 800 nm was 6.8±1.

The main physics goal of MIEL is to obtain secondary photon emission spectra of a FBK VUV-HD3 SiPM and a HPK VUV4 MPPC, varying with over-voltage. For this, the following post-acquisition analysis procedure was devised to convert raw data into the final spectrum:

1. **Background Removal**

   a) Remove cosmic rays from signal and background for measurements in both NIR and visible spectroscopy

   b) Subtract background from signal, pixel-by-pixel

2. **Spectral Analysis**

   a) Correct NIR and visible spectra for wavelength dependent photon losses, e.g. photon detection efficiency, absorption, dispersion, etc.

   b) Normalize NIR and visible spectra to units of photons (γ) emitted per charge carrier (e^-) per unit wavelength (nm)

3. **Final Processing**

   a) Integrate pixels along Y-axis to produce 1D spectra for both NIR and visible spectroscopic measurements

   b) Rebin visible and NIR spectra such that both have equal bin widths

   c) Stitch together the visible and NIR parts of each spectrum corresponding to the same exposure time

The background removal step is discussed in Section 6.3, while spectral analysis is summarized in Section 6.7. Note that parts of the spectral analysis discussion rely on the Calibration and Imaging Measurements sections (Sections 6.4 and 6.5, respectively).

6.3   Background Removal

The primary sources of background in the spectroscopic measurements shown in Section 6.10 were ambient photons within the light-proof enclosure, and high energy cosmogenic particles (hereafter simply referred to as cosmic rays). The ambient photons primarily come from the blackbody radiation of the air and hardware inside the light-proof enclosure, but can also come from leakage current in the SiPM. Cosmic rays are a highly localized background in the CCD, and effectively removing them requires an algorithmic approach.

6.3.1 Cosmic Ray Removal

The cosmic ray flux at sea level is $86.15\,\mu^{\pm}/\mathrm{m}^2/\mathrm{s}$ [74], which would mean that the CCD pixel array, with a surface area of $2.144\times10^{-4}\,\mathrm{m}^2$, can observe as many as $\mathcal{O}(10^3)$ cosmic rays over the exposure times listed in Table 6.4. Cosmic rays generate showers of highly ionizing particles in the upper atmosphere, such as muons or charged mesons. When one of these particles deposits its energy in a set of CCD pixels, there is a current generated in those pixels much larger than that generated by photons. The result is highly localized bright spots on the recorded image, and unnaturally tall and narrow peaks on the resulting spectrum. Figure 6.9 demonstrates how cosmic rays can dominate a measured spectrum, in both a single row and integrated over all rows.
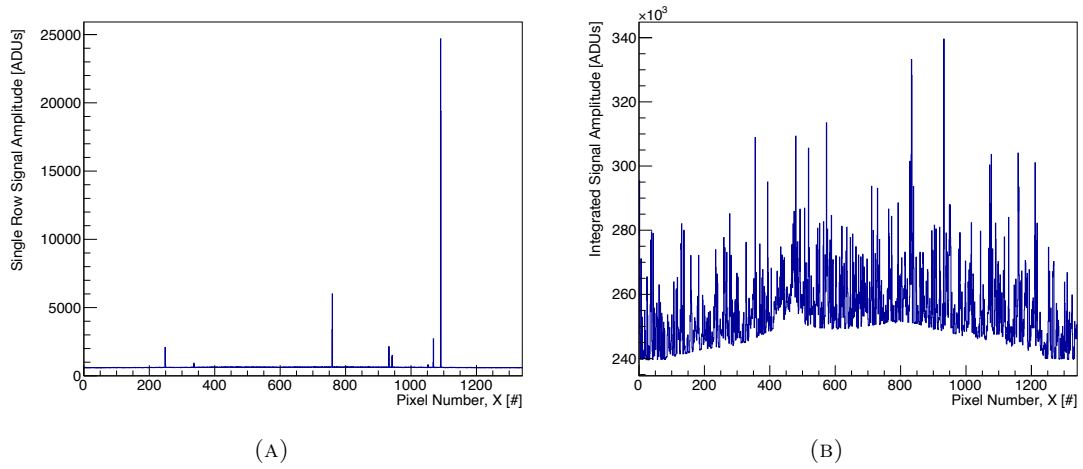
FIGURE 6.9: Signal amplitudes for one row of CCD pixels (A), and integrated over all rows (B) after a 4h 45m exposure to the biased FBK VUV-HD3 SiPM with no cosmic ray removal.

While there is an option in LightField to remove the signature of cosmic rays with an acquisition-time image processing function, the decision was made to move this step to post-acquisition analysis. The cosmic ray removal (CRR) algorithm designed and implemented for MIEL utilizes a C++ class in the ROOT analysis package called `TSpectrum`. This class was designed for γ-ray spectroscopy and has many useful functions for generic spectral analysis, including a background estimation function, called `TSpectrum::Background()`. This function estimates the local background value of an input spectrum using a Sensitive Nonlinear Iterative Peak-clipping (SNIP)[5] algorithm [202, 203]. The SNIP algorithm, as it is implemented in `TSpectrum::Background()`, is provided in Appendix B.2 as a snippet of pseudo-code [203].

---

[5]This acronym is a STrETCH.

The SNIP algorithm starts by performing a "Log-Log-Square Root" (LLS) operation on an input series, S, which selectively enhances smaller peaks so they don't get misidentified as part of the background. The next step of the algorithm compares a sample point on the modified series, S_n, to the average of two other points on the series at a distance m away, i.e. S_{n-m} and S_{n+m}. The sample point is then reassigned to be the smaller of the two,

$$S_n \rightarrow \min\big(S_n, \ ^1\!/\!_2(S_{n-m} + S_{n+m})\big). \tag{6.6}$$

In the case of S_n already being at the background level, the mean of $S_{n\pm m}$ will be approximately equal to S_n, so the SNIP algorithm's choice between the two is inconsequential. Conversely, in the case of S_n being at or near a peak, the average value of $S_{n\pm m}$ will be some amount smaller than S_n, depending on m. Therefore the SNIP algorithm will pick the average rather than the sample point.

The last key feature of the SNIP algorithm is that the user provides a 'width' parameter, σ. The choice of width parameter should be large enough to put $S_{n\pm\sigma}$ at background level in the vicinity of a peak at S_n, but not so large such that, if the background isn't a constant over the whole series, $S_{n\pm\sigma}$ is in a potentially different background regime. The SNIP algorithm repeats the process described thus far, incrementing m from zero up to σ. With each iteration, the sample points converge towards the background level.

The MIEL CRR algorithm is provided in Appendix B.3. This algorithm takes a CCD image of a SiPM spectrum as input, which it reads as a 2D array of pixel amplitudes. It then applies the SNIP algorithm to the image row-by-row, treating each row as a series with extremely tall and narrow peaks from cosmic ray impacts on a small number of CCD pixels. The SNIP algorithm will return an estimate of the "background," i.e. the SiPM emission spectrum, in the nth row of the image, with input from the user describing the width of the cosmic ray peaks, σ_{cr}. The user also provides a threshold value above the background, Y_{thr}. If this threshold is exceeded, that pixel was likely hit by a cosmic ray, and its amplitude is set to the estimated "background" level.

The width of cosmic ray peaks was roughly measured by creating a distribution of the number of consecutive pixels in a given row above a threshold of 1500 ADUs. Based on Figure 6.9a, typical cosmic ray peaks rise above and fall back below this threshold in the span of a couple of pixels. More precisely, 99.78% of cosmic rays generate peaks
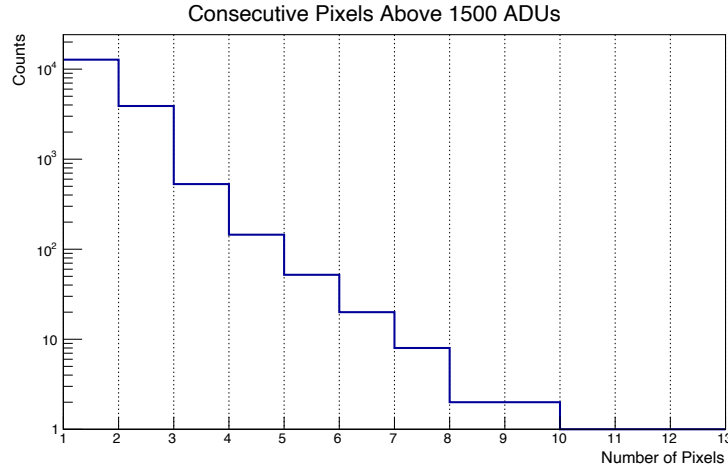
FIGURE 6.10: Distribution of the number of consecutive pixels in a single row above a threshold value of 1500 ADUs.

with widths $\leq$5 pixels, which is reflected in the distribution in Figure 6.10. Therefore a conservative nominal cosmic ray width for the CRR algorithm was set at 15 pixels. The choice of Y_{thr} for the CRR algorithm was set at approximately five times the readout noise RMS value for the relevant PyLoN CCD Camera operating parameters: 25 ADUs. The same logic as the 5σ criteria for claiming a discovery in particle physics experiments was adopted here to flag cosmic rays. Figure 6.11 shows the performance of the CRR algorithm with a sample FBK VUV-HD3 spectrum in NIR over a 4.75 hour exposure time. The top image is the raw measurement and the bottom is the same image after applying the CRR algorithm. Setting the threshold at 25 ADUs allows the CRR algorithm to flag all cosmic rays, while leaving the spectral measurement virtually unaltered. Given the disparity in the amplitudes between pixels that were and were not hit by a cosmic ray, the CRR algorithm's effectiveness is not highly sensitive to the choice of threshold parameter, provided it stays comparable to the baseline RMS.

6.3.2 Ambient and Leakage Current Background Removal

Ambient photons constitute an evenly distributed background across the CCD pixel array and contribute to a flat baseline value for each spectral measurement, while the photons from leakage current in the SiPM have a nonuniform spectrum. To remove these backgrounds, they were first measured using the same procedure outlined at the top of Section 6.6.1, but with the power supply to the SiPM turned off. Next, the raw image of the background measurement was processed with the CRR algorithm described

FIGURE 6.11: A comparison of a raw spectral measurement of the FBK VUV-HD3 over a 4h 45m exposure, before (top) and after (bottom) applying the CRR algorithm described in this section. The z-axis scaling is set so that the SiPM spectrum is visible in the same image as the cosmic rays.

in Section 6.3.1. Figure 6.12 shows the profile of the ambient and leakage current photon background for a NIR spectroscopy measurement over 4h 45m, after passing through the CRR algorithm. After removing cosmic rays in both spectral and background measurements, each background was subtracted from its corresponding spectral measurement.
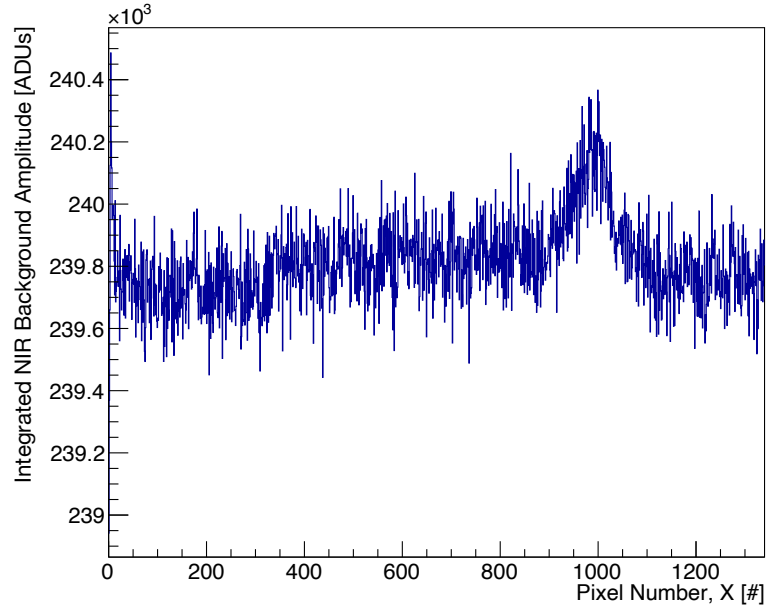
FIGURE 6.12: Integrated baseline measurement of the FBK VUV-HD3 SiPM in NIR spectroscopy mode.

6.4   Calibration of MIEL

To produce a spectrum with MIEL, spectrometer data in raw units—i.e. pixel amplitudes in ADUs and pixel numbers—must be calibrated to return quantities in physically meaningful units. For the measurements reported here, pixel numbers are converted to wavelengths in [nm] and pixel amplitudes are converted to photons per charge carrier per unit wavelength $[\gamma/e^-/\text{nm}]$. Recall from Section 6.1.4 that the CCD camera has a 1340×400 pixel array (in X- and Y-directions, respectively), therefore raw data in MIEL has three components: pixel number in the X-direction, pixel number in the Y-direction, and pixel amplitude in ADUs. By design, the pixel number in X is correlated with wavelength, while the pixel number in Y is completely uncorrelated with anything. The pixel amplitudes along the Y-axis are first integrated, and then the pixel numbers in X and summed amplitudes are subsequently calibrated.

The calibrations described here use parts of the IntelliCal calibration system. This system includes two light sources:

(i) a dual atomic line source containing a Hg vapour lamp and Ne-Ar lamp

(ii) a NIST traceable LED based light source

Source (i) can produce spectral lines between 200 nm and 1000 nm for calibrating the pixel number in X to photon wavelength. Source (ii) is designed for IntelliCal to perform a relative intensity calibration for photon wavelengths between 450–1020 nm. However, this is insufficient for MIEL to obtain a measure of absolute photon emission rates. Therefore the decision was made to perform an intensity calibration using the transmission, reflection, and quantum efficiencies of each component in the optical path of the MIEL apparatus. The known spectrum of source (ii) was used to validate the calibration.

6.4.1   Wavelength Calibration

MIEL was calibrated for photon wavelength in the NIR region using the Ne-Ar atomic line source, and in the visible region using the Hg vapour lamp. To perform the calibration, the user must first setup MIEL with the configuration of the desired spectroscopy

mode, i.e. visible or NIR. Then the dual line source is placed at the focal point of the IX83 objective lens and the appropriate lamp within the dual line source is turned on.

The wavelength calibration algorithm built into IntelliCal is proprietary information, and so is not known exactly to the user, but the general principle is to use input from the user to generate an expected spectrum and compare this with the observed spectrum. The required input is: (1) an estimate of the observed peak width from the spectral lines on the CCD camera; (2) which lamp within the dual line source is turned on. With this information, IntelliCal builds an expected spectrum for the line source like the one in Figure 6.13. The x-axis values of the observed spectrum (x_i in Equation 6.7) are then mapped to wavelength, λ, with a nonlinear model, $X(\lambda|\vec{\theta})$. The parameters of this model, $\vec{\theta}$, are then allowed to float in a nonlinear least-squares fit, where a function M of the form given in Equation 6.7 is minimized.

$$M = \sum_i \left(S_{\mathrm{exp}}(X(\lambda|\vec{\theta})) - S_{\mathrm{obs}}(x_i) \right)^2, \tag{6.7}$$

where S_{exp} is the expected spectrum determined with user input by IntelliCal and S_{obs} is the observed spectrum. Also shown in Figure 6.13, below the observed and expected spectra, is a measure of the calibration error vs. pixel number. This is calculated by computing the residual between spectral peak wavelengths in the observed and expected spectra. For the NIR calibrations, these residuals were never more than 0.4 nm, and in visible calibrations the error never exceeded 0.1 nm. The difference in errors for the two wavelength calibrations is due to the line density of the gratings used; greater line density results in better wavelength resolution, which yields lower error.

6.4.2 Photon Detection Efficiency

Figure 6.14 reports the expected PDE of MIEL as a function of the wavelength, in both the Visible and NIR spectroscopy modes. This was obtained using the reflection, transmission, and quantum efficiencies of all the components listed in Section 6.1 (see Figures 6.4–6.8). More precisely, the PDE as a function of wavelength, $\varepsilon(\lambda)$, was computed as

$$\varepsilon(\lambda) = \varepsilon_{\mathrm{obj}}(\lambda) \times \varepsilon_{\mathrm{fil}}(\lambda) \times \varepsilon_{\mathrm{SP}}(\lambda) \times \left(\varepsilon_{\mathrm{mir}}(\lambda) \right)^3 \times \varepsilon_{\mathrm{gr}}(\lambda) \times \varepsilon_{\mathrm{CCD}}(\lambda), \tag{6.8}$$
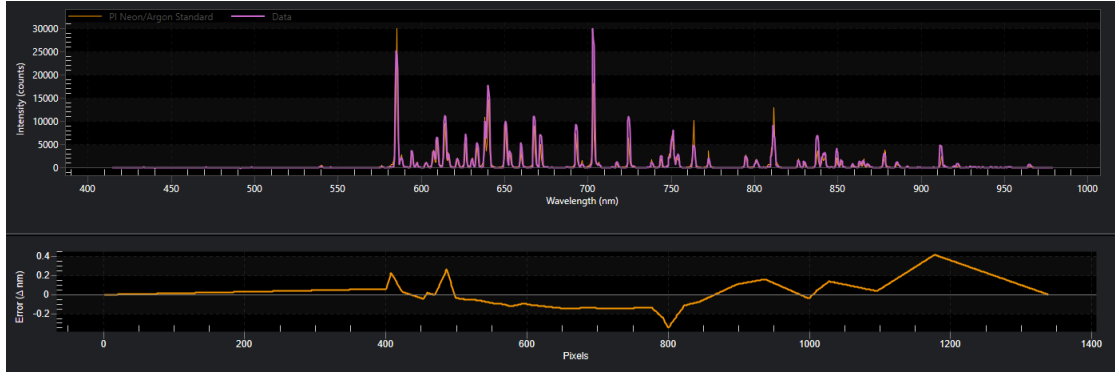
FIGURE 6.13: Example output of the IntelliCal wavelength calibration in NIR. The dual atomic line source was switched to the Ne-Ar setting, and IntelliCal used this information (passed as user input) to generate an expected spectrum and determine a calibration based on a least-squares fit between expected (yellow) and observed (pink) spectra.
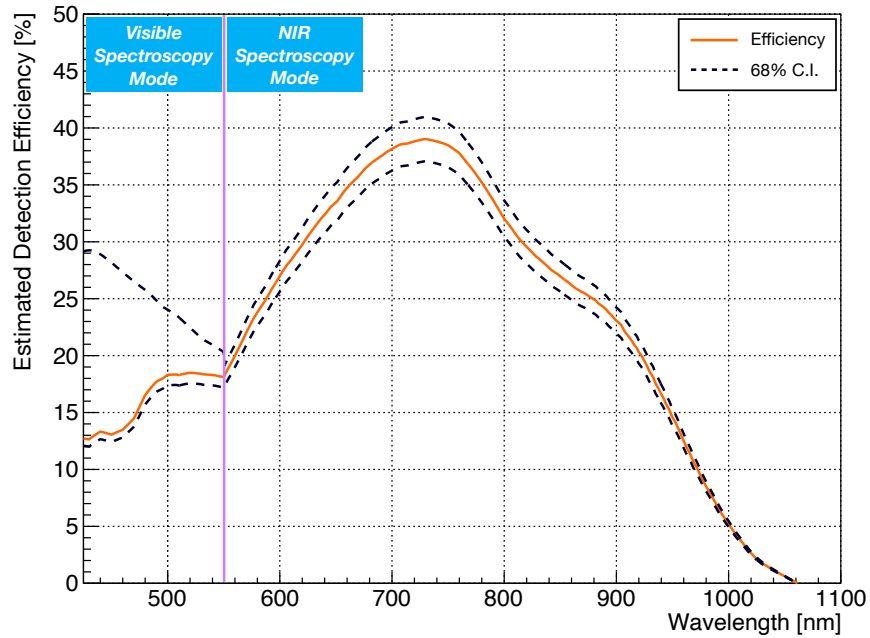
FIGURE 6.14: Estimated detection efficiency of MIEL as a function of the photon wavelength. The 68% Confidence Interval (C.I.) error bands account for systematic uncertainty in the lamp calibration. Moreover below 550 nm the error increases due to a disagreement between the observed IntelliCal LED light source spectrum and its expected spectrum obtained combining the different hardware transmission specifications of the setup. See text for more detailed explanation.

where

$$\varepsilon_{\mathrm{obj}}(\lambda) \equiv \text{IX83 objective lens transmission efficiency}$$

$$\varepsilon_{\mathrm{fil}}(\lambda) \equiv \text{IX83 filter transmission efficiency}$$

$$\varepsilon_{\mathrm{SP}}(\lambda) \equiv \text{IX83 Side Port transmission efficiency}$$

$$\varepsilon_{\mathrm{mir}}(\lambda) \equiv \text{Spectrometer mirror reflection efficiency}$$

$$\varepsilon_{\mathrm{gr}}(\lambda) \equiv \text{Spectrometer grating reflection efficiency}$$

$$\varepsilon_{\mathrm{CCD}}(\lambda) \equiv \text{CCD camera quantum efficiency.}$$

Note that $\varepsilon_{\mathrm{mir}}(\lambda)$ is cubed in Equation 6.8 because there are three mirrors in the optical path inside the spectrometer. The IntelliCal LED light source was used to validate the PDE curve in Figure 6.14 for both the Visible and NIR spectroscopy modes. Figure 6.15 (the left-most plot) shows an independently measured ($< 1\%$ uncertainty) 'true' spectrum of the LED source, provided by PI for the specific unit at TRIUMF. Multiplying the true spectrum by the MIEL PDE curve yields an expectation of the observed spectrum of the LED source in both spectroscopy modes. As shown in Figure 6.15, the expected and observed spectra are in agreement to within 10% at local maxima in the spectrum.
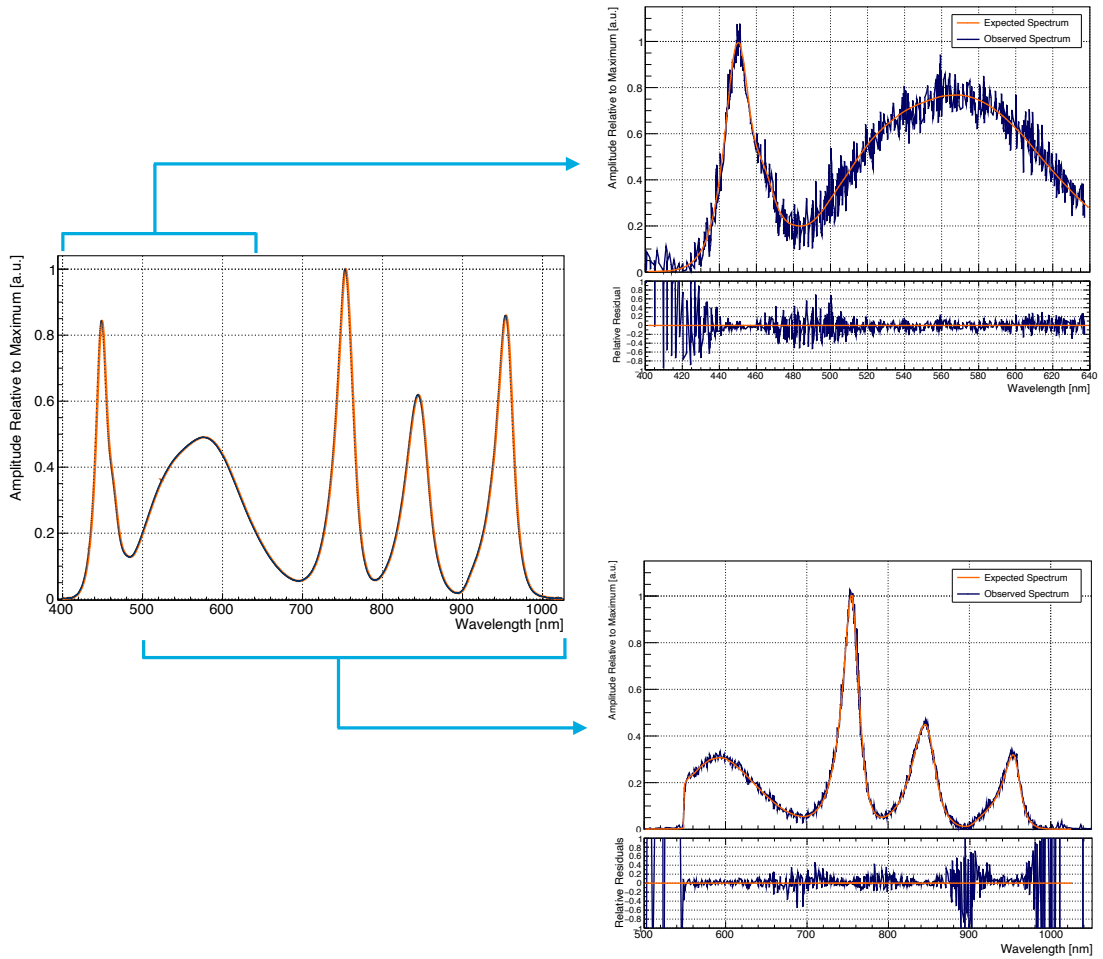
FIGURE 6.15: Validation test of the PDE curve in Figure 6.14. The left-most plot is the true spectrum of the IntelliCal NIST traceable LED source, and the plots on the right are the spectra if the LED source as observed in Visible Spectroscopy mode (upper-right) and NIR Spectroscopy mode (lower-right). Overlaid on both, in orange, is the expected LED source spectrum based on the true spectrum multiplied by the PDE at a given wavelength.

Note that this validation only shows that the shape of the PDE curve in Figure 6.14 can

be used to appropriately reconstruct the spectral shape of the light source. The absolute value of the PDE from Equation 6.8 is based on hardware specifications provided by manufacturers. Per comment from PI and Olympus, the relative systematic uncertainty on these values is roughly 5%, which was adopted in Figure 6.14 as the 68% uncertainty band.

However in Visible Spectroscopy mode, the upper uncertainty bound does not follow a +5% value relative to the PDE in the 420–550 nm range. This is due to a disagreement between the observed IntelliCal LED light source spectrum and its expected spectrum in the 400–640 nm range, assuming a PDE curve from combining the different hardware transmission specifications of the setup. In Figure 6.16, the discrepancy between the two spectra is largest at 450 nm. The same discrepancy was observed when attaching the LED source directly to the spectrometer input, so it was concluded that the microscope was calibrated correctly. However, whether this discrepancy stems from miscalibration of the source or from a significantly lower transmission of the spectrometer+camera system at 450 nm could not be determined. Therefore a modification term was appended to Equation 6.8 for Visible Spectroscopy mode,

$$\varepsilon_{\mathrm{vis}}(\lambda) = \varepsilon(\lambda) \times \varepsilon_{\mathrm{mod}}(\lambda), \qquad (6.9)$$

where $\varepsilon(\lambda)$ is defined in Equation 6.8 and $\varepsilon_{\mathrm{mod}}(\lambda)$ is a correction factor to enforce agreement between the expected and observed calibration spectra. Since the origin of the discrepancy is unknown, $\varepsilon_{\mathrm{mod}}(\lambda)$ could either be properly correcting for the MIEL spectrometer+camera efficiencies, or introducing a bias by forcing the observed LED source spectrum to conform to an erroneous 'true' spectrum. Therefore in the 400–550 nm range, the decision was made to use $\varepsilon_{\mathrm{vis}}(\lambda)$ as the nominal PDE while setting the upper uncertainty bound equal to $\varepsilon(\lambda)$ (Equation 6.9). This greatly increases the systematic upper uncertainty bound in Visible Spectroscopy mode, ranging between 13.8–136%. However, since the light emission below 550 nm is small [197], the large error band was deemed acceptable.
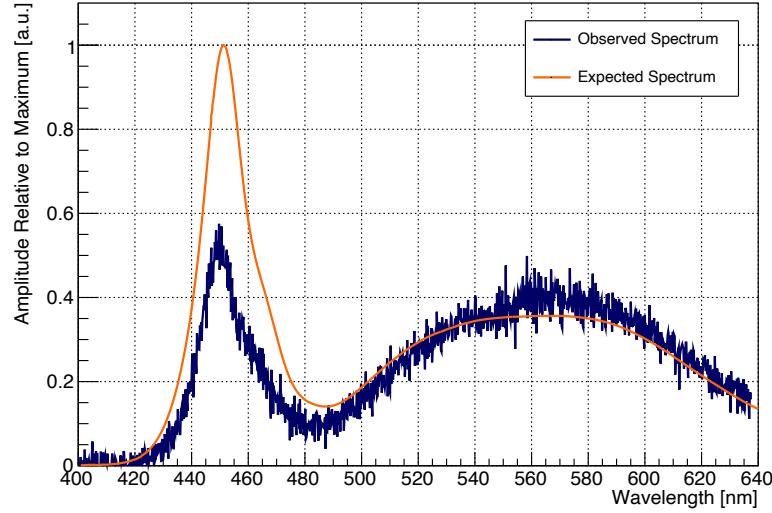
FIGURE 6.16: Expected vs. Observed spectrum of the IntelliCal LED source, with the PDE correction based solely on hardware specs in the 400–640 nm range.

6.5   Imaging Measurements

Imaging mode was used to record images of the biased SiPM as shown in Figures. 6.17 & 6.18. These images were used to compare the geometrical fill factors and topographical variations in photon emission for the HPK VUV4 MPPC and the FBK VUV-HD3 SiPM biased at $11.2 \pm 1.0\,\mathrm{V}$ and $13.0 \pm 1.0\,\mathrm{V}$ of over-voltage, respectively. At these two over-voltages, the current passing through each SiPM was roughly $2\,\mathrm{mA}$. The two images in Figure 6.18, when normalized to the same current per unit area[6], can be used to compare the relative photon emission intensity and uniformity of the two SiPMs under investigation. This assumes that the SiPM current is entirely due to charge avalanches, and that secondary photon emission in the SiPM is also entirely caused by avalanches. Leakage current (i.e. not amplified current) can contribute $\mathcal{O}(10^{-15}\,\mathrm{A})$ to the total current passing through the SiPMs [204], but this is completely negligible compared to $\mu\mathrm{A}$ or mA of current, which is the level relevant to this investigation. The second part of this assumption is also valid, on the grounds that the long list of theorized contributors to secondary photon emission in SiPMs (as discussed in Chapter 5) collectively dominate over blackbody radiation, which would be of order 1% in the NIR end of the 450–1020 nm wavelength range provided the SiPM temperature exceeded $\sim 50\,^{\circ}\mathrm{C}$.

---

[6]The two SiPMs under study have different surface areas therefore Figure 6.17 and Figure 6.18 were scaled accordingly.

Figure 6.18 shows the entire surface of both SiPMs, combining several images at 4× magnification. The left (grey scale) images are single exposures of 100 ms showing the unbiased SiPMs illuminated by the halogen lamp attached to the microscope. The right (heat map) images are single exposures of 2 minutes, showing the spatially resolved emission intensity of the biased SiPMs in complete darkness. In both of the heat map SiPM images, there are several highly localized regions where photon emission is comparatively larger than the surrounding areas—i.e. 'hotspots.' The position of these hotspots have never changed over the duration of the experiment, so they cannot be explained by cosmic rays hitting either the SiPM or the CCD camera. Rather, they are likely the result of crystal defects in the silicon, e.g. nonuniform concentration of impurities or dopants. Therefore the increased photon emission rate in hotspots obeys Shockley-Read-Hall statistics, as explained in Section 5.2.1. Hotspots are peripheral to the focus of this chapter, but were studied in Ref [205] in more detail.

The z-scales in Figures 6.18a & 6.18b show that the HPK VUV4 SiPM tends to have brighter hotspots compared to the FBK VUV-HD3, for which the hotspots appear more randomly distributed and within single SPADs. More generally the RMS of CCD pixel amplitudes of the HPK MPPC is 3.3 times greater than that of the FBK SiPM, and behaves comparably to the one reported in [205] for KETEK PM3350T STD/MOD SiPM. This suggests that the silicon purity and/or dopant concentration uniformity in the FBK VUV-HD3 is superior to that of the HPK VUV4.

6.6 Spectroscopy Measurements

6.6.1 Measurement Procedures

Spectroscopy mode was used to obtain spectral measurements of the biased SiPMs in dark conditions. The general procedure was as follows:

1. Configure MIEL to take a measurement of the visible or NIR portion of the SiPM emission spectrum (i.e. pick visible or NIR spectroscopy mode)

2. Replace the SiPM with the wavelength calibration dual line source; do a (re)calibration of the chosen wavelength range
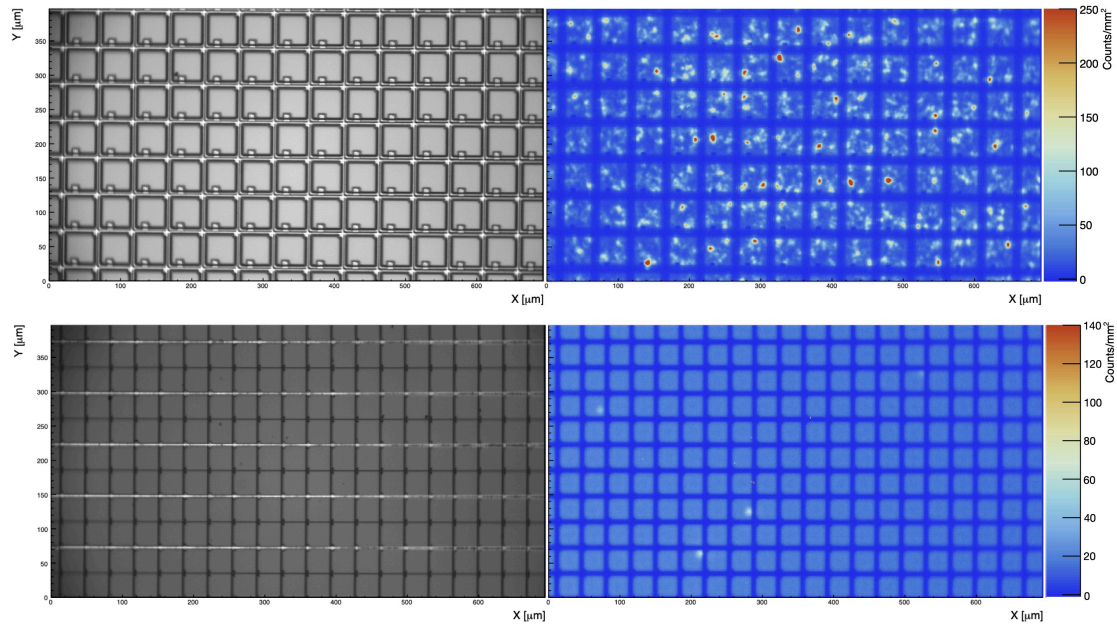
FIGURE 6.17: Top row: (left) Grey scale image of the unbiased HPK VUV4 SiPM illuminated by the microscope halogen lamp, and (right) Secondary photon emission image of the HPK VUV4 biased at 11.2 ± 1.0 V of over-voltage. Bottom row: (left) Grey scale image of the unbiased FBK VUV-HD3 SiPM illuminated by the microscope halogen lamp, and (right) Secondary photon emission image the of FBK VUV-HD3 biased at 13 ± 1 V of over voltage. Unbiased SiPM images were taken with a camera exposure time of $100\,\text{ms}$ and biased SiPM images were taken with a camera exposure time of 2 minutes. All images at 20x magnification.

3. Replace the wavelength calibration source with the SiPM; focus the microscope image on the indicated region in Figure 6.18

4. Choose the over-voltage to be supplied to the SiPM; set the CCD exposure time accordingly

5. Begin applying the chosen over-voltage and begin tracking the current; simultaneously begin the exposure

6. Repeat steps 4 & 5 for exposures of 3h 20m, 4h 45m, and 8h 20m

7. Repeat steps 1–6 for the other spectroscopy mode of measurement

This procedure, step 6 in particular, was designed to minimize the number of reconfigurations of the apparatus. Measuring a complete spectrum from 450–1020 nm with MIEL requires at least one transition from visible to NIR spectroscopy mode, which means there is necessarily at least one change of diffraction grating. The small variation
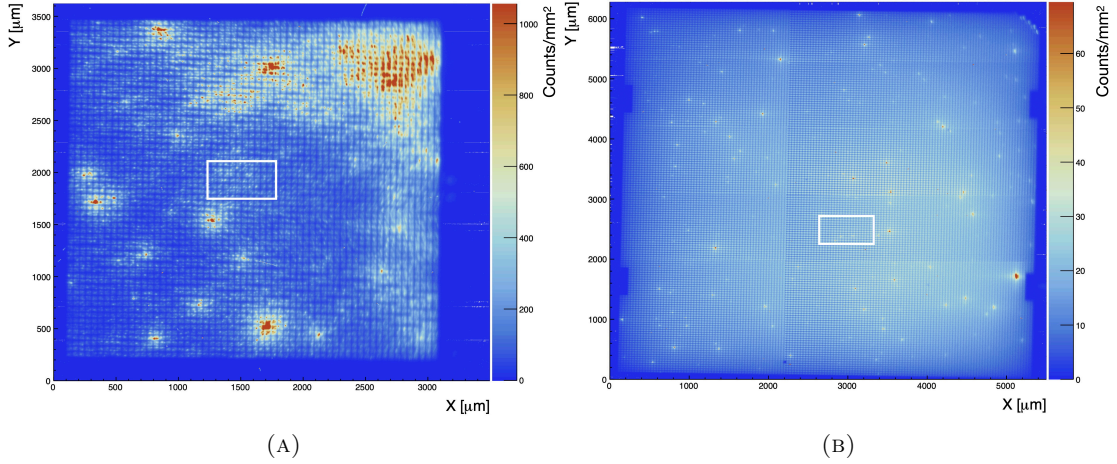
FIGURE 6.18: Composite images of the (A) HPK VUV4 and (B) FBK VUV-HD3 SiPMs at 4× magnification and $V_{ov} = 11.0\,\text{V}$ and $13.0\,\text{V}$ ($\pm 1.0\,\text{V}$), respectively. The regions enclosed in the white boxes are the areas wherein the SiPM image was zoomed to 20× magnification for spectral measurements. Both images were taken with the same camera exposure time and objective lens: PLCN4X-1-7.

in position reproducibility of the grating turret introduced shifts in the wavelength calibration between reconfigurations by as much as $\pm 1\,\text{nm}$. Step 2 in this procedure is a provision to ensure the stability of the wavelength calibration and maintain wavelength resolution.

Step 3 calls for the CCD exposure to be determined based on the over-voltage, such that all CCD exposures would accumulate roughly the same number of photons from the SiPM. Under this constraint, the exposure time must be inversely proportional to the current being driven through the SiPM at the given over-voltage (see Figure 5.5). As previously stated in Section 6.5, this is assuming that charge avalanches are the sole source of photon emission from the SiPM. The set of exposure times and applied over-voltages used for spectral measurements of the SiPMs is summarized in Table 6.4.

Step 4 was achieved using a Keithley 6487 Picoammeter, which was controlled by the TRIUMF lab computer via a MatLab script. The MatLab code was programmed to sample the picoammeter current reading, with its corresponding timestamp, every second throughout a given CCD exposure. Those current values were later used in analysis to obtain the total number of charge carriers passing through the SiPM for that CCD exposure. Since the CCD camera exposure needed to be initiated independently, the MatLab code was also programmed to drive and sample the current for the whole exposure time plus two additional minutes—one minute before and one minute after the exposure—to ensure completeness of each current vs. time measurement.

6.7 Spectral Analysis

The goal of the spectral analysis discussed in this section is to convert raw ADUs recorded by the PI CCD camera, $N_{\mathrm{ADU}}(\lambda)$, to the number of photons emitted per charge carrier, $N_\gamma(\lambda)$, at a given wavelength, λ. Mathematically, this conversion is represented by Equation 6.10.

$$N_\gamma(\lambda) = N_{\mathrm{ADU}}(\lambda) \left(\frac{\eta_{\mathrm{ADU}}^\gamma\, q_e}{Q_{\mathrm{ET}}\, \rho_{\mathrm{surf}}} \right) \left(\frac{1}{A(\lambda)\, \varepsilon(\lambda)} \right), \tag{6.10}$$

where: $\eta_{\mathrm{ADU}}^\gamma$ is the calibrated gain of the CCD camera equal to $0.7\,\gamma/\mathrm{ADU}$ (see Table 6.3); q_e is the elementary electron charge; Q_{ET} is the total charge that passed through the SiPM throughout the fixed exposure time, t_{ET} (Section 6.7.1); ρ_{surf} is the fraction of the SiPM light emitted within the field of view of the spectrometer slit (Section 6.7.2); $A(\lambda)$ is a wavelength dependent photon acceptance correction factor (Section 6.7.3); and $\varepsilon(\lambda)$ is the PDE of MIEL defined in Equation 6.8 and shown in Figure 6.14. The quantities enclosed within the first pair of parentheses pertain to Step 4, and those factors in the other parentheses correspond to Step 5.

6.7.1 Number of Charge Carriers

The quantity Q_{ET} in Equation 6.10 is defined as the integral of the current passing through the SiPM, $i(t)$. Recall from Section 6.1.1 that a Keithley 6487 Picoammeter records the SiPM current throughout the duration of each exposure. Therefore Q_{ET} can be obtained through the measurement of $i(t)$ via,

$$Q_{\mathrm{ET}} = \int_0^{t_{\mathrm{ET}}} i(t)\, dt \tag{6.11}$$

The reason why it was necessary to define Q_{ET} in this way is because current draw by the SiPM in reverse bias beyond avalanche breakdown varies with temperature, over which this experimental apparatus has no control nor ability to measure. Consequently, the current was observed to drift as the plot in Figure 6.19 shows. Table 6.4 summarizes the complete set of Q_{ET} measurements, as well as average current, $\langle i(t) \rangle$, and over-voltage, V_{ov}, for all exposures.
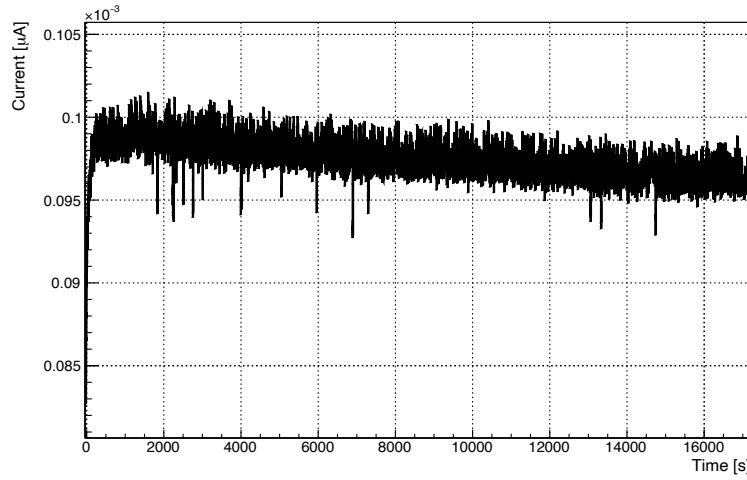
FIGURE 6.19: Current vs. time measurement for the FBK VUV-HD3 SiPM during its 4h 45m exposure in NIR spectroscopy mode.

Exposure Time t_{ET}		FBK VUV-HD3		HPK VUV4	
		Visible	NIR	Visible	NIR
8h 20min	V_{ov} [V]	12.1±1.0	12.1±1.0	10.7±1.0	10.7±1.0
	$\langle i(t) \rangle$ [μA]	59.1±1.2	66.2±1.3	78.8±0.6	33.3±0.3
	Q_{ET} [C]	1.77±0.12	1.99±0.12	2.36±0.12	1.00±0.12
4h 45min	V_{ov} [V]	12.4±1.0	12.4±1.0	10.8±1.0	10.8±1.0
	$\langle i(t) \rangle$ [μA]	87.1±0.6	97.5±1.0	46.4±0.4	88.0±0.6
	Q_{ET} [C]	1.49±0.09	1.67±0.09	0.80±0.09	1.51±0.09
3h 20min	V_{ov} [V]	12.8±1.0	12.8±1.0	11±1	11±1
	$\langle i(t) \rangle$ [μA]	200.9±1.7	165.5±1.3	240.5±1.3	187.8±1.2
	Q_{ET} [C]	2.41±0.08	1.99±0.08	2.89±0.08	2.25±0.08

TABLE 6.4: Summary of exposure time (t_{ET}), over-voltage V_{ov}, total charge Q_{ET} (as defined by Equation 6.11) and average current $\langle i(t) \rangle$ during SiPM spectral measurements.

6.7.2 Evaluation of ρ_{surf}

This section focuses on evaluating the correction factor ρ_{surf}, used to account for the fraction of the SiPM light emitted within the field of view of the spectrometer slit. ρ_{surf} was computed using images of the biased SiPM with and without the slit as follows:

$$\rho_{\mathrm{surf}} = \left(\frac{\sum_{i,j \subseteq R_3} P_{i,j}^{20\times}}{\sum_{i,j \subseteq R_2} P_{i,j}^{20\times}} \right) \left(\frac{\sum_{i,j \subseteq R_2} P_{i,j}^{4\times}}{\sum_{i,j \subseteq R_1} P_{i,j}^{4\times}} \right). \tag{6.12}$$

where: (i) R_k, with $k = \{1, 2, 3\}$ are the regions highlighted in Figure 6.20 for the HPK VUV4 and for the FBK VUV-HD3, and (ii) $P_{i,j}^{M}$ are the number of photons counted in the i, j^{th} pixel recorded by the CCD camera for an image at magnification M. In the
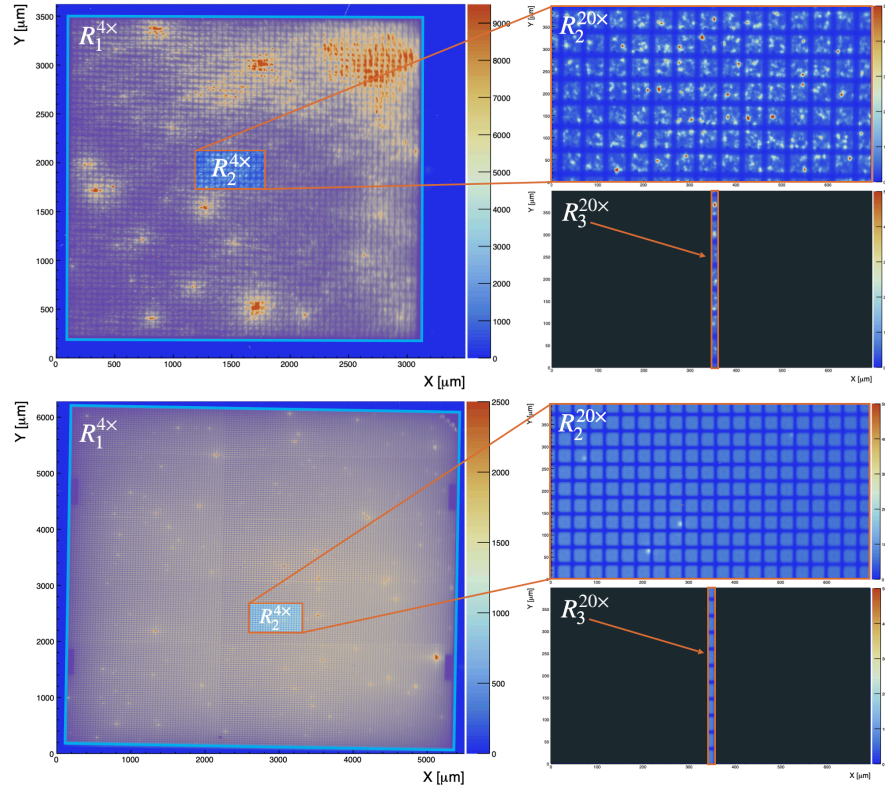
FIGURE 6.20: Pictorial representation of how the quantity ρ_{surf} is calculated for the HPK VUV4 MPPC (top) and FBK VUV-HD3 (bottom) SiPM combining the information of Figure 6.17 and Figure 6.18. R_k, with $k = \{1, 2, 3\}$ are selected regions where the photon count is measured. See text for more details.

notation of Equation 6.12, M takes on the values of $4\times$ and $20\times$, as these images were taken with the PLCN4X-1-7 and LMPLFLN20X objective lenses, respectively. Defining ρ_{surf} in this manner corrects spectrum amplitudes in two steps, corresponding to the two factors enclosed in brackets. The first factor is the ratio of light contained within the spectrometer slit to light contained within the local area immediately surrounding the slit; the second factor is the ratio of light in the local area about the slit to light emitted by the entire SiPM surface. Therefore ρ_{surf} effectively rescales the observed spectrum to what it would have been if the entire SiPM surface area could be enclosed in the spectrometer field of view.

Note that defining ρ_{surf} as in Equation 6.12 not only accounts for the non-uniformity of the light emitted by the SiPM over its entire surface area, but also it removes complications that may arise when comparing images taken with different magnifications[7].

---

[7]The regions R_2 shown in Figure 6.20 are the same enclosed in white boxes of Figure 6.18. These regions are also the ones used in Section 6.10 to perform spectral measurements, after insertion of the slit. They were chosen for their centrality and for the absence of bright hotspots. The exact location of these regions is however not relevant since the spectra in Section 6.10 are always scaled using Equation 6.12 to account for the non-uniformity of the light emitted by the entire SiPM.

The two ratios of Equation 6.12 are in fact done between counts of images taken with the same magnification, i.e. the same objective lens. Ensuring that $R_2^{20\times}$ corresponds to the same area as $R_2^{4\times}$ was done using relative translations from fixed points on the SiPM. For example, starting from the top-left corner and then translating X SPADs to the right and Y SPADs down, or when more precision is needed, locating recognizable hotspots and moving $x\,\mu$m to the right/left and $y\,\mu$m up/down. The ρ_{surf} correction factors for the two SiPM tested are reported in Table 6.5.

	FBK VUV-HD3	HPK VUV4
ρ_{surf}	$(1.72 \pm 0.08) \times 10^{-4}$	$(2.40 \pm 0.12) \times 10^{-4}$

TABLE 6.5: Values of ρ_{surf} for the FBK VUV-HD3 and HPK VUV4 SiPMs.

6.7.3 Photon Acceptance

The photon acceptance correction factor $A(\lambda)$ accounts for: (i) the finite numerical aperture (NA) of the microscope objectives lenses (Equation 6.2), (ii) photon absorption in the silicon and reflection losses due to the SiPM surface coating. In what follows, it is assumed that the light emitted by SiPM avalanches is isotropic and unpolarized. The angular distribution of photon emission is relevant for corrections for the numerical aperture, and polarization can change the probability of reflection at the various interfaces of different dielectric media. Additionally, the correction factor $A(\lambda)$ is computed considering a SiPM surface coating structure constituted by a single layer of SiO_2, as shown in Figure 6.21a. This structure was provided by FBK and used in [206] for a study of the SiPM reflectivity. When asked for comment, Hamamatsu did not disclose the HPK VUV4 surface coating structure, and therefore due to lack of more detailed information, the assumption was made that the HPK MPPC has the same coating structure as the FBK VUV-HD3 SiPM. The correction factor $A(\lambda)$ was then computed neglecting interference and integrating over the solid angle [207] contained within the numerical aperture of the objective lens of the microscope as follows

$$A(\lambda) = \frac{\int_0^{2\pi} d\phi}{\int_0^{2\pi} d\phi \int_0^{\pi} \sin\theta d\theta} \int_0^{\theta_{\mathrm{Si}}} e^{-\frac{d_{\mathrm{P}}}{\cos\theta\,\mu(\lambda)}} (1 - R_{\mathrm{Si}}^{\mathrm{SiO_2}}(\lambda,\theta))(1 - R_{\mathrm{SiO_2}}^{\mathrm{Atm}}(\lambda,\theta')) \sin\theta d\theta \quad (6.13)$$

$$= \frac{1}{2} \int_0^{\theta_{\mathrm{Si}}} e^{-\frac{d_{\mathrm{P}}}{\cos\theta\,\mu(\lambda)}} (1 - R_{\mathrm{Si}}^{\mathrm{SiO_2}}(\lambda,\theta))(1 - R_{\mathrm{SiO_2}}^{\mathrm{Atm}}(\lambda,\theta')) \sin\theta d\theta, \quad (6.14)$$

where: (i) $e^{-\frac{d_P}{\cos\theta\,\mu(\lambda)}}$ (with $\mu(\lambda)$ attenuation length) is a correction factor to account for the self-absorption of the emitted photons in the silicon within a length d_P, as shown in Figure 6.21a, (ii) ϕ is the azimuthal angle, (iii) $R_{\mathrm{Si}}^{\mathrm{SiO_2}}$ is the reflectance at the silicon (Si)-silicon dioxide (SiO$_2$) interface, (iv) $R_{\mathrm{SiO_2}}^{\mathrm{Atm}}$ is the reflectance at the silicon dioxide (SiO$_2$)-atmosphere (Atm) interface. Both reflectances were computed as reported in [207]. θ is the emission angle of photons in the Silicon, and θ_{Si} is the maximum angle for which photons emitted in the silicon can be detected by the microscope objective. This last quantity is shown as the dotted lines in Figure 6.21b and it is determined using the definition of NA in Equation 6.2 and Snell's law [207] as follows

$$\mathrm{NA} = n_{\mathrm{loc}}\sin(\theta_{\mathrm{acc}}) \tag{6.15}$$

$$= n_{\mathrm{Si}}\sin(\theta_{\mathrm{Si}}) \tag{6.16}$$

$$\theta_{\mathrm{Si}} = \sin^{-1}\left(\frac{\mathrm{NA}}{n_{\mathrm{Si}}(\lambda)}\right). \tag{6.17}$$

with: n_i and θ_i ($i = \{\mathrm{Si}, \mathrm{SiO_2}\}$) being the refractive indices and photon angles (measured from the normal of the layer boundaries) of the Silicon (Si) and Silicon dioxide (SiO$_2$) medium. θ' is similarly defined using Snell's law as follows,

$$\theta' = \sin^{-1}\left(\frac{n_{\mathrm{Si}}(\lambda)}{n_{\mathrm{SiO_2}}(\lambda)}\sin(\theta)\right). \tag{6.18}$$

The avalanche region of each SiPM SPAD is located at a certain depth (d_P) from the SPAD surface and the emitted photons need to travel a length equal to this depth before to reach the surface and escape from it. This self-absorption mechanism is significant for wavelengths below 450 nm due to the short attenuation lengths of UV photons in silicon [196], but it is negligible for longer wavelengths. The exact location of the avalanche region was not provided by FBK and HPK, however with the model developed in Ref [159] a lower limit to its depth can be inferred. Therefore, the two depths reported in Ref [159] will be used here to estimate d_P. For the HPK VUV4, a value of $d_P = 0.8 \pm 0.2\,\mu\mathrm{m}$ was used, while for the FBK VUV-HD3 (that shares with the FBK VUV-HD1 studied in [159] the same surface coating and cell structure) $d_P = 0.145 \pm 0.01\,\mu\mathrm{m}$. The wavelength dependent attenuation length was computed accordingly to the data reported in [196].

Equation 6.14 was solved numerically using the refractive index data for each wavelength reported in [208, 209]. Figure 6.21b shows the correction factor $A(\lambda)$ as a function of the wavelength. The discontinuity in the $A(\lambda)$ correction factor for the two SiPMs is due to the two different objective lenses (with different numerical aperture) used in the Visible (LMPLFLN20X) and NIR (LCPLN20XIR) spectroscopy measurement modes, as shown in Section 6.1.2. Moreover the NIR spectroscopy mode has a higher $A(\lambda)$ i.e. smaller correction factor, due to the higher objective lens NA.

(A)   (B)
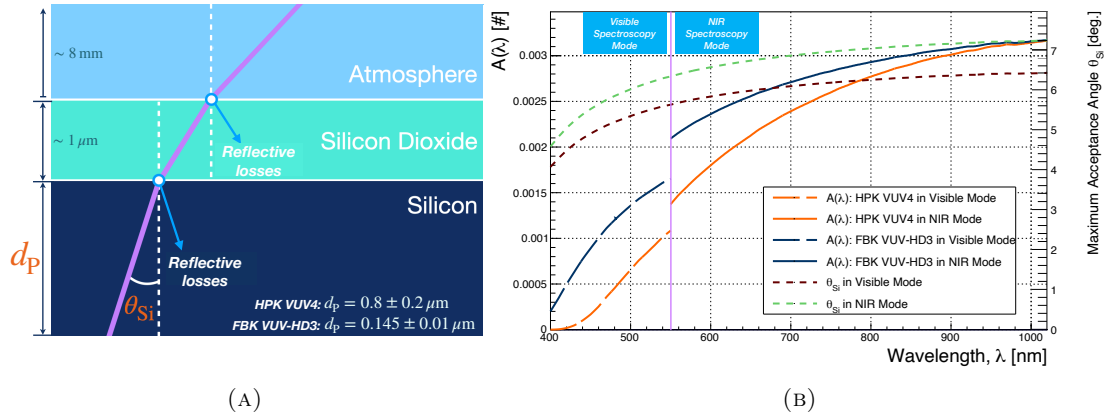
FIGURE 6.21: (A) Schematic representation of the SiPM surface coating structure used to compute the photon acceptance correction factor $A(\lambda)$. θ_{Si} is the maximum angle for which photons emitted in the silicon can be detected by the microscope objective. d_P is the depth of the avalanche region. b) Photon acceptance correction factor $A(\lambda)$ (Equation 6.14) and maximum acceptance angle (θ_{Si}, Equation 6.17) as a function of the wavelength for the two spectroscopy modes introduced in Section 6.2. The discontinuity in the $A(\lambda)$ correction factor for the two SiPMs is due to the two different objective lenses (with different numerical aperture) used in the Visible (LMPLFLN20X) and NIR (LCPLN20XIR) spectroscopy measurement modes.

6.8   Final Spectrum Processing

At this point in the spectrum building procedure, the data still exist in 2D images and are split between the visible and NIR spectroscopic measurements. In order to create the final set of spectra, The 2D images must be integrated over their Y-pixels; i.e. projected onto the wavelength axis. The visible and NIR measurements use diffraction gratings with different line densities, and therefore their wavelength calibrations and bin widths are inherently different. This needs to be corrected in order to properly merge the two into one final spectrum for a given over-voltage. This step is described in Section 6.8.1. The 'stitching' of visible and NIR components is then described in Section 6.8.2.
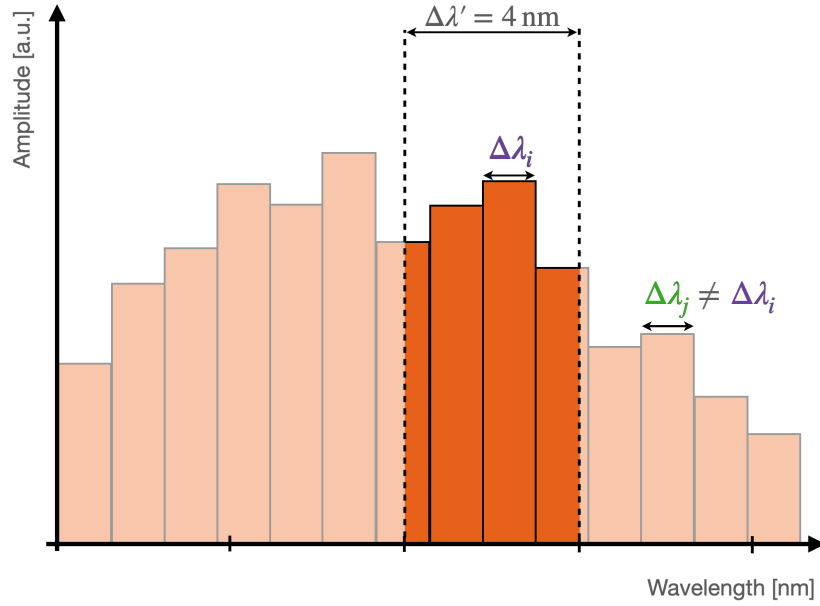
FIGURE 6.22: Cartoon diagram of rebinning MIEL spectral data. As not all $\Delta\lambda_i$ are equal, the case of bins being split between two $\Delta\lambda'$ bins is inevitable.

6.8.1 Wavelength Rebinning

To reduce the effect of statistical noise in the final spectra, the decision was made to widen wavelength bins to $4\,\mathrm{nm}$. Due to the wavelength calibration being slightly nonlinear with the CCD X-pixel number, this was not as simple as amalgamating neighbouring bins. Most of the original wavelength bins fell completely within the new $4\,\mathrm{nm}$ bins, while some others ended up being split between two, as shown in the cartoon diagram in Figure 6.22, where the ith wavelength bin is not equal in width to the jth bin.

To properly rebin the measured spectra, all bins split in this way, and their corresponding bin uncertainties, were distributed according to the percentage of their widths that lie in the wider bins; e.g. if 75% of the original wavelength bin's width ends up in the nth $4\,\mathrm{nm}$ bin, the nth bin gets 75% of the original bin's contents and 75% of its bin error.

6.8.2 Stitching Visible and NIR Spectra

Figure 6.23 shows an example set of visible and NIR spectra prior to stitching (FBK VUV-HD3 over 8h20m exposure time). In the overlapping region of visible and NIR spectra, from 550–600 nm, these two measurements should be in agreement with each other, and no discontinuities should arise by simply plotting the visible spectrum for
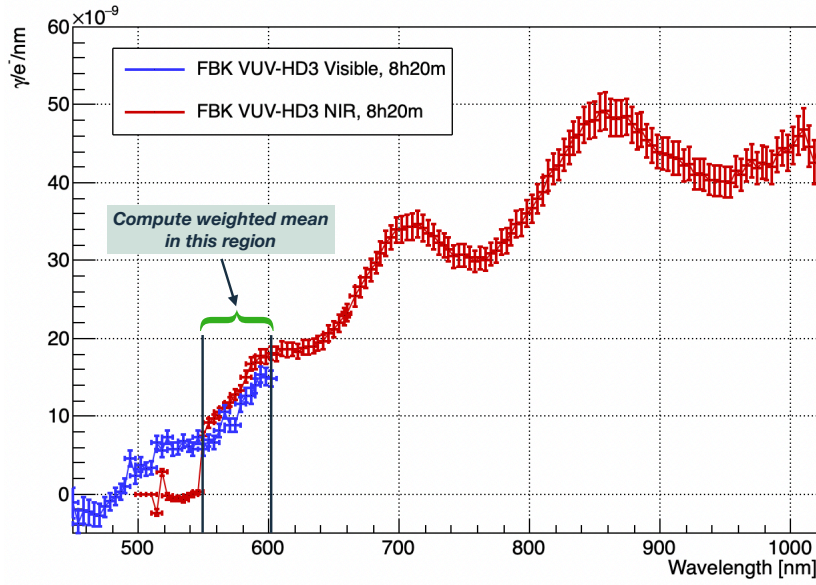
FIGURE 6.23: Visible and NIR spectra for the FBK VUV-HD3 SiPM over an 8h20m exposure time, prior to stitching. The mismatch in the overlapping region from 550–600 nm is corrected by setting the spectrum amplitudes to the weighted mean of the two measurements.

$\lambda < 550$ nm and the NIR spectrum everywhere else. However, as shown in Figure 6.23, small discrepancies in this region do appear. A possible explanation for this that there are minute differences in placement and orientation of the SiPM relative to the objective lenses between visible and NIR measurements. This can slightly change the part of the SiPM surface area enclosed within the spectrometer's field of view, which might, for example, introduce an extra trench in the spectrum image or shift the image closer to a hotspot. Both of these can change the overall observed emission rate of one measurement relative to the other. To correct for this effect, the spectrum amplitudes in the overlapping region are set to the weighted average of the visible and NIR spectrum values.

6.9   Assessment of Uncertainties

The sources of random and systematic uncertainty considered in the analysis as it has been described to this point originate from: (i) photon counting at the CCD, following a binomial distribution plus readout noise; (ii) background estimation within the dark enclosure, equal to readout noise; (iii) measurement of Q_{ET} from current integration;

(iv) measurement of ρ_{surf}; and (v) systematic uncertainty of the PDE calibration discussed in Section 6.4.2. Source (v) the most difficult to account for analytically, as it is discontinuous and correlated with photon counting and background removal. Therefore its contribution to the total spectrum uncertainty, along with sources (i) and (ii), were determined via toy MC simulation. Table 6.6 shows the breakdown of these contributions

	FBK VUV-HD3		**HPK VUV4**	
Source of Error	Visible	NIR	Visible	NIR
Q_{ET}	8.3%	5.1%	6.4%	7.2%
ρ_{surf}	4.6%	4.6%	5%	5%
PDE+counting+Bkg. Sub.		See Figure 6.24		

TABLE 6.6: Breakdown of contributions to total measurement uncertainty in MIEL. These quantities are reported as the average over the relevant wavelength ranges. The PDE+counting+Bkg. Sub. is shown in more detail in Figure 6.24.

6.9.1   Monte Carlo Modelling of Photon Transport

The toy MC model developed to assess the random and systematic uncertainties associated with photon transport from the SiPM to the CCD camera runs 5000 pseudo-experiments with the mean number of photons emitted and the mean PDE provided as user input. To start, it randomly samples a Poisson distribution to get a truth count of emitted photons, N_T, for the pseudo-experiment; the truth PDE, ε_T, is randomly sampled from a Gaussian distribution with the user input mean PDE, and a variance determined by Figure 6.14. The observed number of photons for the pseudo-experiment, N_O is determined by sampling a binomial distribution with N_T trials and probability of success given by ε_T. Following this, the observed count was turned into an estimate of the true photon count by scaling for the mean PDE value and ADU conversion factor, similar to Equation 6.10. These truth photon count estimates were recorded for each pseudo-experiment and their standard deviation calculated as a function of mean PDE and true photon counts. In the case of the upper error band of PDE in visible spectroscopy mode, this toy MC model was modified slightly to make the variance of the truth PDE Gaussian distribution vary according to wavelength, as discussed in Section 6.4.2.

Figure 6.24 shows the standard deviation of the estimated photon count due to sources (i), (ii), and (v) for two cases.
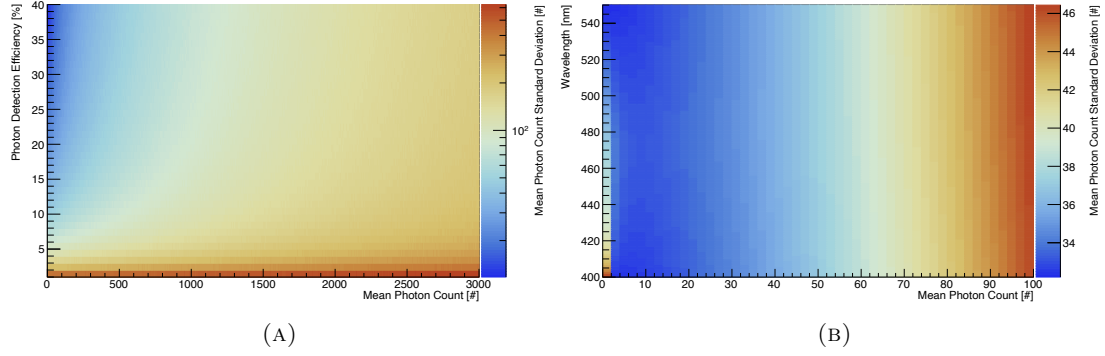
FIGURE 6.24: Toy MC generated look-up "tables" for uncertainty estimates in MIEL. Table (A) was used for NIR spectroscopy mode when the expected mean PDE is >1%, and for the upper error band of the measured spectra in Visible spectroscopy mode. Table (B) was used for the lower error band of spectra taken in Visible spectroscopy mode.

Case A) uncertainty in PDE is proportional to PDE

Case B) uncertainty in PDE depends on wavelength

Case A) applies to both upper and lower uncertainty bounds for spectra taken in NIR spectroscopy mode, and the upper error band for spectra taken in Visible spectroscopy mode. This is because the *lower* error band in the Visible spectroscopy PDE curve is proportional to PDE, and the spectrum itself is anti-correlated with PDE: i.e. a downward shift in PDE from the nominal value would look like an upward fluctuation in the data. Similarly Case B) applies for the lower uncertainty bound in Visible spectroscopy mode only.

6.10   Results

Figures 6.25a & 6.25b report, for the two SiPM designs tested, the number of secondary photons emitted per charge carrier per nm $N_\gamma^*(\lambda)$, defined as

$$N_\gamma^*(\lambda) = \frac{N_\gamma(\lambda)}{\Delta\lambda},\tag{6.19}$$

where $\Delta\lambda$ represents the wavelength resolution, equal to 4 nm. Note, as the measured wavelength range was studied with two modes of operation that comprise different sets of objective lenses, filters, and gratings to maximize the setup detection efficiency, after correcting for PDE, $\varepsilon(\lambda)$, and photon acceptance, $A(\lambda)$, residual discontinuities in the
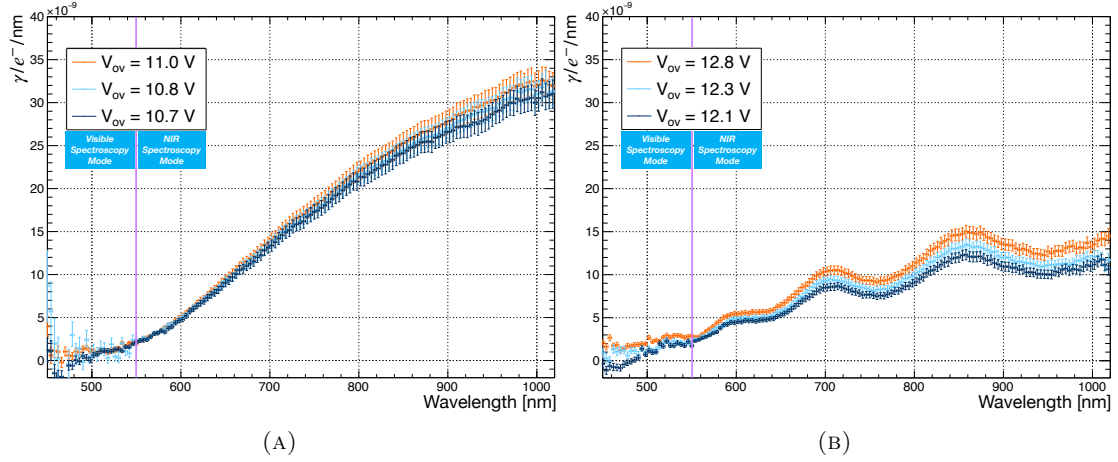
FIGURE 6.25: Spectra of the HPK VUV4 (A) and FBK VUV-HD3 (B) SiPMs as a function of applied over-voltage.

spectra of Figure 6.25 were removed by measuring with the PI camera the wavelength range [550-640] nm with both the Visible and NIR Spectroscopy modes and averaging the CCD counts in order to obtain a smooth transition between the two modes.

The spectra in Figure 6.25 show that the secondary photon emission: (i) is predominantly in the red and NIR: (ii) gradually decreases with decreasing wavelength, and vanishes somewhere between 450 nm and 500 nm; (iii) increases with over-voltage. Since $N_\gamma^*(\lambda)$ is independent of the number of charge carriers flowing through the SiPM and the SiPM electric field increases with increasing over-voltage, the higher $N_\gamma^*(\lambda)$ could be related to electric field dependent processes that contribute to the overall light production, as shown in [167, 195, 210–212]. The increasing $N_\gamma^*(\lambda)$ for increasing wavelength agrees with previous measurements of photon emission in silicon P-N junctions in avalanche breakdown [166–168, 197]. The FBK VUV-HD3, in particular, shows clear oscillations which is a signature of thin-film interference of light traversing the SiO_2 surface coating. The HPK VUV4 does not show a similar interference pattern, most likely due to its thinner coating. Geometry and surface coating can therefore contribute significantly to the final spectral shape.

The presence (FBK VUV-HD3) and absence (HPK VUV4) of an interference pattern was also measured in [206] during reflectivity measurements for the HPK VUV4 MPPC and the previous generation of FBK SiPMs: the FBK VUV-HD1, which shares the same surface coating and cell structure as the FBK VUV-HD3.

The spectra in Figure 6.25 were measured up to 1020 nm. This is a consequence of the low PDE of MIEL above 1020 nm, as shown in Figure 6.14. The PDE of MIEL is $\sim 2.6\%$ at 1020 nm and $< 1\%$ for wavelengths above 1050 nm. Considering the 200 μm spectrometer slit (discussed in Section 6.1.3) the S/N ratio for the longest exposure time (i.e. lowest over-voltage) at the PI CCD camera was approximately 1 at 1020 nm for both SiPMs (compared to S/N $\approx$ 6–8 for 800 nm under the same conditions). Increasing the slit width would have increased the S/N but would not have significantly improved the sensitivity of MIEL above 1020 nm, since the PDE of the apparatus is so low in this wavelength range.

Figure 6.25 can additionally be used to compute the total number of secondary photons emitted per charge carrier—the SiPM secondary photon yield—by integrating $N_\gamma^*(\lambda)$ over the measured emission spectrum as follows

$$N_\gamma = \int_{450\text{nm}}^{1020\text{nm}} N_\gamma^*(\lambda)\, d\lambda \tag{6.20}$$

Results are reported in Table 6.7 and compared with the ones reported in [197] and [168] measured using a S10362-11-100U HPK MPPC and a photo-diode, respectively.

A quantitative comparison with the results reported in [197] is not possible since the author did not provide information on the average current that was flowing in the SiPM during their measurement. The N_γ values reported in this work are 68.1–86.1% smaller than the value reported in [168], which covers a similar reverse current range (Table 6.4). A possible explanation could be found in the different spectral range covered by the two studies. In [168] the authors measured up to 1087 nm while the analysis discussed up to this point limits the wavelength range to 1020 nm, due to the limited efficiency of MIEL above this wavelength (Figure 6.14). According to [168], N_γ keeps increasing with wavelength and therefore limiting the integral of Equation 6.20 up to 1020 nm would systematically reduce the estimation of the SiPM secondary photon yield in MIEL, resulting in a comparatively lower value than that reported in [168].

Overall the number of secondary photons emitted per charge carrier by the HPK VUV4 is roughly a factor of two greater than that of the FBK VUV-HD3 SiPM. The exact reason for this is not known for certain at this time, but a likely explanation lies in the size and number of hotspots due to silicon crystal defects. Ref [205] correlates these hotspots with dark counts based on the Shockley-Read-Hall model. Since this measurement focused

FBK VUV-HD3		HPK VUV4	
V_{ov} [V]	Photon Yield $[\gamma/e^-]$	V_{ov} [V]	Photon Yield $[\gamma/e^-]$
12.1 ± 1.0	$(4.04\pm0.02)\times10^{-6}$	10.7 ± 1.0	$(8.71\pm0.04)\times10^{-6}$
12.4 ± 1.0	$(4.45\pm0.02)\times10^{-6}$	10.8 ± 1.0	$(8.98\pm0.06)\times10^{-6}$
12.8 ± 1.0	$(5.10\pm0.02)\times10^{-6}$	11.0 ± 1.0	$(9.24\pm0.05)\times10^{-6}$
Photon Yield in [197] (500–1117 nm): $1.2\times10^{-5}\,\gamma/e^-$			
Photon Yield in [168] [0.5-4.5] mA (413–1087 nm): $2.9\times10^{-5}\,\gamma/e^-$			

TABLE 6.7: Photon yields (number of photons emitted per charge carrier) measured in the wavelength range [450-1020] nm for the FBK VUV-HD3 and HPK VUV4 SiPMs as a function of the applied over-voltage. The last two line of the table represent the photon yields measured in [197] and [168], respectively.

on dark noise induced avalanches, the greater prevalence of hotspots in the HPK VUV4 MPPC would result in greater photon yields here, assuming this hypothesis is true. However the same is not true for internal cross-talk since, as reported in Figure 6.26 [169] the DiCT probability of the HPK VUV4 MPPCs is of the order of 3% at $V_{\mathrm{ov}} = 4\,\mathrm{V}$, while the DiCT probability of the FBK VUV-HD3 is around 20% for the same V_{ov}[8]. From this last point, it can be deduced that: (i) HPK trenches are highly effective in suppressing internal cross-talk relative to FBK trenches [213]; (ii) the reduction of the SiPM secondary photon emission doesn't necessarily follow the same design optimization loop compatible with the reduction of DiCT.
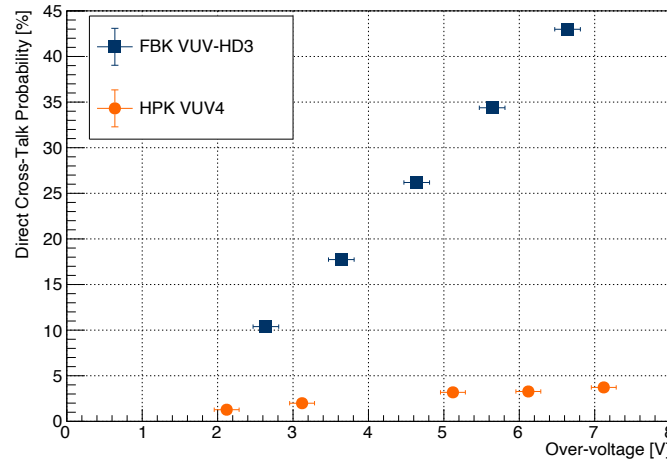
FIGURE 6.26: Direct cross-talk probability (DiCT) as a function of the applied over-voltage measured at 163 K for the two SiPMs tested in this work. DiCT probabilities were measured using pulse counting techniques described in Section 5.2.4. Image reconstructed from data shown in Ref [169].

The data reported in Figure 6.25 (and the results of Table 6.7) can be used as sampling distributions for a Monte Carlo simulation to estimate the probability of photon emission

---

[8]The DiCT probability is measured as the ratio between the number of prompt (or trigger) pulses with an integrated charge bigger than 1.5 Photo-electron Equivalent (PE) divided by the number of prompt pulses with an integrated charge bigger than 0.5 PE.

at a given wavelength per avalanche by each SiPM in the detector. Furthermore, paired with careful measurements of the SiPM Photon Detection Efficiency (PDE) [159] in the IR and NIR, this figure contains enough information to estimate the contribution of the SiPM secondary photon emission on the total background rate for any large-area SiPM-based detectors; this is crucial for experiments like nEXO, DUNE, and DarkSide-20k, where the SiPMs will likely be arranged facing each other.

To conclude this section it should be stressed that, the SiPM secondary photon emission studied here was generated solely from dark noise-induced avalanches. The high over-voltage was then needed to ensure a reasonable S/N ratio at the CCD camera. The number of secondary photons per charge carrier per nm reported in Figure 6.25 could therefore differ from the one emitted at lower over voltages since, on average, SiPMs in pulse counting mode are operated at much smaller over-voltages than the ones reported in Table 6.7. The data in Figure 6.25 are however normalized to the total generated charge in the SiPM and therefore, in principle, independent of the SiPM gain. Another measurement of the SiPM secondary photon emission induced by laser-driven avalanches will be taken at TRIUMF in the near future, with more realistic operating conditions (at vacuum, cryogenic temperature, lower over-voltage, etc.). This will allow for the study of both light propagation between neighbouring SPADs in SiPMs, and also the emission spectrum at lower over-voltages.

Chapter 7

Conclusion And Outlook

7.1 Summary of Results

7.1.1 DEAP-3600 Profile Likelihood WIMP Search

DEAP-3600 is a WIMP search experiment with a ~ 3.3 tonne liquid argon (LAr) target for elastic scattering of WIMPs off of ^{40}Ar nuclei. The WIMP sensitivity achieved in this work with the Profile Likelihood Ratio (PLR) improves upon the previous world-leading sensitivity with a LAr target, reported by DEAP-3600 in Ref [59]. This was a cut-and-count analysis with a 2.1 tonne-year exposure, achieving a maximum sensitivity of 3.9×10^{-45}cm^2 for 100 GeV WIMPs. With a 3.5 tonne-year exposure, the PLR WIMP search reached a sensitivity of 9.8×10^{-46} cm^2. In comparing the observed sensitivity from Ref [59] with the median expected sensitivity of a PLR analysis on a 2.1 tonne-year exposure of DEAP-3600, the average improvement over all WIMP masses is 36.02%. This is approximately the same as the improvement one would expect from the exposure alone, which is estimated to be 40.47% on average. The combined improvement from applying the PLR approach and using a dataset with a greater exposure resulted in an overall improvement in DEAP-3600 WIMP-nucleon cross-section upper limit by a factor of ~ 4 for a WIMP mass of 100 GeV.

7.1.2 SiPM Secondary Photon Emission

Several future dark matter and astroparticle physics experiments; such as nEXO [174], DUNE [183], and DarkSide-20k [62]; are being constructed with Silicon Photomultipliers (SiPMs) as their primary photosensing technology. SiPMs are arrays of Single Photon Avalanche Diodes (SPADs), which generate self-sustaining charge avalanches upon being irradiated by even a single photon. Consequently, SiPMs introduce an additional detector systematic effect, called correlated cross-talk. This refers to when secondary photons are emitted by the charge avalanche process in the silicon, which are subsequently detected by neighbouring SPADs on the same SiPM (internal cross-talk), or by other SiPMs (external cross-talk). To characterize this systematic effect, an experiment called Microscopy with Injected and Emitted Light (MIEL) was constructed at TRIUMF in Vancouver, BC, Canada, which measures the spectrum and photon yield per charge carrier of SiPMs. In this work, two SiPM designs being considered by the nEXO collaboration were studied: the FBK VUV-HD3 and the HPK VUV4. The spectra and photon yields were measured under dark conditions (i.e. avalanches stimulated by dark noise) and as a function of over-voltage. The spectra observed for both devices were found to largely emit in the near-infrared, with emission intensity increasing with over-voltage. The HPK VUV4 was found to emit roughly twice as many photons per charge carrier compared to the FBK VUV-HD3. This is likely due to the presence of Shockley-Read-Hall traps, which facilitate the generation of dark noise avalanches and can be seen as the 'hotspots' in Figure 6.17. These hotspots are in much greater abundance for the HPK VUV4 than the FBK VUV-HD3, resulting in more intense photon emission.

7.2 Conclusion and Outlook

The results of the PLR WIMP search discussed in Chapter 4, along with results reported by the liquid xenon dark matter community [61, 72, 143], demonstrate the effectiveness of the Profile Likelihood approach in WIMP searches. If systematics and backgrounds are studied carefully and well understood, the PLR method is a superior analysis compared to cut-and-count. For next generation WIMP searches like DarkSide-20k, which intends to use SiPMs as its primary photosensing technology, having an understanding of

systematics like correlated cross-talk will be crucial for building detector models. Should DarkSide-20k consider the PLR method for their WIMP search analysis, studies like the one discussed in Chapter 6 will be a crucial part of constraining nuisance parameters corresponding to correlated cross-talk in their detector models. The findings of experiments like MIEL can be also be used to by SiPM manufacturers like Fondazione Bruno Kessler and Hamamatsu Photonics K.K. to improve their designs, potentially leading to reduced impact from effects like dark noise and correlated cross-talk. For example, the emission microscopy images in Ref [194] could help Hamamatsu reduce the number of Shockley-Read-Hall traps in their silicon deposition processes. Therefore Ref [194] and similar studies could aid in detector modelling, as well as the development of technological advancements that bring the dark matter community closer to potential discoveries of new physics beyond the Standard Model.

Appendix A

Extended Mathematical Derivations

A.1 Deriving the WIMP Relic Abundance

The following discussion is a summary of what appears in Ref [24]. We begin here with Equation 1.31, which is

$$a^{-3}\frac{d}{dt}(a^3 n_\chi) = \langle \sigma_{\mathrm{ann}} v \rangle \big((n_\chi^{(0)})^2 - n_\chi^2\big),$$

where a is the time-dependent scale factor of the universe, n_χ is the comoving is the WIMP number density, and $n_\chi^{(0)}$ is the WIMP number density if it remains in thermal equilibrium with the universe. Given that the expansion of the universe is an adiabatic process [25], this means that to good approximation, temperature $T \propto a^{-1}$, and thus the product of Ta is a constant. Using this relation, a change of variable in Equation 1.31 can be done via

$$a^{-3}\frac{d}{dt}\left(a^3 n_\chi \frac{T^3}{T^3}\right) = a^{-3}(aT)^3 \frac{d}{dt}\left(\frac{n_\chi}{T^3}\right)$$

$$= T^3 \frac{dY}{dt}$$

where $Y = n_\chi/T^3$. If we similarly define $Y_{\text{EQ}} = n_\chi^{(0)}/T^3$, then Equation 1.31 can be entirely recast in terms of the new variable Y:

$$T^3 \frac{dY}{dt} = \langle \sigma_{\text{ann}} v \rangle \left((T^3 Y_{\text{EQ}})^2 - (T^3 Y)^2 \right) \tag{A.1}$$

$$\therefore \quad \frac{dY}{dt} = T^3 \langle \sigma_{\text{ann}} v \rangle \left(Y_{\text{EQ}}^2 - Y^2 \right). \tag{A.2}$$

It is also convenient to redefine the time variable, t, in terms of the temperature. Since $T \propto a^{-1}$, which evolves monotonically in time, we can define a new time variable $x \equiv m_\chi/T$, where the factor of m_χ sets the time scale according to the WIMP mass. For example, if $x \ll 1$ (i.e. $T \gg m_\chi$), WIMP creation/annihilation is occurring very rapidly, which keeps the WIMP population in thermal equilibrium ($Y \simeq Y_{\text{EQ}}$) and with relativistic average velocity. Recall the Hubble parameter $H = a^{-1}\dot{a}$. This relations can be used in combination with $T \propto a^{-1}$ to transform the time variable from $t \to x$ via the Jacobian

$$\frac{dx}{dt} = \frac{d}{dt}\left(\frac{m_\chi}{T}\right) = Hx. \tag{A.3}$$

Using Equation A.3 to transform Equation A.2 yields:

$$\frac{dY}{dt} \cdot \frac{dt}{dx} = T^3 \langle \sigma_{\text{ann}} v \rangle \left(Y_{\text{EQ}}^2 - Y^2 \right) \left(\frac{dt}{dx}\right), \tag{A.4}$$

$$\frac{dY}{dx} = \left(\frac{m_\chi}{x}\right)^3 \langle \sigma_{\text{ann}} v \rangle \left(Y_{\text{EQ}}^2 - Y^2 \right) \left(\frac{1}{Hx}\right), \tag{A.5}$$

$$= \frac{m_\chi^3}{Hx^4} \langle \sigma_{\text{ann}} v \rangle \left(Y_{\text{EQ}}^2 - Y^2 \right). \tag{A.6}$$

Assuming that dark matter production occurred in the epoch of a radiation dominated universe, the energy density of the universe, ρ_{uni}, would have scaled as T^4, and the Friedmann equation (Equation 1.11) dictates,

$$H = \sqrt{\frac{8\pi G \rho_{\text{uni}}}{3}}, \tag{A.7}$$

$$H \propto H(T) = \sqrt{\frac{8\pi G}{3}} T^2, \tag{A.8}$$

$$= \sqrt{\frac{8\pi G}{3}} \left(\frac{m_\chi}{x}\right)^2 \tag{A.9}$$

$$\therefore \quad H = \frac{H(m_\chi)}{x^2}, \tag{A.10}$$

where $H(m_\chi)$ refers to the Hubble parameter at the time when $T = m_\chi$.

We now substitute Equation A.10 into Equation A.6, resulting in,

$$\frac{dY}{dx} = -\frac{\lambda}{x^2}\left(Y^2 - Y_{\mathrm{EQ}}^2\right), \tag{A.11}$$

where,

$$\lambda = \frac{m_\chi^3 \langle \sigma_{\mathrm{ann}} v \rangle}{H(m)}. \tag{A.12}$$

Recall that as the universe expanded and cooled to temperatures $T \ll m_\chi$ (i.e. $x \to \infty$) the equilibrium WIMP density $n_\chi^{(0)}$ would have scaled as $e^{-m_\chi/T}$ (see Equation 1.32). Therefore in the limit as $x \to \infty$, Y_{EQ} becomes vanishingly small and Equation A.11 can be further approximated as

$$\frac{dY}{dx} \simeq -\frac{\lambda}{x^2}Y^2. \tag{A.13}$$

Given that λ, x, and Y are all positive values, he right-hand side of Equation A.13 is always negative, which means that Y continuously decreases with time. Consequently, the ratio of $Y^2/x^2 \to 0$ as $x \to \infty$, and therefore dY/dx also must become vanishingly small. As this happens, the WIMP density variable Y asymptotically approaching a constant value, Y_∞, which describes the onset of WIMP freeze-out.

Since Equation A.13 is a separable differential equation, we can get an estimate of the WIMP relic abundance by evaluating,

$$\int_{Y_f}^{Y_\infty} \frac{dY}{Y^2} = -\lambda \int_{x_f}^{\infty} \frac{dx}{x^2} \tag{A.14}$$

$$\frac{1}{Y_\infty} - \frac{1}{Y_f} = \frac{\lambda}{x_f}, \tag{A.15}$$

where variables with the subscript f indicate their values at the moment when WIMPs froze out of thermal equilibrium. The WIMP abundance at the onset of freeze-out would have been much bigger than the relic abundance, and therefore we can further simplify and solve for Y_∞,

$$\frac{1}{Y_\infty} - \frac{1}{Y_f} \simeq \frac{1}{Y_\infty} = \frac{\lambda}{x_f} \tag{A.16}$$

Recalling that $Y \equiv n_\chi/T^3$, we can get the WIMP abundance at the time when Y first reaches its asymptotic value of Y_∞. Say that this time corresponds to temperature T_1; the number density of WIMPs at that time would be $Y_\infty T_1^3$. To extrapolate this value to the current WIMP relic abundance, we need to account for the fact that the number

density scales as a^{-3}, which is done by simply multiplying by $(a_1/a_0)^3$, where a_0 is current scale factor. Lastly, we need to convert the WIMP abundance to its energy density by multiplying by its mass m_χ. To summarize:

$$n_\chi = Y_\infty T_1^3 \qquad \text{when } Y \approx Y_\infty \tag{A.17}$$

$$n_\chi = Y_\infty T_0^3 \left(\frac{a_1 T_1}{a_0 T_0}\right)^3 \qquad \text{today} \tag{A.18}$$

$$m_\chi n_\chi = \rho_\chi = m_\chi Y_\infty T_0^3 \left(\frac{a_1 T_1}{a_0 T_0}\right)^3 \tag{A.19}$$

While typically the proportionality $T \propto a^{-1}$ is true, the annihilation of particles with masses between $100\,\text{GeV}$ and $\sim 1\,\text{MeV}$, would have slowed the cooling of the universe as it evolved. For example, once the temperature of the universe fell below $\sim 200\,\text{MeV}$, the production of muons through the reaction $\gamma\gamma \to \mu^+\mu^-$ would have started to rapidly decrease, but muon annihilation would continue to be a source of high energy (i.e. hot) photons. As a result, to good approximation, the fraction of $(a_1 T_1/a_0 T_0)^3 \simeq 1/30$ [24]. Substituting this into Equation A.19, as well as Equation A.16 then yields,

$$\rho_\chi = \frac{m_\chi T_0^3}{30} \frac{x_f}{\lambda} \tag{A.20}$$

$$= \frac{m_\chi T_0^3}{30} \frac{x_f}{\lambda} \tag{A.21}$$

$$= \frac{T_0^3}{30} \frac{x_f H(m_\chi)}{m_\chi^2 \langle \sigma_{\text{ann}} v \rangle} \quad \text{(Sub. in Eq. A.12)} \tag{A.22}$$

At this point, we must find a way to express $H(m_\chi)$ in terms of known quantities. Combining Equation A.7 and using the exact form of ρ_{uni} in a radiation dominated universe yields,

$$\text{with } \rho_{\text{uni}} = \frac{\pi^2}{30} T^4 \left[\sum_{i=\text{fermions}} g_i + \frac{7}{8} \sum_{i=\text{bosons}} g_i \right] \tag{A.23}$$

$$= \frac{\pi^2}{30} T^4 g_*(T), \tag{A.24}$$

$$H(m_\chi) = \sqrt{\frac{8\pi G}{3} \frac{\pi^2 g_*(m_\chi)}{30}} m_\chi^2 \tag{A.25}$$

$$= \sqrt{\frac{4\pi^3 G g_*(m_\chi)}{45}} m_\chi^2, \tag{A.26}$$

where g_i are the spin degrees of freedom of a given fermion or boson species, and $g_*(T) =$

$\sum_{i=\text{fermions}} g_i + 7/8 \sum_{i=\text{bosons}} g_i$ is the effective number of relativistic degrees of freedom at temperature T. We can now write the WIMP energy density as,

$$\rho_\chi = \frac{T_0^3}{30} \frac{x_f}{m_\chi^2 \langle \sigma_{\text{ann}} v \rangle} \left(\sqrt{\frac{4\pi^3 G g_*(m_\chi)}{45}} m_\chi^2 \right) \tag{A.27}$$

$$= \sqrt{\frac{4\pi^3 G g_*(m_\chi)}{45}} \frac{x_f T_0^3}{30 \langle \sigma_{\text{ann}} v \rangle}. \tag{A.28}$$

Finally, replacing x_f with its definition in terms of WIMP mass and freeze-out temperature (i.e. m_χ/T_f), and dividing Equation A.28 by the critical density of the universe brings us to the closure parameter of the WIMP relic abundance we see in Equation 1.33:

$$\Omega_\chi = \frac{\rho_\chi}{\rho_{\text{crit}}} = \sqrt{\frac{4\pi^3 G g_*(m_\chi)}{45}} \frac{m_\chi}{T_f} \frac{T_0^3}{30 \langle \sigma_{\text{ann}} v \rangle \rho_{\text{crit}}}.$$

QED.

A.2   Effect of the Prompt Window Boundary Placement for PSD

Recall the form of the scintillation time profile for LAr with a singlet-to-triplet ratio $\mathcal{R}$ (Equation 3.17):

$$S(t) = \frac{\mathcal{R}}{\tau_s} e^{-t/\tau_s} + \frac{1}{\tau_T} e^{-t/\tau_T},$$

Integrating $S(t)$ from 0 to some prompt window boundary t_{pr} gives:

$$\int_0^{t_{\text{pr}}} S(t) dt = \int_0^{t_{\text{pr}}} \frac{\mathcal{R}}{\tau_s} e^{-t/\tau_s} dt + \int_0^{t_{\text{pr}}} \frac{1}{\tau_T} e^{-t/\tau_T} dt$$
$$= \mathcal{R}(1 - e^{-t_{\text{pr}}/\tau_s}) + 1 - e^{-t_{\text{pr}}/\tau_T},$$

and integrating $S(t)$ from 0 to ∞ gives:

$$\int_0^\infty S(t) dt = \int_0^\infty \frac{\mathcal{R}}{\tau_s} e^{-t/\tau_s} dt + \int_0^\infty \frac{1}{\tau_T} e^{-t/\tau_T} dt$$
$$= \mathcal{R} + 1.$$

The objective of PSD in DEAP-3600 is to use some measure of the fraction of prompt signal, F_{pr}, as a means of scattering particle identification. Therefore we can define F_{pr}

as

$$F_{\text{pr}} \equiv \frac{\int_0^{t_{\text{pr}}} S(t)dt}{\int_0^\infty S(t)dt} = \frac{\mathcal{R}(1 - e^{-t_{\text{pr}}/\tau_S}) + 1 - e^{-t_{\text{pr}}/\tau_T}}{\mathcal{R} + 1}. \tag{A.29}$$

Equation A.29 is intended to be a near-ideal estimator of the ratio, $\mathcal{R}_0$, of singlet excimers, N_S, to singlet and triplet excimers combined, $N_S + N_T$. Recalling that $\mathcal{R} = {}^{N_S}/N_T$, $\mathcal{R}_0$ can be expressed as

$$\mathcal{R}_0 = \frac{N_S}{N_S + N_T} \tag{A.30}$$

$$= \frac{N_S}{N_T(\mathcal{R} + 1)} \tag{A.31}$$

$$= \frac{\mathcal{R}}{\mathcal{R} + 1}. \tag{A.32}$$

For LAr, where $\tau_T \gg \tau_s$, there should exist a prompt window boundary t_{pr} such that:

(i) $\tau_s < t_{\text{pr}} < \tau_T$

(ii) $\exp(-t_{\text{pr}}/\tau_S) \ll 1$

(iii) $\exp(-t_{\text{pr}}/\tau_T) \approx 1 - {}^{t_{\text{pr}}}/\tau_T$

Therefore with a choice of t_{pr} which satisfies the above conditions, Equation A.29 can be simplified to

$$F_{\text{pr}} = \frac{\mathcal{R}}{\mathcal{R} + 1} + \frac{t_{\text{pr}}/\tau_T}{\mathcal{R} + 1} = \mathcal{R}_0 + \frac{t_{\text{pr}}/\tau_T}{\mathcal{R} + 1}. \tag{A.33}$$

From Equation A.33, we can see that F_{pr} becomes a better estimator for $\mathcal{R}$, with a smaller t_{pr} (provided condition (ii) is still satisfied) and with larger $\mathcal{R}$. It is for this reason that the discrimination power of PSD in DEAP-3600 improved when changing the prompt window boundary from 150 ns to 60 ns.

An *ideal* prompt window boundary, where the bias in F_{pr} is completely unbiased, can be achieved when the contribution of the triplet excimer scintillation within the prompt window offsets the singlet excimer scintillation outside the prompt window, i.e.

$$\int_0^{t_{\text{pr}}} \frac{1}{\tau_T} e^{-t/\tau_T} dt = \int_{t_{\text{pr}}}^\infty \frac{\mathcal{R}}{\tau_s} e^{-t/\tau_s} dt \tag{A.34}$$

$$1 - e^{-t_{\text{pr}}/\tau_T} = \mathcal{R} e^{-t_{\text{pr}}/\tau_S}. \tag{A.35}$$

Equation A.35 shows that the optimal prompt window boundary which results in an unbiased F_{pr} will be dependent on the singlet-to-triplet ratio $\mathcal{R}$.

A.3   Hypothesis Testing and the Neyman-Pearson Lemma

The following is a summary of the discussion of hypotheses and statistical tests from Ref [115], and a proof of the Neyman-Pearson Lemma from Ref [214].

The aim of a statistical test is to quantify how well the predictions of various hypotheses agree with observations. The results of the test are then used to make a decision to either reject or not reject a specific hypothesis under consideration, which is called the *null hypothesis*, H_0. Statements about the validity of H_0 usually involve a comparison against an *alternative hypothesis*, H_1. For example, a search for a new type of particle might define H_0 as a background only hypothesis, and H_1 as the hypothesis with the background plus a viable signal component. Given the assumption that an hypothesis (null or alternative) is true, one might expect an observable quantity, x, to be distributed according to a probability density function (pdf), $f(x|H)$. If that hypothesis uniquely defines the pdf, then that hypothesis is said to be a *simple* hypothesis. If, on the other hand, that hypothesis has some free parameters, then it is called a *composite* hypothesis. However, a composite hypothesis can become simple if one fixes the free parameters, e.g. via measurements or in a regression algorithm.

To perform an hypothesis test, we must first define the significance level, α, of the test. This is the probability of the hypothesis test producing an Error of the First Kind: a rejection of H_0 when H_0 is true. Defining α requires a decision boundary to be drawn, which isolates a *critical region*, R_c. The definition of the critical region is such that if the data tend to fall within R_c, then they disfavour H_0. Therefore if H_0 is a simple hypothesis which predicts that the random variable, x, follows a pdf $f(x|H_0)$, the significance level can then be defined in terms of the critical region as,

$$\alpha = \int\limits_{x \in R_c} f(x'|H_0)dx'. \tag{A.36}$$

Generally, one picks a small significance level ($\alpha \sim 0.05$) as this would limit the probability of producing an Error of the First Kind. However, as most statistical tests require a comparison of H_0 with some H_1, there is another quantity to consider which measures the probability of producing an Error of the Second Kind: i.e. the probability of

rejecting H_1 when H_1 is true. This quantity is defined as,

$$\beta = \int\limits_{x \notin R_c} f(x'|H_1)dx'. \tag{A.37}$$

Generally, there is no uniquely optimal statistical test which minimizes both α and β simultaneously. Thus, the quality of the test can be measured in its ability to discriminate H_0 from H_1, with a quantity called the *statistical power* of the test, $\mathcal{M}$. Statistical power will vary with the choice of R_c and H_1, i.e.

$$\mathcal{M} = \mathcal{M}(R_c, H_1) \equiv 1 - \beta = \int\limits_{x \in R_c} f(x'|H_1)dx'. \tag{A.38}$$

The conventional procedure when designing a test is to pick a significance level, and then draw the critical region such that statistical power is maximized. Determining the critical region in this way is a non-trivial exercise, but fortunately there is a closed-form solution to this problem via the Neyman-Pearson Lemma, which states:

Lemma A.1. *A test of the simple hypothesis H_0 with respect to the simple alternative hypothesis H_1 is a "most powerful test" if the critical region R_c is chosen such that*

$$\frac{f(x|H_0)}{f(x|H_1)} \begin{cases} \leq K & \text{for all } x \in R_c \\ \geq K & \text{for all } x \notin R_c \end{cases} \tag{A.39}$$

Ref [214] contains a simple conditional proof of this statement, which will be summarized here. Suppose we picked a significance level α for our hypothesis test comparing H_0 (predicting x follows the pdf $f(x|H_0)$) against H_1 (predicting x follows the pdf $f(x|H_1)$). Also, suppose there exists a "most powerful" critical region, R_c, and another distinct choice of critical region, S, which both satisfy,

$$\int\limits_{x \in R_c} f(x'|H_0)dx' = \int\limits_{x \in S} f(x'|H_0)dx' = \alpha \tag{A.40}$$

The critical region candidates can overlap with each other as seen in Figure A.1.
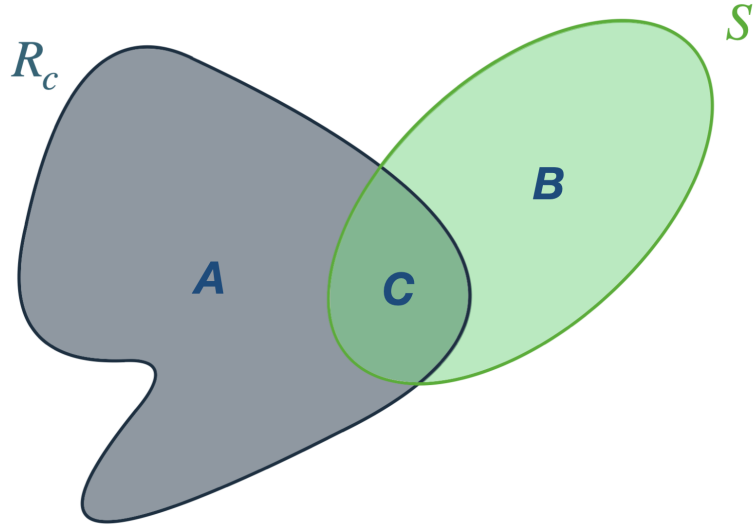
FIGURE A.1: Critical regions R_c and S.

Using the notation in Figure A.1, we can say:

$$\int\limits_{x \in A} f(x'|H_0)dx' = \int\limits_{x \in R_c} f(x'|H_0)dx' - \int\limits_{x \in C} f(x'|H_0)dx' \tag{A.41}$$

$$= \int\limits_{x \in S} f(x'|H_0)dx' - \int\limits_{x \in C} f(x'|H_0)dx' \quad \text{(from Eq. A.40)} \tag{A.42}$$

$$= \int\limits_{x \in B} f(x'|H_0)dx' \tag{A.43}$$

Here we assert that the antecedent in Lemma A.1 (i.e. Equation A.39) is true and show that this leads to the stated conclusion. If Lemma A.1 is indeed true, then since the region A is entirely contained within R_c, the following statements are also true:

$$\frac{f(x|H_0)}{f(x|H_1)} \leq K \text{ for all } x \in A \tag{A.44}$$

$$\Rightarrow \quad \frac{\int_{x \in A} f(x'|H_0)dx'}{\int_{x \in A} f(x'|H_1)dx'} \leq K \tag{A.45}$$

$$\therefore \quad \int\limits_{x \in A} f(x'|H_0)dx' \leq K \int\limits_{x \in A} f(x'|H_1)dx'. \tag{A.46}$$

An analogous statement can be made of the region B contained within the other critical region S. Although since B is also entirely outside R_c, Lemma A.1 implies

$$\int\limits_{x \in B} f(x'|H_0)dx' \geq K \int\limits_{x \in B} f(x'|H_1)dx'. \tag{A.47}$$

Now can use Equations A.43, A.46, and A.47 in the definition of statistical power:

$$\mathcal{M}(R_c, H_1) = \int\limits_{x \in R_c} f(x'|H_1)dx' \tag{A.48}$$

$$= \int\limits_{x \in A} f(x'|H_1)dx' + \int\limits_{x \in C} f(x'|H_1)dx' \tag{A.49}$$

$$\geq \frac{1}{K} \int\limits_{x \in A} f(x'|H_0)dx' + \int\limits_{x \in C} f(x'|H_1)dx' \quad \text{(from Eq. A.46)} \tag{A.50}$$

$$\geq \frac{1}{K} \left(\int\limits_{x \in B} f(x'|H_0)dx' \right) + \int\limits_{x \in C} f(x'|H_1)dx' \quad \text{(from Eq. A.43)} \tag{A.51}$$

$$\geq \frac{1}{K} \left(K \int\limits_{x \in B} f(x'|H_1)dx' \right) + \int\limits_{x \in C} f(x'|H_1)dx' \quad \text{(from Eq. A.47)} \tag{A.52}$$

$$\geq \int\limits_{x \in B} f(x'|H_1)dx' + \int\limits_{x \in C} f(x'|H_1)dx' \tag{A.53}$$

$$\geq \mathcal{M}(S, H_1), \tag{A.54}$$

or more directly,

$$\mathcal{M}(R_c, H_1) \geq \mathcal{M}(S, H_1). \tag{A.55}$$

Since the alternative critical region S was defined arbitrarily, Equation A.55 is true in general. Therefore a statistical test with the critical region R_c satisfies the definition of a "most powerful test."

Appendix B

Computational Algorithms

B.1 `MBLikelihood` Position Reconstruction Routine

The `MBLikelihood` position reconstruction algorithm uses the observed number of PEs in each PMT and the inverse-square law to find the event position which maximizes the likelihood function:

$$\mathcal{L}(\mathbf{r}) = \prod_{i=1}^{255} \text{Poisson}(Q_i; E_i(\mathbf{r})), \tag{B.1}$$

where,

$$\text{Poisson}(x; \lambda) = \frac{\lambda^x e^{-\lambda}}{\Gamma(x+1)},$$

$$Q_i \equiv \text{Observed PE count in } i^{\text{th}} \text{ PMT},$$

$$E_i(\mathbf{r}) \equiv \text{Expected PE count in } i^{\text{th}} \text{ PMT},$$

$$= \frac{1}{|\mathbf{R}_i - \mathbf{r}|^2} \sum_{i=1}^{255} Q_i,$$

$$\mathbf{r} \equiv \text{Event position},$$

$$\mathbf{R}_i \equiv \text{Position of } i^{\text{th}} \text{ PMT}.$$

The pseudo-code in Algorithm 1 will call on the following:

1. `SORT(array` XX`, array` YY`)`

   Orders the elements of XX from smallest to greatest, and rearranges elements of

238

YY accordingly; i.e. if $XX[i]$ becomes $XX[j]$, then $YY[i]$ becomes $YY[j]$. Note: arrays XX and YY are the same size.

2. `PMT::GetPECount()`

   Returns the number of PEs detected (`nSCBayes`) in a specified PMT.

3. `PMT::GetPosition()`

   Returns the 3D vector position of a specified PMT relative to the centre of the detector.

Algorithm 1 `MBLikelihood` Nelder-Mead Simplex Algorithm

Require: Input (`vector array` $\mathbf{r}_{\mathrm{init}}$, `PMT array` P, `int` $n_{\max}$)
 1: `const int` $N_{\mathrm{dim}} \leftarrow 3$ ▷ Number of spatial dimensions
 2: `const int` $N_{\mathrm{v}} \leftarrow N_{\mathrm{dim}} + 1$ ▷ Number of simplex vertices
 3: `float` $\alpha \leftarrow 1.0$
 4: `float` $\beta \leftarrow 0.5$
 5: `float` $\gamma \leftarrow 2.0$
 6: `float` $\delta \leftarrow 0.5$
 7:
 8: `float` $Q_{\mathrm{tot}} \leftarrow 0$ ▷ Get total PE count
 9: `int` $i \leftarrow 1$
10: **while** $(i \leq \mathtt{length}(P))$ **do**
11:     $Q_{\mathrm{tot}} \leftarrow Q_{\mathrm{tot}} + P[i] :: \mathrm{GetPECount}()$
12:     $i \leftarrow i + 1$
13: **end while**
14:
15: `int` $n_{\mathrm{con}} \leftarrow 0$ ▷ Number of consecutive simplex contractions
16: `vector array` $\mathbf{r}_{\mathrm{simp}} \leftarrow \mathbf{r}_{\mathrm{init}}$ ▷ Declare initial simplex vertices
17: **while** $(n_{\mathrm{con}} < n_{\max})$ **do**
18:     `vector` $L \leftarrow (1,1,1,1)$
19:     $i \leftarrow 1$
20:     **while** $(i \leq \mathtt{length}(\mathbf{r}_{\mathrm{simp}}))$ **do**
21:        $L[i] \leftarrow -\ln(\mathcal{L}(\mathbf{r}_{\mathrm{simp}}[i]))$ ▷ As in Eq.B.1
22:        $i \leftarrow i + 1$
23:     **end while**
24:     $\mathrm{SORT}(L, \mathbf{r}_{\mathrm{simp}})$ ▷ See Item 1 above
25:     `vector` $\mathbf{r}_{\mathrm{cen}} \leftarrow \frac{1}{N_{\mathrm{dim}}} \sum_{i=1}^{N_{\mathrm{dim}}} \mathbf{r}_{\mathrm{simp}}[i]$ ▷ Compute centroid
26:     `vector` $\mathbf{r}_{\mathrm{ref}} \leftarrow \mathbf{r}_{\mathrm{cen}} + \alpha(\mathbf{r}_{\mathrm{cen}} - \mathbf{r}_{\mathrm{simp}}[N_{\mathrm{v}}])$ ▷ Compute reflected point
27:     `float` $L_{\mathrm{ref}} \leftarrow -\ln(\mathcal{L}(\mathbf{r}_{\mathrm{ref}}))$
28:     **if** $(L[1] \leq L_{\mathrm{ref}} \leq L[N_{\mathrm{dim}}])$ **then**
29:        $\mathbf{r}_{\mathrm{simp}}[N_{\mathrm{v}}] \leftarrow \mathbf{r}_{\mathrm{ref}}$
30:        $n_{\mathrm{con}} \leftarrow 0$
31:        **next iteration**
32:     **end if**
33:     **if** $(L_{\mathrm{ref}} < L[1])$ **then**
34:        `vector` $\mathbf{r}_{\mathrm{exp}} \leftarrow \mathbf{r}_{\mathrm{cen}} + \gamma(\mathbf{r}_{\mathrm{cen}} - \mathbf{r}_{\mathrm{ref}})$ ▷ Compute expanded point

```
35:            float L_exp ← −ln(𝓛(r_exp))
36:            if (L_exp < L_ref) then
37:                r_simp[N_v] ← r_exp
38:            else
39:                r_simp[N_v] ← r_ref
40:            end if
41:            n_con ← 0
42:            next iteration
43:        end if
44:        if (L_ref ≥ L[N_dim]) then
45:            vector r_con ← r_cen + β(r_simp[N_v] − r_cen)        ▷ Compute contracted point
46:            float L_con ← −ln(𝓛(r_con))
47:            if (L_con < L[N_v]) then
48:                r_simp[N_v] ← r_con
49:                n_con ← 0
50:                next iteration
51:            end if
52:        end if                                                   ▷ Compute shrink point
53:        i ← 2
54:        while (i ≤length(r_simp)) do
55:            r_simp[i] ← r_simp[1] + δ(r_simp[i] − r_simp[1])
56:        end while
57:        n_con ← n_con + 1
58: end while
59: return r_simp[1]
```

B.2 Sensitive Nonlinear Iterative Peak Finding Algorithm

Algorithm 2 The SNIP Algorithm

Require: Input (`float array` S, `int` σ)

1: `int` $n \leftarrow 0$
2: `float array` $L \leftarrow$ `zeroes(length`(S)`)`
3: `float array` $B \leftarrow$ `zeroes(length`(S)`)`
4: **while** $(n < $ `length`$(L))$ **do**
5:      $L[n] = \log\left(\log(\sqrt{S[n]+1}+1)+1\right)$
6:      $n \leftarrow n+1$
7: **end while**
8: `int` $m \leftarrow 0$
9: **while** $(m < \sigma)$ **do**
10:      $n \leftarrow m$
11:      **while** $(n < $ `length`$(L) - m)$ **do**
12:          `float` $V_1 \leftarrow L[n]$
13:          `float` $V_2 \leftarrow \frac{1}{2}\left(L[n-m] + L[n+m]\right)$
14:          $L[n] \leftarrow$ `min`(V_1, V_2)
15:          $n \leftarrow n+1$
16:      **end while**
17:      $m \leftarrow m+1$
18: **end while**
19: $n \leftarrow 0$
20: **while** $(n < $ `length`$(L))$ **do**
21:      $B[n] \leftarrow \left(\exp\big(\exp(L[n]) - 1\big) - 1\right)^2 - 1$
22: **end while**
23: **return** B

B.3   MIEL Cosmic Ray Removal Algorithm

Algorithm 3 The MIEL CRR Algorithm

Require: Input (`float 2Darray` S, `int` σ_{cr}, `float` Y_{thr})

 1: `int` $n \leftarrow 0$
 2: **while** $(n < \mathtt{lengthY}(S))$ **do**
 3:     `float array` $S_{\mathrm{bkg}} \leftarrow S[n][:]$
 4:     $S_{\mathrm{bkg}} \leftarrow \mathtt{SNIP}(S_{\mathrm{bkg}}, \sigma_{\mathrm{cr}})$ ▷ where `SNIP` is defined in Algorithm 2
 5:     `int` $m \leftarrow 0$
 6:     **while** $(m < \mathtt{lengthX}(S))$ **do**
 7:         **if** $(\mathtt{abs}(S[n][m] - S_{\mathrm{bkg}}[m]) > Y_{\mathrm{thr}})$ **then**
 8:             $S[n][m] \leftarrow S_{\mathrm{bkg}}[m]$
 9:         **else**
10:             do nothing
11:         **end if**
12:         $m \leftarrow m + 1$
13:     **end while**
14:     $n \leftarrow n + 1$
15: **end while**
16: **return** S

Appendix C

PLR Background Model Plots

C.1 ^{210}Po α Backgrounds

(A)

(B)
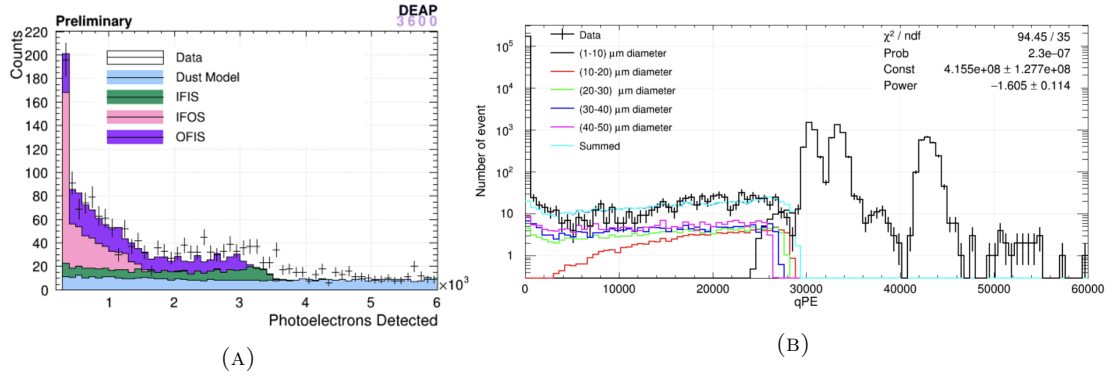
FIGURE C.1: (A) Neck α control region fit and (B) dust α control region fit.
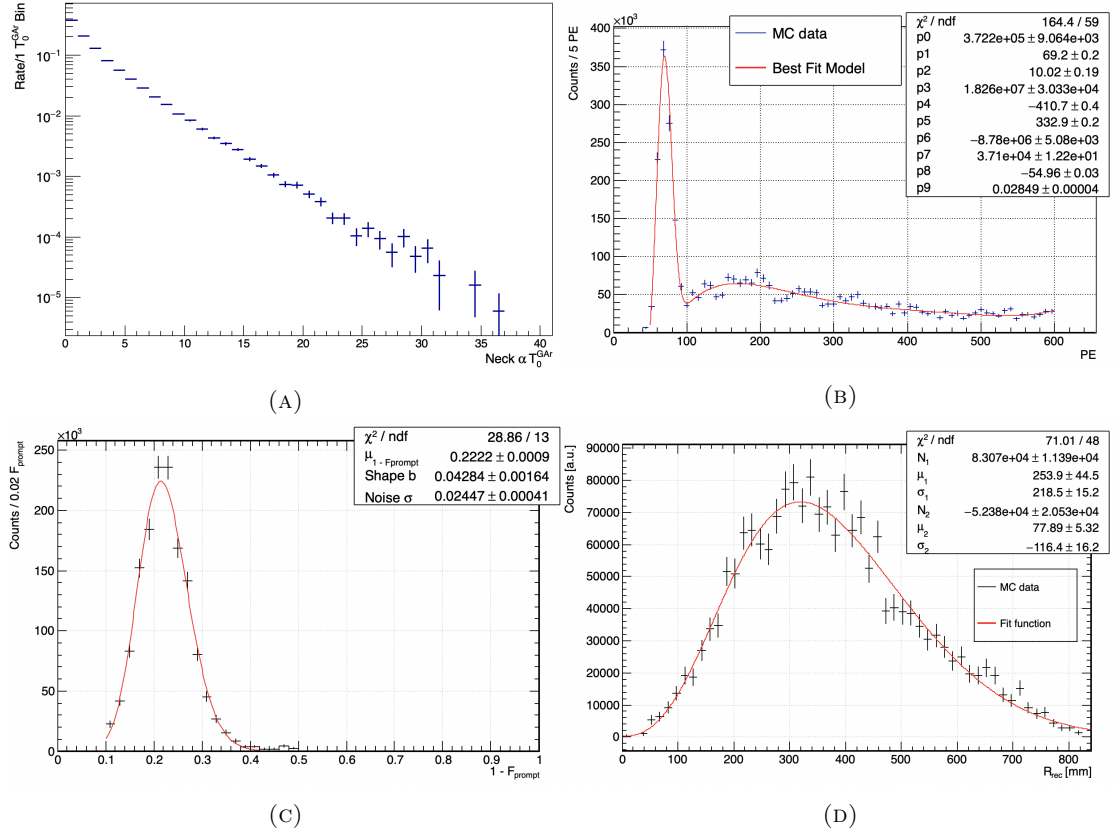
FIGURE C.2: (A) Neck α T_0^{GAr} distribution. (B) Neck α `nSCBayes` distribution for $T_0^{GAr} \leq 2$ with fit results of Equation 4.50. (C) Neck α `Fprompt` distribution for $T_0^{GAr} \leq 2$ with fit results of Equation 4.51. (D) Neck α `Rrec` distribution for $T_0^{GAr} \leq 2$ with fit results of Equation 4.52.
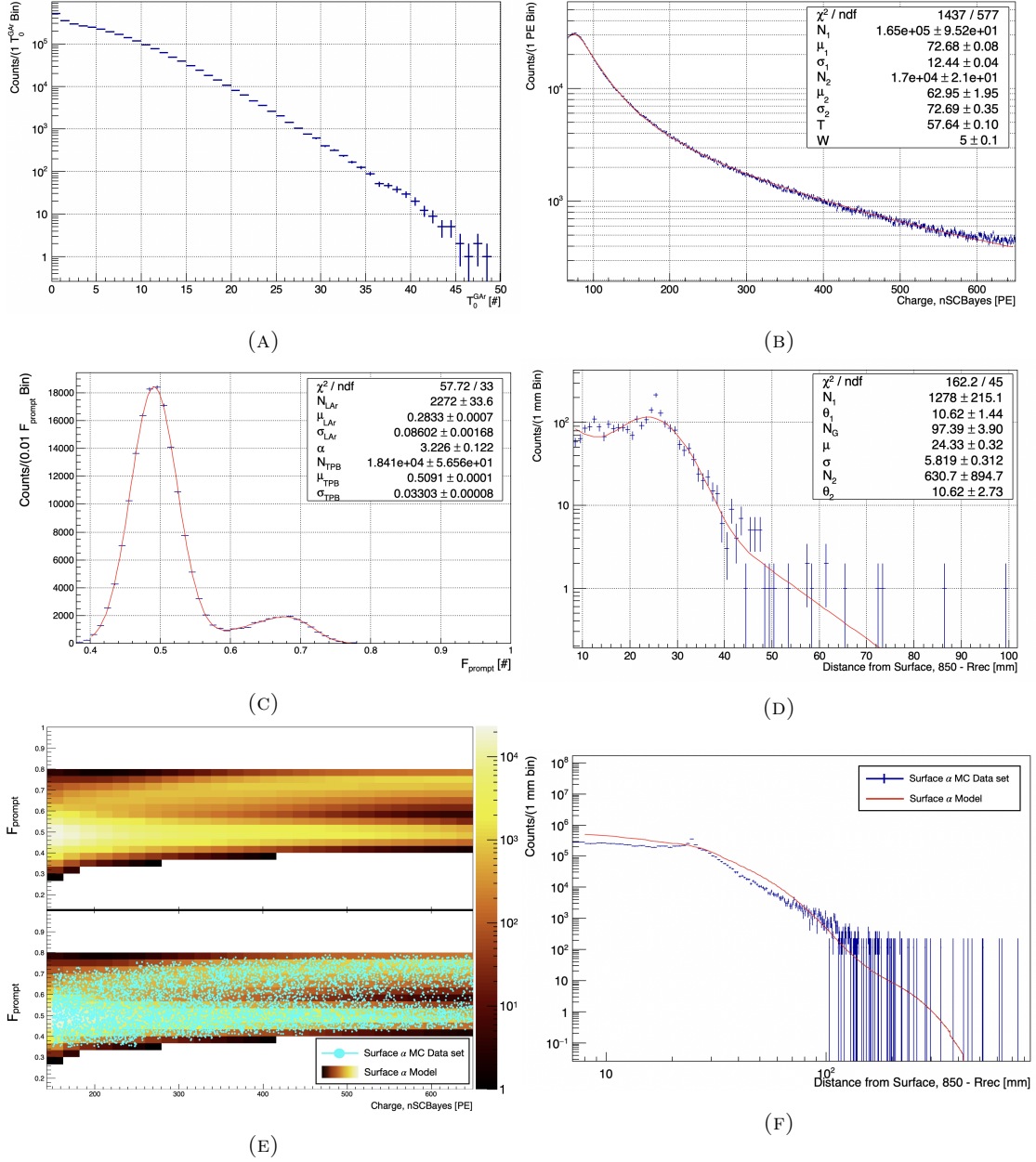
FIGURE C.3: (A) Surface α $\mathtt{T}_0^{\mathrm{GAr}}$ distribution. (B) Surface α `nSCBayes` distribution with fit results of Equation 4.46. (C) Surface α `Fprompt` distribution with fit results of Equation 4.47. (D) Surface α `Rrec` distribution with fit results of Equation 4.48. (E) Full PE-dependent Surface α `Fprompt` pdf with overlaid MC data set. (F) Surface α `Rrec` pdf integrated from 65–650 PE with MC data set overlaid.
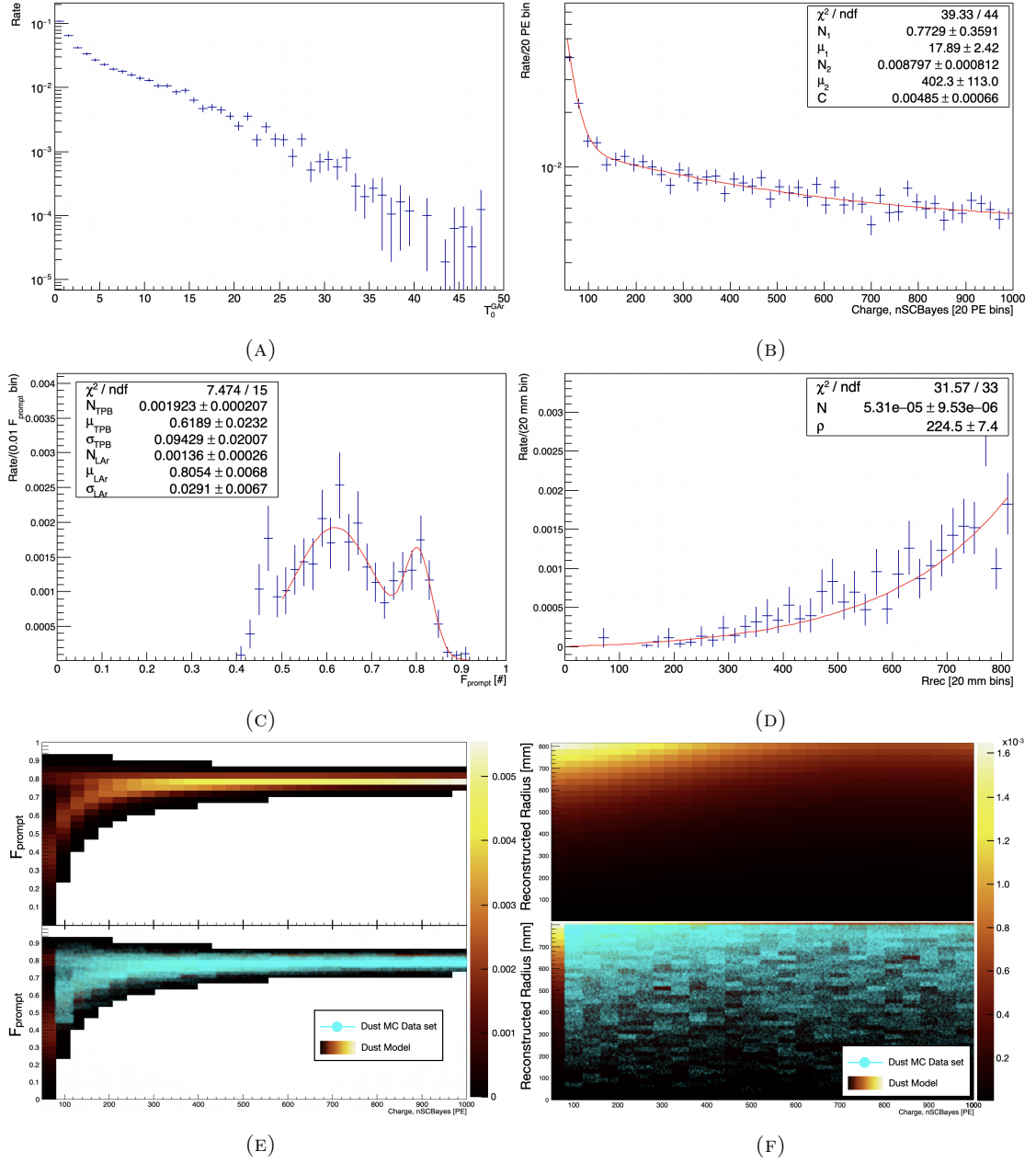
FIGURE C.4: (A) Dust α $\mathtt{T}_0^{\mathrm{GAr}}$ distribution. (B) Dust α $\mathtt{nSCBayes}$ distribution with fit results of Equation 4.53. (C) Dust α $\mathtt{Fprompt}$ distribution with fit results of Equation 4.54. (D) Dust α $\mathtt{Rrec}$ distribution with fit results of Equation 4.55. (E) Full PE-dependent dust α $\mathtt{Fprompt}$ pdf with overlaid MC data set. (F) Full PE-dependent dust α $\mathtt{Rrec}$ pdf with overlaid MC data set.

C.2 Radiogenic Neutrons
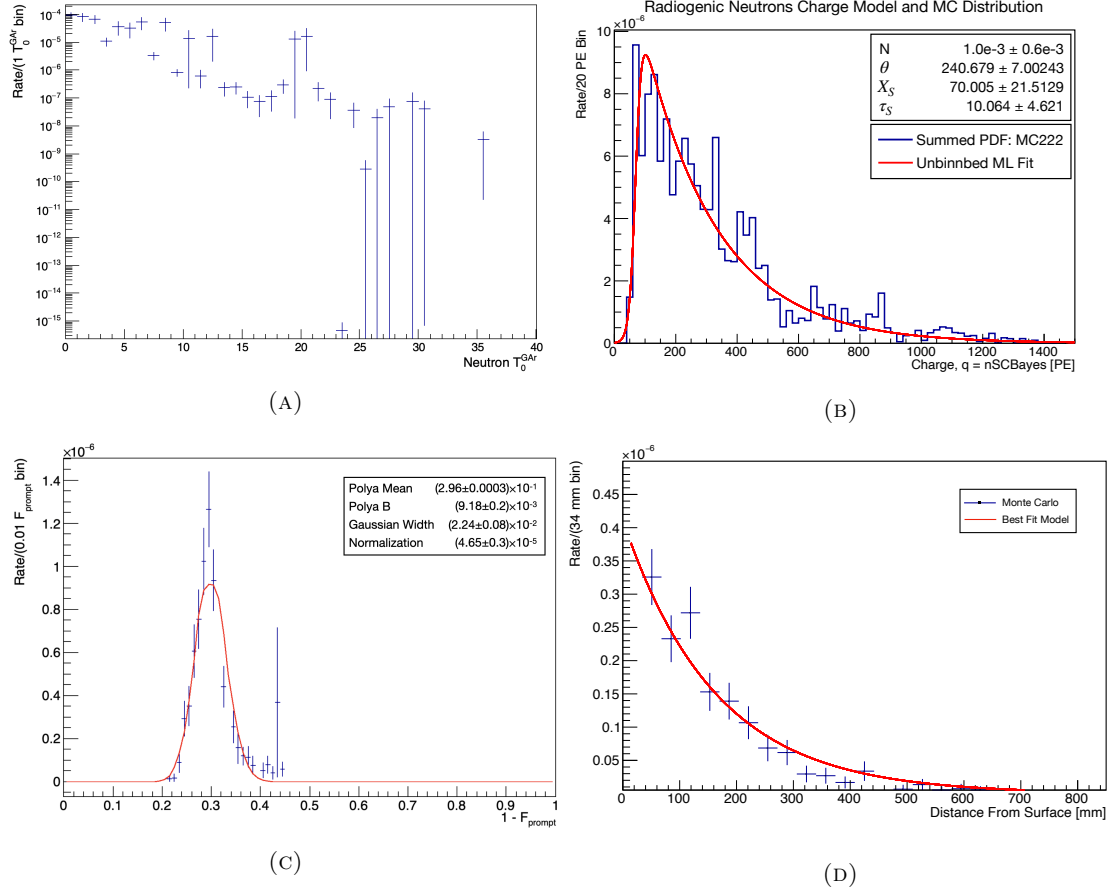

(A)

(B)

(C)

(D)

FIGURE C.5: (A) Radiogenic neutron T_0^{GAr} distribution. (B) radiogenic neutron `nSCBayes` distribution with fit results of Equation 4.56. (C) Radiogenic Neutron `Fprompt` distribution with fit results of Equation 4.57. (D) Radiogenic neutron `Rrec` distribution with fit results of Equation 4.58.

Bibliography

[1] Georges Aad, Tatevik Abajyan, B Abbott, J Abdallah, S Abdel Khalek, Ahmed Ali Abdelalim, R Aben, B Abi, M Abolins, OS AbouZeid, et al. Observation of a new particle in the search for the standard model higgs boson with the atlas detector at the lhc. *Physics Letters B*, 716(1):1–29, 2012.

[2] E Radermacher. The experimental discovery of the intermediate vector bosons w^+, w^- and z^0 at the cern pp collider. *Progress in Particle and Nuclear Physics*, 14:231–328, 1985.

[3] Michael E Peskin. *An introduction to quantum field theory*. CRC press, 2018.

[4] Horaţiu Năstase. Evidence for dark matter and the λ-cdm model. In *Cosmology and String Theory*, pages 41–51. Springer, 2019.

[5] Nabila Aghanim, Yashar Akrami, Mark Ashdown, J Aumont, C Baccigalupi, M Ballardini, AJ Banday, RB Barreiro, N Bartolo, S Basak, et al. Planck 2018 results-vi. cosmological parameters. *Astronomy & Astrophysics*, 641:A6, 2020.

[6] Lord William Thomson Kelvin. *Baltimore lectures on molecular dynamics and the wave theory of light*. CUP Archive, 1904.

[7] Gianfranco Bertone and Dan Hooper. History of dark matter. *Reviews of Modern Physics*, 90(4):045002, 2018.

[8] Edwin Hubble and Milton L Humason. The velocity-distance relation among extra-galactic nebulae. *The Astrophysical Journal*, 74:43, 1931.

[9] Fritz Zwicky. Republication of: The redshift of extragalactic nebulae. *General Relativity and Gravitation*, 41(1):207–224, 2009.

[10] Edwin P Hubble. Extragalactic nebulae. *The Astrophysical Journal*, 64, 1926.

[11] Sinclair Smith. The mass of the virgo cluster. *The Astrophysical Journal*, 83:23, 1936.

[12] Harold Irving Ewen and Edward Mills Purcell. Observation of a line in the galactic radio spectrum: Radiation from galactic hydrogen at 1,420 mc./sec. *Nature*, 168 (4270):356–356, 1951.

[13] Vera C Rubin and W Kent Ford Jr. Rotation of the andromeda nebula from a spectroscopic survey of emission regions. *The Astrophysical Journal*, 159:379, 1970.

[14] Horace W Babcock. The rotation of the andromeda nebula. *Lick Observatory Bulletin*, 19:41–51, 1939.

[15] Robert N Whitehurst and Morton S Roberts. High-velocity neutral hydrogen in the central region of the andromeda galaxy. *The Astrophysical Journal*, 175:347, 1972.

[16] Claude Carignan, Laurent Chemin, Walter K Huchtmeier, and Felix J Lockman. The extended hi rotation curve and mass distribution of m31. *The Astrophysical Journal*, 641(2):L109, 2006.

[17] Kenneth C Freeman. On the disks of spiral and s0 galaxies. *The Astrophysical Journal*, 160:811, 1970.

[18] DH Rogstad and GS Shostak. Gross properties of five scd galaxies as determined from 21-centimeter observations. *The Astrophysical Journal*, 176:315, 1972.

[19] Vera C Rubin, W Kent Ford Jr, and Norbert Thonnard. Extended rotation curves of high-luminosity spiral galaxies. iv-systematic dynamical properties, sa through sc. *The Astrophysical Journal*, 225:L107–L111, 1978.

[20] Douglas Clowe, Maruša Bradač, Anthony H Gonzalez, Maxim Markevitch, Scott W Randall, Christine Jones, and Dennis Zaritsky. A direct empirical proof of the existence of dark matter. *The Astrophysical Journal*, 648(2):L109, 2006.

[21] Yannick Mellier. Probing the universe with weak lensing. *Annual Review of Astronomy and Astrophysics*, 37(1):127–189, 1999.

[22] Dennis J Hegyi and Keith A Olive. Can galactic halos be made of baryons? *Physics Letters B*, 126(1-2):28–32, 1983.

[23] Charles Alcock, RA Allsman, David R Alves, TS Axelrod, Andrew C Becker, DP Bennett, Kem H Cook, N Dalal, Andrew John Drake, KC Freeman, et al. The macho project: microlensing results from 5.7 years of large magellanic cloud observations. *The Astrophysical Journal*, 542(1):281, 2000.

[24] Scott Dodelson. *Modern cosmology*. Elsevier, 2003.

[25] Donald H Perkins. *Particle astrophysics*. Oxford University Press, 2009.

[26] Scott Burles and David Tytler. The deuterium abundance toward q1937-1009. *The Astrophysical Journal*, 499(2):699–712, jun 1998. doi: 10.1086/305667. URL https://doi.org/10.1086/305667.

[27] Scott Burles and David Tytler. The deuterium abundance toward QSO 1009+2956. *The Astrophysical Journal*, 507(2):732–744, nov 1998. doi: 10.1086/306341. URL https://doi.org/10.1086/306341.

[28] Scott Burles, Kenneth M Nollett, James W Truran, and Michael S Turner. Sharpening the predictions of big-bang nucleosynthesis. *Physical Review Letters*, 82(21): 4176, 1999.

[29] Charles L Bennett, Davin Larson, Janet L Weiland, N Jarosik, G Hinshaw, N Odegard, KM Smith, RS Hill, B Gold, M Halpern, et al. Nine-year wilkinson microwave anisotropy probe (wmap) observations: final maps and results. *The Astrophysical Journal Supplement Series*, 208(2):20, 2013.

[30] Planck Collaboration et al. Planck 2015 results: I. overview of products and scientific results. *Astronomy & Astrophysics*, 594:1–38, 2015.

[31] George F Smoot, Charles L Bennett, A Kogut, EL Wright, J Aymon, NW Boggess, ES Cheng, G De Amici, S Gulkis, MG Hauser, et al. Structure in the cobe differential microwave radiometer first-year maps. *The Astrophysical Journal*, 396: L1–L5, 1992.

[32] Nabila Aghanim, Yashar Akrami, Mark Ashdown, J Aumont, Carlo Baccigalupi, M Ballardini, Anthony J Banday, RB Barreiro, N Bartolo, S Basak, et al. Planck 2018 results-v. cmb power spectra and likelihoods. *Astronomy & Astrophysics*, 641:A5, 2020.

[33] George R Blumenthal, SM Faber, Joel R Primack, and Martin J Rees. Formation of galaxies and large-scale structure with cold dark matter. *Nature*, 311(5986): 517–525, 1984.

[34] Olga Cucciati, BC Lemaux, G Zamorani, O Le Fèvre, LAM Tasca, NP Hathi, K-G Lee, Sandro Bardelli, P Cassata, BIANCA Garilli, et al. The progeny of a cosmic titan: a massive multi-component proto-supercluster in formation at z= 2.45 in vuds. *Astronomy & Astrophysics*, 619:A49, 2018.

[35] PA Oesch, G Brammer, PG Van Dokkum, GD Illingworth, RJ Bouwens, I Labbé, M Franx, I Momcheva, MLN Ashby, GG Fazio, et al. A remarkably luminous galaxy at z= 11.1 measured with hubble space telescope grism spectroscopy. *The Astrophysical Journal*, 819(2):129, 2016.

[36] Linhua Jiang, Nobunari Kashikawa, Shu Wang, Gregory Walth, Luis C Ho, Zheng Cai, Eiichi Egami, Xiaohui Fan, Kei Ito, Yongming Liang, et al. Evidence for gn-z11 as a luminous galaxy at redshift 10.957. *Nature Astronomy*, 5(3):256–261, 2021.

[37] Marc Aaronson. Accurate radial velocities for carbon stars in draco and ursa minor: the first hint of a dwarf spheroidal mass-to-light ratio, 1983.

[38] Sean M Carroll. *Spacetime and geometry.* Cambridge University Press, 2019.

[39] Ruprecht Machleidt, Karl Holinde, and Ch Elster. The bonn meson-exchange model for the nucleon—nucleon interaction. *Physics Reports*, 149(1):1–89, 1987.

[40] Peter W Graham, Igor G Irastorza, Steven K Lamoreaux, Axel Lindner, and Karl A van Bibber. Experimental searches for the axion and axion-like particles. *Annual Review of Nuclear and Particle Science*, 65:485–514, 2015.

[41] Christopher Abel, Samer Afach, Nicholas J Ayres, Colin A Baker, Gilles Ban, Georg Bison, Kazimierz Bodek, Vira Bondar, Martin Burghoff, E Chanel, et al. Measurement of the permanent electric dipole moment of the neutron. *Physical Review Letters*, 124(8):081803, 2020.

[42] Roberto D Peccei and Helen R Quinn. Cp conservation in the presence of pseudoparticles. *Physical Review Letters*, 38(25):1440, 1977.

[43] Ron Mayle, James R Wilson, John Ellis, Keith Olive, David N Schramm, and Gary Steigman. Constraints on axions from sn 1987a. *Physics Letters B*, 203(1-2): 188–196, 1988.

[44] MA Acero, P Adamson, G Agam, L Aliaga, T Alion, V Allakhverdian, N Anfimov, A Antoshkin, E Arrieta-Diaz, L Asquith, et al. Supernova neutrino detection in nova. *Journal of Cosmology and Astroparticle Physics*, 2020(10):014, 2020.

[45] Igor G Irastorza and Javier Redondo. New experimental approaches in the search for axion-like particles. *Progress in Particle and Nuclear Physics*, 102:89–159, 2018.

[46] Howard Baer, Ki-Young Choi, Jihn E Kim, and Leszek Roszkowski. Dark matter production in the early universe: beyond the thermal wimp paradigm. *Physics Reports*, 555:1–60, 2015.

[47] C Bartram, T Braine, E Burns, R Cervantes, N Crisosto, N Du, H Korandla, G Leum, P Mohapatra, T Nitta, et al. Search for invisible axion dark matter in the 3.3–4.2 μ ev mass range. *Physical review letters*, 127(26):261803, 2021.

[48] Julien Billard, Mark Boulay, Susana Cebrián, Laura Covi, Giuliana Fiorillo, Anne M Green, Joachim Kopp, Béla Majorovits, Kimberly Palladino, Federica Petricca, et al. Direct detection of dark matter–appec committee report. *Reports on Progress in Physics*, 2022.

[49] Savas Dimopoulos, Glenn D Starkman, and Bryan W Lynn. Atomic enhancements in the detection of weakly interacting particles. *Physics Letters B*, 168(1-2):145–150, 1986.

[50] Gerard Jungman, Marc Kamionkowski, and Kim Griest. Supersymmetric dark matter. *Physics Reports*, 267(5-6):195–373, 1996.

[51] David E Kaplan, Markus A Luty, and Kathryn M Zurek. Asymmetric dark matter. *Physical Review D*, 79(11):115016, 2009.

[52] Kalliopi Petraki and Raymond R Volkas. Review of asymmetric dark matter. *International Journal of Modern Physics A*, 28(19):1330028, 2013.

[53] Carlos E Yaguna. New constraints on xenonphobic dark matter from deap-3600. *Journal of Cosmology and Astroparticle Physics*, 2019(04):041, 2019.

[54] J.D. Lewin and P.F. Smith. Review of mathematics, numerical factors, and corrections for dark matter experiments based on elastic nuclear recoil. *Astroparticle Physics*, 6(1):87–112, 1996. ISSN 0927-6505. doi: https://doi.org/10.1016/S0927-6505(96)00047-3. URL https://www.sciencedirect.com/science/article/pii/S0927650596000473.

[55] F. Donato, N. Fornengo, and S. Scopel. Effects of galactic dark halo rotation on wimp direct detection. *Astroparticle Physics*, 9(3):247–260, 1998. ISSN 0927-6505. doi: https://doi.org/10.1016/S0927-6505(98)00025-5. URL https://www.sciencedirect.com/science/article/pii/S0927650598000255.

[56] Richard H Helm. Inelastic and elastic scattering of 187-mev electrons from selected even-even nuclei. *Physical Review*, 104(5):1466, 1956.

[57] Chanpreet Amole, M Ardid, IJ Arnquist, DM Asner, D Baxter, E Behnke, M Bressler, B Broerman, G Cao, CJ Chen, et al. Dark matter search results from the complete exposure of the pico-60 c 3 f 8 bubble chamber. *Physical Review D*, 100(2):022001, 2019.

[58] Quentin Arnaud, D Asner, J-P Bard, A Brossard, B Cai, M Chapellier, M Clark, EC Corcoran, T Dandl, A Dastgheibi-Fard, et al. First results from the news-g direct dark matter search experiment at the lsm. *Astroparticle Physics*, 97:54–62, 2018.

[59] R Ajaj, P-A Amaudruz, GR Araujo, M Baldwin, M Batygov, B Beltran, CE Bina, J Bonatt, MG Boulay, B Broerman, et al. Search for dark matter with a 231-day exposure of liquid argon using deap-3600 at snolab. *Physical Review D*, 100(2):022004, 2019.

[60] P Adhikari, R Ajaj, GR Araujo, M Batygov, B Beltran, CE Bina, Mark Guy Boulay, B Broerman, JF Bueno, A Butcher, et al. The liquid-argon scintillation pulseshape in deap-3600. *The European Physical Journal C*, 80(4):1–12, 2020.

[61] J Aalbers, DS Akerib, CW Akerlof, AK Al Musalhi, F Alder, A Alqahtani, SK Alsum, CS Amarasinghe, A Ames, TJ Anderson, et al. First dark matter search results from the lux-zeplin (lz) experiment. *arXiv preprint arXiv:2207.03764*, 2022.

[62] C. E. Aalseth and et al. Darkside-20k: A 20 tonne two-phase lar tpc for direct dark matter detection at lngs. *The European Physical Journal Plus*, 133(3):131, 2018.

[63] P Agnes, IFM Albuquerque, T Alexander, AK Alton, GR Araujo, M Ave, HO Back, B Baldin, G Batignani, K Biery, et al. Darkside-50 532-day dark matter search with low-radioactivity argon. *Physical Review D*, 98(10):102006, 2018.

[64] Z Ahmed, DS Akerib, S Arrenberg, CN Bailey, D Balakishiyeva, L Baudis, DA Bauer, PL Brink, T Bruch, R Bunker, et al. Results from a low-energy analysis of the cdms ii germanium data. *Physical Review Letters*, 106(13):131302, 2011.

[65] R Agnese, T Aralis, T Aramaki, IJ Arnquist, E Azadbakht, W Baker, S Banik, D Barker, DA Bauer, T Binder, et al. First dark matter constraints from a supercdms single-charge sensitive detector. *Physical review letters*, 121(5):051301, 2018.

[66] Pietro Giampa. The Scintillating Bubble Chamber (SBC) Experiment for Dark Matter and Reactor CEvNS. *PoS*, ICHEP2020:632, 2021. doi: 10.22323/1.390. 0632.

[67] Ciaran AJ O'Hare. New definition of the neutrino floor for direct dark matter searches. *Physical review letters*, 127(25):251802, 2021.

[68] Ahmed H Abdelhameed, G Angloher, P Bauer, A Bento, E Bertoldo, C Bucci, L Canonica, Antonio D'Addabbo, X Defay, S Di Lorenzo, et al. First results from the cresst-iii low-mass dark matter program. *Physical Review D*, 100(10):102002, 2019.

[69] G Angloher, S Banik, G Benato, A Bento, A Bertolini, R Breier, C Bucci, L Canonica, A D'Addabbo, S Di Lorenzo, et al. Latest observations on the low energy excess in cresst-iii. *arXiv preprint arXiv:2207.09375*, 2022.

[70] P Agnes, Ivone Freire da Mota Albuquerque, T Alexander, AK Alton, GR Araujo, David M Asner, M Ave, Henning O Back, B Baldin, G Batignani, et al. Low-mass dark matter search with the darkside-50 experiment. *Physical review letters*, 121 (8):081307, 2018.

[71] Elena Aprile, Jelle Aalbers, F Agostini, M Alfonsi, L Althueser, FD Amaro, Vasile C Antochi, E Angelino, F Arneodo, Derek Barge, et al. Light dark matter search with ionization signals in xenon1t. *Physical Review Letters*, 123(25):251801, 2019.

[72] Yue Meng, Zhou Wang, Yi Tao, Abdusalam Abdukerim, Zihao Bo, Wei Chen, Xun Chen, Yunhua Chen, Chen Cheng, Yunshan Cheng, et al. Dark matter search

results from the pandax-4t commissioning run. *Physical Review Letters*, 127(26): 261802, 2021.

[73] Cristiano Galbiati and The Global Argon Dark Matter Collaboration. Future dark matter searches with low-radioactivity argon. *input to the European particle physics strategy update*, 2018–2020.

[74] J.F. Ziegler. The background in detectors caused by sea level cosmic rays. *Nuclear Instruments and Methods in Physics Research*, 191(1):419–424, 1981. ISSN 0167-5087. doi: https://doi.org/10.1016/0029-554X(81)91039-9. URL https://www.sciencedirect.com/science/article/pii/0029554X81910399.

[75] NJT Smith. The snolab deep underground facility. *The European Physical Journal Plus*, 127(9):1–8, 2012.

[76] Jens Lindhard, V Nielsen, M Scharff, and PV Thomsen. Integral equations governing radiation effects. *Mat. Fys. Medd. Dan. Vid. Selsk*, 33(10):1–42, 1963.

[77] D.-M. Mei, Z.-B. Yin, L.C. Stonehill, and A. Hime. A model of nuclear recoil scintillation efficiency in noble liquids. *Astroparticle Physics*, 30(1):12–17, 2008. ISSN 0927-6505. doi: https://doi.org/10.1016/j.astropartphys.2008.06.001. URL https://www.sciencedirect.com/science/article/pii/S0927650508000765.

[78] A Hitachi, T Doke, and A Mozumder. Luminescence quenching in liquid argon under charged-particle impact: Relative scintillation yield at different linear energy transfers. *Physical Review B*, 46(18):11463, 1992.

[79] Tadayoshi Doke, Akira Hitachi, Jun Kikuchi, Kimiaki Masuda, Hiroyuki Okada, and Eido Shibamura. Absolute scintillation yields in liquid argon and xenon for various particles. *Japanese Journal of Applied Physics*, 41(Part 1, No. 3A):1538–1545, mar 2002. doi: 10.1143/jjap.41.1538. URL https://doi.org/10.1143/jjap.41.1538.

[80] I.D. Clark, A.J. Masson, and R.P. Wayne. Penning ionization of no and o2(1Δg) by argon in the 3p1 state. *Molecular Physics*, 23(5):995–1005, 1972. doi: 10.1080/00268977200100981. URL https://doi.org/10.1080/00268977200100981.

[81] John Betteley Birks. Scintillations from organic crystals: specific fluorescence and relative response to different radiations. *Proceedings of the Physical Society. Section A*, 64(10):874, 1951.

[82] Akira Hitachi, Tan Takahashi, Nobutaka Funayama, Kimiaki Masuda, Jun Kikuchi, and Tadayoshi Doke. Effect of ionization density on the time dependence of luminescence from liquid argon and xenon. *Phys. Rev. B*, 27:5279–5285, May 1983. doi: 10.1103/PhysRevB.27.5279. URL https://link.aps.org/doi/10.1103/PhysRevB.27.5279.

[83] M.G. Boulay and A. Hime. Technique for direct detection of weakly interacting massive particles using scintillation time discrimination in liquid argon. *Astroparticle Physics*, 25(3):179–182, 2006. ISSN 0927-6505. doi: https://doi.org/10.1016/j.astropartphys.2005.12.009. URL https://www.sciencedirect.com/science/article/pii/S0927650505001830.

[84] P-A Amaudruz, M Baldwin, M Batygov, B Beltran, CE Bina, D Bishop, J Bonatt, G Boorman, Mark Guy Boulay, B Broerman, et al. Design and construction of the deap-3600 dark matter detector. *Astroparticle Physics*, 108:1–23, 2019.

[85] Václav Prajzler, Pavla Nekvindova, Petr Hyps, Oleksiy Lyutakov, and Vitezslav Jerabek. Flexible polymer planar optical waveguides. *Radioengineering*, 23(3): 776–782, 2014.

[86] Wageeh Ramadan, Khaled Sakr, Magda Sayed, Nabila Maziad, and Nabil El-Faramawy. Investigation of acrylic/boric acid composite gel for neutron attenuation. *Nuclear Engineering and Technology*, 52(11):2607–2612, 2020.

[87] Ltd. Proterial. Nanocrystalline soft magnetic material finemet. https://www.proterial.com/e/products/elec/tel/p02_21.html, 1997. Accessed: 2023-04-25.

[88] P-A Amaudruz, M Batygov, B Beltran, CE Bina, D Bishop, J Bonatt, G Boorman, Mark Guy Boulay, B Broerman, T Bromwich, et al. In-situ characterization of the hamamatsu r5912-hqe photomultiplier tubes used in the deap-3600 experiment. *Nuclear Instruments and Methods in Physics Research Section A: Accelerators, Spectrometers, Detectors and Associated Equipment*, 922:373–384, 2019.

[89] D-M Mei and A Hime. Muon-induced background study for underground laboratories. *Physical Review D*, 73(5):053004, 2006.

[90] M Asamoah, BJB Nyarko, JJ Fletcher, RBM Sogbadji, S Yamoah, SE Agbemava, and E Mensimah. Neutron flux distribution in the irradiation channels of am–be neutron source irradiation facility. *Annals of Nuclear Energy*, 38(6):1219–1224, 2011.

[91] T Heindl, T Dandl, M Hofmann, R Krücken, L Oberauer, W Potzel, J Wieser, and A Ulrich. The scintillation of liquid argon. *EPL (Europhysics Letters)*, 91(6): 62002, 2010.

[92] Joseph Reader, Charles H Corliss, WL Wiese, and GA Martin. Wavelengths and transition probabilities for atoms and atomic ions: Part 1. wavelengths, part 2. transition probabilities. *Wavelengths and transition probabilities for atoms and atomic ions: Part 1. Wavelengths*, 1980.

[93] P Linstorm. Nist chemistry webbook, nist standard reference database number 69. *J. Phys. Chem. Ref. Data, Monograph*, 9:1–1951, 1998.

[94] W Krötz, A Ulrich, B Busch, G Ribitzki, and J Wieser. Third excimer continuum of argon excited by a heavy-ion beam. *Physical Review A*, 43(11):6089, 1991.

[95] GM Seidel, RE Lanou, and W Yao. Rayleigh scattering in rare-gas liquids. *Nuclear Instruments and Methods in Physics Research Section A: Accelerators, Spectrometers, Detectors and Associated Equipment*, 489(1-3):189–194, 2002.

[96] Emily Grace, Alistair Butcher, Jocelyn Monroe, and James A Nikkel. Index of refraction, rayleigh scattering length, and sellmeier coefficients in solid and liquid argon and xenon. *Nuclear Instruments and Methods in Physics Research Section A: Accelerators, Spectrometers, Detectors and Associated Equipment*, 867:204–208, 2017.

[97] VM Gehman, SR Seibert, K Rielage, A Hime, Yongchen Sun, D-M Mei, J Maassen, and Daniel Moore. Fluorescence efficiency and visible re-emission spectrum of tetraphenyl butadiene films at extreme ultraviolet wavelengths. *Nuclear Instruments and Methods in Physics Research Section A: Accelerators, Spectrometers, Detectors and Associated Equipment*, 654(1):116–121, 2011.

[98] KK Hamamatsu Photonics. Photomultiplier tubes: Basics and applications. *Edition 3a*, 310, 2007.

[99] Glenn F Knoll. *Radiation detection and measurement*. John Wiley & Sons, 2010.

[100] Shu Xia Tao, Hong Wah Chan, and Harry Van der Graaf. Secondary electron emission materials for transmission dynodes in novel photomultipliers: A review. *Materials*, 9(12):1017, 2016.

[101] P-A Amaudruz, M Baldwin, M Batygov, B Beltran, CE Bina, D Bishop, J Bonatt, G Boorman, Mark Guy Boulay, B Broerman, et al. First results from the deap-3600 dark matter search with argon at snolab. *Physical review letters*, 121(7): 071801, 2018.

[102] Heinz Hugo Loosli. A dating method with39ar. *Earth and planetary science letters*, 63(1):51–62, 1983.

[103] P Benetti, F Calaprice, E Calligarich, M Cambiaghi, F Carbonara, F Cavanna, AG Cocco, F Di Pompeo, N Ferrari, G Fiorillo, et al. Measurement of the specific activity of 39ar in natural argon. *Nuclear Instruments and Methods in Physics Research Section A: Accelerators, Spectrometers, Detectors and Associated Equipment*, 574(1):83–88, 2007.

[104] P Adhikari, R Ajaj, M Alpízar-Venegas, P-A Amaudruz, DJ Auty, M Batygov, B Beltran, H Benmansour, CE Bina, J Bonatt, et al. Pulse-shape discrimination against low-energy ar-39 beta decays in liquid argon with 4.5 tonne-years of deap-3600 data. *The European Physical Journal C*, 81(9):1–13, 2021.

[105] R Ajaj, GR Araujo, M Batygov, B Beltran, CE Bina, MG Boulay, B Broerman, JF Bueno, PM Burghardt, A Butcher, et al. Electromagnetic backgrounds and potassium-42 activity in the deap-3600 dark matter detector. *Physical Review D*, 100(7):072009, 2019.

[106] P-A Amaudruz, M Batygov, B Beltran, K Boudjemline, Mark Guy Boulay, B Cai, T Caldwell, M Chen, R Chouinard, BT Cleveland, et al. Radon backgrounds in the deap-1 liquid-argon-based dark matter detector. *Astroparticle Physics*, 62: 178–194, 2015.

[107] Tina Pollmann, Mark Boulay, and Marcin Kuźniak. Scintillation of thin tetraphenyl butadiene films under alpha particle excitation. *Nuclear Instruments and Methods in Physics Research Section A: Accelerators, Spectrometers, Detectors and Associated Equipment*, 635(1):127–130, 2011.

[108] Huajie Cao, T Alexander, A Aprahamian, R Avetisyan, HO Back, AG Cocco, F DeJongh, G Fiorillo, Cristiano Galbiati, L Grandi, et al. Measurement of scintillation and ionization yield and scintillation pulse shape from nuclear recoils in liquid argon. *Physical Review D*, 91(9):092007, 2015.

[109] P Giampa. On the deap-3600 resurfacing. In *AIP Conference Proceedings*, volume 1921, page 070005. AIP Publishing LLC, 2018.

[110] J Kenneth Shultis and Richard E Faw. *Fundamentals of nuclear science and engineering*. CRC press, 2016.

[111] VA Kudryavtsev, P Zakhary, and B Easeman. Neutron production in (α, n) reactions. *Nuclear Instruments and Methods in Physics Research Section A: Accelerators, Spectrometers, Detectors and Associated Equipment*, 972:164095, 2020.

[112] Joe McLaughlin. The pulse-level saturation correction algorithm. Technical report, Royal Holloway University of London and TRIUMF, 06 2020.

[113] A Butcher, L Doria, J Monroe, F Retiere, B Smith, and J Walding. A method for characterizing after-pulsing and dark noise of pmts and sipms. *Nuclear Instruments and Methods in Physics Research Section A: Accelerators, Spectrometers, Detectors and Associated Equipment*, 875:87–91, 2017.

[114] Joel Kostensalo, Jouni Suhonen, and Kai Zuber. Spectral shapes of forbidden argon β decays as background component for rare-event searches. *Journal of Physics G: Nuclear and Particle Physics*, 45(2):025202, 2017.

[115] Glen Cowan. *Statistical data analysis*. Oxford university press, 1998.

[116] Robert Stainforth. Cuts and Acceptances. Technical report, Carleton University, 06 2017.

[117] Robert Stainforth. Cuts & Acceptances. Technical report, Carleton University, 02 2019.

[118] Jerzy Neyman and Egon Sharpe Pearson. Ix. on the problem of the most efficient tests of statistical hypotheses. *Philosophical Transactions of the Royal Society of London. Series A, Containing Papers of a Mathematical or Physical Character*, 231(694-706):289–337, 1933.

[119] Glen Cowan, Kyle Cranmer, Eilam Gross, and Ofer Vitells. Asymptotic formulae for likelihood-based tests of new physics. *The European Physical Journal C*, 71 (2):1–19, 2011.

[120] Abraham Wald. Tests of statistical hypotheses concerning several parameters when the number of observations is large. *Transactions of the American Mathematical society*, 54(3):426–482, 1943.

[121] Samuel S Wilks. The large-sample distribution of the likelihood ratio for testing composite hypotheses. *The annals of mathematical statistics*, 9(1):60–62, 1938.

[122] Glen Cowan, Kyle Cranmer, Eilam Gross, and Ofer Vitells. Power-constrained limits. *arXiv preprint arXiv:1105.3166*, 2011.

[123] S. Seibert et al. Reactor analysis tool. https://rat.readthedocs.io/en/latest/index.html, 2014.

[124] Ashlea Kemp and Joe McLaughlin. Searching for wimp dark matter with the deap-3600 detector: a profile likelihood approach. Technical report, Royal Holloway University of London, 03 2022.

[125] Phillip DelGobbo. Attenuated alpha backgrounds in the deap-3600 dark matter search experiment. Master's thesis, Carleton University, 2021.

[126] Fred Schuckman Reegan Wormington. Neck alpha analysis trigger rates. Technical report, Carleton University, 12 2022.

[127] Pushpa Adhikari. Dust alpha systematics. Technical report, Carleton University, 01 2023.

[128] Robert Stainforth Shawn Westerdale, Damien Goeldi. Radiogenic neutron backgrounds in the 230 live-day dataset. Technical report, Carleton University, 08 2018.

[129] Shawn Westerdale, theDEAP 3600 Collaboration, et al. Radiogenic neutron background predictions in deap-3600 and in situ measurements. In *Journal of Physics: Conference Series*, volume 1342, page 012081. IOP Publishing, 2020.

[130] James F Ziegler, Matthias D Ziegler, and Jochen P Biersack. Srim–the stopping and range of ions in matter (2010). *Nuclear Instruments and Methods in Physics Research Section B: Beam Interactions with Materials and Atoms*, 268(11-12): 1818–1823, 2010.

[131] Arjan J Koning and Dimitri Rochman. Modern nuclear data evaluation with the talys code system. *Nuclear data sheets*, 113(12):2841–2934, 2012.

[132] Gurpreet Kaur. ^{39}ar lifetime measurement in deap-3600. Technical report, Carleton University, 05 2022.

[133] Werner Brandt and MJPRB Kitagawa. Effective stopping-power charges of swift ions in condensed matter. *Physical Review B*, 25(9):5631, 1982.

[134] Richard J Mathar and Matthias Posselt. Effective-charge theory for the electronic stopping of heavy ions in solids: Stripping criteria and target-electron models. *Physical Review B*, 51(1):107, 1995.

[135] James F Ziegler and Jochen P Biersack. The stopping and range of ions in matter. In *Treatise on heavy-ion science*, pages 93–129. Springer, 1985.

[136] Tadayoshi Doke, Henry J Crawford, Akira Hitachi, Jun Kikuchi, Peter J Lindstrom, Kimiaki Masuda, Eido Shibamura, and Tan Takahashi. Let dependence of scintillation yields in liquid argon. *Nuclear Instruments and Methods in Physics Research Section A: Accelerators, Spectrometers, Detectors and Associated Equipment*, 269(1):291–296, 1988.

[137] S Seth. Alpha quenching factor in liquid argon. In *Canadian Association of Physicists Annual Conference*. Presented at the Canadian Association of Physicists Congress at McMaster University, Hamilton Ontario, Canada, 2022.

[138] AC Sinnock and BL Smith. Refractive indices of the condensed inert gases. *Physical Review*, 181(3):1297, 1969.

[139] M Babicz, S Bordoni, T Cervi, Z Collins, A Fava, U Kose, M Meli, A Menegolli, M Nessi, F Pietropaolo, et al. Experimental study of the propagation of scintillation light in liquid argon. *Nuclear Instruments and Methods in Physics Research Section A: Accelerators, Spectrometers, Detectors and Associated Equipment*, 936: 178–179, 2019.

[140] Shawn Westerdale. Updating the lar optics with new measurements at 128 nm. Technical report, Carleton University, 03 2019.

[141] Dustin Stolp, Olivia Dalager, Navneet Dhaliwal, Benjamin Godfrey, Michael Irving, Kareem Kazkaz, Aaron Manalaysay, Christian Neher, Scott Stephenson, and Mani Tripathi. An estimation of photon scattering length in tetraphenylbutadiene. *Journal of Instrumentation*, 11(03):C03025, 2016.

[142] Ettore Segreto. Evidence of delayed light emission of tetraphenyl-butadiene excited by liquid-argon scintillation light. *Physical Review C*, 91(3):035503, 2015.

[143] XENON Collaboration, E Aprile, J Aalbers, F Agostini, M Alfonsi, L Althueser, FD Amaro, M Anthony, F Arneodo, L Baudis, et al. Dark matter search results from a one ton-year exposure of xenon1t. *Physical review letters*, 121(11):111302, 2018.

[144] I. Ostrovskiy, F. Retiere, D. Auty, J. Dalmasson, T. Didberidze, R. DeVoe, G. Gratta, L. Huth, L. James, L. Lupin-Jimenez, N. Ohmart, and A. Piepke. Characterization of silicon photomultipliers for nexo. *IEEE Transactions on Nuclear Science*, 62(4):1825–1836, 2015. doi: 10.1109/TNS.2015.2453932.

[145] *VUV-MPPC 4th Generation (VUV4)*. Hamamatsu Photonics K.K., 2017.

[146] L. Baudis and et al. Characterisation of Silicon Photomultipliers for liquid xenon detectors. *Journal of Instrumentation*, 13(10):P10022, 2018. ISSN 1748-0221. doi: 10.1088/1748-0221/13/10/P10022. URL http://stacks.iop.org/1748-0221/13/i=10/a=P10022?key=crossref.708451f1c52b236a6b91d6bafd39b59e.

[147] *MPPC: S13360 Series*. Hamamatsu Photonics K.K., 2022.

[148] A. Falcone and et al. Cryogenic sipm arrays for the dune photon detection system. *Nuclear Instruments and Methods in Physics Research Section A*, 985:164648, 2021. ISSN 0168-9002. doi: https://doi.org/10.1016/j.nima.2020.164648.

[149] F. Carnesecchi. Light detection in DarkSide-20k. *Journal of Instrumentation*, 15 (03):C03038–C03038, 2020. doi: 10.1088/1748-0221/15/03/c03038.

[150] G. Gallina and et al. Characterization of the hamamatsu vuv4 mppcs for nexo. *Nuclear Instruments and Methods in Physics Research Section A*, 940:371–379, 2019. ISSN 0168-9002. doi: https://doi.org/10.1016/j.nima.2019.05.096. URL https://www.sciencedirect.com/science/article/pii/S0168900219308034.

[151] Massimo Mazzillo, Giovanni Condorelli, Delfo Sanfilippo, Giuseppina Valvo, Beatrice Carbone, Giorgio Fallica, Sergio Billotta, Massimiliano Belluso, Giovanni Bonanno, Luigi Cosentino, Alfio Pappalardo, and Paolo Finocchiaro. Silicon photomultiplier technology at stmicroelectronics. *IEEE Transactions on Nuclear Science*, 56(4):2434–2442, 2009. doi: 10.1109/TNS.2009.2024418.

[152] Stephen T Thornton and Andrew Rex. *Modern physics for scientists and engineers*. Cengage Learning, 2012.

[153] Joachim Wagner and Jesús A del Alamo. Band-gap narrowing in heavily doped silicon: A comparison of optical and electrical data. *Journal of applied physics*, 63 (2):425–429, 1988.

[154] S. Gundacker and A. Heering. The silicon photomultiplier: fundamentals and applications of a modern solid-state photon detector. *Physics in Medicine & Biology*, 65(17):17TR01, 2020.

[155] Jiali Jiang, Jianquan Jia, Tianqi Zhao, Kun Liang, Ru Yang, and Dejun Han. Recovery time of silicon photomultiplier with epitaxial quenching resistors. *Instruments*, 1(1):5, 2017.

[156] F. Acerbi and et al. Nuv silicon photomultipliers with high detection efficiency and reduced delayed correlated-noise. *IEEE Transactions on Nuclear Science*, 62 (3):1318–1325, 2015. doi: 10.1109/TNS.2015.2424676.

[157] C. Piemonte and et al. Performance of nuv-hd silicon photomultiplier technology. *IEEE Transactions on Electron Devices*, 63(3):1111–1116, 2016. doi: 10.1109/ TED.2016.2516641.

[158] Martin A Green and Mark J Keevers. Optical properties of intrinsic silicon at 300 k. *Progress in Photovoltaics: Research and applications*, 3(3):189–192, 1995.

[159] G. Gallina and et al. Characterization of sipm avalanche triggering probabilities. *IEEE Transactions on Electron Devices*, 66(10):4228–4234, 2019. doi: 10.1109/ TED.2019.2935690.

[160] G Vincent, A Chantre, and D Bois. Electric field effect on the thermal emission of traps in semiconductor junctions. *Journal of Applied Physics*, 50(8):5484–5487, 1979.

[161] F. Acerbi and et al. Cryogenic Characterization of FBK HD Near-UV Sensitive SiPMs. *IEEE Transactions on Electron Devices*, 64(2):521–526, feb 2017. ISSN 0018-9383. doi: 10.1109/TED.2016.2641586. URL http://ieeexplore.ieee. org/document/7807295/.

[162] WTRW Shockley and WT Read Jr. Statistics of the recombinations of holes and electrons. *Physical review*, 87(5):835, 1952.

[163] Roger Newman. Visible light from a silicon $p - n$ junction. *Phys. Rev.*, 100:700–703, 1955. doi: 10.1103/PhysRev.100.700. URL https://link.aps.org/doi/10. 1103/PhysRev.100.700.

[164] J. Rosado and et al. Modeling crosstalk and afterpulsing in silicon photomultipliers. *Nuclear Instruments and Methods in Physics Research Section A*, 787: 153–156, 2015. ISSN 01689002. doi: 10.1016/j.nima.2014.11.080.

[165] A. Nepomuk Otte. On the efficiency of photon emission during electrical breakdown in silicon. *Nuclear Instruments and Methods in Physics Research Section A*, 610(1):105–109, 2009. ISSN 01689002. doi: 10.1016/j.nima.2009.05.085.

URL http://dx.doi.org/10.1016/j.nima.2009.05.085https://linkinghub.
elsevier.com/retrieve/pii/S0168900209010390.

[166] N. Akil and et al. A multimechanism model for photon generation by silicon junctions in avalanche breakdown. *IEEE Transactions on Electron Devices*, 46(5): 1022–1028, 1999.

[167] DK. Gautam and et al. Photon emission from reverse-biased silicon pn junctions. *Solid-state electronics*, 31(2):219–222, 1988.

[168] A.L. Lacaita and et al. On the bremsstrahlung origin of hot-carrier-induced photons in silicon devices. *IEEE Transactions on Electron Devices*, 40(3):577–582, 1993. ISSN 00189383. doi: 10.1109/16.199363.

[169] Giacomo Gallina. *Development of a single vacuum ultra-violet photon-sensing solution for nEXO*. PhD thesis, University of British Columbia, 2021. URL https://open.library.ubc.ca/collections/ubctheses/24/items/1.0396697.

[170] K. Boone and et al. Delayed avalanches in Multi-Pixel Photon Counters. *Journal of Instrumentation*, 12(07):P07026–P07026, 2017. ISSN 1748-0221. doi: 10.1088/1748-0221/12/07/P07026. URL http://ieeexplore.ieee.org/document/6551378/http://stacks.iop.org/1748-0221/12/i=07/a=P07026?key=crossref.0cd023e7bf556fc7cf3aa7cdc368e1b5https://iopscience.iop.org/article/10.1088/1748-0221/12/07/P07026.

[171] A. N. Otte and et al. Characterization of three high efficiency and blue sensitive silicon photomultipliers. *Nuclear Instruments and Methods in Physics Research Section A: Accelerators, Spectrometers, Detectors and Associated Equipment*, 846:106–125, 2017. ISSN 01689002. doi: 10.1016/j.nima.2016.09.053. URL http://arxiv.org/abs/1606.05186http://dx.doi.org/10.1016/j.nima.2016.09.053http://linkinghub.elsevier.com/retrieve/pii/S0168900216309901https://linkinghub.elsevier.com/retrieve/pii/S0168900216309901.

[172] A. Jamil and et al. VUV-Sensitive Silicon Photomultipliers for Xenon Scintillation Light Detection in nEXO. *IEEE Transactions on Nuclear Science*, 65(11):2823–2833, 2018. ISSN 0018-9499. doi: 10.1109/TNS.2018.2875668. URL https://ieeexplore.ieee.org/document/8490731/.

[173] M Grodzicka-Kobylka, T Szczesniak, and M Moszyński. Comparison of sensl and hamamatsu 4×4 channel sipm arrays in gamma spectrometry with scintillators. *Nuclear Instruments and Methods in Physics Research Section A: Accelerators, Spectrometers, Detectors and Associated Equipment*, 856:53–64, 2017.

[174] S Al Kharusi, A Alamre, JB Albert, M Alfaris, G Anton, IJ Arnquist, I Badhrees, PS Barbeau, D Beck, V Belov, et al. nexo pre-conceptual design report. *arXiv preprint arXiv:1805.11142*, 2018.

[175] Q. R. Ahmad and et al. Measurement of the rate of $\nu_e + d \rightarrow p + p + e^-$ interactions produced by ^8b solar neutrinos at the sudbury neutrino observatory. *Phys. Rev. Lett.*, 87:071301, Jul 2001. doi: 10.1103/PhysRevLett.87.071301. URL https://link.aps.org/doi/10.1103/PhysRevLett.87.071301.

[176] Carlo Giunti and Chung W Kim. *Fundamentals of neutrino physics and astrophysics.* Oxford university press, 2007.

[177] RN Mohapatra, S Antusch, KS Babu, Gabriela Barenboim, Mu-Chun Chen, A De Gouvêa, P De Holanda, B Dutta, Y Grossman, A Joshipura, et al. Theory of neutrinos: a white paper. *Reports on Progress in Physics*, 70(11):1757, 2007.

[178] N Ackerman, B Aharmim, M Auger, DJ Auty, PS Barbeau, K Barry, L Bartoszek, E Beauchamp, V Belov, C Benitez-Medina, et al. Observation of two-neutrino double-beta decay in xe 136 with the exo-200 detector. *Physical Review Letters*, 107(21):212501, 2011.

[179] Govinda Adhikari, S Al Kharusi, E Angelico, G Anton, IJ Arnquist, I Badhrees, J Bane, V Belov, EP Bernard, T Bhatta, et al. nexo: neutrinoless double beta decay search beyond 1028 year half-life sensitivity. *Journal of Physics G: Nuclear and Particle Physics*, 49(1):015104, 2021.

[180] VN Solovov, A Hitachi, V Chepel, MI Lopes, R Ferreira Marques, and AJPL Policarpo. Detection of scintillation light of liquid xenon with a laapd. In *2000 IEEE Nuclear Science Symposium. Conference Record (Cat. No. 00CH37149)*, volume 1, pages 7–58. IEEE, 2000.

[181] M Auger, DJ Auty, PS Barbeau, L Bartoszek, E Baussan, E Beauchamp, C Benitez-Medina, M Breidenbach, D Chauhan, B Cleveland, et al. The exo-200 detector, part i: detector design and construction. *Journal of Instrumentation*, 7 (05):P05010, 2012.

[182] Babak Abi, Roberto Acciarri, Mario A Acero, Giorge Adamov, David Adams, Marco Adinolfi, Zubayer Ahmad, Jhanzeb Ahmed, Tyler Alion, S Alonso Monsalve, et al. Volume i. introduction to dune. *Journal of instrumentation*, 15(08): T08008, 2020.

[183] Dune Collaboration et al. Long-baseline neutrino facility (lbnf) and deep underground neutrino experiment (dune) conceptual design report volume 1: The lbnf and dune projects. *arxiv. org*, 2016.

[184] B Abi, R Acciarri, MA Acero, G Adamov, D Adams, M Adinolfi, Z Ahmad, J Ahmed, T Alion, S Alonso Monsalve, et al. Long-baseline neutrino oscillation physics potential of the dune experiment. *The European Physical Journal C*, 80 (10):1–34, 2020.

[185] X Qian and P Vogel. Neutrino mass hierarchy. *Progress in Particle and Nuclear Physics*, 83:1–30, 2015.

[186] Babak Abi, Roberto Acciarri, Mario A Acero, Giorge Adamov, David Adams, Marco Adinolfi, Zubayer Ahmad, Jhanzeb Ahmed, Tyler Alion, S Alonso Monsalve, et al. Deep underground neutrino experiment (dune), far detector technical design report, volume ii: Dune physics. *arXiv preprint arXiv:2002.03005*, 2020.

[187] AA Machado, E Segreto, D Warner, A Fauth, B Gelli, R Maximo, A Pissolatti, L Paulucci, and F Marinho. The x-arapuca: an improvement of the arapuca device. *Journal of Instrumentation*, 13(04):C04026, 2018.

[188] Alberto Gola, Fabio Acerbi, Massimo Capasso, Marco Marcante, Alberto Mazzi, Giovanni Paternoster, Claudio Piemonte, Veronica Regazzoni, and Nicola Zorzi. Nuv-sensitive silicon photomultiplier technologies developed at fondazione bruno kessler. *Sensors*, 19(2):308, 2019.

[189] *MPPC: S14160/S14161 Series*. Hamamatsu Photonics K.K., 2020.

[190] Bianca Bottino. Darkside-20k and the future liquid argon dark matter program. *PoS, EPS-HEP2021*, 169, 2022.

[191] E Aprile, Jelle Aalbers, F Agostini, M Alfonsi, L Althueser, FD Amaro, Vasile C Antochi, E Angelino, JR Angevaare, F Arneodo, et al. Projected wimp sensitivity of the xenonnt dark matter experiment. *Journal of Cosmology and Astroparticle Physics*, 2020(11):031, 2020.

[192] DS Akerib, CW Akerlof, SK Alsum, HM Araújo, M Arthurs, X Bai, AJ Bailey, J Balajthy, S Balashov, D Bauer, et al. Projected wimp sensitivity of the lux-zeplin dark matter experiment. *Physical Review D*, 101(5):052002, 2020.

[193] F Carnesecchi. Light detection in darkside-20k. *Journal of Instrumentation*, 15 (03):C03038, 2020.

[194] Joseph Biagio McLaughlin, Giacomo Gallina, Fabrice Retière, De St Croix, Pietro Giampa, Mahsa Mahtab, Peter Margetak, Lars Martin, Nicolas Massacret, Jocelyn Monroe, et al. Characterisation of sipm photon emission in the dark. *Sensors*, 21 (17):5947, 2021.

[195] W Haecker. Infrared radiation from breakdown plasmas in si, gasb, and ge: Evidence for direct free hole radiation. *physica status solidi (a)*, 25(1):301–310, 1974.

[196] A. G. Martin. Self-consistent optical parameters of intrinsic silicon at 300 k including temperature coefficients. *Solar Energy Materials and Solar Cells*, 92: 1305–1310, 2008. ISSN 0927-0248. doi: 10.1016/j.solmat.2008.06.009. URL http://www.sciencedirect.com/science/article/pii/S0927024808002158.

[197] R Mirzoyan and et al. Light emission in si avalanches. *Nuclear Instruments and Methods in Physics Research Section A*, 610(1):98–100, 2009.

[198] Charles Kittel. *Introduction to solid state physics*, volume 6. Wiley New York, 1986.

[199] Jason McClure and Ed Gooding. Intellical: A novel method for calibration of imaging spectrographs. In *AIP Conference Proceedings*, volume 1267, pages 806–807. American Institute of Physics, 2010.

[200] John Bertrand Johnson. Thermal agitation of electricity in conductors. *Physical review*, 32(1):97, 1928.

[201] Harry Nyquist. Thermal agitation of electric charge in conductors. *Physical review*, 32(1):110, 1928.

[202] CG Ryan, E Clayton, WL Griffin, SH Sie, and DR Cousens. Snip, a statistics-sensitive background treatment for the quantitative analysis of pixe spectra in geoscience applications. *Nuclear Instruments and Methods in Physics Research Section B: Beam Interactions with Materials and Atoms*, 34(3):396–402, 1988.

[203] Miroslav Morháč, Ján Kliman, Vladislav Matoušek, Martin Veselský, and Ivan Turzo. Background elimination methods for multidimensional coincidence γ-ray spectra. *Nuclear Instruments and Methods in Physics Research Section A: Accelerators, Spectrometers, Detectors and Associated Equipment*, 401(1):113–132, 1997.

[204] J. C. Jackson and et al. Comparing leakage currents and dark count rates in Geiger-mode avalanche photodiodes. *Applied Physics Letters*, 80(22):4100–4102, 2002. ISSN 0003-6951. doi: 10.1063/1.1483119.

[205] E. Engelmann and et al. Spatially resolved dark count rate of sipms. *The European Physical Journal C*, 78(11):1–8, 2018.

[206] P. Lv and et al. Reflectance of silicon photomultipliers at vacuum ultraviolet wavelengths. *IEEE Transactions on Nuclear Science*, 67(12):2501–2510, 2020. doi: 10.1109/TNS.2020.3035172.

[207] David J Griffiths. *Introduction to electrodynamics*. Prentice Hall New Jersey, 1962.

[208] David E Aspnes and AA Studna. Dielectric functions and optical parameters of si, ge, gap, gaas, gasb, inp, inas, and insb from 1.5 to 6.0 ev. *Physical review B*, 27(2):985, 1983.

[209] Luis V. Rodríguez-de Marcos and et al. Self-consistent optical constants of sio2 and ta2o5 films. *Opt. Mater. Express*, 6(11):3622–3637, 2016. doi: 10.1364/OME. 6.003622.

[210] Z. Zhang and et al. Light emission from si avalanche mode leds as a function of e field control, impurity scattering, and carrier density balancing. In *Fifth Conference on Sensors, MEMS, and Electro-Optic Systems*, volume 11043, page 1104307. International Society for Optics and Photonics, 2019.

[211] PA Wolff. Theory of optical radiation from breakdown avalanches in germanium. *Journal of Physics and Chemistry of Solids*, 16(3-4):184–190, 1960.

[212] T. Figielski and A. Torun. On the origin of light emitted from reverse biased pn junctions. In *Proc. Int. Conf. Phys. Semiconductors*, page 853, 1962.

[213] C. Piemonte and et al. Performance of NUV-HD Silicon Photomultiplier Technology. *IEEE Transactions on Electron Devices*, 63(3):1111–1116, 2016. ISSN 00189383. doi: 10.1109/TED.2016.2516641.

[214] Siegmund Brandt and S Brandt. *Data analysis*. Springer, 1998.